

https://dspace.org/

# Manganese micro-alloyed titanium aluminide alloys fabricated using laser engineering net shaping

**Motha, Sibusisiwe**

**2022**

https://hdl.handle.net/10539/34907

Downloaded from a DSpace repository. https://dspace.org/




UNIVERSITY OF THE
WITWATERSRAND,
JOHANNESBURG

# Manganese micro-alloyed titanium aluminide alloys fabricated using laser engineered net shaping

Sibusisiwe Motha

A dissertation submitted to the Faculty of Engineering and the Built Environment, University of the Witwatersrand, Johannesburg, in fulfilment of the requirements for the degree of Master of Science in Engineering

Johannesburg, 2022

# Declaration

I declare that this thesis is my own unaided work. It is being submitted to the Degree of Master of Science in Engineering to the University of the Witwatersrand, Johannesburg. It has not been submitted before for any degree of examination to any other University.

(Signature of Candidate)

30th day of September  2022 year

# Abstract

This dissertation focuses on the fabrication of Ti-Al-Mn alloys using Laser Engineered Net Shaping (LENS) as a fabrication process. Through the determination of the best combination of LENS parameters, Ti-based alloy microstructures yielding the best combination mechanical properties which include improved ductility and strength, were established.

Microstructures and nanostructures were analysed through Scanning Electron Microscopy, X-ray Diffraction and Electron Backscatter Diffraction. Mechanical properties were studied by performing microhardness tests, nano indentation, measurement of post process thermal cracks and Gleeble tests. Studies of these structures and mechanical behaviour were connected using literature. Numerical models were established to illustrate the thermodynamics behind using LENS as a fabrication process to produce Ti-based alloys.

It was established that high Mn powder feed rates in the production of Ti-Mn alloys led to the production of undesirable $Mn_{0.52}Ti_{0.48}$(s) phase which is brittle and has high density. However, the production of TiMn using low Mn powder feed rates yielded structures comprised of disordered α-HCP dendrites within a β-BCC matrix with mechanical properties that include improved mechanical strength. However, the addition of Al to TiMn, is detrimental for ductility. Heat treatment procedures led to an increase in dislocation densities and reduced hardness. Low Mn TiMn alloys yield improved fracture stress compared to TiAl and TiAlMn, and can withstand temperatures as high as 1300℃. It has also been observed that lower laser power settings led to rapid post processing thermal cracking due to reduced thermal gradients which lead to higher thermal residual stresses during processing which rapidly exceed the fracture toughness. High temperature ductility and mechanical strength of TiAlMn improved simultaneously until a strain value of 34.58%, beyond which yield strength deteriorated. It was also established that ductility and mechanical strength are favoured by dislocation motion. However, beyond the strain value of 34.58%, dislocation densities reduce with reducing yield strength, which further supports the existing imbalance between mechanical strength and ductility in TiAl based alloys

Keywords: Titanium alloys; Manganese; Aluminium; 3-Dimensional printing; Laser Processing; Microstructures; High Temperature alloys; Lightweight materials.

# Dedication

Dedicated to my brother Smangaliso Ngwenya.

In loving memory of my mother

Evelyn Smash Sibaca (1961/09/20-2013/04/30),

my grandmother Joyce Nomasiko Sibaca (1929/06/29-2012/02/05)

and my Mkhulu, my favourite mathematics teacher Sibangani Answer Sibaca (1939/06/25-1996/11/20).

Love you always!!

Forever in my heart.

And to all my friends and family who supported me throughout this process.

# Acknowledgements

I would like to thank God almighty for carrying me through great hardships leading me to a point of granting me an opportunity to finalise this dissertation.

I would firstly like to express great gratitude to my supervisor, Prof Nthabiseng Maledi for consistent supervision, motivation, guidance, nurture and for believing in me. I am thankful to her for giving me hope and another chance to dream about success. Thank you for the support and life advice which assisted in putting together this dissertation. Secondly, I would like to express gratitude to my other supervisor Dr Monamme Tlotleng for supervision, assisting with the construction of the alloys studied, academic guidance and support throughout this research. Thank you to CSIR for allowing me to carry out this research in their facility. Thank you to Manganese Mining Company (MMC) for supplying Mn powder metal for this research.

I would also like to thank Dr Michael Oluwatosin Bodunrin for assisting with Gleeble Testing and great academic advice.

I would like to thank Dr Clive Oliphant form NMISA for assisting with EBSD.

I would also like to thank Mr Dzara for glass blowing services and Dr David Whitefield for allowing me to use his furnace for heat treatment, and Mr Shadrak for helping me with sample preparation and Microhardness testing. I would like to thank Mrs Petra Dinham for helping me with SEM and EDS.

I would like to thank Rudolf Kanyane at Tshwane University of Technology for assisting with nano indentation tests.

I would like to thank Dr Sadiq Abiola RAJI from Tshwane University of Technology and Nana Arthur from CSIR and University of Pretoria for teaching me how to use the LENS machine.

I would like to thank Orevaoghene Eterigho-Ikelegbe for assisting with TGA.

I would like to thank Professor Micheal Lee from Nelson Mandela University for great academic advice.

I would like to thank Dr Roy Forbes for academic assistance with XRD results.

Lastly, I would like to thank my brother for constantly inspiring me, loving me and supporting me throughout.

# Contributions from this study

***Journal Articles***

Motha, S., Maledi, N. and Tlotleng, M., 2022. Characterization of Mn micro alloyed TiAl fabricated using Laser Engineered Net Shaping (LENS). *Materials Today: Proceedings*. https://doi.org/10.1016/j.matpr.2022.04.817

***Conference Proceedings***

Motha, S.N., Maledi, N. and Tlotleng, M., Characterization of titanium aluminide alloys fabricated using laser engineered net shaping, The 21st Annual International RAPDASA Conference, November 2020. https://site.rapdasa.org/wp-content/uploads/2021/02/12-Characterization-of-titanium-aluminide-alloys.pdf

# Contents


Declaration i
Abstract ii
Dedication iii
Acknowledgements iv
Contributions from this study v
List of Figures viii
Nomenclature xix
Chapter 1 1
Chapter 2: Literature Review 6
Chapter 3: Experimental Procedure 39
3.1 Numerical Models used for characterisation 49
Chapter 4: Results 53
4.1 Binary TiAl 53
4.1.1 Microstructures of as-produced TiAl binary alloys 53
4.1.2 Microstructures of heat-treated TiAl binary alloys 56
4.1.3 X-ray Diffraction (XRD) of TiAl alloy 58
4.1.4 Electron Backscatter Diffraction (EBSD) of TiAl alloy 65
4.1.5 Microhardness of TiAl alloys 66
4.1.7 Mechanical Properties of Binary TiAl according to nanoindentation 68
4.1.8 Thermogravimetric analysis (TGA) of TiAl alloys 70
4.2. Binary TiMn 74
4.2.1 Microstructures of As-produced TiMn alloys 74
4.2.2 Microstructures of Heat-Treated Ti-Mn alloys 79
4.2.3 X-ray diffraction (XRD) for TiMn alloys 85
4.2.5 Microhardness of TiMn Alloys 97
4.2.6 Fracture stress of TiMn alloys 99
4.2.7 Mechanical Properties of Binary TiMn alloys according to Nanoindentation 100
4.2.8 Thermogravimetric Analysis 102
4.3. Ternary TiAlMn 107
4.3.1 Microstructures of As produced TiAlMn alloys 107
4.3.2 Microstructures of Heat Treated TiAlMn Alloys: 108
4.3.3 X-ray Diffraction of TiAlMn alloys 108
4.3.4 Electron Backscatter Diffraction (EBSD) for TiAlMn alloys 112
4.3.5 Microhardness of TiAlMn alloys 119

4.3.6 Fracture stress of TiAlMn alloys 119
4.3.7 Thermogravimetric Analysis 120
4.3.8 Mechanical Properties of Ternary TiAlMn alloys according to Nanoindentation 124
4.3.9 Gleeble Testing 127
4.4. Numerical Modelling 134
4.5.Densification 141
Chapter 5: Discussions 142
Chapter 6: Conclusions and Recommendations 153
7. References 155
8. APPENDICES 160
APPENDIX A: Microhardness Profiles 161
APPENDIX B: SOLVING FOR $T_S$ ON MICROSOFT EXCEL 163
9. PUBLICATIONS 165

# List of Figures

Figure 2.1: Tetragonal TiAl Gamma phase 7
Figure 2.2: Hexagonal $Ti_3Al$ Alpha-2 7
Figure 2.3: Orientation of $\alpha_2$ as parent grain and $\gamma$ as the domain structure within a lamella colony 8
Figure 2.4: Hexagonal Close Packed α-phase 17
Figure 2.5: Body Centred Cubic β-phase 17
Figure 2.6: Burger's orientation relationship between β and α phase. 18
Figure 2.7: Binary Ti-Mn Phase Diagram by Murray *et al* (1981) 19
Figure 2.8: Ternary Phase diagrams for Ti-Al-Mn compiled by Kianuma *et al* (2000) 23
Figure 2.9: Binary Ti-Al phase diagram 28
Figure 2.10: Bulky 3-D geometries 36
Figure 3.1: SEM micrograph of TiAl powder 39
Figure 3.2: SEM micrograph of Mn powder obtained from MMC. 39
Figure 3.3: Set up used for LENS to produce samples 40
Figure 3.4: Ti-Mn Samples printed on Ti-6Al-4V substrate 41
Figure 3.5: TiAlMn samples printed on Ti-6Al-4V substrate 41
Figure 3.6: Image displaying how SEM functions 44
Figure 3.7: Sketch displaying how EBSD functions 45
Figure 3.8: Equipment Setup of EBSD 45
Figure 3.9: Illustration displaying how XRD functions 46
Figure 3.10: TGA Setup used for analysis 48
Figure 3.11: Aerial view of reprinted TiAlMn-1 49
Figure 3.12: Width measurement of reprinted TiAlMn-1 (20mm). 49
Figure 3.13: Display of height of reprinted TiAlMn-1 (20mm) 49
Figure 3.14: Length measurement of reprinted TiAlMn-1 (40mm) 49
Figure 4.1: Ti-Al-2.1 microstructure containing β equiaxed lamellar dendrites 54
Figure 4.2: Ti-Al-2.2 microstructure containing nearly α+γ lamella dendrite. 54
Figure 4.3: Ti-Al-2.3 microstructure comprises of α+γ nearly lamella equiaxed grains 54
Figure 4.4: Ti-Al-2.4 microstructure comprises of equiaxed $\alpha_2$ +γ lamella grains with γ rich grains 54
Figure 4.5: Ti-Al-3.1 microstructure comprises of α columnar dendrites 55
Figure 4.6: Ti-Al-3.2 microstructure comprises of α columnar dendrites. 55
Figure 4.7: Ti-Al-3.3 microstructure comprises of α+γ basket weave like microstructure displaying the precipitation of γ on α. 55
Figure 4.8: Ti-Al-3.4 microstructure comprising of $\alpha_2$ +γ equiaxed lamellar grains. 55
Figure 4.9: Heat treated Ti-Al-2.1 comprises of fine $\alpha_2$ +γ equiaxed lamellar grains 57
Figure 4.10: Heat treated Ti-Al-2.2 comprises of $\alpha_2$ +γ equiaxed lamellar grains 57

Figure 4.11: Heat treated Ti-Al-2.3 comprises of coarser $\alpha_2+\gamma$ equiaxed lamellar grains 57
Figure 4.12: Heat treated Ti-Al-2.4 comprises of coarse $\alpha_2+\gamma$ equiaxed grains 57
Figure 4.13: Heat treated Ti-Al-3.1 comprising of uniform γ duplex microstructure 58
Figure 4.14: Heat treated Ti-Al-3.2 also comprising of uniform γ duplex microstructure 58
Figure 4.15: Heat treated Ti-Al-3.3 uniform γ duplex microstructure is porous. 58
Figure 4.16: Heat treat Ti-Al -3.4 microstructure has high number of large pores 58
Figure 4.17: Rietveld refinement of XRD outcomes of as produced TiAl 2.3 displaying phases. 59
Figure 4.18: Rietveld refinement of XRD outcomes of heat treated TiAl2.3. 59
Figure 4.19: As produced tetragonal $Ti_{0.4}Al_{0.6}$ with lattice parameters: a=b=5.65844Å; c=4.27050Å 60
Figure 4.20: Heat treated tetragonal $Ti_{0.15}Al_{0.85}$ with lattice parameters: a=b=9.03931Å; c=4.65872Å 60
Figure 4.21: As produced hexagonal $Ti_{0.7}Al_{0.3}$ with lattice parameters: a=2.48044Å; c= 1.70823Å 61
Figure 4.22: Heat treated hexagonal $Ti_3Al$ with lattice parameters: a=2.33136Å; c=2.78449Å 61
Figure 4.23: Rietveld refinement of XRD outcomes of as produced TiAl 2.4 61
Figure 4.24: Rietveld Refinement of XRD outcomes of heat treated TiAl 2.4. 61
Figure 4.25:As-produced tetragonal $Ti_{0.25}Al_{0.75}$ with Lattice parameters: a=b=5.65642Å; c=4.25863Å 62
Figure 4.26: Heat treated tetragonal TiAl with lattice parameters a=b=4.02903Å; c=1.31601Å. 62
Figure 4.27: As produced hexagonal $Ti_{0.6}Al_{0.4}$ with lattice parameters: a=b=2.47547Å; c=1.99574Å 62
Figure 4.28: Heat treated hexagonal $Ti_{19}Al_6$ with lattice parameters: a=b=4.14000Å; c=14.07095Å. 62
Figure 4.29: Plot illustrating peak width broadening of as produced TiAl2.3. 63
Figure 4.30: Plot illustrating peak broadening of heat treated TiAl2.3 63
Figure 4.31: Plot illustrating peak width broadening of as produced TiAl2.4 63
Figure 4.32: Plot illustrating peak broadening of heat treated TiAl2.4. 63
Figure 4.33: EBSD colour coded image displaying $\alpha_2$ phase with traces of γ in as produced Ti-Al-2.3 65
Figure 4.34: EBSD inverse pole figure (IPF) displaying crystal orientation map for as produced Ti-Al-2.3 65

Figure 4.35: Graphical representation of the effect of Al feed rates and Ar carrier gas flowrates on microhardness of as produced TiAl alloys 66
Figure 4.36: Microhardness of Heat-treated Ti-Al alloys 67
Figure 4.37: Optical micrograph of crack length of as produced Ti-Al-2.3. 68
Figure 4.38: Optical micrograph of crack length of heat treated Ti-Al-2.3. 68
Figure.4.39: Relationship between indentation displacement and applied load for twelve indentations on as-produced TiAl 2.3. 69
Figure 4.40: Curve representing average relationship of indentation displacement and applied load for as-produced TiAl 2.3. 69
Figure 4.41: Relationship between indentation displacement and applied load for twenty indentations on heat-treated TiAl 2.3 69
Figure 4.42: Curve representing average relationship of indentation displacement and applied load for heat-treated TiAl 2.3. 69
Figure 4.43: Relationship between indentation displacement and applied load for twelve indentations on as-produced TiAl 2.4. 70
Figure 4.44: Curve representing average relationship of indentation displacement and applied load for as-produced TiAl 2.4. 70
Figure 4.45: Relationship between indentation displacement and applied load for twenty indentations on heat-treated TiAl 2.4. 70
Figure 4.46: Curve representing average relationship of indentation displacement and applied load for heat-treated TiAl 2.4. 70
Figure 4.47: Mass loss as a function of time for as-produced and heat-treated TiAl-2.4 oxidation behaviour. 71
Figure 4.48: Mass loss as a function of temperature for as-produced and heat-treated TiAl-2.4 72
Figure 4.49: Oxide scale thickness of as-produced TiAl-2.4 73
Figure 4.50 Thickness of various oxide layers of as-produced TiAl-2.4 73
Figure 4.51: Microstructure underneath oxide scale of as-produced TiAl-2.4 73
Figure 4.52: EDX of $Al_2O_3$- 67.62(at%O); 28.34(at%Al); 4.04(at%Ti) 73
Figure 4.53: EDX of $TiO_2$- 51.22(at%O); 27.72(at%Ti); 21.06(at%Al) 73
Figure 4.54: Oxide scale thickness of heat-treated TiAl-2.4 74
Figure 4.55: Thickness of various oxide layers of heat-treated TiAl-2.4 74
Figure 4.56: Microstructure underneath oxide scale of heat treated TiAl-2.4 74
Figure 4.57: As-produced Ti-Mn-1. 75
Figure 4.58: As-produced Ti-Mn-2 75
Figure 4.59: As-produced Ti-Mn-3 75
Figure 4.60: As-produced Ti-Mn-4 75
Figure 4.61: As-produced Ti-Mn-5 75

Figure 4.62: As-produced Ti-Mn-6 75
Figure 4.63: As-produced Ti-Mn-7 76
Figure 4.64: As-produced Ti-Mn-8 76
Figure 4.65: As-produced Ti-Mn-9 76
Figure 4.66: As produced Ti-Mn-10 77
Figure 4.67: As-produced Ti-Mn-11 77
Figure 4.68: As-produced Ti-Mn-12 77
Figure 4.69: As-produced Ti-Mn-13 77
Figure 4.70: As-produced Ti-Mn-14 77
Figure 4.71: As-produced Ti-Mn-15 77
Figure 4.72: As-produced Ti-Mn-16 78
Figure 4.73: As-produced Ti-Mn-17 78
Figure 4.74: As-produced Ti-Mn-18 78
Figure 4.75: Heat-treated Ti-Mn-1 80
Figure 4.76: Heat-treated Ti-Mn-2 80
Figure 4.77: Heat-treated Ti-Mn-3 80
Figure 4.78: Heat-treated Ti-Mn-4 80
Figure 4.79: Heat-treated Ti-Mn-5 80
Figure 4.80: Heat-treated Ti-Mn-6 80
Figure 4.81: Heat-treated Ti-Mn-7 80
Figure 4.82: Heat-treated Ti-Mn-8 80
Figure 4.83: Heat-treated Ti-Mn-10 81
Figure 4.84: Heat-treated Ti-Mn-11 81
Figure 4.85.: Heat-treated Ti-Mn-12 81
Figure 4.86: Heat-treated Ti-Mn-13 82
Figure 4.87: Heat-treated Ti-Mn-14 82
Figure 4.88: Heat-treated Ti-Mn-15 82
Figure 4.89: Heat-treated Ti-Mn-16 83
Figure 4.90: Heat-treated Ti-Mn-17 83
Figure 4.91: Heat-treated Ti-Mn-18 83
Figure 4.92: As-produced Ti-Mn-1 Average grain width 3,54µm, Average grain length 45,83µm for ductile dendrites; Average diameter 5,63µm for refined dendrites 84
Figure 4.93: As-produced Ti-Mn-10; Average grain width 5,63µm, Average grain length 78,54µm for ductile dendrites; Average diameter 7,29µm for refined dendrites 84
Figure 4.94: As-produced Ti-Mn-13; Average grain width 7,08µm, Average grain length 35,21µm for ductile dendrites; Average diameter 8,33µm for refined dendrites 84

Figure 4.95: Heat-treated Ti-Mn-1; Average grain width 8,15μm, Average grain length 70,49μm for ductile dendrites; Average diameter 9,51μm for refined dendrites. 84
Figure 4.96: Heat-treated Ti-Mn-10; Average grain width 8,80μm for ductile dendrites; Average diameter for refined dendrites 10,80μm. 84
Figure 4.97: Heat treated Ti-Mn-13; Average grain width 9,12μm, Average grain length 53,53μm for ductile dendrites; Average diameter 13,82μm. 84
Figure 4.98: Rietveld refinement of as-produced TiMn10 XRD data 85
Figure 4.99: Rietveld refinement of as-produced TiMn11 XRD data 85
Figure 4.100: Crystal orientation of hexagonal α-Ti in as-produced TiMn10 with lattice parameters: a=4.79187Å; c=6.50513Å 85
Figure 4.101: Crystal orientation of hexagonal α-Ti in as-produced TiMn11 with lattice parameters: a=3.86376Å; c=1.36555Å 85
Figure 4.102: Crystal orientation of cubic β-$Ti_{17}Mn_3$ in as-produced TiMn10 with lattice parameters: a=b=c=8.24423Å 86
Figure 4.103: Crystal orientation of cubic β-$Ti_{17}Mn_3$ in as-produced TiMn11 with lattice parameters: a=b=c=8.23881Å 86
Figure 4.104: XRD patterns for heat treated TiMn-11 87
Figure 4.105: Crystal orientation of hexagonal ω-Ti in heat treated TiMn11 with lattice parameters: a=5.60523Å; c=4.06776Å 87
Figure 4.106: Crystal orientation of cubic β with lattice parameters: a=b=c=9.63481Å 87
Figure 4.107: Plot illustration peak broadening of as-produced TiMn10. 88
Figure 4.108: Plot illustrating peak broadening of as-produced TiMn11 88
Figure 4.109: Plot illustrating peak broadening of heat treated TiMn-11 88
Figure 4.110: Rietveld refinement of heat treated TiMn8 88
Figure 4.111 to 4.114: Electron Backscatter Diffraction (EBSD) images of as produced TiMn-10
Figure 4.111: Phase distribution of β and α phases 89
Figure 4.112: Backscatter diffraction Scanning Electron Micrograph (BSD-SEM) image displaying elemental distribution 91
Figure 4.113: Inverse Polar Figure-Z (IPF-Z) displaying crystal orientation of different grains relative to z-axis 91
Figure 4.114: Band contrast image displaying grain boundaries 91
Figure 4.115: Phase distribution of ω and β 93
Figure 4.116: SEM-BSD image displaying elemental distribution 93
Figure 4.117: IPF-Z displaying crystal orientations of different grains 93
Figure 4.118: Band contrast image displaying different grain boundaries of heat treated TiMn-11. 93
Figure 4.119: 252 crystal orientations of β phase in as produced TiMn-10 detected by EBSD on {1 1 0} standard projection of cubic system 94

Figure 4.120: 306 crystal orientations of α phase in as produced TiMn-10 detected by EBSD on $\{10\underline{1}0\}$ standard projection of hexagonal system 94
Figure 4.121:140 crystal orientations of β phase in heat treated TiMn-11 detected by EBSD on {1 1 0} standard projection of cubic system 94
Figure 4.122: 105 crystal orientations of ω phase in heat treated TiMn-11 detected by EBSD on $\{10\underline{1}0\}$ standard projection of hexagonal system 94
Figure 4.123: texture distribution of β phase in as produced TiMn-10 detected by EBSD on {1 0 0} standard projection of cubic system 96
Figure 4.124: texture distribution of α - phase in as produced TiMn-10 detected by EBSD on {0 0 0 1} standard projection of hexagonal system 96
Figure 4.125: texture distribution of β phase in heat-treated TiMn-11 detected by EBSD on {1 0 0} standard projection of cubic system 96
Figure 4.126: texture distribution of ω -phase in heat-treated TiMn-11 detected by EBSD on {0 0 0 1} standard projection of hexagonal system. 96
Figure 4.127:Co-ordinate system of HCP crystal 97
Figure 4.128: Microhardness of as produced TiMn alloys 98
Figure 4.129: Microhardness of heat treated TiMn alloys 99
Figure 4.130: Optical micrograph of crack length of as produced Ti-Mn-10 100
Figure 4.131: Optical micrograph of crack length of heat treated Ti-Mn-11 100
Figure 4.132: TiMn-8 contains largest phase proportion of $Mn_{0.52}Ti_{0.48}$(s) in Ti-Mn alloys and is the most brittle TiMn alloys and has lowest calculated ductility. 100
Figure 4.133: Relationship between indentation depth and load of β and α obtained from nanoindentation. 101
Figure 4.134: Relationship between indentation depth and load of β and α+ω obtained from nanoindentation. 102
Figure 4.135: Mass loss as a function of time for as-produced TiMn-10 (SAMPLE AB), as-produced TiMn-11 (SAMPLE B) and heat-treated TiMn-11 (SAMPLE A) oxidation behaviour 103
Figure 4.136: Mass loss as a function of temperature for TiMn alloys 104
Figure 4.137: Oxide scale thickness of as-produced TiMn-10. 105
Figure 4.138: Thickness of various layers of oxide scale of as-produced TiMn-10 105
Figure 4.139: Microstructure underneath oxide scale of oxidised as-produced TiMn-10. 105
Figure 4.140: EDX of $MnO_2$ - 69.20(at%O); 26.36(at%Mn); 4.44(at%Ti) 105
Figure 4.141: EDX of $TiO_2$- 72.01(at%O); 27.19(at%Ti); 0.80(at%Mn) 105
Figure 4.142: EDX of $Mn_3Ti_3O$- 68.28(at%O); 23.06(at%Ti); 8.66(at%Mn 105
Figure 4.143: Oxide scale thickness of as-produced TiMn-11. 105
Figure 4.144: Thickness of various layers of oxide scale of as-produced TiMn-11 105

Figure 4.145: Microstructure underneath oxide scale of oxidised as-produced TiMn-11. 105
Figure 4.146: Oxide scale thickness of heat-treated TiMn-11. 106
Figure 4.147: Thickness of various layers of oxide scale of heat-treated TiMn-11 106
Figure 4.148: Microstructure underneath oxide scale of oxidised heat-treated TiMn-11. 106
Figure 4.149: EDX of $Ti(NO_3)_4$- 41.87(at%Ti); 46.48(at%N); 9.31(at%O); 2.34(at%Mn). 106
Figure 4.150: Microstructure of as-produced TiAlMn-1. 107
Figure 4.151: Microstructure of as-produced TiAlMn-2 107
Figure 4.152: Microstructure of as-produced TiAlMn-3 107
Figure 4.153: Microstructure of heat-treated TiAlMn-1 108
Figure 4.154: Microstructure of heat-treated TiAlMn-2 108
Figure 4.155: Microstructure of heat-treated TiAlMn-3 108
Figure 4.156: Rietveld Refinement of as produced TiAlMn1 XRD data 109
Figure 4.157: Rietveld Refinement of heat treated TiAlMn1 XRD data 109
Figure 4.158: Crystal orientation of Mn micro alloyed tetragonal TiAl with lattice parameters: a=b=2.48789Å; c=7.32984Å 109
Figure 4.159: Crystal orientation of tetragonal $TiAl_2$ in heat treated TiAlMn-1 with lattice parameters: a=b=2.48079Å; c=8.16362Å. 109
Figure 4.160: Crystal orientation of hexagonal $TiMn_{1.20}Al_{0.80}$ in as produced TiAlMn1 with lattice parameters: a=3.89761Å; c=4.71199Å 110
Figure 4.161: Crystal orientation of hexagonal $Ti_{0.965}Al_{0.035}$ in heat treated TiAlMn1 with lattice parameters: a=4.73510Å; c=3.68838Å 110
Figure 4.162: Crystal orientation of cubic β-$Ti_{17}Mn_3$ in as produced TiAlMn1 with lattice parameter: a=b=c=9.36638Å 110
Figure 4.163: Crystal Orientation of cubic $Ti_{0.85}Mn_{0.15}$ in heat treated TiAlMn1 with lattice parameter: a=b=c=9.65303Å 110
Figure 4.164: Crystal orientation of orthorhombic $Al_{2.91}Mn_{1.09}$ in as produced TiAlMn1 with lattice parameters: a=3.17246Å; b=4.71166Å; c=3.60870Å 111
Figure 4.165: Crystal orientation of orthorhombic $Al_{2.91}Mn_{1.09}$ in heat treated TiAlMn1 with lattice parameter: a=3.24097Å; b= 3.48005Å; c=4.39517Å 111
Figure 4.166: Plot illustrating peak width broadening of as produced TiAlMn1. 111
Figure 4.168: Phase distribution of β, $\alpha_2$ and γ phases 113
Figure 4.169: Backscatter diffraction Scanning Electron Micrograph (BSD-SEM) image displaying elemental distribution 113
Figure 4.170: Inverse Polar Figure-Z (IPF-Z) displaying crystal orientation of different grains relative to z-axis 113
Figure 4.171: Band contrast image displaying grain boundaries. 113
Figure 4.172 to 4.175: EBSD images of heat-treated TiAlMn-1

Figure 4.172: phase distribution of $\alpha_2$, β, $Ti_{0.965}Al_{0.035}$ and $TiAl_2$ 115
Figure 4.173: SEM-BSD image displaying elemental distribution 115
Figure 4.174: IPF-Z displaying crystal orientations of different grains 115
Figure 4.175: Band contrast image displaying different grain boundaries of heat treated TiAlMn-1 115
Figure 4.176: 396 crystal orientations of β phase in as produced TiAlMn-1 detected by EBSD on {1 1 0} standard projection of cubic system 116
Figure 4.177: 635 crystal orientations of $\alpha_2$ phase in as produced TiAlMn-1 detected by EBSD on $\{10\underline{1}0\}$ standard projection of hexagonal system 116
Figure 4.178: crystal orientations of γ phase in as produced TiAlMn-1 detected by EBSD on {1 1 1} standard projection of cubic system 116
Figure 4.179: 309 crystal orientations of β phase in heat treated TiAlMn-1 detected by EBSD on {1 1 0} standard projection of cubic system 116
Figure 4.180: 480 crystal orientations of $\alpha_2$ phase in heat treated TiAlMn-1 detected by EBSD on $\{10\underline{1}0\}$ standard projection of hexagonal system 116
Figure 4.181:18 crystal orientations of γ phase in heat treated TiAlMn-1 detected by EBSD on {1 1 1} standard projection of cubic system 116
Figure 4.182: texture distribution of β phase in as produced TiAlMn-1 detected by EBSD on {1 0 0} standard projection of cubic system. 118
Figure 4.183: Texture distribution of $\alpha_2$ - phase in as produced TiAlMn-1 detected by EBSD on {0 0 0 1} standard projection of hexagonal system. 118
Figure 4.184: texture distribution of γ phase in as produced TiAlMn-1 detected by EBSD on {0 0 1} standard projection of cubic system. 118
Figure 4.185: texture distribution of β phase in heat treated TiAlMn-1 detected by EBSD on {1 0 0} standard projection of cubic system 118
Figure 4.186: texture distribution of $\alpha_2$ - phase in heat treated TiAlMn-1 detected by EBSD on {0 0 0 1} standard projection of hexagonal system. 118
Figure 4.187: texture distribution of γ phase in heat treated TiAlMn-1 detected by EBSD on {0 0 1} standard projection of cubic system. 118
Figure 4.188: Average microhardness values for as produced and heat treated Ti-Al-Mn alloys 119
Figure 4.189: Optical micrographs displaying crack lengths of as produced TiAlMn-1 120
Figure 4.190: Optical micrographs displaying crack lengths of heat treated TiAlMn-1 120
Figure 4.191: Mass loss as a function of time for as-produced (labelled SAMPLE TIALMN-1) and heat-treated (labelled SAMPLE-BC) TiAMn-1 121
Figure 4.192: Mass loss as a function of temperature for as-produced and heat-treated TiAlMn-1.. 122
Figure 4.193: Oxide scale thickness of as-produced TiAlMn-1 123
Figure 4.194: Various layers of oxide scale thickness of as-produced TiAlMn-1. 123

Figure 4.195: Microstructure underneath oxide scale of as-produced TiAlMn-1 123
Figure 4.196: EDX for $MnO_2$ -64.64(at%O); 31.56 (at%Mn); 3.27(at%Ti); 0.53(at%Al) 123
Figure 4.197: EDX for $TiO_2$- 68.40(at%O); 30.49(at%Ti); 0.93(at%Mn); 0.17(at%Al) 123
Figure 4.198: Thickness of various layers of oxide scale of heat-treated TiAlMn-1. 124
Figure 4.199: Protective oxide scale of heat-treated TiAlMn-1 124
Figure 4.200 Microstructure underneath oxide scale of oxidised heat-treated TiAlMn-1. 124
Figure 4.201:EDX for $TiO_2$ -71.43(at%O); 28.57(at%Ti 124
Figure 4.202: EDX for $Al_2O_3$- 64.17(at%O); 35.83(at%Al) 124
Figure 4.203: EDX for $Mn_3O_4$ - 63.58(at%O); 33.82(at%Mn); 2.28(at%Ti); 0.32(at%Al) 124
Figure 4.204: Relationship between indentation depth and load obtained from nano indentations on ternary TiAlMn alloy. 125
Figure 4.205: Relationship between Vickers's Hardness and calculated indentation 0,2% offset yield stress. 125
Figure 4.206: Relationship between Vicker's Hardness and calculated indentation strain. 126
Figure 4.207: Relationship between calculated indentation stress and strain 126
Figure 4.208: Unrefined gleeble compression stress-strain curves 127
Figure 4.209: Refined gleeble compression stress-strain curves 128
Figure 4.210: Graphical representation of the effect of strain reduction of microhardness 129
Figure 4.211: microstructure of undeformed TiAlMn sample taken at Magnification of 20μm (x1000). 129
Figure 4.212: Determination of β phase volume proportion (22.37%) using Image J for undeformed TiAlMn sample. 129
Figure 4.213: Microstructural features and grain boundaries of undeformed TiAlMn sample taken at magnification of 4μm (x1000). 129
Figure 4.214: Microstructure of TiAlMn sample deformed to 10.78% strain reduction taken at Magnification of 20μm (x1000). 130
Figure 4.215: Determination of β phase volume proportion (39.51%) using Image J for TiAlMn sample deformed to 10.78% strain reduction 130
Figure 4.216: Microstructural features and grain boundaries of TiAlMn sample deformed to 10.78% strain reduction taken at magnification of 4μm (x1000). 130
Figure 4.217: Microstructure of TiAlMn sample deformed to 10.89% strain reduction taken at Magnification of 20μm (x1000). 130
Figure 4.218: Determination of β phase volume proportion (41.14%) using Image J for TiAlMn sample deformed to 10.89% strain reduction 130
Figure 4.219: Microstructural features and grain boundaries of TiAlMn sample deformed to 10.89% strain reduction taken at magnification of 4μm (x1000). 130

Figure 4.220: Microstructure of TiAlMn sample deformed to 22.75% strain reduction taken at Magnification of 20μm (x1000). 131
Figure 4.221: Determination of β phase volume proportion (50.46%) using Image J for TiAlMn sample deformed to 22.75% strain reduction. 131
Figure 4.222: Microstructural features and grain boundaries of TiAlMn sample deformed to 22.75% strain reduction taken at magnification of 4μm (x1000). 131
Figure 4.223: Microstructure of TiAlMn sample deformed to 34.58%strain reduction taken at Magnification of 20μm (x1000). 131
Figure 4.224: Determination of β phase volume proportion (44.34%) using Image J for TiAlMn sample deformed to 34.58% strain reduction 131
Figure 4.225: Microstructural features and grain boundaries of TiAlMn sample deformed to 34.58% strain reduction taken at magnification of 4μm (x1000) 131
Figure 4.226: Microstructure of TiAlMn sample deformed to 46.50% strain reduction taken at Magnification of 20μm (x1000). 132
Figure 4.227: Determination of β phase volume proportion (51.84%) using Image J for TiAlMn sample deformed to 46.50% strain reduction. 132
Figure 4.228: Microstructural features and grain boundaries of TiAlMn sample deformed to 46.50% strain reduction taken at magnification of 4μm (x1000). 132
Figure 4.229: Effects of strain Reduction on Lattice Parameters 133
Figure 4.230: Effects of Strain Reduction on Lattice Volume 133
Figure 4.231: Effects of strain reduction on dislocation density 134
Figure 4.232: Effect of strain on c/a lattice ratios 134
Figure 4.233: Visual presentation of phase transformation processes during laser deposition 137
Figure 4.234: Influence of Mn feed rates and LEPUL on thermal gradients with respect to the X-direction dimension of Ti-α phase. 139
Figure 4.235: Influence of Mn feed rates and LEPUL on thermal gradients with respect to the x dimension of Ti-α phase. 140
Figure 5.1: Crystal orientation depicting phase transformation of Al addition in TiAlMn alloys (Li *et al.,* 2018). 150

**List of Tables**

Table 3.1: Powder feed rates, Ar carrier gas flowrates and Laser power variables. 42
Table 4.1: Microstructural features and compositions of as produced TiAl alloys. 56
Table 4.2: Details regarding atoms illustrated in Figures 60
Table 4.3: Effects of increasing Ar carrier gas flow rates on d-spacings of tetragonal crystal lattices 63
Table 4.4: Effects of increasing Ar carrier gas flow rates on d-spacings of hexagonal crystal lattices 63
Table 4.5: Densities of TiAl alloys 64
Table 4.6: Microstructural features of as produced TiMn alloys and their compositions. 78
Table 4.7: Compositions of microstructural features of heat treated TiMn alloys 83
Table 4.8: Effects of Mn addition on d-spacing of cubic crystal orientation 86
Table 4.9: Dislocation densities of TiMn alloys 88
Table 4.10: Numerical documentation of EBSD and SEM-BSD analysis of as produced TiMn-10 90
**T**able 4.11: Numerical illustration of EBSD and SEM-BSD analysis of heated treated TiMn-11 92
Table 4.12: Microstructural features and compositions of TiAlMn alloys obtained through EDS/EDX 108
Table 4.13: Dislocation densities of TiAlMn Alloys 111
Table 4.14: Microstructural features of as-produced TiAlMn-1 detected by EBSD and SEM 112
Table 4.15: Microstructural features of heat-treated TiAlMn-1 detected by EBSD and SEM-BSD 114
Table 4.16: Strain and Stress values attained from Gleeble testing 127
Table 4.17: Specific Heat values for various phases with respect to Temperature 136
Table 4.18: Phase transformation reactions in various alloys. 136
Table 4.19: Theoretical Density alongside measured density 141

# Nomenclature

BCC: Body Centred Cubic

FCC: Face Centred Cubic

HCP: Hexagonal Close Packed

LENS: Laser Engineer Net Shaping

CAD: Computer Aided Design

HIPping: Hot Isostatic Pressing

LEPUL: Laser Enerrgy Per Unit Length

T: Temperature

HV: Hardness Value

# Chapter 1

## 1.1 Introduction and Background

Two phase ($\gamma+\alpha_2$) TiAl alloys with 35-50 at% Al are ordered intermetallic alloys which can be used to produce aeroengine parts such as low pressure turbine blades and vanes, bearing supports, compressor casings, high and low pressure hangars, frames and low pressure brush seal supports (Lapin, 2009). TiAl based alloys are being considered as potential substitutes for Ni-based superalloys in the aerospace engine manufacturing industry, due to their low density, high temperature strength and good creep resistance (Tryggvason, 1997). However, the use of TiAl in aero engines is restricted by their low ambient temperature ductility which results in brittleness and limited processing capacity due to the inability to bend components into desirable shapes such as fan blades (Austin *et al*., 1996).

The low temperature ductility of TiAl alloys, like the ductility of most ordered intermetallic alloys, results from a combination of both intrinsic and extrinsic factors. Increasing the temperature of ordered intermetallic alloys results with an improvement in yield strength and ductility, which makes these materials appropriate for high temperature application. However, it is challenging to use and fabricate these components into complex shapes at ambient temperatures. Improved ductility at high temperatures is due to twinning induced plasticity (TWIP). Mechanical twinning occurs during deformation and can be enhanced by additional alloying elements such as manganese, which can improve ductility at both high and low temperatures (Appel, 2010; Appel *et al.,* 2011a).

Several methods have been used to resolve the challenges faced in the practical application of TiAl-based alloys due to the low ambient temperature ductility. Directional solidification, electromagnetic cold crucible directional solidification and the promotion of twinning induced plasticity (Jiao *et al.,* 2016) have been applied to improve room temperature ductility. Ductility values of up to 5% were attained in TiAl alloys from the promotion of twinning induced plasticity, where Mn was used as an additional microalloying element (Shu *et al.,* 2012, Wang *et al*., 2018). However, these methods are used during the fabrication of TiAl parts by traditional methods, such as ingot casting, hot isostatic pressing and hot forging, which are usually very costly, time consuming and have large amounts of material wastage (Gu, 2015).

To hinder challenges faced in fabrication using traditional processes, additive manufacturing methods have been under study as replacement methods. Additive manufacturing is a fabrication method which print 3 dimensional components in a layer upon layer fashion according to a computer aided design (CAD). Additive manufacturing methods use minimal energy and materials, and consume less time compared to traditional fabrication methods (Santos *et al.,* 2006). This research focuses on the study of Laser Engineered Net Shaping (LENS) fabrication process. This method was selected to be studied because its equipment has the ability to print components containing Al (Attar *et al.,* 2017), which makes it appropriate for the production of TiAl based components. However, LENS fabricated TiAl based components are subjected to post process thermal cracking which result from a combination of the brittle nature of the material and thermal residual stresses resulting from LENS mechanisms. The purpose of this work is to study and evaluate the Ti-Al-Mn alloys produced by LENS.

## 1.2. Motivation for Research

Additive manufacturing processes such as electron beam melting (EBM), selective laser melting (SLM) and laser engineered net shaping (LENS) are continuously being investigated due to their ability to fabricate complex components with superior mechanical properties at minimal processing time and costs compared to traditional fabrication methods. The fabrication of TiAl components using LENS has been shown to improve mechanical properties and has successfully produced the desirable γ-lamella phase required in aeroengine components (Ruan *et al,* 2006).

The addition of manganese as a ternary element has been proven to improve ambient temperature ductility in TiAl based alloys (Wang *et al.,* 2018). Improving ambient temperature ductility can assist in the reduction of post processing thermal cracking and potentially enable bending during fabrication. On the other hand, using LENS can mitigate the numerous challenges faced with traditional fabrication methods such as material wastage and tedious labour. Thus, a combination of these methods has the potential to resolve challenges faced in the production of TiAl components. However, there is limited research on combining the improvement of ductility of TiAl alloys through Mn addition and using the LENS as a fabrication process. Improving ambient temperature ductility of TiAl based alloys has the

potential to contribute to moving towards the practical use to TiAl based alloys in military jet aero engines at more affordable production costs. The practical use of TiAl based components have the potential to reduce fuel consumption and improve the efficiency of the military jet engine.

## 1.3. Research Questions

Investigating the effects of using LENS to fabricate Mn ternary alloyed TiAl can assist in deriving an appropriate alloy design and fabrication procedure to produce TiAl based alloys with improved ambient temperature ductility for aeroengine application.

Throughout this research, answers will be sought for the listed questions:

I. What are the effects of using Mn as an additive alloying element on the microstructure and mechanical properties of LENS produced TiAl components?
II. What are the effects of process parameters of LENS on the microstructure and mechanical properties of Mn micro alloyed TiAl alloys?
III. What are the effects of using heat treatment as a post processing step on LENS fabricated alloys?
IV. How does Mn addition affect the high temperature properties of the TiAl-based alloys produced using LENS?

## 1.4. Hypothesis

The addition of Mn to TiAl has the potential to improve ductility since Mn preferably substitutes on Al sub lattices which results in reduced tetragonality and interplanar spacings, and increased lattice symmetry. These effects on the crystal structure led to enhanced dislocation cross glide relaxation which improves mechanical strength and ductility.

## 1.5. Research Aim and Objectives

This research aims to investigate the effects of Mn addition to TiAl which are fabricated using LENS, on microstructures and mechanical properties.

The aim of the project will be conducted by addressing the following objectives:

- Establish and determine LENS process parameters most suitable for producing TiAlMn alloys
- Study microstructural evolution though phase identification by performing microscopic analysis (SEM, EDX/EDS and EBSD) and X-ray Diffraction (XRD).
- Study the effects of heat-treatment on the microstructures and mechanical properties of LENS produced TiAlMn alloys.
- Investigate the effect of Mn addition on oxidation behaviour of TiAlMn alloys.
- Study mechanical behaviour of LENS produced TiAlMn alloys by conducting microhardness and nanoindentation tests on as-produced and heat-treated samples.
- Study the high temperature mechanical behaviour by conducting Gleeble compression tests.

## 1.6. Approach

This research was approached by studying the effects of changing LENS parameters by focusing on the microstructures generated. Parameters of these structures were studied by investigating lattice parameters and phase proportions. The mechanical behaviour of these structures was studied through mechanical testing and observation of post processing thermal cracking.

## 1.7 Structure of Thesis

The characterization of LENS generated and heat-treated TiAlMn alloys is explored in this dissertation, where the Literature Review is covered in Chapter 2, experimental procedures and numerical models used are presented in Chapter 3, resultant microstructural morphologies and mechanical properties are displayed in Chapter 4 and the research is discussed in Chapter 5 and concluded in Chapter 6.

# Chapter 2: Literature Review

This chapter is a general review of the nature of TiAlMn alloys and LENS as a fabrication process. In addition, it addresses and illustrates the effects of fabrication methods (including LENS and traditional processes) on material structures, deformation and mechanical behavior which lead to material shortcomings. The chapter is concluded by a review based on the environment the aeroengine is exposed to during application and how the oxidation may be potentially affected.

## 2.1. Two phase ($\alpha_2+\gamma$) fully lamellar TiAl alloys

Titanium aluminide (TiAl) alloys are intermetallic alloys which have been under investigation for the past four decades as possible substitutes for Ni-based super alloys in the aeroengine manufacturing industry. TiAl alloys have attracted a great deal of interest because in comparison to most intermetallic alloys, they have high elastic modulus, high temperature strength and fracture toughness, good creep and oxidation resistance up to 800°C and low density, making them appropriate for aeroengine applications (Kim and Dimiduk, 1991; Lapin, 2009).

The density of TiAl is almost half that of Ni-based superalloys but their strength is almost as high as that of Ni-based superalloys. TiAl alloys are also suitable for aeroengine application because they display an increase in strength with increasing temperatures, making these alloys suitable for applications in high temperature environments (Kim, 1994). However, TiAl alloys have shortcomings such as inverse proportionality between creep resistance and ambient temperature ductility where an increase in temperature eventually leads to the susceptibility to the gradual reduction in strength (Kim and Dimiduk, 1991). This imbalance in the mechanical properties hinders the practical application for these alloys. Therefore, important mechanical properties of TiAl alloys can be attributed to various aspects of these materials which include the microstructure, nanostructure and deformation mechanisms which are influenced by processing routes followed during production.

## 2.2. Microstructure and nanostructure of TiAl

The unique combination of properties of $\alpha_2+\gamma$ phase TiAl is attributed by the crystal orientation in the nanostructure. This two-phase alloy is comprised of hexagonal $\alpha_2$-$Ti_3Al$ phase with an

ordered $D0_{19}$ orientation and tetragonal γ-TiAl phase with an ordered $L1_0$ orientation as displayed in Figures 2.1 and 2.2:

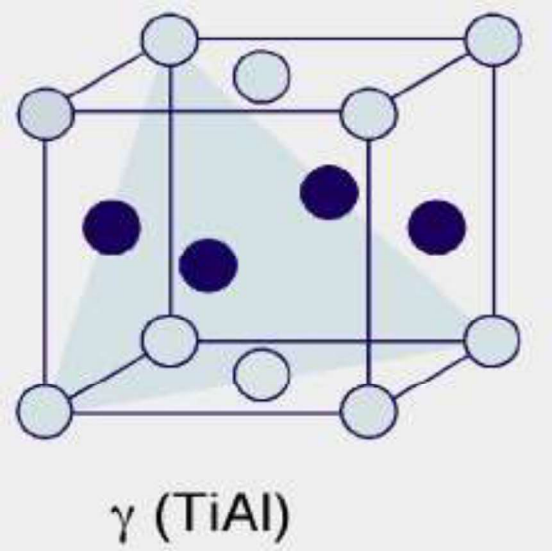


*Figure 2-1: Tetragonal TiAl Gamma phase (Light spheres-Al Dark spheres-Ti)*

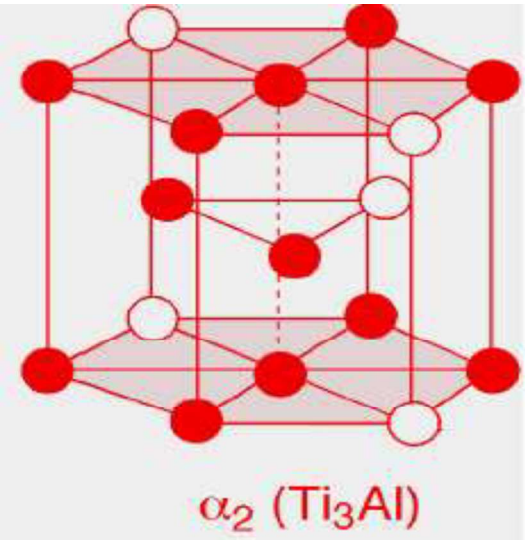


*Figure 2-2: Hexagonal Ti3Al Alpha-2 (Dark spheres-Ti and Light spheres-Al)*

The crystal structures depicted in Figures 2.1 and 2.2 are oriented in a fashion where the $\alpha_2$-$Ti_3Al$ phase assumes the parent grain and the γ-TiAl phase assumes the domain structure as displayed in Figure 2.3. The basal plane of the $\alpha_2$- phase (0001) is parallel to the close packed plane in the γ-phase (111)(Appel, 2010; Appel *et al.,* 2011a), and the orientation relationship in these two phases can be depicted as $(111)_\gamma \parallel (0001)_\alpha$ and $[110]\gamma \| 1120]\alpha_2$.

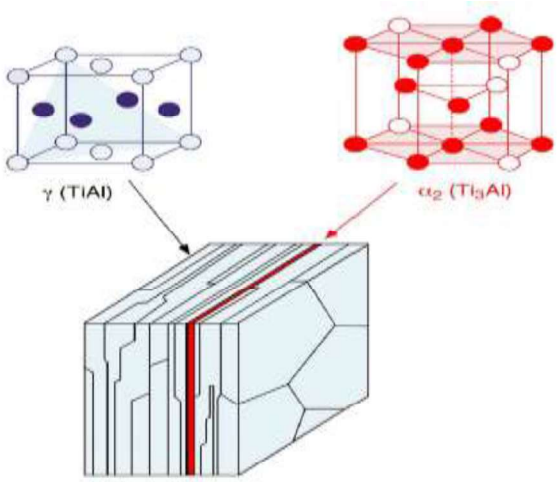


*Figure 2.3: Orientation of $\alpha_2$ as parent grain and $\gamma$ as the domain structure within a lamella colony*

These crystal orientations and the lamellar microstructure are highly accountable for the deformation mechanisms and a variety of mechanical properties such as ductility and strength in TiAl alloys (Appel and Wagner, 1998)

Poor ambient temperature ductility is due to the presence of covalent d-d bonds between Al and Ti atoms in the TiAl matrix, which leads to a lack of electron density and mobility within the TiAl matrix, which leads to a lack of metallic bonding and poor ductility (Morinaga *et al.,* 1990). Poor ambient temperature ductility is also accounted for by the lack of mechanical twinning at ambient temperatures, lack of symmetry in the γ-TiAl orthorhombic structure and the presence of dislocation glide resistances at low temperatures. The ambient temperature ductility can be controlled by controlling variables in both the nanostructure and the microstructure of TiAl (Appel, 2010; Kumpfert, 2001; Yoo and Fu, 1998).

For this study, it has been established that the lamellar microstructure is more desirable for aeroengine application as opposed to the duplex microstructure, because lamellar microstructures have good high temperature strength and fracture toughness although they suffer from low ambient temperature ductility, while duplex microstructures have improved ductility due to the finer grain sizes, but suffer poor high temperature strength and creep resistance (Appel and Wagner, 1998; Kim, 1994)

Thus a microstructure with the best combination of mechanical properties would consist of a fine grained lamellar microstructure because the fine grains allow for the formation of microcracks during fracture. Microcracking is a fracture mechanism which hinders rapid crack propagation. Slower crack propagation indicates improved ductility, creep resistance, high temperature strength and fracture toughness (Froes *et al*., 1992; Kim, 1994).

Mechanical properties and microstructures can also be controlled by controlling the alloy compositions, phase proportions and post processing heat treatment. (Kim *et al.,* 2014) reported that parameters such as inter-lamellar spacing, width of the lamellar, distance between $\alpha_2$-$\alpha_2$ , size of lamellar colonies and angle between the lamellar colony boundary and tensile axis can be adjusted through various selected processes and have the ability to control the ductility and strength of TiAl alloys (Kim *et al.*, 2014). The larger the values of these parameters, the more improved the ductility because it allows for translamellae ductile fracture as opposed to combined intergranular and intragranular brittle fracture.

The $\alpha_2$ -phase is also important because it acts as crack initiation sites during micro cracking (Kim *et al.*, 2014). However, trans-lamellar fracture allows for crack propagation to take place within the $\alpha_2$-lamellar where the crack can propagate until it is stopped by γ-lamellar. Cracks are initiated again at the brittle $\alpha_2$-lamellar and join with other cracks from different $\alpha_2$ site. These nucleated cracks continue to propagate in a ligament joining fashion until they are stopped by γ-lamellar again (Kim *et al*., 2014; Mercer and Soboyejo, 1997).

This process continues until deformation is complete. Trans-lamellar fracture mode has the ability to suppress rapid crack propagation and lead to improved ductility in a TiAl (Kim *et al.,* 2014). Inui *et al.,* 1992 reported that the ambient temperature ductility of TiAl is at its highest (20%) when the angle between the tensile axis and lamellar colony boundary is 31, but the best combination of strength and ductility occurs when the tensile axis is parallel to the lamellar colony boundary.

Various strategies have been employed to improve mechanical properties of TiAl alloys. Among these strategies, the most used strategy is the micro alloying of TiAl alloys (up to 2 at.%X) with small additions of ternary elements (Austin *et al.,* 1996). This has led to the accepting of the general composition illustrated in Equation 2.1 as follows:

$$Ti - (42 - 49)Al + X \qquad (2.1)$$

Where, X depicts elements such as Cr, Nb, Mn, V, C, W, Ta, B and Si (Appel *et al.,* 2011a; Prasad *et al.,* 2002). These ternary elements have various effects on TiAl alloy properties. Concentrations of Mn, V and Cr up 2.0at% can improve the ductility of TiAl. Moreover, the addition of Nb up to 15at% can significantly improve the strength. Both these improvements are achieved through substitutional solid solution strengthening. Small additions of W, Nb, Mo, Si and C can improve creep resistance, and the additions of B, Si and N in certain amounts

results in grain refinement. The additions of Nb and Ta can improve oxidation resistance (Appel *et al.,* 2011a; Prasad *et al.,* 2002).

Micro alloying can also be executed depending on the process route followed. For example, small additions of B and W can modify the lamellar microstructure in wrought alloys (Appel, 2010; Jiao *et al.,* 2016). Reducing the Al levels in the alloy can shift the entire phase boundary of the ($\alpha_2$+$\gamma$) phase to the Ti rich side of the phase where the generation of the $\alpha_2$-phase is more enhanced. The $\alpha_2$-phase has the ability to scavenge oxygen from the $\gamma$-phase, minimizing impurities in the $\gamma$-phase and improving ductility (Appel, 2010).

The brittle behaviour of $\alpha_2$ –phase makes it important for the $\alpha_2/\gamma$ phase volume ratio to be within 5-15%. Above this value, the $\alpha_2$-phase begins to contribute to the brittleness of the alloy and below this value, the grain growth becomes prominent, which is also undesirable for the strength of TiAl (Kim, 1994). The ductility of TiAl is also determined by the deformation behaviour which is highly influenced by the nanostructure and microstructure of a given specimen (Kim, 1994).

### 2.2.1 Deformation behaviour and ductility

The deformation behaviour of TiAl is highly accountable for various mechanical properties such as creep properties, ductility and damage tolerance. Appel and Wagner, (1998) reported that the deformation of TiAl alloys occurs on the close packed (111) planes of ordered $\gamma$-TiAl phase and is governed by ordinary dislocations with Burger's vector b = ½<110], super dislocations with Burger's vectors b = ½<112] and b = <011] and ordered twinning along 1/6<112]{111}.

Ordinary dislocations are most dominant in the deformation of two phase ($\alpha_2$+$\gamma$) TiAl because they require less stresses compared to super dislocations, which require the highest stress due to their sensitivity to dissociations reactions which lead to planar faults such as intrinsic stacking faults, complex stacking faults and antiphase boundary. Differences in these fault energies lead to non-planar core spreading and asymmetry in the lattice structure which leads to high friction stresses, making the glide resistance of super dislocations highly sensitive to direction of motion (Appel *et al.,* 2011a).

Deformation mechanisms of TiAl have been studied at both high and low temperatures to obtain an understanding of the factors which influence poor ductility at ambient temperatures and improved ductility at higher temperatures. Deformation is highly dependent on the

multiplication and mobility of dislocations by cross slip or climb, which determines the dislocation density and mobility, which in turn influences the ductility (Appel *et al.,* 2011a).

It has been established that at ambient temperatures, deformation is mainly dependent upon glide resistance, which is provided by localized obstacles, jog dragging and lattice friction (Fantozzi *et al.,* 1982). Dislocation jogs are generated by cross slip and are accountable for the multiplication of dislocations at ambient temperatures. Because jogs are immobile to the direction of the screw dislocation, this leads to dislocation dipoles being trailed adjacent to the jogs in a Frank-Read source fashion where the dipole arms elastically interact with each other until the applied shear stress exceeds $\tau_d = \mu b/[8\pi(1-v)h$ (Froes *et al.,* 1992).

When the elastic interaction between the dipole arms stops, the dipole arms bow out and can behave as single ended dislocations, which marks the initial stages of the dislocation multiplication mechanism. Since dislocation dipoles are generated from cross slip, this implies that these dislocation anchorings can easily cross slip from one plane to the next, forming a dislocation band (Appel and Wagner, 1998). The high flow stress of TiAl alloys allows for narrow dislocation dipoles to act as dislocation sources, while dipoles which are too small in height to multiply, get pinched off the system and can be effective as dislocations sources at a later stage of the deformation process when the flow stress is higher. As temperature increases, glide resistance gradually decreases until the temperature reaches 250°C where the glide resistance disappears (Appel and Wagner, 1998). At elevated temperatures, dislocations are formed by nucleation and growth of prismic loops. Prismic loops grow through the removal of a single plane, which exhausts the system after a single cycle. However, the system has a regenerative mechanism and allows for the formation of a new loop. This leads to the conclusion that vacancies are the more dominant defects over interstitials in equilibrium TiAl. The multiplication of dislocations at elevated temperatures can be managed by operating the Bardeen Herring climb sources since they require low critical vacancy supersaturation (Appel *et al.,* 2011a).

The deformation of TiAl has been studied from various temperatures including both ambient and elevated temperatures. A general commonality has been established for TiAl alloys tested at various temperatures, being that dislocations are also emitted at lamella interfaces by induced coherence stresses which result from a possible variety of mismatches in density, crystal lattice and/or microstructure (Appel, 2010; Fantozzi *et al.,* 1982). The dislocations emitted have burger's vector b = 1/2<110] and are a major contribution to the accommodation of stress

concentrations. The development of constraint stresses due to deformed adjacent lamellae, assist in the overcoming of high Peierls stresses for super dislocations to glide. Peierls stresses and extrinsically faulted dipoles lead to the generation of sessile components of both super dislocations and ordinary dislocations, which are a contribution to poor ambient temperature ductility (Appel, 2010; Fantozzi *et al.,* 1982).

At elevated temperatures ranging from 650-750°C, diffusion assisted climb of ordinary dislocations proceed and stop at 750°C, which is also known as the brittle-to-ductile transition (BDT) temperature, where TiAl alloys undergo a significant improvement in ductility mainly due to mechanical twinning (Yamaguchi *et al.,* 2000). Defects such as precipitates and misfits in the $\alpha_2/\gamma$ interface can also behave as twin nucleation sites, where the twin nucleation mechanisms are governed by coherency stresses (Shirai and Yamaguchi, 1992). However, twinning nucleation in Al-rich γ-phase is extremely difficult at low temperatures, which is a contributing factor to poor ambient temperature ductility (Shirai and Yamaguchi, 1992).

Twin toughening is a result of the presence of twin boundaries. Twin boundaries hinder the motion of dislocations and crack propagation during deformation. Repulsion forces between twin boundaries and dislocations induce energy storage within the material leading to improved mechanical strength. However, hindering dislocation motion improves high temperature strength but cripples ambient temperature ductility since the material is incapable of relaxation by dislocation glide (Appel *et al.,* 2011a; Yoo and Fu, 1998). Deformation mechanisms such as the multiplication and mobility of dislocations, and twin nucleation can be beneficial for ambient temperature ductility but detrimental for high temperature strength, stability and creep resistance (Brossmann *et al.,* 1994).

### 2.2.2. Effects of Electronics on Ductility of binary TiAl

Morinaga *et al.* (1990) reported that the low temperature ductility of TiAl alloys can be attributed to the presence of electron density among Ti and Al atoms. This leads to strong covalent bonding between Ti and Al atoms, ultimately causing strong d-d directional bonding between Ti and Al atoms, which is a large cause of brittleness in TiAl alloys at ambient temperatures.

### 2.2.3. Mechanical Properties of Binary Ti-Al

One of the largest challenges faced in the production of TiAl, is striking a good balance between high temperature and ambient temperature mechanical properties. Mechanical

properties of TiAl alloys are highly sensitive to the microstructure. It has been established that improved ambient temperature ductility is achieved by generating duplex microstructures which are comprised of finer grains and are subject to grain boundary strengthening, which is more prominent in finer grains than coarse grains due to increased flow stresses (Kim, 1994) . However, achieving improved ambient temperature ductility by generating duplex structures comes at compromising high temperature strength and creep resistance (Kim, 1994). In contrast to the effects of generating a duplex microstructure, the coarse grained fully lamellar microstructure is highly favourable for good high temperature strength and creep resistance but suffers from poor ambient temperature ductility (Kim, 1994).

#### 2.2.3.1 Ductility of binary TiAl

The ambient temperature ductility of TiAl alloys ranges from 0-4 %, depending on alloys compositions, forming processes, microstructure, and nanostructure. The highest value of ambient temperature ductility achieved to date is 20%, which was obtained by applying directional solidification during the casting of TiAl, where the angle between the tensile axis and lamellar colony boundary was 31° (Inui *et al.*, 1992; Jiao *et al.,* 2016). At elevated temperatures above 700°C, TiAl alloy undergo a rapid brittle-to-ductile transformation due to mechanical twinning, dislocation climb and slip, making the ductility reach values higher than 20% (Appel *et al.,* 2011a; Inui *et al.,* 1992).

#### 2.2.3.2 Strength of binary TiAl

The yield strength of TiAl ranges from 250-600 MPa, and the tensile strength ranges from 300-700MPa. These values representing strength are highly dependent on alloy composition, processing method, grain size and microstructure (Appel *et al.*, 2011a; Liu and Maziasz, 1998). The strength of lamellar microstructure increases with decreasing grain size, without compromising the ductility and fracture toughness of the lamella (Appel *et al.,* 2011a; Liu and Maziasz, 1998).

#### 2.2.3.3 Creep Behaviour of binary Ti-Al

Creep resistance is inversely proportional to room temperature ductility. Creep properties of TiAl alloys are highly dependent on alloy compositions, microstructure and test temperatures (Maruyama *et al.,* 1997). Creep properties of TiAl can be improved by an increase in Al in two phase ($\alpha_2+\gamma$) alloys and an increase in the lamellar volume fraction, but the presence of $\gamma$ and $\beta$ at lamellar interfaces is detrimental for creep properties (Maruyama *et al.*, 1997). It has been

established that the fully lamellar microstructure exhibits the most superior creep characteristics over those of duplex structures due to their serrated grain boundary morphologies and refined lamellar spacing. However, fully lamellar microstructures exhibit a higher primary creep rate compared to duplex microstructures which are accounted for by the emission of dislocations at lamellar interfaces (Maruyama *et al.,* 1997). At later stages (during secondary and tertiary creep), creep behaviour is characterised by dynamic recrystallization at higher temperatures and stresses, or mostly dislocation climb at temperature ranges of 650-750°C and stress ranges of 100-200 MPa (Maruyama *et al.,* 1997). Long term creep of the lamellar can eventually lead to structural changes in the γ/γ interphases and leads to the formation of multiple height ledges. The general creep strength is good until the temperature reaches 800°C (Maruyama *et al.,* 1997).

#### 2.2.3.4 Fracture Behaviour of binary Ti-Al

The fracture mechanism of TiAl is brittle at ambient temperatures and is highly dependent on microstructure and temperature (Campbell *et al.,* 1999; Kim *et al.,* 1997). The lamellar microstructure has improved fracture toughness compared to duplex structures because lamellar microstructures experience trans-lamellar fracture, interfacial delamination and decohesion of lamellar colonies as opposed to duplex structures which experience cleavage and intergranular fracture (Campbell *et al.,* 1999; Kim *et al.,* 1997).

The fracture toughness is poor until the temperature is 700°C, where it undergoes a brittle to ductile transition due to mechanical twinning and dislocation climb mechanisms. The fracture toughness is controlled by the crack tip plastic zone, which consists of a concentration of dislocations and deformation twins, which lies ahead of the crack tip during crack propagation. The dislocation slip mechanisms at ambient temperatures are affected by factors which affect the glide resistance of dislocation and can lead to the crack outrunning the dislocation slips, but at elevated temperatures, dislocation climb leads to an improvement in ductility due to the ability of dislocations to glide at higher temperatures due to energy present in the TiAl matrix (Campbell *et al.,* 1999; Kim *et al.,* 1997).

### 2.3. Methods to improve the ductility of binary TiAl

The deformation mechanisms of TiAl alloys make the alloy suitable for high temperature applications but these applications are restricted by the poor ambient temperature ductility which poses challenges in the processing and fabrication of TiAl aeroengine complex parts (Lapin, 2009). Various methods (Jiao *et al.*, 2016) have been studied in an attempt to mitigate

the challenge of poor ambient temperature ductility of ordered intermetallic alloys in general (Jiao *et al.,* 2016). These methods include directional solidification, controlling of the ordered crystal, engineering of the grain boundary structure and chemistry, elimination of environmental embrittlement, optimization of the microstructure, controlling of phase stability and promotion of transformation or twinning induced plasticity (Jiao *et al.,* 2016; Yamaguchi *et al.,* 2000; Yoo and Fu, 1998). These methods have previously resulted in improved ductility of various ordered intermetallic alloys such as nickel aluminides (NiAl), iron aluminides (FeAl) and Zr-Co-Ni alloys (Jiao *et al.,* 2016). Studies have shown that the optimization of the microstructure and promotion of twinning induced plasticity have successfully improved the ductility of TiAl alloys (Yoo and Fu, 1998). The optimization of the microstructure is achieved through directional solidification, controlling the lamella colony sizes and electromagnetic cold crucible directional solidification (Kim *et al.,* 2014; Liu and Maziasz, 1998; Yamaguchi *et al.*, 2000).

Mechanical properties of TiAl alloys are highly dependent on the sizes of lamella colonies and their orientation relative to the tensile axis (Appel and Wagner, 1998; Yamaguchi *et al.,* 2000). Directional solidification is applied to control the orientation of the lamella colony boundary. In solidification during casting, the lamella boundary is oriented perpendicular to the direction of the heat flow, which is detrimental to the mechanical properties of the alloy. However, this information can be used to establish a manner of controlling the lamella colony boundary orientation (Yamaguchi *et al.,* 2000). It has been established that the angle between the lamella colony boundary and the tensile axis (Θ) has an influence on the mechanical properties of TiAl. The highest values of strength (400 MPa) occur when Θ=90° and lowest values of strength (100MPa) occur when Θ=30°- 60° (Inui *et al.,* 1992). While the highest levels of ductility (20%) occur when Θ=31° and the lowest ductility levels (0%) occur when Θ=90° (Inui *et al.,* 1992; Yamaguchi *et al.,* 2000).

The best combination of strength and ductility occurs when the lamella colony boundary is oriented parallel to the tensile axis. Directional solidification using arc melted TiAl buttons with compositions that are similar to that of the alloy as a seeding material can control the lamella orientation to make it parallel to the tensile axis (Yamaguchi *et al.,* 2000; Zhang *et al.,* 2013). Seeding material are obtained by heating the arc melted button to temperatures below

the liquidus and cooling them down to room temperature; if the microstructure of the button is replaced by equiaxed lamella grains, the button would not meet the requirements to use as a seeding material during directional solidification. Using this method can be extremely tedious and time consuming because the seeding material for each alloy is established through trial and error (Zhang *et al.,* 2013).

Electromagnetic cold crucible directional solidification is also a directional solidification method where ceramic crucibles are used to align the lamella boundary in a direction parallel to the tensile axis (Yamaguchi *et al.*, 2000). This method can be executed using the container-less process or the Brigdeman process. The Bridgeman process allows for the production of intermetallics with improved microstructural homogeneity and service performance because it allows higher superheating temperatures and more complex geometries (Zhang *et al.,* 2013). However, since $Al_2O_3$, $ZrO_2$ and CaO are used as ceramic crucible in this process, the high reactivity between molten TiAl and these ceramic crucibles leads to oxygen pick up and contamination inclusions, which are extremely detrimental to the microstructure and mechanical properties of TiAl alloys (Zhang *et al.,* 2013).

In recent developments it has been established that $Y_2O_3$ with low concentrations of porosity is a suitable candidate for use as a ceramic in this process because it is stable and has low reactivity with molten TiAl (Zhang *et al.,* 2013). Because $Y_2O_3$ is costly, it can be used to coat the cheaper ceramics like $Al_2O_3$ and $ZrO_2$ in the Bridgeman process directional solidification of TiAl alloys, which can reduce production costs of higher quality TiAl alloys with improved chemical and mechanical performance. $Y_2O_3$ coated $Al_2O_3$ can be successfully used in the Bridgeman process to produce TiAl alloys with an improved combination of mechanical properties and reduced contamination inclusions but $Y_2O_3$ is very costly and results in the production of better quality TiAl being too costly (Zhang *et al.*, 2013).

### 2.4. TiMn alloys

TiMn alloys are under study and consideration for both aeroengine and biomedical application. These alloys owe their increasing demand in the medical industry to their biocompatibility due to Mn being naturally present in the human anatomy as opposed to vanadium and aluminum obtained in Ti-6Al-4V alloy ( which is currently used in bio medical operations) (Long and Rack, 1998; Zhang *et al.,* 2009). The increasing demand of Ti-β alloys in the aeroengine

industry is due to their attractive low densities which enable a reduction of fuel consumption during operation (Boyer and Briggs, 2005).

The β phase in TiMn alloys with low Mn concentrations is vital because it is three times stronger than the α-phase, which is ductile compared to the β phase (Holden *et al.,* 1954). The brittleness of the β-phase is accounted by various deformation mechanisms which include coarse slip of β-phase during strain, which yields a brittle structure compared to ductile α, which deforms by very fine slip during strain (Ankem and Margolin, 1983). In a two phase α-β structure, interface sliding occurs during deformation where no strain is observed in the β phase, but twinning and plastic strain is observed in the α-phase grain. These deformation mechanisms are accounted for by a Burger's orientation relationship between ordered BCC-β phase (Figure 2.4) and HCP-α phase (Figure 2.5) oriented as follows:

$(101)_{\beta} || (0001)_{\alpha}$ (Tong *et al.,* 2017).

This crystal orientation enables dislocations to cross slip from close packed β to α planes which are oriented in a parallel fashion as displayed in Figures 2.4 and 2.5. It has been established that dislocations in softer HCP α phase can be injected into the α-β interface and cause sliding during strain and deformation (Ankem and Margolin, 1983) in a Burger's crystal orientation relationship displayed in Figure 2.6

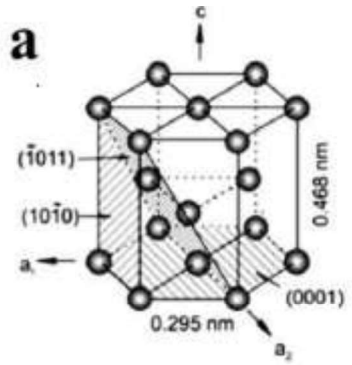


*Figure 2.4: Hexagonal Close Packed α-phase.*

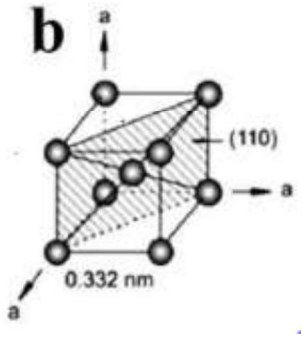


*Figure 2.5: Body Centred Cubic β-phase*

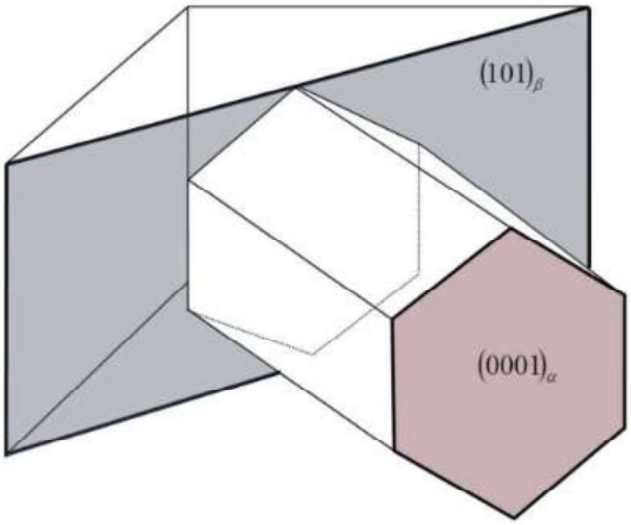


*Figure 2.6: Burger's orientation relationship between β and α phase*

The state and formation of TiMn microstructures with low Mn are highly dependent on solidification and solid state phase transformation reactions (Murray, 1981). Low Mn (less than 20Mn at%) TiMn alloys that are quenched rapidly from high temperatures within the liquidus (1180°C-1669°C) as displayed in Figure 2.7, recrystallize as disordered primary α-HCP dendrites which are suspended in a frozen non crystalized disordered TiMn β matrix (Murray, 1981).

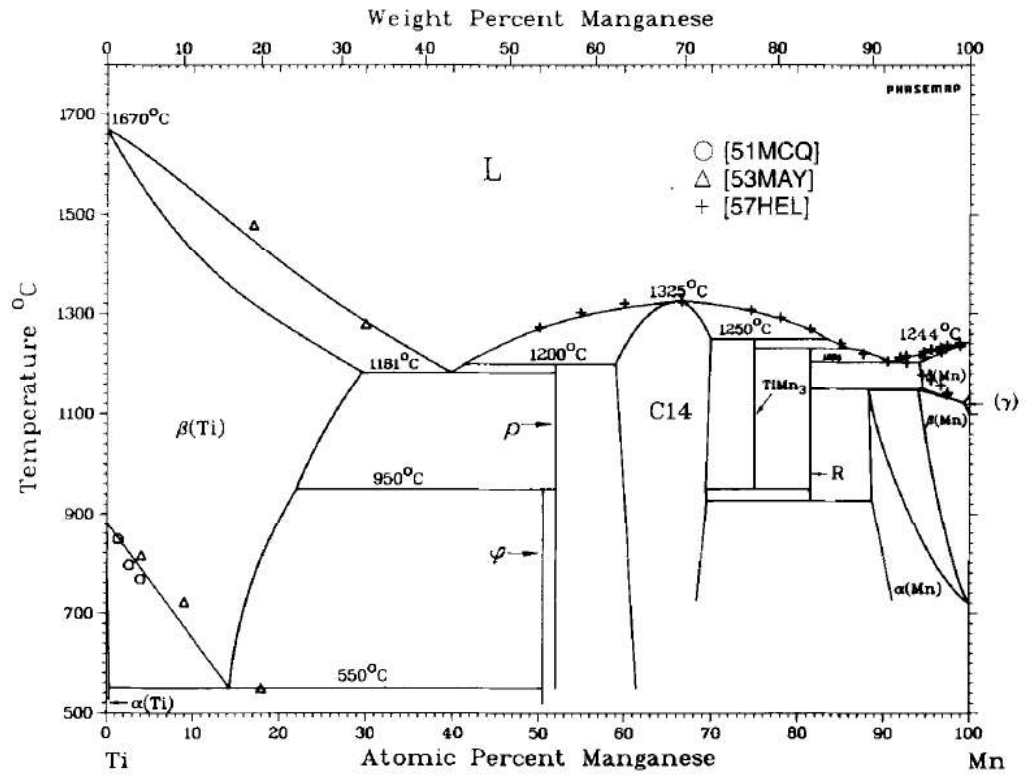


*Figure 2.7: Binary TiMn Phase Diagram by Murray (1981)*

General hardness values of TiMn alloys are highly dependent on the distribution of the α-phase (which is soft) throughout the equiaxed microstructure (Ankem and Margolin, 1983; Holden *et al.,* 1954). Thus, this has the implication that there is a relationship of direct proportionality between hardness and the proportion of β phase in α-β microstructure. However, the β-phase is extremely unstable at high temperature due to the occurrence of age hardening which is detrimental to mechanical properties (Holden *et al.,* 1954).

Heat treatment has various effects on the microstructure depending on the heat treatment temperature, heating rate, size of specimen being heated and quenching methods. Quenching from temperatures above 850°C, allows the formation of α, simultaneously retaining the existing β phase, which lead to an increase in strength and a corresponding loss in ductility (Holden *et al.,* 1954). Increasing annealing temperatures increases strength of low Mn (less than 20Mn at%) TiMn alloy, which is detrimental to the ductility and impact resistance (Gouda *et al.,* 2016). This embrittlement is caused by the presence of β phase which can result from coherency hardening (which is challenging to suppress at low Mn compositions) (Holden *et al.,* 1954).

Two phase α-β alloys are harder than pure α and pure β phases (Ankem *et al.,* 1989). The hardness of this two-phase alloy is accounted for by the matrix effect and grain refinement in the α-β microstructure. The proportion of the β-phase is directly proportional to the grain sizes and hardness, which corresponds with an increase in tensile ductility due to equiaxed grain size reduction. The effect of β-phase in this α-β solid solution is referred to as solid solution strengthening (Ankem *et al.*, 1989).

The proportion of β phase is controlled by controlling the Mn compositions. Prior existing disordered β phases can reduce thermal instability. Increasing the general composition of Mn, reduces the β transus temperature which increases the stability of β phase both at high and low temperatures, which results with the production of high volume β phase over a wider temperature range leading to increased hardness due to the presence of a higher proportion of β phase and lower proportion of α phase, leading to rapid grain growth, which causes embrittlement (Murray, 1981; Santos *et al.*, 2006). The embrittlement resulting from increased Mn is also accounted by an increase in a lattice parameter which leads to a decrease in c/a lattice ratio, which enhances solid solution hardening, which decreases UTS and elongation causing a gradual transformation from ductile to brittle fracture (Santos *et al.,* 2006; Zhang *et al.*, 2009).

Heat treatment conducted in atmospheric environments suffer from environmental embrittlement due to the absorption of hydrogen into the β phase. Dissolution of hydrogen in the β phase is caused by higher solubility of hydrogen compared to α phase (Holden *et al.,* 1954). Murray (1981) was unable to establish microstructures produced with low Mn at temperatures above 1200°C due to limited methods available to allow for rapid solidification.

### 2.5. Effects of Mn Addition on TiAl

Inui *et al.,* (1992) reported that ambient temperature ductility of polysyntheticaly twinned TiAl crystals can be improved by promoting twinning induced plasticity which can be carried out by micro alloying TiAl with Mn. Micro-alloying TiAl alloys with manganese does not lead to the formation of new compounds in the TiAl alloy. The effects of Mn on ductility has attracted great interest for study because manganese has low density (7.43kg/m$^3$), which will be appropriate for aeroengine application, and it is very affordable in comparison to other transition metals with the potential to improve the ductility of TiAl (Appel, 2010; Jiao *et al.,* 2016). The capability of Mn to improve ductility can be explained by conventional dislocation slip mechanisms, twinning induced plasticity, electronics and microstructural morphologies

(Shu *et al.,* 2012). However, research regarding the effects of micro alloying TiAl with Mn is still quite limited.

### 2.5.1. Electronic Effect of ternary Mn addition

Morinaga *et al.*, (1990) studied the effects of various ternary element additions on the electronic structure in a TiAl matrix. Through these studies, it was established that ductility of TiAl is highly influenced by the electronic structure and charge density changes of TiAl, which governs the kind of bonding and interactions between atoms. The types of bonding between atoms are influenced by the substitution of Al atoms into Ti sub-lattices or substitution of Ti atoms into Al sub-lattices (Morinaga *et al.*, 1990). When an Al atom substitutes into a Ti sub-lattice in an Al rich matrix, it leads to d-p bonding between Ti and Al atoms. These Al atoms have extremely low electron density change which spreads to the first neighbouring atoms. The neighbouring atoms are comprised of eight Al atoms and 4 Ti atoms, resulting in lowered bond orders and weakened bonds (Morinaga *et al.,* 1990). In contrast, when Al atoms are substituted with Ti atoms in a Ti rich matrix, it leads to d-d covalent bonding between atoms, which have larger charge density change spreading to the first neighbouring atoms comprised of eight Ti atoms and four Al atoms, which results in a higher bond orders and strengthening of bonds (Morinaga *et al.,* 1990). Thus, in selecting an appropriate additional ternary transitional element, it is important that the element enhances covalent bonding between particles. It has been established that Mn occupying an Al site increases the electron density between the Mn and Ti atoms, leading to metallic bonding between Ti and Mn atoms, which contributes to the improved ductility (Kawabata *et al.,* 1998).

Manganese has been selected as a ternary additional element because of its ability to preferentially substitute into Al sub lattice due to the formation enthalpies of Mn occupying the Al sub lattice being lower than Mn occupying the Ti sub lattice (Shu *et al.,* 2012). Mn has the capability to enhance covalent d-d bonding between Ti atoms and metallic bonding between Ti and Mn atoms which is highly beneficial for the ductility in TiAl (Shu *et al*., 2012).

### 2.5.2. Lattice shrinkage

Since Mn has a smaller radius (0.179nm) than Al (0.182nm), when Mn occupies the Al sub-lattice, it leads to lattice shrinkage of the $L1_o$ ordered γ-TiAl structure along the *c*-axis, which leads to a reduction of the *c/a* ratio (Shu *et al.,* 2012). The reduction of the *c/a* ratio has the

implication that the tetragonality of the $L1_o$ structure is also reduced which leads to increased symmetry in the crystal structure (Shu *et al.,* 2012). The reduction of *c/a* is attributed by the contraction of the lattice along the a-axis which is accounted for by the increase in Al atoms in the Ti sub lattices, which reduce the Ti-Al bonds (which have a smaller bond length than Ti-Ti bonds) along the *c*-axis thus causing a reduction of the lattice parameter along the *a*-axis (Shu *et al.*, 2012; Vujic *et al.,* 1988).

As symmetry increases, more dislocation glide systems become activated. The lattice shrinkage also results in the reduction of inter planar spacing, which allows for cross gliding dislocations during fracture strain and increases the dislocation mobility during deformation (Shu *et al.,* 2012; Vujic *et al.,* 1988). Dislocation mobility allows for larger fracture strain before metallurgical failure, which results in improved ductility. Therefore, Mn can enhance ductility by improving lattice symmetry and the multiplication of glide systems (Wang *et al.,* 2018).

### 2.5.3. Grain Refinement

The lattice shrinkage of TiAl leads to shrinkage of individual grains. The shrinkage of bulk individual grains causes grain refinement of a structure (Shu *et al.,* 2012). The presence of refined lamellar grains in a structure, allow the initiation, propagation and nucleation of micro cracks during applied stress (Shu *et al.,* 2012). Micro cracks propagate in a trans-lamella fashion during ductile fracture and in an intergranular fashion during brittle facture (Liu and Maziasz, 1998; Shu *et al.,* 2012). Micro cracks (<50μm) improve mechanical properties because they are able to hinder rapid crack growth during fracture (Hu, 2001).

### 2.5.4. Solid Solution Strengthening

Lattice shrinkage causes the formation of a stress field around solute atoms. Solute atoms and dislocations interact (attract or repel) with one another, which results in the presence of solute atom-dislocation interaction energy (Wang *et al.,* 2018). The values of interaction energy are influenced by various factors. The interaction energy is negative when the solute atom is located above the dislocation glide because the solute atom reduces dislocation energy resulting from compressed volume above the dislocation core (Wang *et al.,* 2018). This results in attraction between dislocation and solute atoms. In contrast, the interaction energy is positive when the solute atom is located below the dislocation glide plane leading to the repulsion of solute atoms by dislocations (Wang *et al.,* 2018).

For deformation to take place, stress is required to overcome the sum of modulus interaction energy and solute atom and edge dislocation interaction energy. Higher total interaction energy implies that more stress is required to move dislocations to overcome interaction energy for deformation to occur (Wang *et al.,* 2018). When TiAl is micro alloyed with Mn, the yield strength of the TiAl increases with increasing Mn content, which implies that Mn has the capability of improving the strength and ductility of TiAl through substitutional solid solution strengthening which is accounted for by the increased modulus interaction energy and solute atom - dislocation interaction energy (Wang *et al.,* 2018).

Ternary phase diagrams of TiAlMn alloys have been constructed by performing heat treatment at three different temperatures: 1300°C, 1200°C and 1000°C. From the findings of these experiments, it can be observed in Figure 2.8, that the formation of $\alpha_2+\gamma$ is more favourable at lower temperatures (1000°C) over a larger composition range compared to higher temperatures ( 1300°C and 1200°C) (Kainuma *et al.,* 2000).

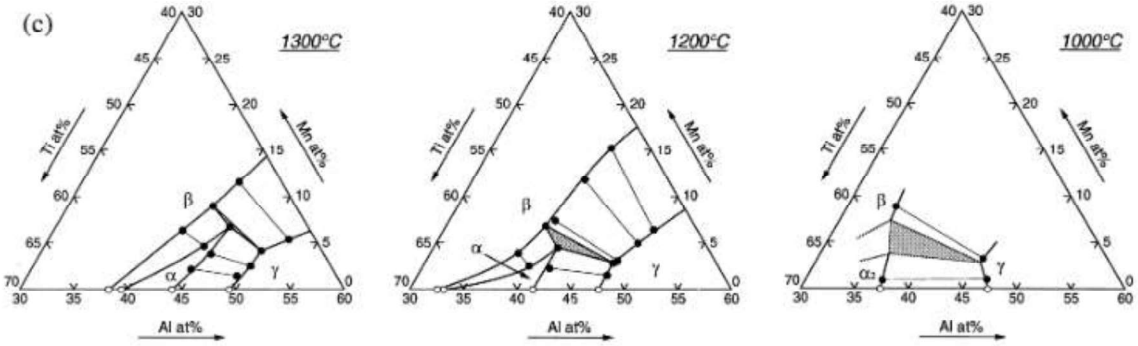


*Figure 2.8: Ternary Phase diagrams for Ti-Al-Mn compiled by Kianuma et al (2000)*

### 2.5.5. Twin Toughening Effects

In previous studies (Appel *et al.,* 2011a; Yoo and Fu, 1998), it has been proven that deformation induced twinning contributes significantly to the toughening of course γ-TiAl lamellar alloys. This mechanism is called twin toughening and plays a huge role in ductility prior to micro crack nucleation and propagation of Mn micro alloyed TiAl (Soboyejo *et al.,* 1995). Twin toughening is governed by the distribution of stresses in the twin process zone (TPZ) which is situated around the crack (Soboyejo *et al.,* 1995). The average smear stress within the twin process zone is comparable to the shear stress obtained from a tensile test. The twin toughening effect can be calculated by multiplying the estimated toughening increment due solely to

deformation-induced twinning by the estimated fraction of the plasticity that is attributed to deformation twinning (Mercer and Soboyejo, 1997)

### 2.5.6. Challenges faced due to Mn addition

The addition of Mn can improve room temperature ductility and high temperature strength of TiAl at low compositions (Mn <2 at %) due to the twin toughening effect, lattice shrinkage, grain refinement and solid solution strengthening. However, when the concentration of Mn exceeds 2 at %, the ductility and strength gradually begins to decrease. The reduction of high temperature strength and ambient temperature ductility can be accounted for by lattice distortion which results from excess Mn atoms (Vujic *et al.,* 1988).

Additional Mn also has the ability to stabilize the B2 phase in a lamellar microstructure, which is brittle and acts as crack initiation sites. B2 phase increases with increasing Mn concentration and it is undesirable for the mechanical properties of TiAl because it enables rapid crack propagation to occur within more B2 sites which happen to be present at larger proportions as Mn concentration increases (Inui *et al.,* 1992).

However, the presence of Mn in duplex microstructures stabilises the $\alpha_2$-phase, which precipitates on grain boundaries, promoting grain refinement by inhibiting grain growth at increased temperatures (Wang *et al.,* 2018). The type of fracture is highly dependent on grain sizes, where coarse grains are usually subject to brittle intergranular fracture and fine grains are subject to ductile trans granular fracture.

The $\alpha_2$-phase at grain boundaries is usually found to contain Ti, Al, C, $O_2$ and Mn (Wang *et al.,* 2018). The segregation of Mn to grain boundaries promotes intergranular fracture due to reduction in grain boundary cohesion. Reduction of grain boundary cohesion leads to a fracture mode where crack initiation occurs at grain boundaries during fracture and progress as grain boundary fracture as the specimen undergoes intergranular fracture during intergranular separation. This leads to a reduction in high temperature strength and ambient temperature ductility, which is highly undesirable for aero engine application (Wang *et al.,* 2018).

Segregation of Mn to grain boundaries can be caused by high temperature annealing at lengthy holding times. In duplex structures, the effects of the reduction in grain boundary cohesion can surpass the effects of twin toughening thus leading to the presence of Mn being detrimental to duplex structures. However, the presence of Mn was proven to be beneficial for the high

temperature strength and ambient temperature ductility in lamellar microstructures (Wang *et al.,* 2018).

Mn can improve ambient temperature ductility of TiAl, but since there is an imbalance in mechanical properties between high temperature creep resistance and ambient temperature ductility, this has the implication that Mn has a detrimental effect on high temperature creep resistance of TiAl.

Coarse grain (100 μm) lamellar microstructures have excellent creep resistance at elevated temperatures but poor room temperature ductility, while finer grained (50 μm) duplex microstructures have improved room temperature ductility but poor creep resistance (Maruyama *et al.,* 1997). The superior creep of fully lamellar TiAl is attributed to the large grain sizes which interlock at grain boundaries in a zig-zag fashion. However, it was established that equi-axed grain structure yields better creep strength than fully lamellar microstructure (Maruyama *et al.,* 1997). Creep rates are highly affected by microstructural factors such as inter lamellar spacing, grain sizes and volume fractions. It has been proven that at high temperatures, creep rates decrease with decreasing lamellar spacing which implies that fine lamellar spacing can effectively improve the creep strength due to strain hardening. However, strain hardening is not effective at low stresses (Maruyama *et al.,* 1997).

It has been proven that a higher fraction of γ-phase yields improved creep resistance (Maruyama *et al.*, 1997). Creep resistance of TiAl is independent of grain size when grain size is ≥ 100 μm, which means the structure cannot be weakened due to grain size. The instability of creep resistance of TiAl reducing with grain size when the lamellar grain size ≤ 100 μm, is attributed to the occurrence of dynamic recrystallization during creep along the grain boundaries (Maruyama *et al.,* 1997). This implies that it is important to stabilize grain boundaries when grain size is ≤100 μm. However, a study by (Maruyama *et al.,* 1997) reported that a composition of Ti-48mol%-2%Mn-2%Nb with a fine grain size yield relatively good creep resistance. The addition of Mn enhances grain refinement, thus it has the potential to impair high temperature creep properties of TiAl (Maruyama *et al.,* 1997).

Improving ductility of TiAl by Mn addition has only been carried out using traditional fabrication methods such as ingot casting, hot isostatic pressing and heat treatment processes, which pose large challenges such as high material wastage and costs (Kelly *et al.,* 2001).

## 2.6. Traditional Processing Methods

This section gives a description of traditional fabrication processes which have been performed in attempt to improve ductility of TiAl alloys. These processes have also been applied in combination with micro alloying using various ternary alloying element mentioned previously.

### 2.6.1 Hot Isostatic Pressing

Hot Isostatic Pressing (HIPping) is a traditional processing method that has been used to fabricate TiAl components, which includes applying high pressure and temperature on a workpiece without altering the net shape (Loh and Sia, 1992). The TiAl HIPping process to produce components includes four steps. The first step is providing TiAl alloying powders with compositions capable of generating α, $\alpha_2$ and γ phases (46-50at%Al) (Kelly *et al.,* 2001). According to the TiAl binary phase diagram, the compositions in this range pass through a high temperature peritectic reaction, and into the α phase field and through a eutectoid temperature into the $\alpha_2$+γ phase field, upon cooling from molten form (Appel *et al.,* 2011a). The second step is determining the α-transus temperature which can be accomplished with various methods such as extracting several TiAl alloy pieces and heating them to temperatures near the expected α-transus temperature and quenching those pieces (Kelly *et al.,* 2001; Loh and Sia, 1992). Through metallographic examinations, γ grains and α phase transformations are observed for heat treatment temperatures below the actual α-transus temperature, while α phase transformation are produced in the form of large lamella colonies, are observed for heat treatment temperatures above the α-transus temperatures (Kelly *et al.,* 2001). The determination of the α-transus temperature allows one the ability to establish the appropriate heat treatment temperatures which will result in the workpiece being 10-90%volume of the gamma phase (Kelly *et al.,* 2001; Kim and Dimiduk, 1991). The third step is the consolidation of the workpiece where HIPping is applied by placing the workpiece in a pressure vessel which contains inert gas such as argon or nitrogen. The HIPping temperature is set at temperatures approximately from 30°C to 140°C below the α transus and the pressure from 140 MPa to 200 MPa (Kelly *et al.,* 2001). The procedure is carried out for a period of 20 hours to allow for the elimination of porosity, density homogenization and formation of the γ phase. After the HIPping process is complete, the workpiece is furnace cooled to prevent thermal cracking. Heat treatment is employed as a post processing step to achieve and refine the final desired microstructure (Kelly *et al.,* 2001). HIPping is capable of producing TiAl alloys with ambient temperature ductility with values between 1-2% (Kelly *et al.,* 2001; Loh and Sia, 1992). These

phase transformation reactions can be observed in the binary TiAl phase diagram displayed in Figure 2.9. However, this process is highly time consuming, requires large amounts of energy to execute and is extremely costly. However, the parameters applied in the HIPping process can be useful in understanding the physical metallurgical fundamentals for this research.

### 2.6.2 Ingot Casting

Ingot casting is another procedure used in the fabrication of TiAl alloy components, where molten TiAl alloy is poured into molds and allowed to solidify into desired shapes during cooling. Casting of Ti-Al alloys results in the formation of a dendritic microstructure with a strong texture (Austin *et al.,* 1996). These dendrites are grown in the preferred crystallographic directions near $<0002>_{\alpha}$ during solidification and α dendrites are transformed to γ-lamellar microstructure with a $<111>_{\gamma}$ direction parallel to the initial $<0002>_{\alpha}$ during cooling, making the radial direction nearly parallel to the normal direction and the direction of heat flow during solidification (Appel *et al.,* 2011a). This results in directional solidification which leads to strong mechanical anisotropies. These columnar grains and textures can be refined by the employment of heat treatment (Appel *et al.,* 2011a).

Heat treatment can also allow for the formation of the lamella microstructure which has properties that are dependent on lamella microstructural variables such as thickness, grain size and the inter-lamellar spacing of γ and $\alpha_2$, and the lamella orientation with respect to the loading axis (Liu and Maziasz, 1998).

A fine grained fully lamella microstructure has superior mechanical properties including high temperature strength, fracture toughness and room temperature ductility (Kim and Dimiduk, 1991). A microstructure with the grain size range of 50-80 μm is most appropriate for jet engine parts (Chesnutt, 1992).

The γ-phase can be attained by tempering in α and α+γ phase fields where phase transformations are highly dependent on the cooling rates (Kim and Dimiduk, 1991). However, these transformations are extremely complex and cannot be applied to precision-cast components such as engine valves and compressor or low pressure turbine blades (Chesnutt, 1992; Lapin, 2009). These limitations pose a challenge in the production of complex TiAl alloy engine parts, thus resulting in low ambient temperature ductility in those components.

However, crystal orientation fundamentals applied in ingot casting to improve ductility can be useful in understanding the effects of crystal orientation on TiAl ductility (Appel *et al.,* 2011a).

### 2.6.3 Heat Treatment

Heat treatment is usually employed as a post processing step for processes employed in the production of TiAl parts to attain and refine the desired microstructure. Heat treatment can result in the formation of duplex (DP), near γ (NG), fully lamellar (FL), and near lamellar (NL) microstructures depending on the composition and heat treatment employed. A fine fully lamellar microstructure is most preferred for aerospace application because they have good balanced mechanical properties (Ahmadi *et al.,* 2016). The morphology of γ- TiAl and $\alpha_2$–$Ti_3Al$ is complex and depends on aluminum levels, processing and heat treatment. These morphologies can be observed in the binary TiAl phase diagram displayed in Figure 2.9.

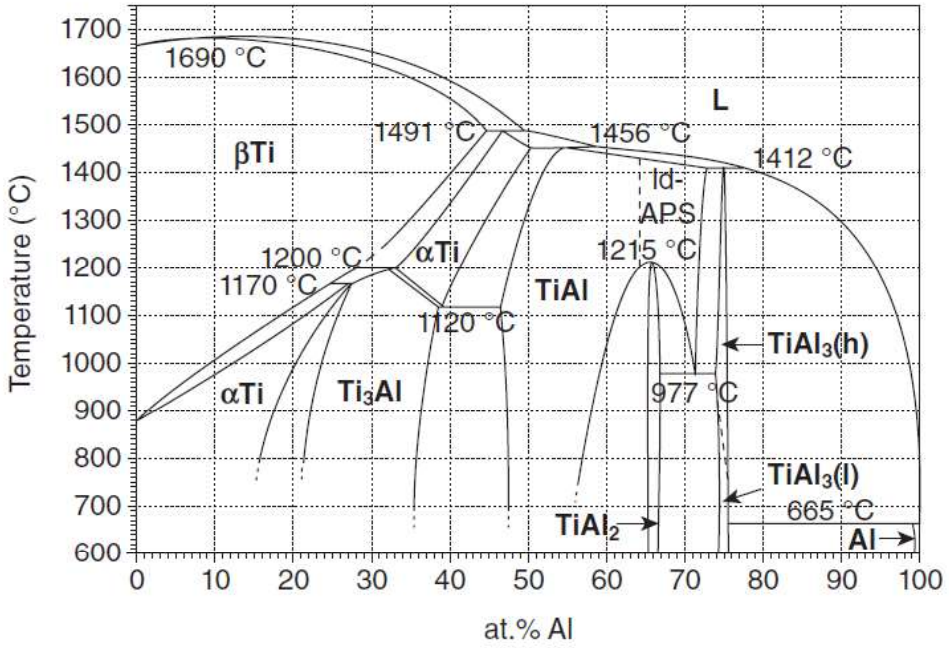


*Figure 2.9: Binary TiAl phase diagram (Schuster and Palm, 2006)*

The duplex structure which results from heat treatment in α + γ phase field is generally preferred. On cooling, the structure transforms to a mixture of γ and $\alpha_2$ grains and colonies of lamellar γ and $\alpha_2$. This is similar to typical α-β titanium alloys which occur at higher temperatures, commonly used for high temperature application. The lamellar constituent

actually begins to form during cooling within α + γ phase field (Clemens *et al.,* 2006; Wu and Hu, 2005).

There is little interfacial energy involved in the formation of γ laths within α phase, and this is the most convenient way in which to maintain the equilibrium proportions of the two phases. Upon cooling below the eutectoid, additional γ phase forms, either through thickening of existing laths or creation of new laths. The α phase orders to become $\alpha_2$; at this point, the $\alpha_2$ laths make up a small fraction of the lamellar constituent. The presence of γ grains, as opposed to laths, must arise from other processes (Küstner *et al.,* 2003; McCullough *et al.,* 1989). Extended periods of heat treatment low within α + γ phase field can lead to coarsening of gamma laths. Alternatively, γ grains can form in the interdendritic, aluminium-rich areas of the microstructure during cooling from the casting operation and persist through subsequent heat treatment provided temperatures are kept low and/or aluminium is high (Kelly *et al.,* 2001).

When such a composition (46-50at%Al) in this range is cooled from the molten state, it passes through a high-temperature peritectic reaction and into the alpha-titanium phase field. Upon cooling, the alloy passes into α+ γ phase field. α- Transus that lies between α and α+ γ is highly dependent on aluminium levels (Schuster and Palm, 2006).

Upon further cooling, the alloy passes through a eutectoid temperature and into $\alpha_2$+ γ phase field. When such an alloy is formed and cooled from the molten stage, it contains high levels of porosity and irregular microstructures, which result in low and uncontrolled ductility (Wang *et al.,* 2018). However, heat treatment can be applied as a post processing step to other fabrication processes to refine the desired microstructure with desirable properties and will most likely be applied in this work to achieve the same result.

Ingot metallurgy, investment casting and powder metallurgy followed by hot isostatic pressing, ageing, annealing and hot working have been used successfully to generate TiAl parts with desirable mechanical properties (Kelly *et al.,* 2001). However, these processing methods have a variety of short falls which may restrict practical applications.

In ingot metallurgy and investment casting, TiAl alloys are prone to chemical inhomogeneity in the microstructure and segregation resulting from columnar grains formed due the peritectic solidification reactions from the α-phase and also from density differences in the elements of the constituents.

A microstructure that is more refined with improved homogenization is obtained through dynamic recrystallization. Dynamic recrystallization can be achieved by post-process heat treatment and thermo-mechanical processes such as hot rolling, forging and extrusion. Thermo-mechanical processes produce duplex structures with an average grain size of 50μm at temperatures from 1200-1250°C and fully lamellar microstructure with average colony size of 100 μm at 1350°C.

TiAl ingots and casts can also be subjected to small concentrations of impurities during processing. Impurities are avoided by the introduction of cleaner processing methods such as cold hearth plasma arc melting and vacuum arc remelting (Kothari *et al.,* 2012).

### 2.6.4 Powder Metallurgy

In an attempt to resolve challenges faced in the production of ingots and cast, powder metallurgy has been used to produce TiAl parts. Powder metallurgy production involves the gas atomization of pre-alloyed powders, followed by consolidation by extrusion to full density or by hot isostatic pressing at temperatures ranges 1200-1400°C and pressure range 100-200 MPa from 2 to 6 hours (Ding *et al.,* 2015). This production method results in final products which have improved porosity, homogeneous microstructure, and less segregation. However, during production, impurities and interactions with the inert gas environment can lead to increased porosity due to gas entrapment and interstitials which can be extremely detrimental for the strength of the product (Ding *et al.,* 2015).

Near net shaping of TiAl to produce complex products can be achieved by spray forming and metal injection moulding (MIM) which involve mixing metal powders with binders such as wax and polymers, moulding of the part and removal of binders, followed by sintering. Products produced by MIM also suffer from impurities and porosity (Kothari *et al.,* 2012).

Although TiAl has been successfully produced using aforementioned processes, numerous economic and technical challenges are being faced in these productions. These challenges arise from the lack of ductility of TiAl alloys at ambient temperatures which restricts their process ability. This has the implication that production temperatures should be kept as high as the melting point temperatures to allow for the shaping of the desired final product, which is extremely costly, energy intensive, and time consuming. Most TiAl alloys require post process heat treatments and thermomechanical treatments to attain desired microstructures, which means, additional energy and time will be consumed post process. Powder metallurgy processes are less costly compared to casting and ingot metallurgy productions, but the milling

of the powder to desired particle sizes is energy and time consuming because milling can take up to 50 hours (Bartels and Schillinger, 2001).

To overcome challenges faced in the production of TiAl alloys, spark plasm sintering, direct rolling and laser forming processes such as laser engineered net shaping (LENS) and selective laser melting are continuously being investigated as potential substitutes for the traditional fabrication processes. These more modern processes can produce more complex parts at lower costs, time and energy consumption but can also face the challenge of porosity and scalability (Griffith *et al.,* 1996).

## 2.7 Laser Engineered Net Shaping (LENS)

Since there are numerous disadvantages associated with traditional fabrication processes, additive manufacturing processes are currently under continuous investigation as possible substitutes for traditional fabrication processes in the production of TiAl components (Griffith *et al.,* 1996). Laser engineered net shaping (LENS), also commonly known as direct metal deposition, is an additive manufacturing process which fabricates 3-D components from computer aided design (CAD) models by depositing, melting and re-solidifying powder metal on a substrate in a layer by layer fashion from bottom to top until the component is complete (Zheng *et al.,* 2008).

LENS can fabricate components with both simple and complex geometries at extremely high precision in a cost effective and time efficient manner due to the absence of thermochemical processes and due to minimal post processing steps required. LENS only consists of an atmospheric glove box, YAG laser, powder feed nozzle, substrate and a 3-axis computer controlled positioning system (Griffith *et al.,* 1996; Gu, 2015).

During LENS, metal powder is deposited on a substrate through a powder feed nozzle, while the laser beam supplies the powder metal with heat energy at a set power value, which allows the powder metal to melt and form a molten pool. The molten pool solidifies as the laser beam continuously scans through the deposited metal powder according to the CAD model, which results in a layer by layer construction of the CAD model as the molten pool solidifies (Griffith *et al.,* 1996).

The solidification rates and dimensions of the molten pool are controlled by controlling various LENS parameters such as laser scan speeds, the workpiece wall thickness, powder feed rates

and laser power. Controlling the solidification rates and dimensions of the molten pool controls resultant microstructures, phase compositions and mechanical properties of LENS fabricated components (Liu *et al.*, 2016; Sciammarella and Salehi Najafabadi, 2018).

Since LENS has the potential to replace traditional fabrication processes in the production of TiAl components, it is highly important that it has the ability to fabricate components with improved mechanical properties in comparison to components fabricated with traditional processes (Griffith *et al.,* 1996).

The LENS process has been selected for this work because it is able to fabricate parts with high densification of more than 99.5%, which is higher than the densification of most traditional processes and additive manufacturing processes, at extremely high precision and no material wastage (Gu, 2015). LENS is also selected for this work because it has successfully fabricated components with superior mechanical properties with aluminium, titanium alloys, steel, stainless steels, copper, nickel, Inconel, cobalt and tungsten. LENS has also been selected over selective laser melting (SLM) and the wire feed system for this study because unlike SLM, it can print using Aluminium powder as feed stock. LENS is also more suitable for this study, because unlike SLM, the produced part does not require much time to cool down before testing. Using LENS also does not leave excess powder in the form of material wastage (Attar *et al.,* 2017; Gu, 2015).

LENS has successfully generated TiAl parts with 80% γ- phase, with fine grain lamellar microstructures, which is desirable because it enables improved ductility of TiAl (Liu and DuPont, 2002).

Although LENS can successfully fabricate components with superior mechanical properties, it is faced with the challenge of post processing thermal cracking. Thermal cracking is caused by thermal induced stresses which are due to high thermal gradients (Sharman *et al.,* 2018).

Liu and Weiping (2002) generated a sample with reduced post processing thermal cracks by preheating the substrate to reduce thermal gradients and thermal stresses in the LENS produced part but did not eliminate the post processing thermal cracks completely. However, (Sharman *et al.,* 2018) successfully generated a crack free TiAl sample by optimizing the laser focus position. This allows for the preheating of the metal powder before it undergoes melting to form a molten pool. It has been established that this can reduce thermal gradients and stresses to a point which allows LENS to produce a crack free sample (Sharman *et al.,* 2018).

During the use of LENS, various variables have an influence on the microstructure and physical properties, such a densification, of the LENS generated samples. Variables such as laser powers, scan speeds, powder feed rates and hatch spacing have been optimized in previous studies, where LENS was used to generate conventional titanium alloys, to examine the effects on the microstructure (Gu *et al.*, 2015).

The Laser Energy per Unit Length (LEPUL) also known as Linear Energy Density (LED) of the laser beam (J/m) has an influence on the densification of LENS produced specimen and can be determined in Equation 2.2 (Gu *et al.,* 2015)

$$LEPUL = \frac{P}{v} \tag{2.2}$$

Where:

$$v = \ Laser\ scanning\ speed\ \left(\frac{cm}{s}\right)$$

$$P = Laser\ power\ (W)$$

The effects of optimizing the LEPUL on densification can be observed by examining the microstructure under optical microscopes where comparisons can be made by plotting graphs. Energy Density (E) also known as volumetric laser density can be used to determine densification and the total energy input during LENS. E can be obtained using Equation 2.3 (Liu *et al.,* 2016).

$$E = \frac{P}{vht} \tag{2.3}$$

Where;

$$h = hatching\ distance\ (cm)$$

$$t = layer\ thickness\ (cm)$$

The higher the value of Energy Density results in higher temperature in a specimen. This creates a relationship of direct proportionality between temperature and Energy Density and a relationship of inverse proportionality between temperature and laser scanning speeds (Liu *et al.*, 2016).

The amount of liquid phase formed in the molten pool during LENS also has an influence on the resulting microstructure and densification of the processed specimen by controlling the changes in characteristics such as liquid-solid rheological properties, wettability and viscosity (Bontha *et al.,* 2006; Gu *et al.,* 2015). The densification activity of the melt is controlled by the

base viscosity ($\mu_o$) which is highly temperature dependent, it decreases with increasing temperature. The dynamic viscosity can be defined by Equation 2.4.

$$\mu = \mu_0 \left(1 - \frac{1-\varphi_l}{\varphi_m}\right)^{-2} \quad (2.4)$$

Where

$$\mu = \ Dynamic\ Viscosity\ (Kg/(cm.s))$$

$$\mu_0 - \ Base\ Viscosity\ (Kg/(cm.s))$$

$$\varphi_t = \ Volumetric\ fraction\ of\ liquid\ phase$$

$$\varphi_m = Critical\ Volume\ Fraction\ of\ solids$$

Thermal gradients and solidification cooling rates are key parameters which control the microstructure and morphologies in laser deposited structures. The 2D Rosenthal solution for a moving heat source can be used to determine solidification cooling rates and thermal gradients. This model incorporates the non-linear effects of temperature dependent properties, latent heat of transformation and temperature independent material response. These thermodynamic mechanisms are governed by convection currents during deposition (Kamara *et al.,* 2014).

$\bar{\bar{t}}$ is the dimensionless time given by Equation 2.5 (Bontha *et al.,* 2006).

$$\underline{t} = \frac{t}{2k/\rho c V^2} \quad (2.5)$$

Where

$$k \ = \ Thermal\ Conductivity\ (W/(cm.K))$$

$$c = \ Specific\ Heat\ (J/(Kg.K))$$

$$\rho \ = \ Density\ (Kg/(cm^{\,3}))$$

The dimensionless cooling rate is related to the actual cooling rate (Bontha *et al.,* 2006) as shown in Equation 2.6

$$\frac{\partial \underline{T}}{\partial \underline{t}} = \left(\frac{2\pi k^2 b}{\alpha Q \rho c V^2}\right)\frac{\partial T}{\partial t} \quad (2.6)$$

Where

$$\alpha Q = Absorbed\ Power\ (W)$$

$$b = Wall\ thickness\ (cm)$$

$$V = Velocity\ (cm/s)$$

The effect of laser power and scanning speed on the microstructure and morphologies is related to the solidification rates (Bontha *et al.,* 2006) and can be determined using Equation 2.7.

$$R = \frac{1}{G}\frac{\partial T}{\partial t} \tag{2.7}$$

Where

$$R = solidification\ rates\ (K/s)$$

$$G = thermal\ gradients\ (s/K)$$

$\frac{\partial T}{\partial t}$: Cooling rate

It has been established through previous work that there is a relationship of direct proportionality between laser scanning speeds and solidification rates and cooling rates, and a relationship of inverse proportionality between laser power and cooling rates. Increased laser power results in a reduced thermal gradient.

Rosenthal solution can also be used to determine the cooling and solidification rates of bulky 3-D geometry (Bontha *et al.,* 2006) and is expressed in Equation 2.8.

$$\underline{T} = \frac{e^{(-\underline{x_0}+\sqrt{\underline{x_0}^2+\underline{y_0}^2+\underline{z_0}^2})}}{2\sqrt{\underline{x_0}^2+\underline{y_0}^2+\underline{z_0}^2}} \tag{2.8}$$

Where

$\underline{T} = cooling\ and\ solidification\ rates\ (\frac{K}{s})$

$x; y\ and\ z = spatial\ dimensions\ (coordinates\ relative\ to\ where\ the\ build's\ point\ of\ origin$

Cooling rate can also be illustrated according to coordinates as displayed in Equation 2.9.

$$\underline{T} = \frac{T-T_0}{(\frac{\alpha Q}{\pi k})(\frac{\rho c V}{2k})},\ \underline{x_0} = \frac{x_0}{2k/\rho c V},\ \underline{y_0} = \frac{y_0}{2k/\rho c V} \text{ and } \underline{z_0} = \frac{z_0}{2k/\rho c V} \tag{2.9}$$

These values can also be represented in the form of a diagram as displayed in Figure 2.10.

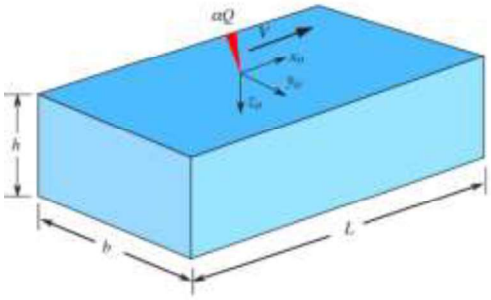

*Figure 2.10: Bulky 3-D geometries (Bontha et al., 2006)*

Unlike in 2-D geometries where normalization is only a function of power, the normalization of 3-D geometries depends on both laser power and velocity. Thus the dimensionless cooling rate and thermal gradient for bulky 3-D geometries are defined by Equation 2.10:

$$\frac{\partial \underline{T}}{\partial \underline{t}} = \left(\frac{2k}{\rho cV}\right)^2 \left(\frac{\pi k}{\alpha QV}\right) \frac{\partial T}{\partial t}, \; |\underline{\nabla T}| = \left(\frac{2k}{\rho cV}\right)^2 \left(\frac{\pi k}{\alpha QV}\right) |\nabla T| \qquad (2.10)$$

According to Equation 2.11, dimensionless melting point temperature for bulky 3-D geometries is defined in terms of both laser power and velocity as

$$\underline{T_m} = \frac{T_m - T_0}{(\rho Q/\pi k)(\rho cV/2k)} \qquad (2.11)$$

Equation 2.7 can also be used to calculate cooling rates and solidification rates for bulky 3-D geometries (Bontha *et al.,* 2006).

## 2.7. Oxidation behaviour of TiAl and TiMn based alloys in Aero Engines

A jet turbo engine has four main sections. These sections include the fan section, compression section, combustion section and turbine section. During operation, the fan section which is composed of fan blades attached to a fan casing, takes air into the engine and is heated to approximately 800°C (Okura, 2015). After air enters through the fan section, it is taken into the compressor section which is comprised of two sections: a low pressure compressor and a high pressure compressor which are also subjected to temperatures of approximately 900°C (Essienubong *et al.*, 2016).

The compressor section compresses air, which leads to an increase in temperature where low pressure compressors are subjected to lower temperatures compared to high pressure compressors which are situated closer to the combustion chamber (Okura, 2015) . In the combustion chamber, compressed air is mixed with fuel, resulting in the production of hot gases with high energy and forces to propel the aircraft and is subjected to temperatures between 1000°C and 1370°C (Essienubong *et al.*, 2016; Okura, 2015). The turbine section is responsible for power generation to rotate the shaft which goes through the entire engine and connects and holds all four sections together. This leads to the rotation of all the sections during operation (Okura, 2015).

These parts are produced using various materials including Co,Ni, Fe and Ti6Al4V. Heat exchangers were previously used to maintain lower temperatures in jet engines to prevent material failures, but using high temperature strength materials such as Ni- and TiAl based alloys has led to lighter aeroengines since heavy heat exchangers were no longer necessary (Jafari and Nikolaidis, 2018). These aeroengine parts take 5 minutes to heat from room temperature to their operating temperatures and 2 minutes to cool down to temperatures below 50°C (Karaoglanli *et al.,* 2013). A combination of air and high temperatures in the aeroengine environments leads to oxidation of TiAl-based alloys. The oxidation of TiAl based alloys occur by the chemical reactions listed in Equations 2.12 and 2.13 (Dai *et al.,* 2016)

$$Ti + O_2 = TiO_2 \quad (2.12)$$

$$2Al(s) + \frac{3}{2}O_2 = Al_2O_3 \quad (2.13)$$

$TiO_2$ and $Al_2O_3$ are highly susceptible to spallation and serve as a non-protective oxide film at temperatures above 900°C (Chang, 2007), $TiAl_3$ can also be produced at high temperature and can serve as a protective film at high temperatures (Kung, 1990).

The oxidation of binary TiMn and ternary TiAlMn can lead to the production of $Mn_3O_4$, $Mn_2O_3$ and $MnO_2$ alongside oxides produced in Equations 2.12 and 2.13 The oxidation of Mn is illustrated in Equations 2.14, 2.15 and 2.16.

$$3Mn + 2O_2 = Mn_3O_4 \quad (2.14)$$

$$2Mn + \frac{3}{2}O_2 = Mn_2O_3 \quad (2.15)$$

$$Mn + O_2 = MnO_2 \quad (2.16)$$

## 2.9. Chapter Summary

From reviewing literature concerning TiAlMn microstructures, crystal structures and nanostructures alongside the mechanical behaviour, it can be observed and established that great difficulty has been experienced in balancing the mechanical properties of TiAlMn alloys. The imbalance in the mechanical behaviour of TiAlMn alloys centres around the inverse proportionality between high temperature creep resistance and ambient temperature ductility. Adjustments in the microstructures which include controlling lamella colony sizes, controlling angles between the lamella colony boundaries and tensile axis, controlling crystal lattice parameters and interplanar spacings, which are beneficial for ambient temperature ductility, are detrimental for high temperature creep resistance. Inverse proportionality in mechanical properties is the largest challenge which poses a limitation in the manufacturing and practical application of TiAlMn alloys for aero engines.

Challenges faced in the traditional fabrication of Ti-Al-Mn components lead to increased production costs and large material wastage. The introduction of LENS as a fabrication process in the production of TiAlMn alloys has the potential to assist in mitigating challenges faced in the traditional fabrication of TiAlMn alloy components. LENS enables the production of a wider variety of microstructures since solidification processes are controlled by controlling parameters such as laser power, laser scanning speeds, argon carrier gas flowrates and powder metal feed rates. Using LENS enables one to explore the mechanical behaviour of a greater variety of TiAlMn structures. This research explores the mechanical behaviour of rapidly solidified and heat-treated TiAlMn structures produced using LENS.

# Chapter 3: Experimental Procedure

This chapter covers the methodology which includes the synthesis of binary TiAl and TiMn alloys, and ternary TiAlMn alloys using LENS. Microstructural and mechanical properties of as-produced and heat-treated samples were evaluated to determine optimum process parameters and the resulting microstructures. This section is concluded with the numerical models used to characterise the microstructures and mechanical properties.

## 3.1 Powders

The three powder materials used in this study were titanium, aluminium, and manganese. Figure 3.1 shows the titanium and aluminium powders which were supplied by TLS Technik GmbH & Co Spezialpulver. These powders had a spherical morphology and particle size distribution of 45-90μm. Figure 3.2 shows manganese powder metal which was supplied by Manganese Mining Company (MMC). The manganese powder had an irregular morphology with a particle size distribution of 45-75μm. EDX was used to confirm that the powders used were 100% pure.

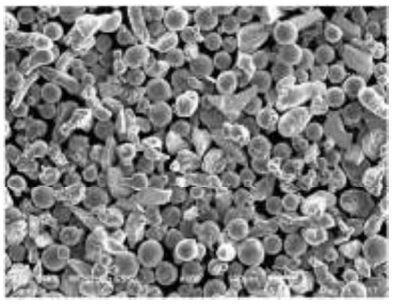

*Figure 3.1:SEM micrograph of Ti and Al powder metal from TLS* (Tlotleng and Pityana, n.d.)

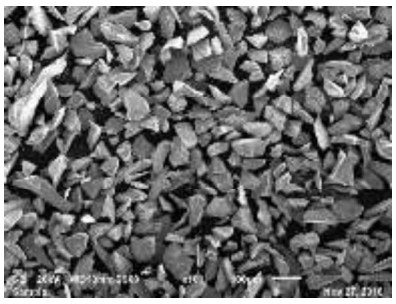

*Figure 3.2: SEM micrograph of Mn powder obtained from MMC.*

## 3.2. Synthesis

The samples were printed using LENS Optomec Additive Manufacturing systems Model 850-R machine with the setup displayed in Figure 3.3

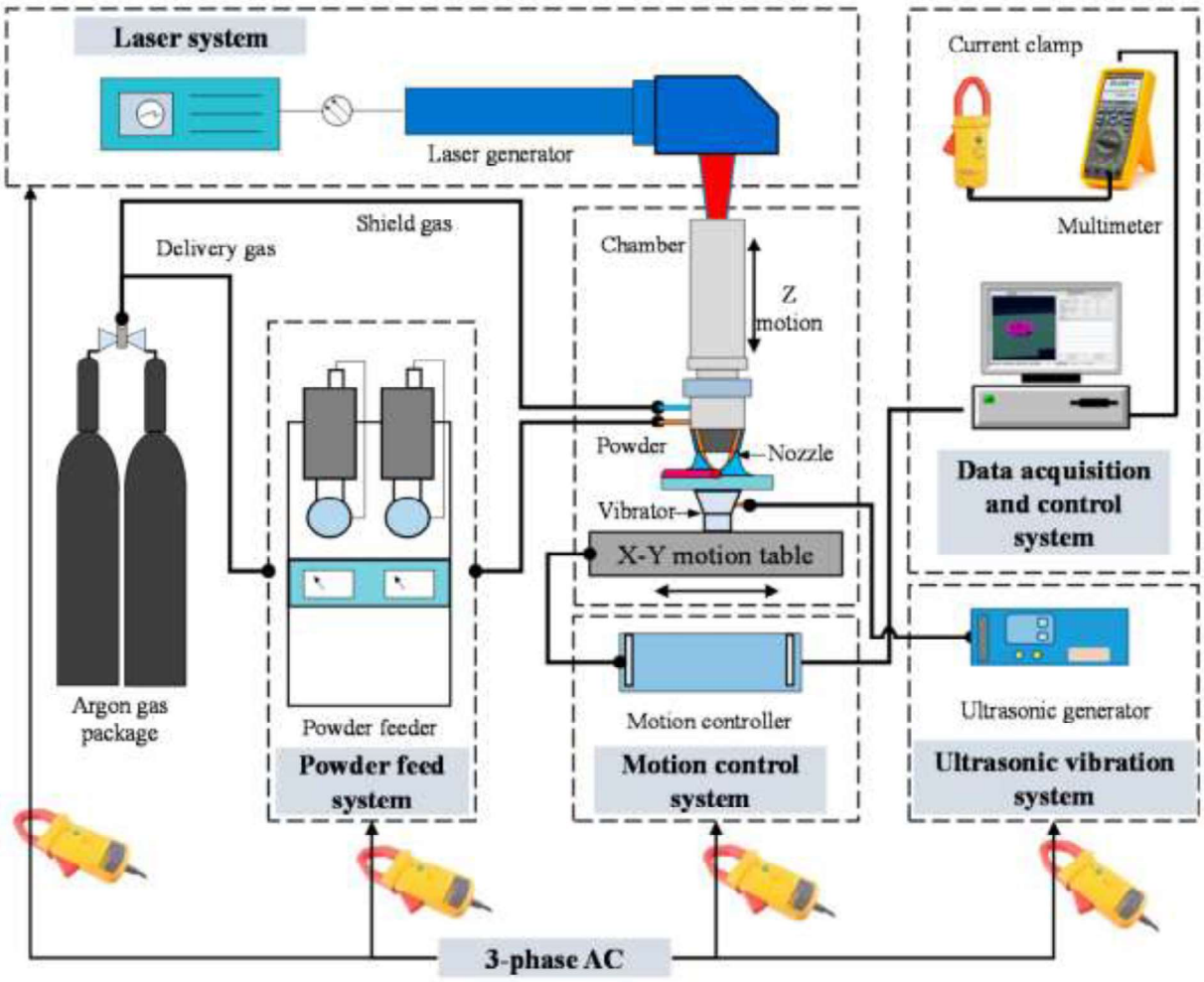


*Figure 3.3: Set up used for LENS to produce samples (Liu and Shuichang, 2016)*

TiMn, TiAl and ternary TiAlMn alloy cubes of 1x1x0.7cm$^3$ which were printed on Ti-6Al-4V substrates are shown in Figures 3.4 and 3.5.




*Figure 3.4: Ti-Mn samples printed on Ti-6Al-4V substrate.*




*Figure 3.5: TiAlMn sample printed on Ti-6Al-4V substrate*

Process parameters that were varied included the powder feed rate and the laser power, while the scan speed remained constant at 1.19807cm/s. All the process variables that were used to produce the cubes are presented in Table 3.1. Titanium feed rate was kept constant at 2.5 rpm and Ti carrier gas flowrates at 3.0L/min. The Mn feed rate was varied from 0.3 rpm to 1.3 rpm, whilst Al feed rate varied from 1.5 rpm to 2.0 rpm to produce TiMn and TiAlMn alloys. Argon carrier gas flowrate was varied from 3L/min to 6L/min to produce TiAl samples.

Powder metals stored in powder feed hoppers were carried with argon carrier gas to the deposition nozzle during laser deposition. Controlling the shield Ar gas flowrates enabled control over powder deposition mechanisms and minimised oxidation during deposition. Powder metal was then injected into laser beam focus at a rate referred to as powder feed rate. The nozzle was attached to three powder feed hoppers which contained Ti, Mn, and Al, and controlling the feed rates of the powder feed systems allowed for control over compositions of the printed cubes.

Interaction between YAG laser beam and metal powder allowed the powder to absorb heat energy from laser beam, melt and be deposited onto substrate in molten/liquid state forming a melt pool which underwent solidification onto the substrate. Laser power (W) adjustments were used to control the melt pool heating and cooling rates. Laser power was varied from 450W to 600W for the fabrication of TiMn alloys, and from 500W to 550W for TiAlMn alloys. Constant power of 350W was used to produce TiAl alloys. Process parameters used in this study are summarised in Table 3.1. It was determined through previous work that the combination of the range of parameters within which this study was carried out, was appropriate because it prevented power from fusing, possible explosions, equipment, and material damage. The

parameters studied were rendered safe for the working environment. It was also established that the parameters selected could allow one to study microstructural development of alloys studied.

*Table 3.1: Powder feed rates and Ar carrier gas flowrates used in the production of TiAl, TiMn and TiAlMn alloys*

| **Sample number** | **Ti** | | **Mn** | | **Al** | | |
|---|---|---|---|---|---|---|---|
| | **Feed rate (rpm)** | **Ar Carrier gas flowrates(L/min)** | **Feed rates (rpm)** | **Ar carrier gas flowrates (L/min)** | **Feed rates (rpm)** | **Ar carrier gas flowrates (L/min)** | **Laser Power (W)** |
| Ti-Mn-1 | 2,5 | 3 | 0,3 | 3 | - | - | 500 |
| Ti-Mn-2 | 2,5 | 3 | 0,5 | 3 | - | - | 500 |
| Ti-Mn-3 | 2,5 | 3 | 0,7 | 3 | - | - | 500 |
| Ti-Mn-4 | 2,5 | 3 | 0,9 | 3 | - | - | 500 |
| Ti-Mn-5 | 2,5 | 3 | 1,1 | 3 | - | - | 500 |
| Ti-Mn-6 | 2,5 | 3 | 1,3 | 3 | - | - | 500 |
| Ti-Mn-7 | 2,5 | 3 | 0,9 | 3 | - | - | 450 |
| Ti-Mn-8 | 2,5 | 3 | 1,1 | 3 | - | - | 450 |
| Ti-Mn-9 | 2,5 | 3 | 1,3 | 3 | - | - | 450 |
| Ti-Mn-10 | 2,5 | 3 | 0,3 | 3 | - | | 550 |
| Ti-Mn-11 | 2,5 | 3 | 0,5 | 3 | - | | 550 |
| Ti-Mn-12 | 2,5 | 3 | 0,7 | 3 | - | | 550 |
| Ti-Mn-13 | 2,5 | 3 | 0,3 | 3 | - | | 600 |
| Ti-Mn-14 | 2,5 | 3 | 0,5 | 3 | - | | 600 |
| Ti-Mn-15 | 2,5 | 3 | 0,7 | 3 | - | | 600 |
| Ti-Mn-16 | 2,5 | 3 | 0,9 | 3 | - | | 550 |
| Ti-Mn-17 | 2,5 | 3 | 1,1 | 3 | - | | 550 |
| Ti-Mn-18 | 2,5 | 3 | 1,3 | 3 | - | | 550 |
| Ti-Al-2.1 | 2,5 | 3 | - | - | 1,5 | 3 | 350 |
| Ti-Al-2.2 | 2,5 | 3 | - | - | 1,5 | 4 | 350 |
| Ti-Al-2.3 | 2,5 | 3 | - | - | 1,5 | 5 | 350 |
| Ti-Al-2.4 | 2,5 | 3 | - | - | 1,5 | 6 | 350 |
| Ti-Al-3.1 | 2,5 | 3 | - | - | 2 | 3 | 350 |
| Ti-Al-3.2 | 2,5 | 3 | - | - | 2 | 4 | 350 |
| Ti-Al-3.3 | 2,5 | 3 | - | - | 2 | 5 | 350 |
| Ti-Al-3.4 | 2,5 | 3 | - | - | 2 | 6 | 350 |
| Ti-Al-Mn-1 | 2,5 | 3 | 0,3 | 1,2 | 1 | 6 | 500 |
| Ti-Al-Mn-2 | 2,5 | 3 | 0,3 | 1,2 | 1,5 | 6 | 550 |
| Ti-Al-Mn-3 | 2,5 | 3 | 0,3 | 1,2 | 2 | 6 | 550 |

### 3.3 Heat Treatment

As-produced samples were sectioned in halves using the Brilliant 200 Cut off Machine. The samples were encapsulated in silica glass tubes purged with argon gas and sealed to prevent oxidation of samples during heat-treatment. Heat-treatment was conducted in a Nabertherm muffle furnace. Heat-treatment was initially attempted at 1300°C but due the undesirable liquifying of TiMn alloys containing high concentrations of Mn (above 20at%Mn), the heat-treatment temperatures were reduced to 950°C. Samples were heated at a heating rate of 3.333°C/s (set at 200°C per hour), and held at a temperature of 950°C for a period of 3 hours, and then furnace cooled overnight to room temperature.

As-produced and heat-treated samples were subjected to various characterization methods to study the microstructure and mechanical properties of the alloys.

### 3.4. Characterization of As-produced and Heat-treated TiAl, TiMn and TiAlMn alloys

#### 3.4.1 Sample preparation for metallographic examination

Samples were mounted into black Phenolic Resin using OPAL 410 mounting press. Grinding was carried out using Struers SiC paper of grit sizes #320, #1200 and #4000. The samples were then polished using the OPS suspension (0.05µm) on a MD-Chem polishing cloth. Polished samples were etched with Kroll's reagent (10 Vol. % HCl; 90 Vol% $H_2O$).

##### 3.4.1.1 Optical microscopy

Optical micrographs of etched samples were taken using Olympus optical microscope at X5, X10, X20 and X50 magnification, to observe general microstructural features such as grain types and boundaries. Lengths of post processing thermal cracks were measured using the optical microscope.

##### 3.4.1.2 Scanning Electron Microscope (SEM)-with Energy Dispersive Spectroscopy (EDX/EDS)

Scanning electron microscope uses a combination of electrons and electromagnets to produce an image with controllable high magnification. An electron gun situated on top of the microscope produces electrons which follow in a vertical path through the microscope within a vacuum, this is referred to as an incident beam. The beam travels through electromagnetic fields and lenses, which focus the beam toward the sample. Once the beam hits the sample, electrons and X-rays are ejected from the sample. X-rays, backscattered electrons, and

secondary electrons are collected by detectors and converted to a signal which is sent to a display screen where the images can be saved (Koçak and Karasu, 2018). Figure 3.6 displays how SEM functions.

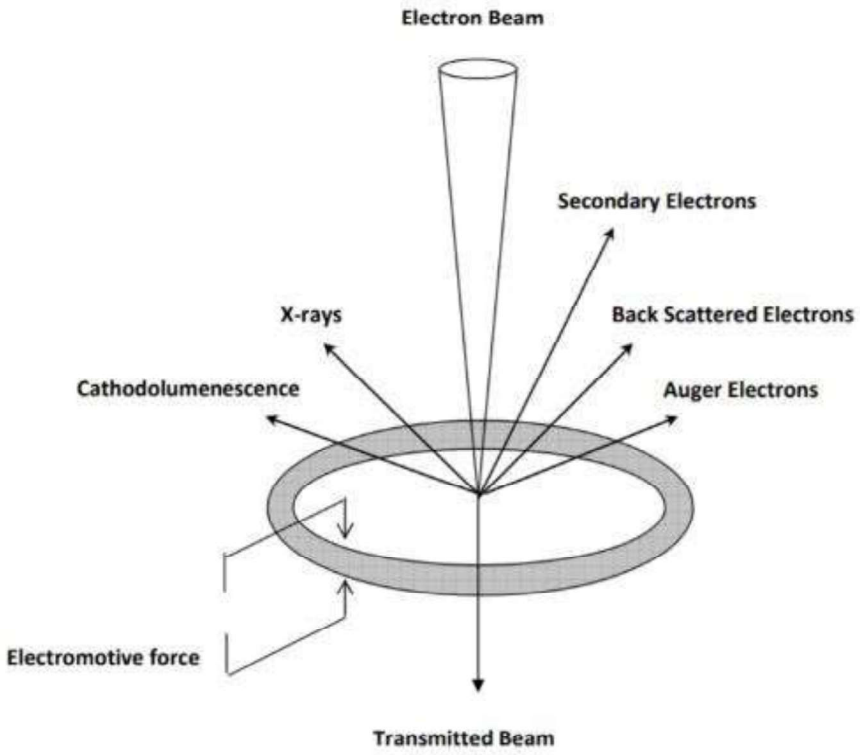


*Figure 3.6: Image displaying how SEM functions (Koçak and Karasu, 2018)*

SEM micrographs of unetched builds were taken using ZEISS Sigma 300VP Scanning Electron Microscope with Backscatter Diffraction (BSD) mode and electron high tension (EHT) was set at 20 kV. A magnification of X5000 was used to examine and study grain boundaries and precipitates, while the magnification of X700 was used to examine the general distribution and proportion of the phases. SEM micrographs were taken at three different sections of the samples (i.e. bottom, middle and top). EDS analyses was conducted using OXFORD INCA Software to determine compositions of various microstructural features.

### 3.4.1.3 Electron Backscatter Diffraction (EBSD)

EBSD is a SEM based method which provides crystallographic information about the specimen analysed such as phases, grain sizes and crystal orientations. EBSD is performed by tilting the sample so that the beam impacts at a shallow angle (~20° above the surface) and measuring the

Kikuchi pattern that arises from the diffraction of incoherently scattered electrons. Figure 3.7 illustrates the mechanism behind how EBSD functions (Gintalas and Rivera-Diaz-del-Castillo, 2022).

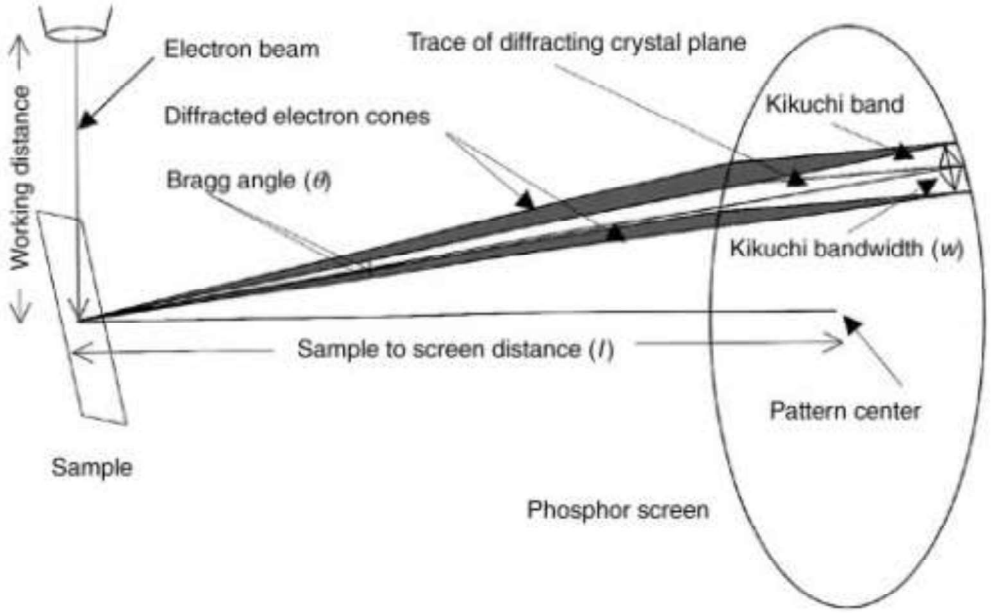


*Figure 3.7: Sketch displaying how EBSD functions (Gintalas and Rivera-Diaz-del-Castillo, 2022).*

Figure 3.8 displays the equipment setup used for this research (Carneiro and Simões, 2020). As one can observe, the scattered electrons are detected by an EBSD detector and information about the crystallography can be saved on the computer attached.

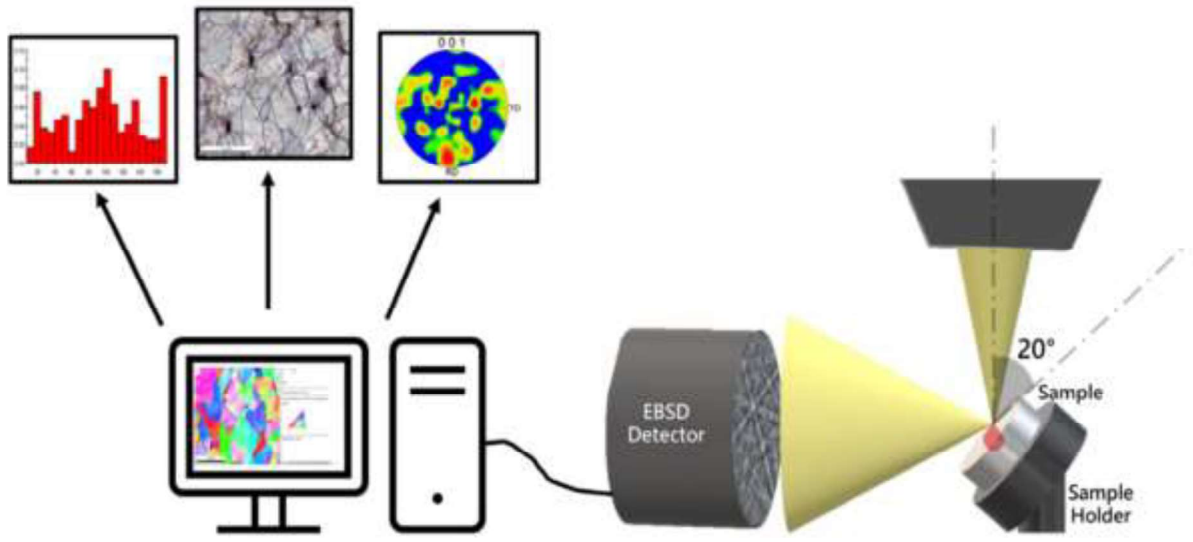


*Figure 3.8: Equipment setup for EBSD*

Electron Backscatter Diffraction (EBSD) analysis was conducted at National Metrology Institute of South Africa (NMISA). EBSD patterns were acquired using Zeiss Cross-Beam 540 Scanning Electron Microscope at an electron acceleration voltage of 25 kV and a probe current of 10 nA. The EBSD data analysis was performed on an Oxford EBSD detector with Aztec analysis software and EBSD reference patterns database.

### 3.4.1.4 X-ray Diffraction (XRD) - Phase Identification and Lattice Parameters

X-ray diffraction peaks are produced by constructive interference of a monochromatic beam of X-rays scattered at specific angles from each set of lattice planes in a sample. The peak intensities are determined by the distribution of atoms within the lattice. The reflection of X-ray beams on different lattice planes at various angles can provide a variety of information about the crystallography of sample (Bunaciu *et al.,* 2015). Figure 3.9 displays how XRD functions, where the incident X-ray is generated by the X-ray source and the reflections which produce peaks are detected by the detector.

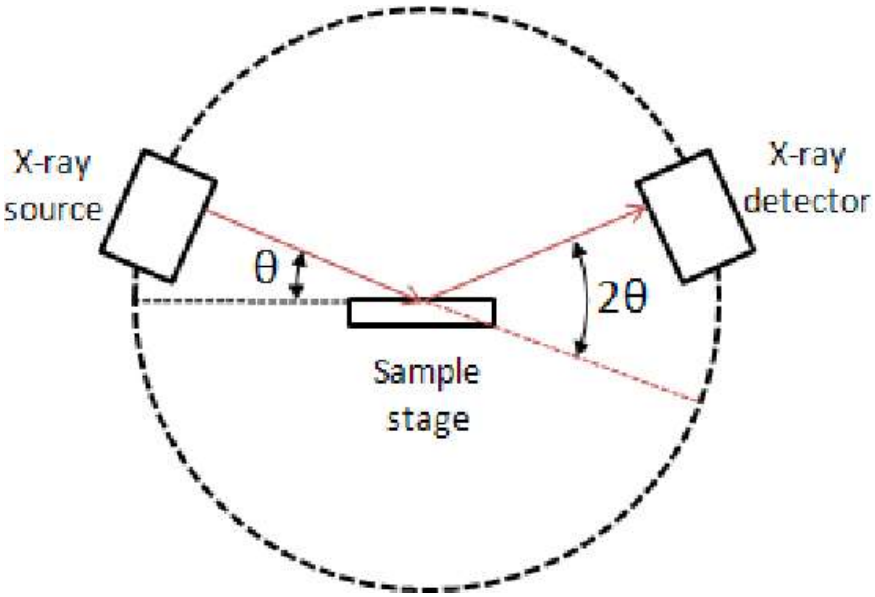


*Figure 3.9: Illustration of depicting how XRD functions (Mulder, 2016)*

X-Ray diffraction was performed on produced samples to identify the phases. The XRD patterns were obtained through X-Ray diffraction analysis using XRD BRUKER D2 PHASER with a Copper anode ($K_{\alpha 1}$= λ=1.54Å) as the source. The 2-theta range was from 5°- 90° at 0.026° step size and scan rate of 8.5°/min. The radiation source had a current of 10 mA and voltage of 30kV. Phases were identified using DIFFRAC.EVA V.4.2.2 XRD software. Lattice

parameters and dislocation densities were calculated using Bragg's Diffraction Model and Rietveld Refinements using GSAS2 software (Toby *et al.,* 2013).

### 3.5 Micro-hardness Testing

Hardness testing was carried out using the Future-Tech Micro hardness Tester Model FM-700, with a load of 500 gf and dwell time of 15 seconds. Three hardness profile patterns were carried out on each sample and the average hardness values were calculated. Approximately 90 indentations were made per sample as shown in Appendix A

### 3.6 Nano-indentation Testing

Nano indentation tests were carried out using Anton Paar TriTec SA nano indenter with a Berkovich type indenter. Tests were carried out at a loading and unloading rate of 200 mN/min. Maximum load was set at 100 mN and stiffness threshold was set at 500μN/μm.

### 3.7 Density Measurements

Density measurements were carried out using the Anton Paar Gas Pycnometer, Model Ultrapyc3000. Helium gas at a pressure of 0.69000 bar was used as a measuring medium. Measurements were allowed to run three times and averages were obtained. The masses of the samples were measured using the BOECO Germany-Boeckel + Co (GmbH+Co) measuring scale model BAS31plus.

### 3.8 Thermogravimetric analysis (TGA)

Thermogravimetric analysis measures weight loss as a function of temperature and time. The TGA instrument is comprised of a computer and a multi sample furnace which can hold multiple samples to be analysed simultaneously. An analysis method is selected by selecting gas, time and temperature over which the analysis is made. Empty crucibles are then loaded into the furnace carousel. The carousel, furnace, and balance operation are controlled by the analysis method selected. The starting sample weight is measured and stored automatically on the computer attached, using an easy-to-follow menu-driven software program. Once all the crucibles have been loaded, analysis begins. The weight loss of each sample is monitored, and the furnace temperature is controlled according to the selected analysis method. The percent weight loss for each sample is reported at the end of each analysis step (Varol *et al.*, 2010).

Figure 3.10 displays the TGA setup used for this research, which was obtained from the LECO TGA user's guide.

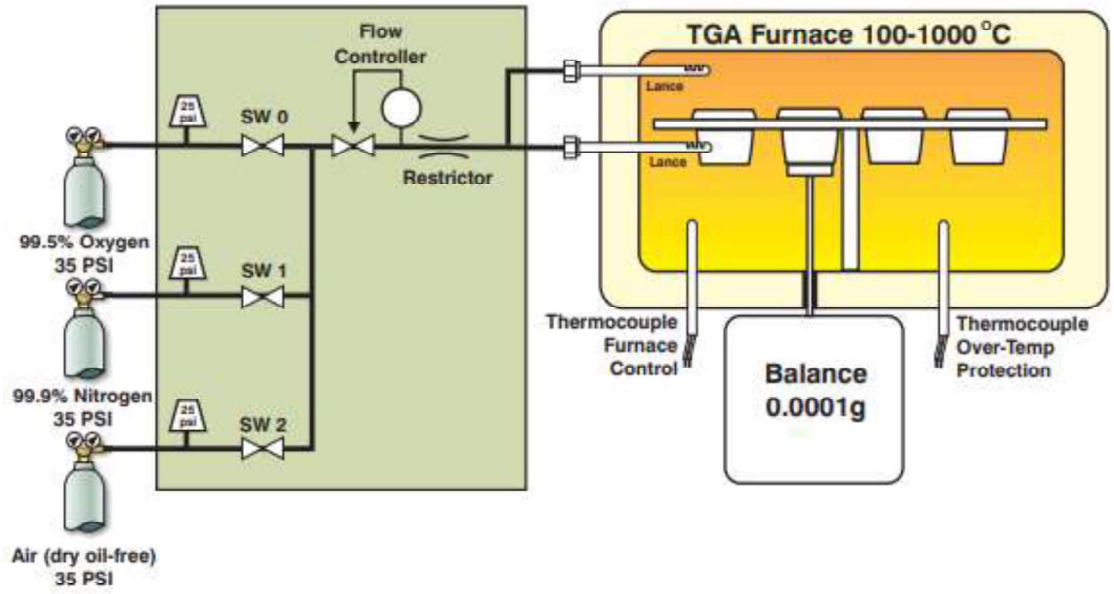


*Figure 3.10: TGA setup used for analysis: http://www.usbioecuador.com/descargas/TGA701-c.pdf*

Oxidation behaviour was analysed by performing thermogravimetric analysis using a Thermogravimetric Analyzer Model TGA701 (manufactured by LECO Corp. USA). Selected samples were heated to 900°C in an air environment at a heating rate of 3°C/s with holding times of 340 minutes, followed by cooling at a rate of 7°C/s. Thermo balance micro sensitivity was kept at 1µm. The phases resulting from the TGA were obtained using XRD and microstructures were studied using SEM and EDS.

### 3. 9 Compression test using Gleeble simulations

Printed sample with dimensions 20×20×40 mm was sectioned into 8 test pieces that were 8×8×12mm$^3$ in dimension for testing. Figures 3.11-3.14 shows the different views and dimensions of the printed as-produced sample. Gleeble compression tests were performed using the Gleeble 3500 machine where samples were heated to 1000°C at a heating rate of 5°C/s and held at that temperature for 3 minutes before compression to reduction strains of 10.78%, 10.89%, 21.5%, 33% and 46.5% at a strain rate of 0.01s$^{-1}$. These tests were conducted in an Ar gas environment to prevent oxidation. The samples were then allowed to cool to room temperature before being removed from the gleeble tester.



*Figure 3.11: Arial view of reprinted TiAlMn-1*



*Figure 3.12: Width measurement of reprinted TiAlMn-1 (20mm).*



*Figure 3.13: Display of height of reprinted TiAlMn-1 (20mm)*

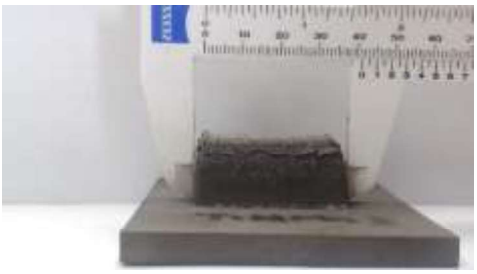

*Figure 3.14: Length measurement of reprinted TiAlMn-1 (40mm)*

## 3.1 Numerical Models used for characterisation

3.1.1 *XRD Analysis*

Bragg's Equation (Kasap, 2006) was used to determine interplanar spacings and lattice parameters as displayed in Equation 3.1

$$n\lambda_{Cu\,K\alpha} = 2 * d_{[hkl]} sin\theta_{(hkl)}^{BRAGG} \quad (3.1)$$

Where the detector position is depicted by 2θ, λ depicts the wavelength of $K_\alpha$ radiation (λ=1.54Å), the interplanar spacing is depicted by d and the Miller Indices are depicted by [h k l] as displayed in Equation 3.2

$$d_{(hkl)}^{cubic} = \frac{a}{\sqrt{h^2+k^2+l^2}} \quad (3.2)$$

Equation 3.3 was used to calculate lattice parameters for hexagonal structures (Suryanarayana, and Norton, 1998)

$$a = \frac{\lambda_{Cu\,K\alpha} * \sqrt{h^2+hk+k^2}}{\sqrt{3} * sin\theta} \quad (3.3)$$

Dislocation densities were calculated by performing Rietfield refinement with respect Lorentzian (HL) and Gaussian (HG) functions (Khalili *et al.*, 2016) to produce plots where $\frac{\Delta Q}{Q}$

was plotted against Q. The broadening of peak widths was calculated using the Equations 3.4 and 3.5:

$$\frac{\Delta Q}{Q} = \frac{\Delta d}{d} \quad (3.4)$$

$$\frac{\Delta d}{d} * Q = \Delta d \quad (3.5)$$

Where ΔQ and Δd are equivalent to the full width at half maximum (FWHM), also known as ΔK (Woo *et al.*, 2010). Δd can then be substituted into the Scherrer formula (Khojier *et al.,* 2013) in Equation 3.6 to calculate crystal size.

$$D = \frac{K\lambda}{\Delta d * cos(\theta)} \quad (3.6)$$

Where D is the crystal size (nm), K is the shape factor and λ the wavelength (nm) of X ray. The crystal size was used to estimate dislocation density using Equation 3.7

$$\delta = \frac{1}{D^2} \quad (3.7)$$

Where δ is the dislocation density ($nm^{-2}$)

*3.1.2 Mechanical Properties*

Vickers micro hardness is equivalent to the load applied by indenter divided by the product of two diagonals, which is displayed in Equation 3.8:

$$HV = \frac{2Fsin(\frac{136^\circ}{2})}{d_1 d_2} \quad (3.8)$$

Where HV depicts the hardness value, F depicts the load applied by indenter (kgf) and d depicts the length of diagonals (μm) (Chandler, 1999).

*Ductility according to microhardness*

The relationship between microhardness and ductility/stress is displayed in Equation 3.9 (Cahoon *et al.,* 1971; Krishna *et al.*, 2013)

$$\sigma = \frac{H_v}{3}(0.1)^{n-2} \quad (3.9)$$

Where σ depicts ductility, n depicts strain hardening coefficients; n=0.04 to 0.085 for Ti alloys (Rajendran *et al.,* 2014). $H_V$ depicts the Vicker's microhardness values.

*3.1.3 Fracture stress according to crack lengths*

Furthermore, since thermal gradients induce thermal residual stresses which are directly proportional to strain and lead to post processing thermal cracks (Liu and DuPont, 2002; Sharman *et al.,* 2018; Weisheit *et al.,* 2000). Fracture stress was calculated using crack lengths and fracture toughness as displayed in Equation 3.10:

$$\sigma_f = \frac{K_{IC}}{\pi a} \quad (3.10)$$

Where a depicts crack length; $K_{IC}$ depicts fracture toughness (Voice *et al.,* 2005)

The following values were used to calculate fracture stress $\sigma_f$.

$K_{IC\ (Ti\text{-}Mn)}$ $4.500\sqrt{m}$ MPa(Varin *et al.,* 2001)

$K_{IC\ (Ti\text{-}Al\text{-}Mn)}$= 4.00MPa$\sqrt{m}$ (Varin *et al.,* 2001)

$K_{IC(Ti\text{-}Al)}$= 1.00MPa$\sqrt{m}$ (Appel *et al.,* 2011a)

*3.1.4 Mechanical Properties from Nano indentation*

Indentation Young's Modulus $E_{IT}$ (Pa) was obtained from nanoindentation measurements using Oliver and Pharr Method and was used to calculate contact radius $a_{Hertz}$ using Equation 3.11 (Ruiz-Moreno *et al.,* 2020). Berkovich nanoindentation data was converted to spherical stress and strain values using Young's Modulus alongside Hertz Theory similar to work reported by (Basu *et al.,* 2006). Assumption: $E_{(IT,berkovich)} = E_{(IT,sperical)}$

$$a_{Hertz} = \frac{S}{3E_{IT}} \quad (3.11)$$

Where S depicts stiffness (N/m).

$a_{Hertz}$ was used to calculate representative indentation strain $\varepsilon_{IT}$ using Equation 3.12 (Pathak and Kalidindi, 2015)

$$\varepsilon_{IT} = \frac{4h_t}{3\pi a_{Hertz}} \quad (3.12)$$

Where $h_t$ is the total penetration depth.

$\varepsilon_{IT}$ was used to calculate the yield strength $\sigma_{IT}$ with Equation 3.13 (Heinrich *et al*., 2009; Pathak and Kalidindi, 2015; Ruiz-Moreno *et al*., 2020) and Equation 3.14 depicts the yield strength with 0.2% offset.

$$\sigma_{IT} = E_{IT}(\varepsilon_{IT} - 0.002) \quad (3.13)$$

$$\sigma_{IT} = E_{IT}(\varepsilon_{IT}) \quad (3.14)$$

### *3.1.5 Laser Energy Per Unit Length*

Varying laser power varied the laser energy per unit length (LEPUL) during deposition. LEPUL is calculated as displayed in Equation 3.15.

$$LEPUL = \frac{Laser\ Power\ (\frac{J}{s})}{Scanning\ Speed\ (\frac{cm}{s})} \quad (3.15)$$

# Chapter 4: Results

This section is divided into three sections which demonstrate the findings from binary TiAl, and TiMn, and ternary TiAlMn alloys. Each section is comprised of SEM micrographs, EDS analysis, EBSD analysis, XRD analysis, microhardness data, nanoindentation outcomes and thermogravimetric analysis. Microstructural features were observed in SEM micrographs, EBSD and XRD, and correlated to mechanical behaviour through observations of post processing thermal cracks using optical microscope (OM), microhardness test results and nano indentation. Thermogravimetric analysis and Gleeble tests were conducted to determine the oxidation behaviour and high temperature mechanical behaviour. This section then ends with the numerical modelling derived from the findings.

## 4.1 Binary TiAl

### 4.1.1 Microstructures of as-produced TiAl binary alloys

TiAl alloys produced using low Al feed rates (1.0 rpm) and Ar carrier gas flow rates (3.0 L/min) produced microstructures which comprised of equiaxed lamellar β dendrites with low Al levels (42.71at%Al57.29at%Ti) as shown in Figure 4.1. These results are similar to findings by McCullough *et al.* (1989) who investigated the solidification paths of TiAl alloys with Al composition ranging between 40 and 55 at.%. Increasing the Ar carrier gas flowrate to 4L/min and 5L/min formed microstructure that was comprised of nearly lamellar α+γ phases shown in Figures 4.2 and 4.3. High flowrates led to the formation of microstructure that was a mixture of nearly lamellar and fully lamellar. A fully lamellar ($\alpha_2$+γ) microstructure depicted in Figure 4.4 was produced when the gas flow rate was set at 6L/min. The γ lamellae volume fraction increased with increasing Al compositions.

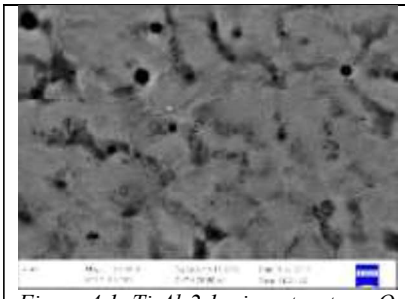

*Figure 4.1: Ti-Al-2.1 microstructure. Overall composition: 42.71at%Al57.29at%Ti*

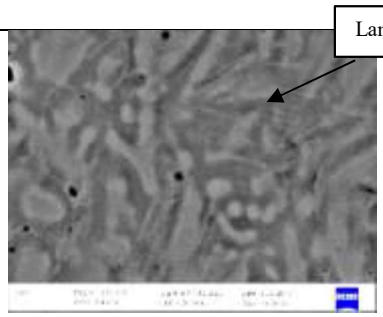


*Figure 4.2: Ti-Al-2.2 microstructure. Overall Composition: 55.57at%Al44.43at%Ti*

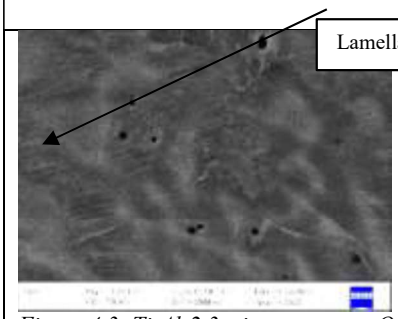


*Figure 4.3: Ti-Al-2.3 microstructure. Overall composition: (56.02at%Al43.98at%Ti)*

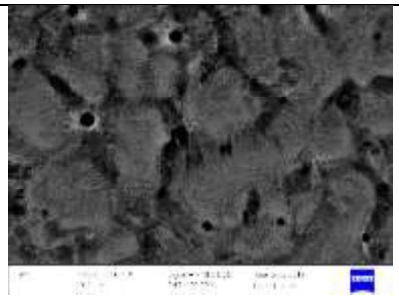

*Figure 4.4: Ti-Al-2.4 microstructure. Overall Composition: 57.42at%Al42.58at%Ti*

*Figures 4.1 to 4.4: SEM micrographs taken with BSD mode, EHT set at 20.0kV and the magnification of x5000 (2μm) illustrating as produced TiAl alloys. Compositions attained using EDS*

An increased feed rate of 2 rpm coupled with a low Ar carrier gas flowrates of 3 L/min and 4.0L/min led to the formation of microstructures depicted in Figure 4.5 and 4.6. The microstructure comprised of α columnar dendrites. These findings were similar to observations made by McCullough *et al.* (1989). A further increase in flowrates to 5.0 L/min produced a basket weave microstructure depicted in Figure 4.7. The basket weave microstructure formation was due to the precipitation of γ on α (Küstner *et al*., 2003). High gas flowrate of 6.0 L/min led to a coarse grained fully lamellar $\alpha_2+\gamma$ equiaxed microstructure depicted in Figure 4.8. These findings were similar to findings by (Küstner *et al.,* 2003) who investigated the development of γ-TiAl microstructure.

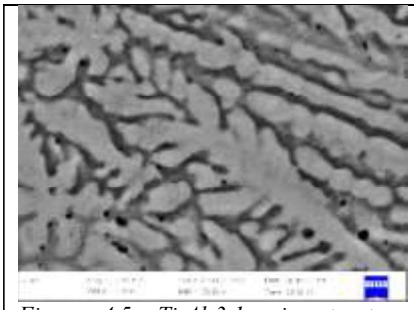

*Figure 4.5: Ti-Al-3.1 microstructure. Overall composition: 48.17at%Al51.83at%Ti*

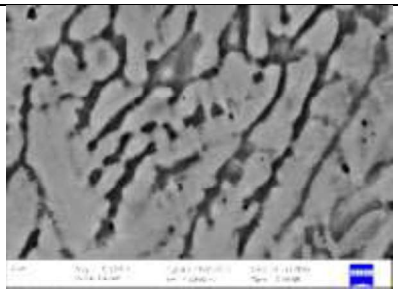

*Figure 4.6: Ti-Al-3.2 microstructure. Overall composition: 61.9at%Al38.10at%Ti*

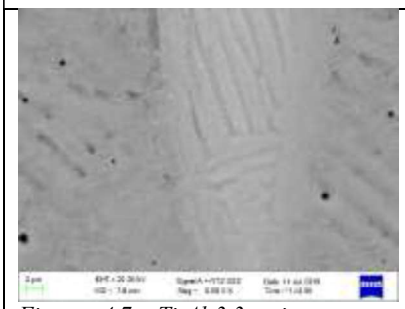

*Figure 4.7: Ti-Al-3.3 microstructure. Overall composition: 63.22at%Al36.78at%Ti*

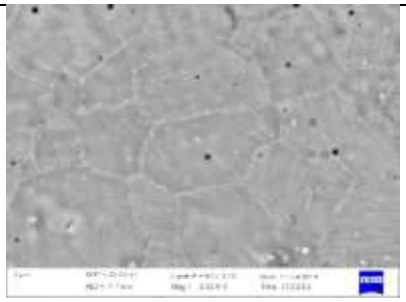

*Figure 4.8: Ti-Al-3.4 microstructure.. Overall Composition: 53.38at%Al46.62at%Ti.*

*Figures 4.5 to 4.8: SEM micrographs taken with BSD mode, EHT set at 20.0kV and the magnification of x5000 (2µm) illustrating as produced TiAl alloys. Compositions attained using EDS*

Microstructural features of as-produced TiAl alloys and their compositions are listed in Table 4.1. It can be observed that the formation of α dendrites occurred when Al compositions was greater than 45at.%. However, at low Al feed rates the alloys followed the β solidification route (Appel *et al.*, 2011a). From Table 4.1, it can be observed that inter-dendritic regions and grain boundaries had higher composition of Al than other areas within the microstructure. It was also observed that Al in the overall composition increased significantly as Al powder feed rates were increased.

*Table 4.1: Microstructural features and compositions of as produced TiAl alloys.*

| Microstructure | Description | BSD contrast | at% Al | at% Ti | Phases |
|---|---|---|---|---|---|
| Equiaxed Dendrites | Dendritic | Light grey | 41.41 - 48.29 | 51.72-58.59 | β |
| | Inter-dendritic | Grey | 47.25 - 52.14 | 47.86-52.75 | α |
| Nearly Lamellar | Within grain | Light Grey | 30.54 - 47.48 | 52.52-69.46 | α |
| | Grain boundary | Dark grey | 32.78 - 47.60 | 52.40-67.36 | γ |
| Equiaxed fully lamellar | Within grain | Light Grey | 39.92 – 42.06 | 57.94 - 60.08 | $\alpha_2$ |
| | Grain boundary | Dark Grey | 41.95 – 43.18 | 56.82 – 58.05 | γ |
| Columnar Dendrites | Dendritic | Light grey | 46.93 – 53.64 | 46.36 – 53.07 | α |
| | Inter-dendritic | Dark grey | 44.63 – 56.56 | 43.44 – 55.37 | α (Al rich) |
| Basket Weave structure | - | Grey | 47.28 – 54.60 | 45.4 – 52.72 | α+γ |
| Equiaxed fully lamellar | Within grain | Grey | 46.66 – 48.39 | 51.61 – 53.34 | $\alpha_2$+γ |
| | Grain boundary | Light Grey | 47.36 – 53.38 | 46.62 – 52.64 | $\alpha_2$+γ |

### 4.1.2 Microstructures of heat-treated TiAl binary alloys

The microstructures of heat-treated TiAl alloys differed significantly from the as-produced structures. The microstructures of low Al alloys (produced at 1.5 rpm) comprised of $\alpha_2$+γ lamellar equiaxed grain microstructures illustrated in SEM micrographs displayed in Figures 4.9 to 4.12. The closer the as-produced structure was to the lamellar microstructure, the coarser the appearance of the equiaxed grains in the heat-treated state.

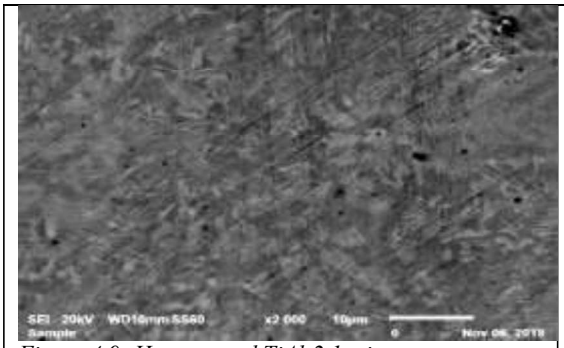

*Figure 4.9: Heat-treated TiAl-2.1 microstructure*

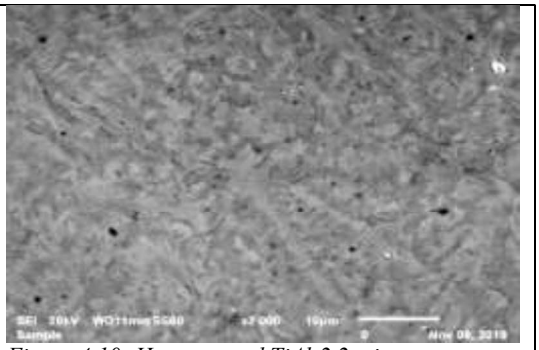

*Figure 4.10: Heat- treated TiAl-2.2 microstructure*

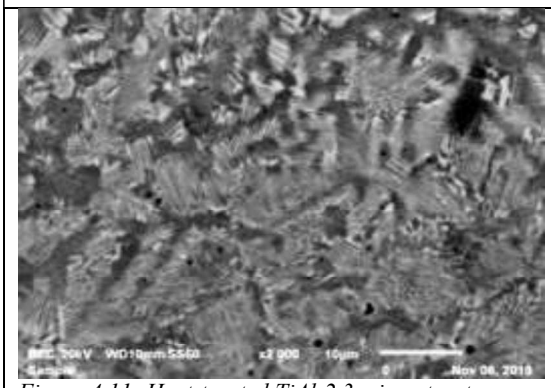

*Figure 4.11: Heat-treated TiAl-2.3 microstructure*

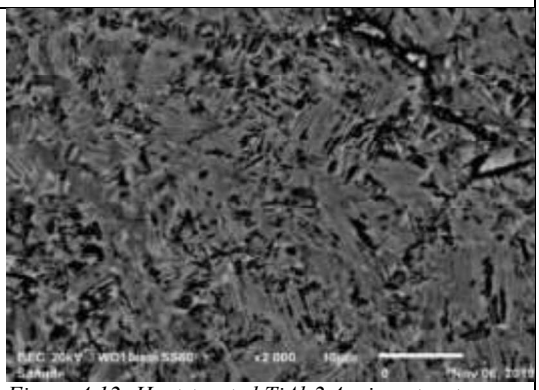

*Figure 4.12: Heat-treated TiAl-2.4 microstructure*

*Figures 4.9 to 4.12: SEM micrographs taken with BSD mode, EHT set at 20.0kV and the magnification of x2000 (10μm) illustrating as produced TiAl alloys.*

Higher Al heat-treated alloys (produced at 1.5 rpm) comprised of a uniform γ duplex microstructure (Appel *et al.,* 2011a; Kim and Dimiduk, 1991) illustrated by SEM micrographs in Figures 4.13 to 4.16. Duplex microstructures were friable. Overall compositions of the heat-treated samples were like as produced samples.

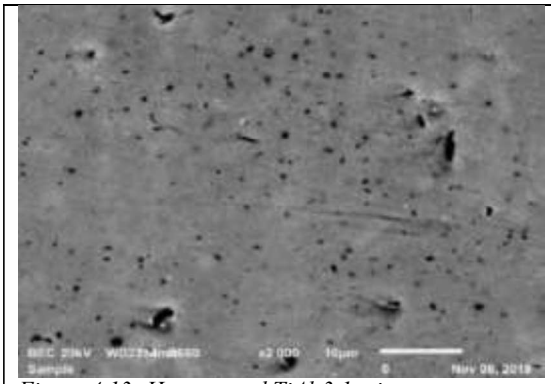

*Figure 4.13: Heat treated TiAl-3.1 microstructure.*

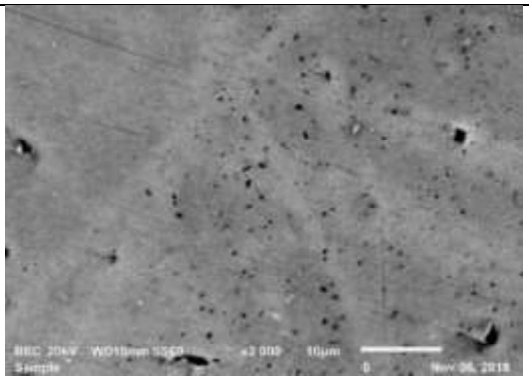

*Figure 4.14: Heat treated TiAl-3.2 also comprising of uniform γ duplex microstructure*

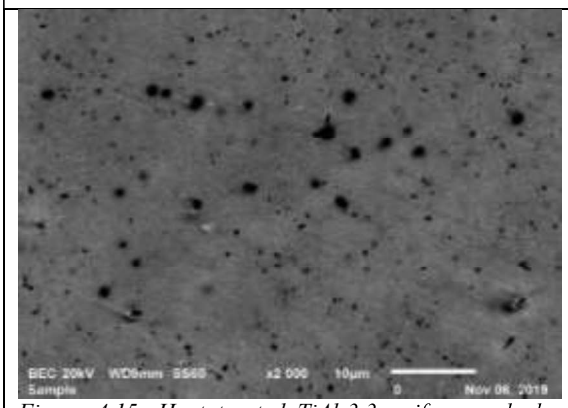

*Figure 4.15: Heat treated TiAl-3.3 uniform γ duplex microstructure is porous.*

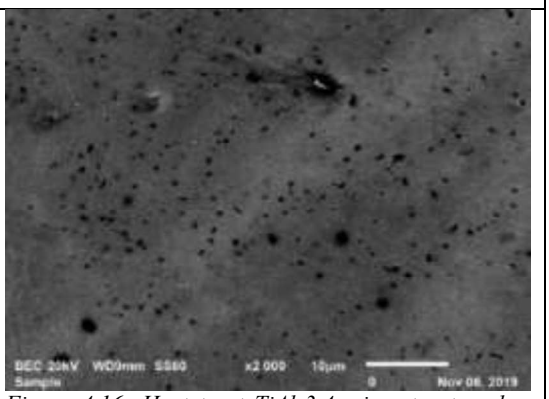

*Figure 4.16: Heat treat TiAl-3.4 microstructure has high number of large pores.*

*Figures 4.13 to 4.16: SEM micrographs taken with BSD mode, EHT set at 20.0kV and the magnification of x2000 (10μm) illustrating as produced Ti-Al alloys.*

### 4.1.3 X-ray Diffraction (XRD) of TiAl alloy

TiAl 2.3

According to EVA software and Rietveld Refinements, γ-$Ti_{0.4}Al_{0.6}$ with a tetragonal orientation was produced during deposition, shown in Figure 4.17. Heat-treatment produced tetragonal γ-$Ti_{0.15}Al_{0.85}$ - Figure 4.18. α-$Ti_{0.7}Al_{0.3}$ with a hexagonal crystal orientation was also produced during laser deposition and hexagonal α-$Ti_3Al$ was produced during heat-treatment as displayed in Figures 4.17 and 4.18.

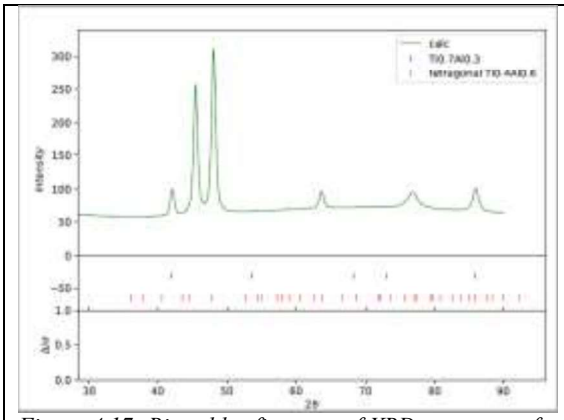

*Figure 4.17: Rietveld refinement of XRD outcomes of as produced TiAl 2.3 displaying phases.*

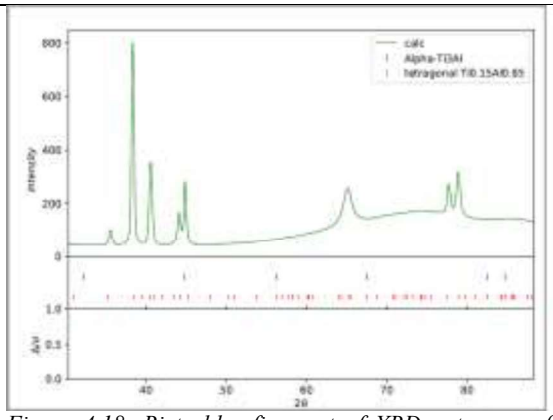

*Figure 4.18: Rietveld refinement of XRD outcomes of heat treated TiAl2.3.*

Tetragonal lattice parameters $a_\gamma$ and $c_\gamma$ of as-produced TiAl 2.3 were 5.65844Å and 4.27050Å respectively, as shown in Figure 4.19 and increased to 9.03931Å and 4.65872Å during heat-treatment (Figure 4.20). The tetragonal lattice volume increased from 136.73Å$^3$ to 380.66Å$^3$ due to heat treatment. The colour codes for atomic diagrams are displayed in Table 4.2.

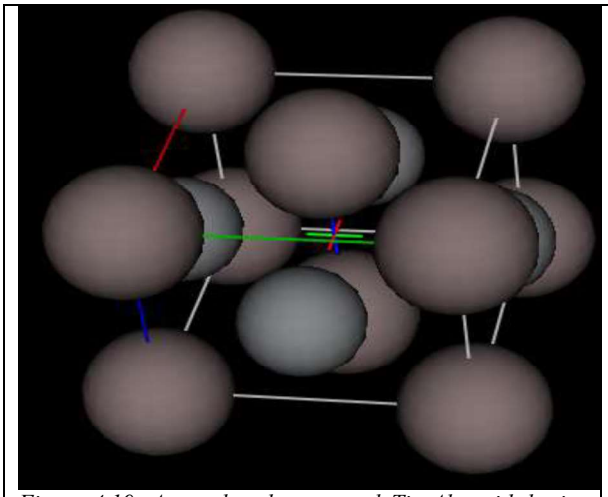

*Figure 4.19: As produced tetragonal $Ti_{0.4}Al_{0.6}$ with lattice parameters: a=b=5.65844Å; c=4.27050Å.*

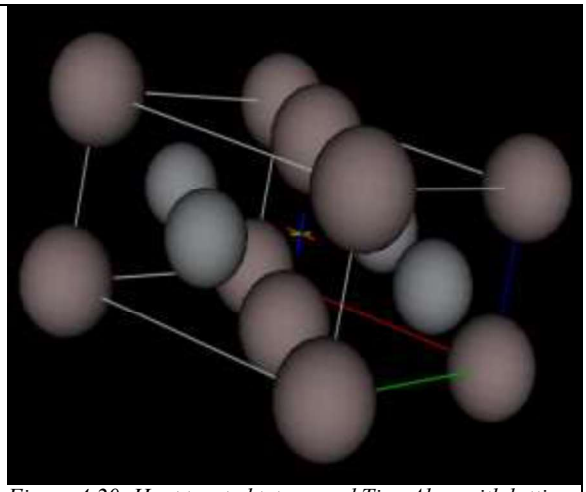

*Figure 4.20: Heat treated tetragonal $Ti_{0.15}Al_{0.85}$ with lattice parameters: a=b=9.03931Å ; c=4.65872Å*

*Table 4.2: Details regarding atoms illustrated in Figures.*

| Elements | Al | Mn | Ti |
|---|---|---|---|
| Isotope | Nat. Abund. | Nat. Abund. | Nat. Abund. |
| No. per cell | 1.7 | 2.8 | 17.5 |
| Atom weight | 26.982 | 54.938 | 47.900 |
| Bond radii | 1.60 | 1.54 | 1.66 |
| Angle radii | 1.43 | 1.30 | 1.46 |
| van der Waals radii | 2.05 | 1.70 | 1.70 |
| Default color | | | |

The hexagonal lattice parameter $a_\alpha$ was reduced from 2.48044Å to 2.33136Å and $c_\alpha$ increased from 1.70823Å to 2.78449Å due to heat treatment (Figures 4.21 and 4.22). Hexagonal lattice volume increased from 9.10Å$^3$ to 13.11Å$^3$ due to heat treatment.

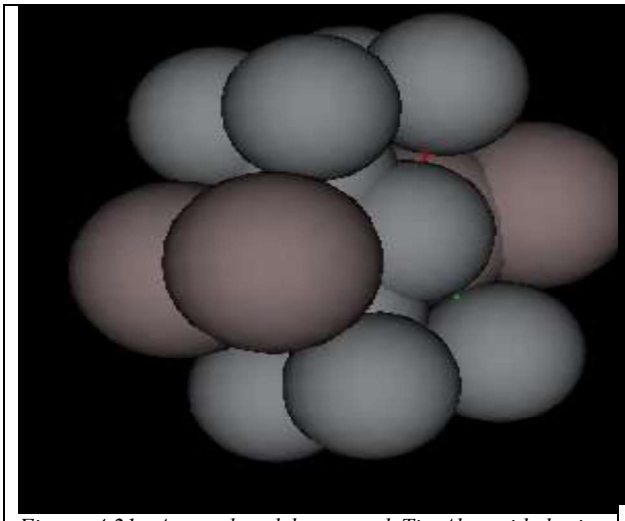

*Figure 4.21: As produced hexagonal $Ti_{0.7}Al_{0.3}$ with lattice parameters: a=2.48044Å ; c= 1.70823Å*

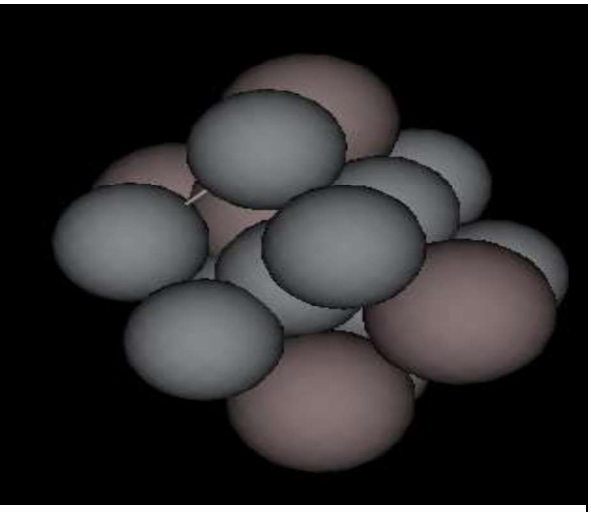

*Figure 4.22: Heat treated hexagonal $Ti_3Al$ with lattice parameters: a=2.33136Å ; c=2.78449Å*

TiAl 2.4:

γ-$Ti_{0.25}Al_{0.75}$ with a tetragonal orientation was produced during laser deposition (Figure 4.23) and tetragonal γ-TiAl was produced during heat-treatment (Figure 4.24). α-$Ti_{0.6}Al_{0.4}$ with a hexagonal crystal orientation was also produced during laser deposition (Figure 4.23) and hexagonal α-$Ti_{19}Al_6$ was produced during heat-treatment (4.24).

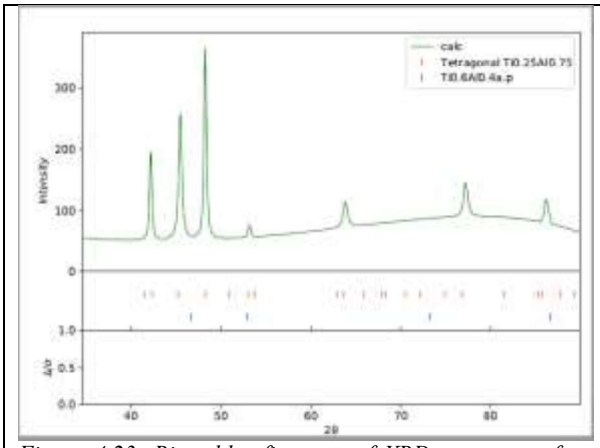


*Figure 4.23: Rietveld refinement of XRD outcomes of as produced TiAl 2.4*

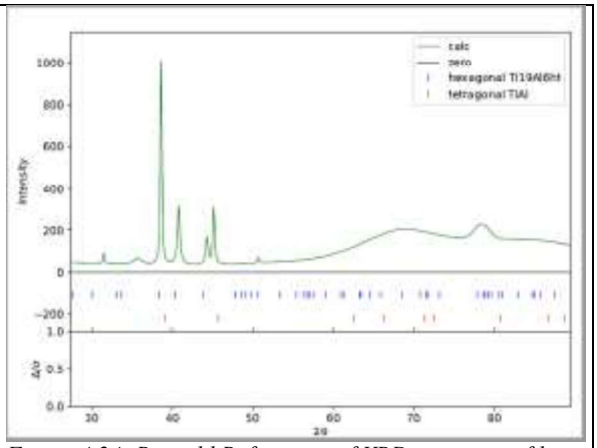


*Figure 4.24: Rietveld Refinement of XRD outcomes of heat treated TiAl 2.4.*

Tetragonal lattice parameters $a_\gamma$ and $c_\gamma$ were reduced from 5.65642Å and 4.25863Å (Figure 4.25) to 4.02903Å and 1.31601Å (Figure 4.26) due to heat treatment. The tetragonal lattice volume was reduced from 136.26Å$^3$ to 21.36Å$^3$ during heat treatment.

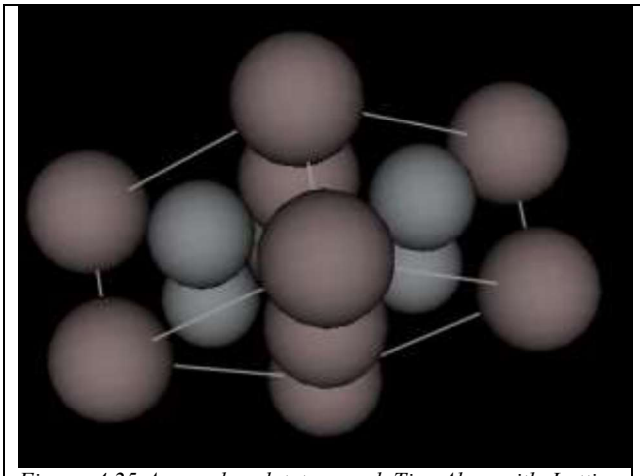

*Figure 4.25:As produced tetragonal $Ti_{0.25}Al_{0.75}$ with Lattice parameters: a=b=5.65642Å; c=4.25863Å*

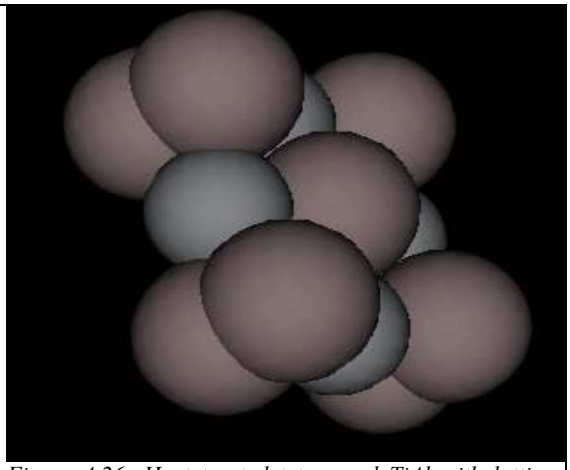

*Figure 4.26: Heat treated tetragonal TiAl with lattice parameters a=b=4.02903Å; c=1.31601Å.*

Hexagonal lattice parameters $a_\alpha$ and $c_\alpha$ increased from 2.47547Å and 1.99574Å (Figure 4.27) to 4.14000Å and 14.07095Å (Figure 4.28) during heat treatment. Hexagonal lattice volume increased from 10.56Å$^3$ to 208.47Å$^3$.

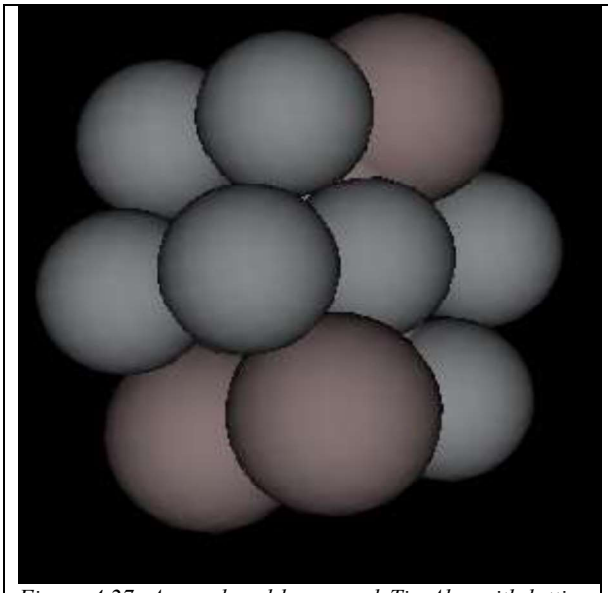

*Figure 4.27: As produced hexagonal $Ti_{0.6}Al_{0.4}$ with lattice parameters: a=b=2.47547Å; c=1.99574Å*

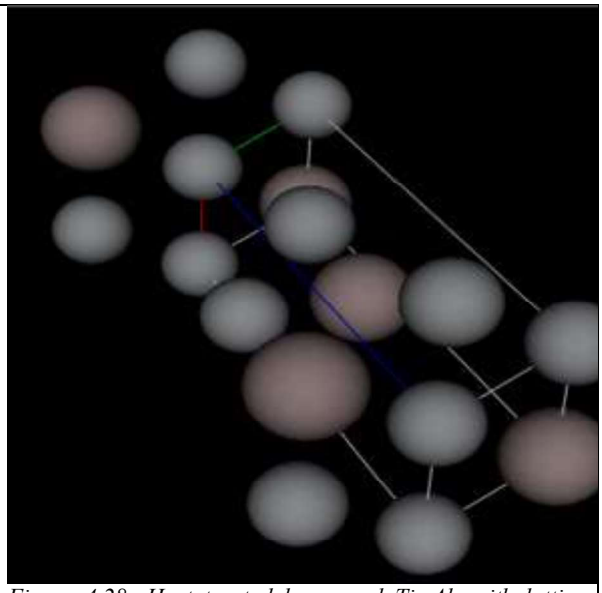

*Figure 4.28: Heat treated hexagonal $Ti_{19}Al_6$ with lattice parameters: a=b=4.14000Å; c=14.07095Å.*

Increasing Ar carrier gas flowrates led to a reduction in lattice parameters both in the as-produced and heat-treated states of tetragonal crystal lattices. The d-spacings along common crystal planes of as-produced TiAl 2.3 and TiAl 2.4 reduced as displayed in Table 4.3.

*Table 4.3: Effects of increasing Ar carrier gas flow rates on d-spacings of tetragonal crystal lattices*

| d- spacings – Tetragonal | As produced TiAl 2.3 | As produced TiAl 2.4 |
|---|---|---|
| $d_{(2\,2\,0)}$ | 2.00056Å | 1.99985Å |
| $d_{(1\,1\,2)}$ | 1.88379Å | 1.87956Å |
| $d_{(2\,2\,2)}$ | 1.45991Å | 1.45773Å |
| $d_{(2\,1\,3)}$ | 1.24067Å | 1.23794Å |
| $d_{(3\,3\,2)}$ | 1.13118Å | 1.13000Å |

However, the simultaneous reduction and increase of certain lattice parameters in the hexagonal crystal lattices led to reduction and increase of various d-spacings along common crystal planes when Ar carrier gas flow rates were increased as shown in Table 4.4

*Table 4.4: Effects of increasing Ar carrier gas flow rates on d-spacings of hexagonal crystal lattices*

| d-spacing – Hexagonal | As produced TiAl 2.3 | As produced TiAl 2.4 |
|---|---|---|
| $d_{(1\,0\,0\,0)}$ | 2.14813Å | 2.14382Å |
| $d_{(0\,1\,1\,2)}$ | 1.70823Å | 1.99574Å |
| $d_{(0\,2\,2\,2)}$ | 1.33702Å | 1.46075Å |
| $d_{(0\,2\,1\,3)}$ | 1.24022Å | 1.23773Å |

Figures 4.29 and 4.30 illustrate the peak broadening of as-produced and heat-treated TiAl 2.3. The peak broadening of as-produced and heat-treated TiAl 2.4 are illustrated in Figure 4.31 and 4.32. These plots were used to calculate dislocation densities displayed in Table 4.5.

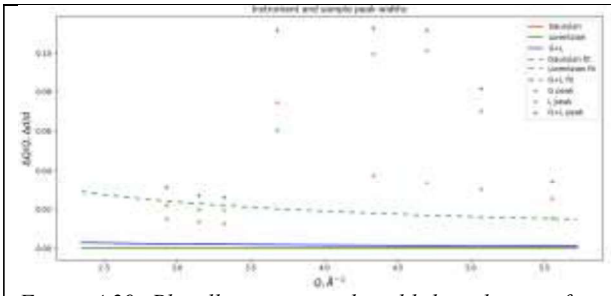

*Figure 4.29: Plot illustrating peak width broadening of as produced TiAl2.3.*

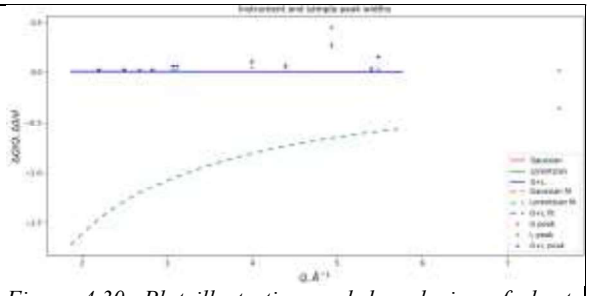

*Figure 4.30: Plot illustrating peak broadening of heat treated TiAl2.3.*

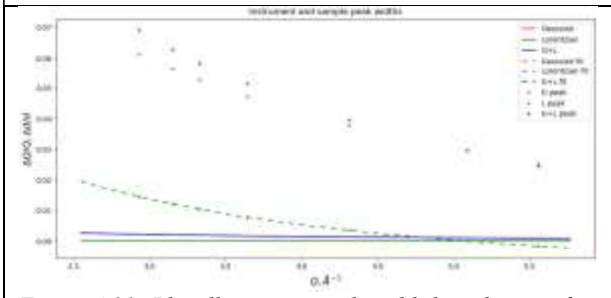

*Figure 4.31: Plot illustrating peak width broadening of as produced TiAl2.4*

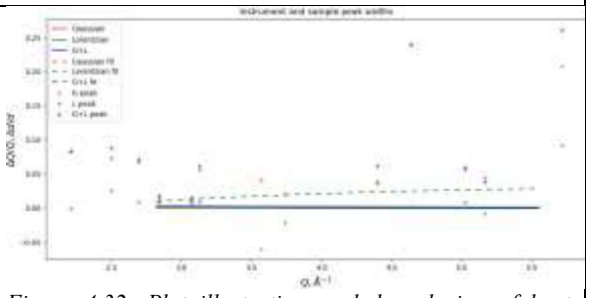

*Figure 4.32: Plot illustrating peak broadening of heat treated TiAl2.4.*

Table 4.5 displays calculated dislocation densities of TiAl alloys. Dislocation densities of TiAl2.3 and TiAl2.4 increased during heat-treatment. Dislocations have burger's vectors: $\frac{1}{3}a\ [1\ 1\ \underline{2}\ 0]$ for hexagonal structure; $\frac{1}{2}a < \underline{1}\ 1\ 0]$; $\frac{1}{2}a < \underline{1}\ \underline{1}\ 2]$; $< 0\ \underline{1}\ 1]\ and < 1\ 0\ \underline{1}]$ for tetragonal structure (Appel *et al.,* 2011a) along close packed planes $(1\ 1\ 1)_{\gamma}||(0\ 0\ 0\ 1)_{\alpha}$ and $(\ 1\ 1\ 0)_{\gamma}||(1\ 1\ 2\ 0)_{\alpha}$ (Appel *et al.,* 2011a).

*Table 4.5: Dislocation densities of TiAl alloys*

| **Sample** | **Phase** | **Dislocation density (x10$^{-4}$ nm$^{-2}$)** |
|---|---|---|
| TiAl 2.3 as produced | $Ti_{0.7}Al_{0.3}$ | |
| | $Ti_{0.4}Al_{0.6}$ | **11,54** |
| TiAl 2.3 heat treated | $Ti_{0.15}Al_{0.85}$ | |
| | $Ti_3Al$ | **53,11** |
| TiAl 2.4 as produced | $Ti_{0.25}Al_{0.75}$ | |
| | $Ti_{0.6}Al_{0.4}$ | **3,60** |
| TiAl 2.4 heat treated | TiAl | |
| | $Ti_{19}Al_6$ | **29,72** |

### 4.1.4 Electron Backscatter Diffraction (EBSD) of TiAl alloy

EBSD revealed the basket weave nature of TiAl-2.4 where both the primary and secondary basket weaves were mostly comprised of the hexagonal close packed (HCP) α phase as displayed in colour coded image in Figure 4.33. These HCP crystals had various orientations with respect to the z-axis as observed in the Inverse Polar Figure Z displayed in Figure 4.34. The secondary basket weave had the appearance of lamellae on SEM micrographs displayed in Figures 4.2 and 4.3.

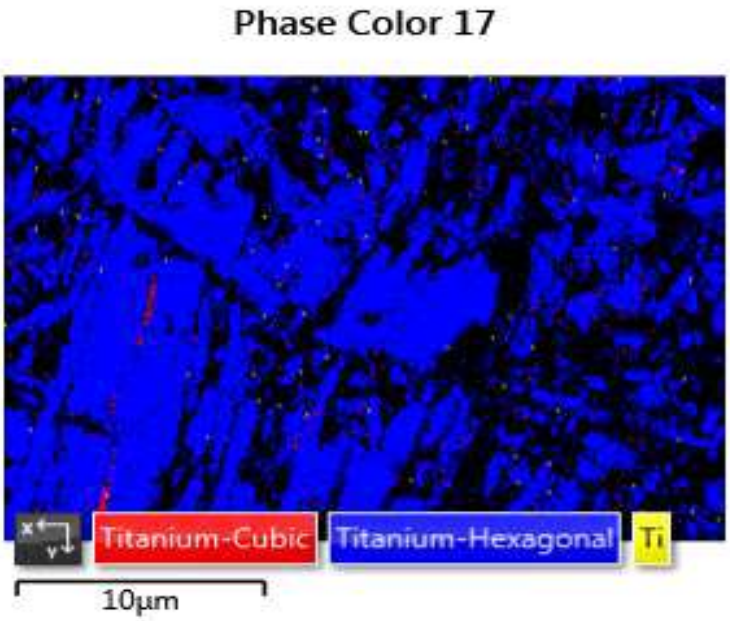


*Figure 4.33: EBSD colour coded image displaying $\alpha_2$ phase with traces of γ in as produced Ti-Al-2.3*

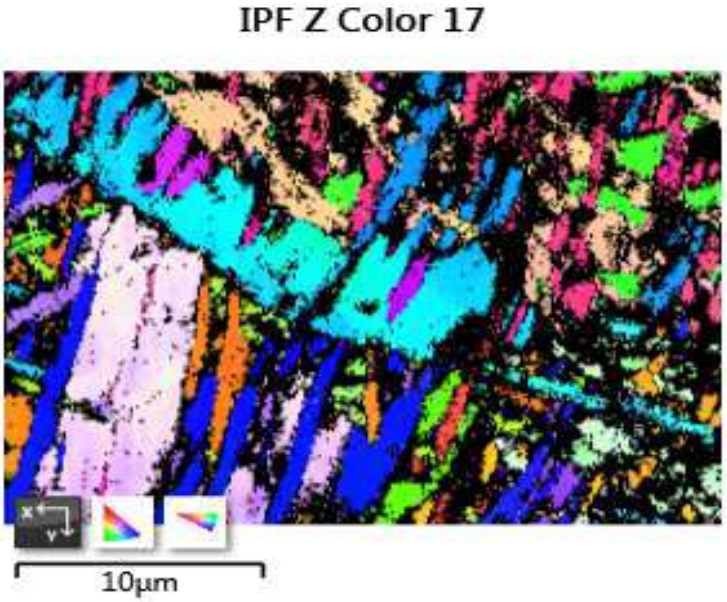


*Figure 4.34: EBSD inverse pole figure (IPF) displaying crystal orientation map for as produced Ti-Al-2.3*

### 4.1.5 Microhardness of TiAl alloys

Microhardness of as-produced TiAl alloys:

As-produced samples yielded micro-hardness values demonstrated in the bar graph in Figure 4.35 where microhardness is displayed with respect to Ar carrier gas flowrates. Micro hardness values for samples generated at low Al feed rate (1.5 rpm) ranged from 509,056 HV to 535,556 HV with an average hardness of 523,792HV. Microhardness values dropped when Al feed rates were increased to 2.0 rpm. Microhardness values at high Al feed rates dropped to values ranging from 464,056HV to 498,889HV, with the reported average hardness of 476,24HV. It was also observed that equiaxed dendritic and nearly lamellar microstructures yielded higher microhardness values compared to microstructures which contained columnar dendrites, basket weave structure and fully lamellar equiaxed grains.

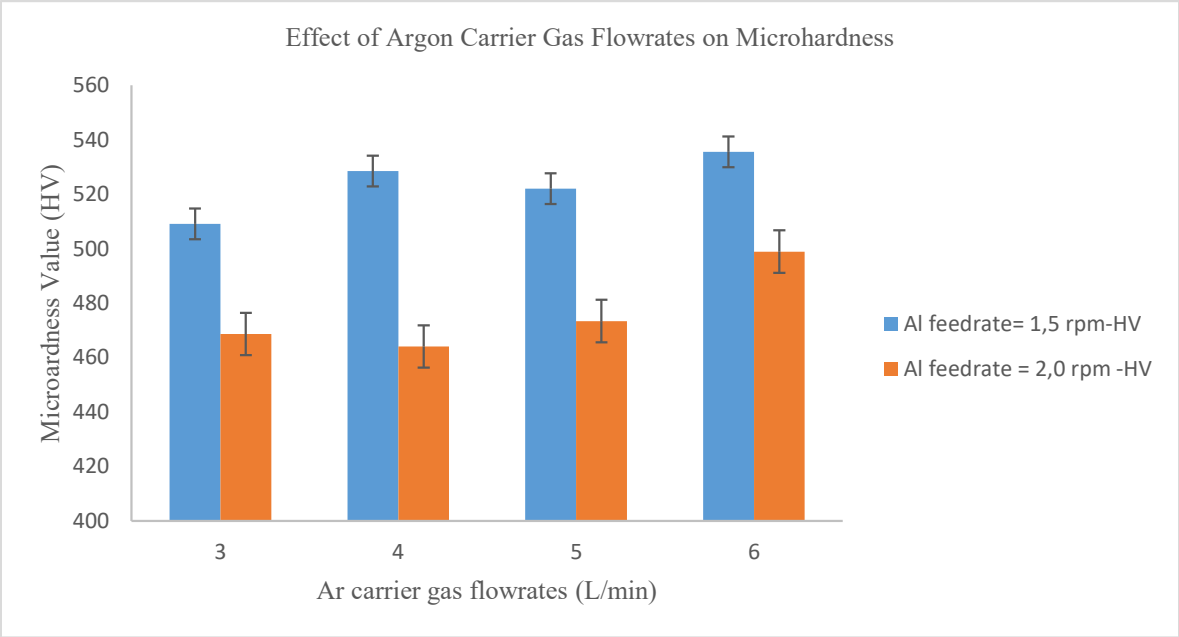


*Figure 4.35: Graphical representation of the effect of Al feed rates and Ar carrier gas flowrates on microhardness of as produced TiAl alloys*

Microhardness of heat-treated TiAl alloys:

The microhardness values of heat-treated TiAl samples dropped significantly compared to the as-produced alloys as observed in the bar graph illustrated in Figure 4.36. Microhardness values of heat-treated TiAl alloys produced with low Al feed rate (1.5 rpm) dropped to hardness values ranging between 386,74HV and 447,53HV. It can be observed that microhardness values increased with grain sizes as it was observed in Figures 4.9 to 4.12. Microhardness values of

heat-treated TiAl samples produced with Al feed rate of 2.0rpm dropped to a range from 304,13HV to 334,34HV and an average of 315,42HV.

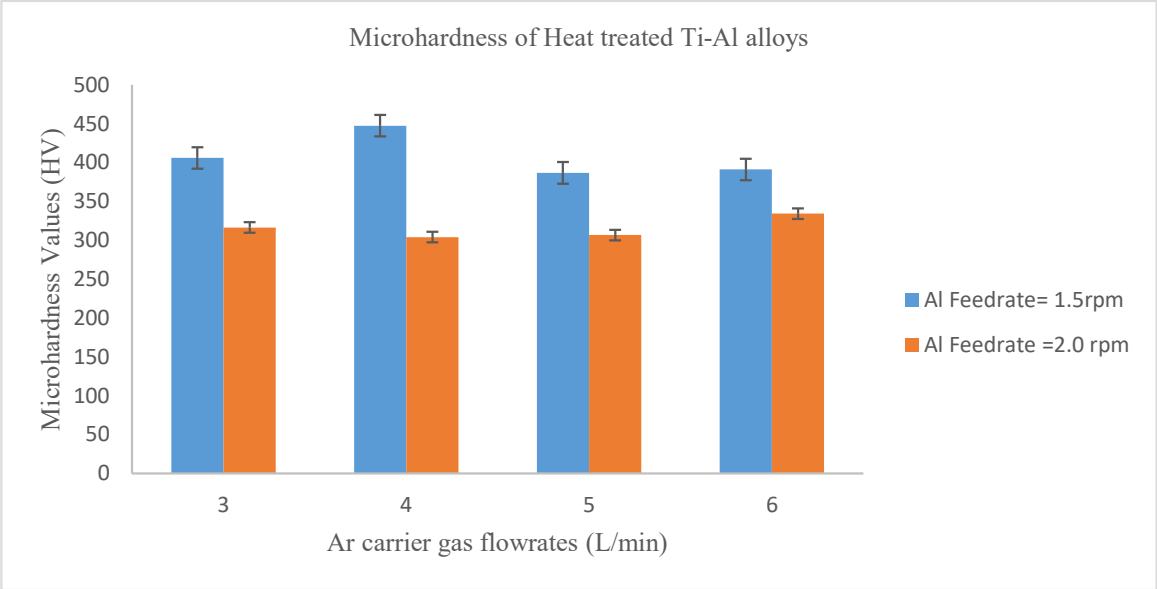


*Figure 4.36: Microhardness of Heat treated Ti-Al alloys*

### 4.1.6 Fracture stress of Ti-Al alloy

As-produced and heat-treated TiAl-2.4 appeared to have highest calculated fracture stress which was evident in the smallest post processing thermal crack lengths among all TiAl alloys produced. These samples were further studied to explore properties which contributed to their improved fracture stress compared to the rest of the samples. Fracture stress was calculated using a model by Voice *et al.* (2005) with fracture toughness obtained from Appel *et al.*, (2011) as indicated in Figures 4.37 and 4.38. The calculated fracture stress reduced from $117.22\ MPa$ in as-produced state to $95.083\ MPa$ in the post heat-treated state. However, bulk tensile tests could not be performed on the samples due to numerous cracks and unavailability of appropriate sample sizes to perform tensile tests.



*Figure 4.37: Optical micrograph of crack length of as-produced Ti-Al-2.4.*

Average crack length (a)= 23.165 x$10^{-6}$ m ; fracture toughness= 1.0 MPa$\sqrt{m}$

$\sigma_f = \frac{K_{IC}}{\sqrt{\pi a}} = 117.22\ MPa$

Microhardness: 522,06HV

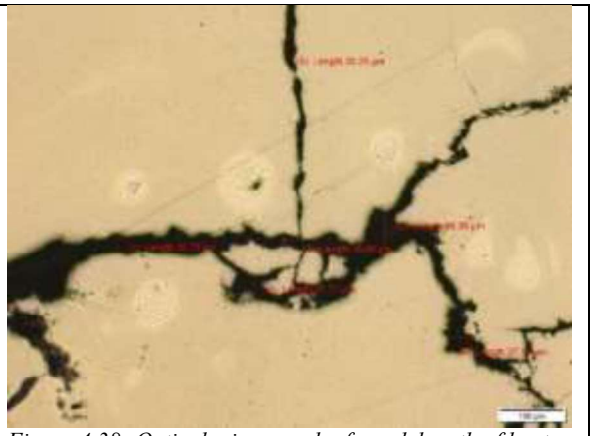

*Figure 4.38: Optical micrograph of crack length of heat-treated Ti-Al-2.4.*

Average crack length (a)= 35.208 x$10^{-6}$ m ; fracture toughness= 1.00 MPa$\sqrt{m}$

$\sigma_f = \frac{K_{IC}}{\sqrt{\pi a}} = 95.083\ MPa$

Microhardness: 386,74HV

### 4.1.7 Mechanical Properties of Binary TiAl according to nanoindentation

Nanoindentation carried out on as-produced sample TiAl-2.3 led to calculated yield stress of 300MPa and elastic modulus of 118.6GPa. The relationship between indentation displacement and applied load for as produced TiAl-2.3 are illustrated in Figures 4.39 and 4.40, where various indentations are displayed in Figure 4.39 and a curve representing the overall average is illustrated in Figure 4.40. Heat-treatment led to an increase in yield stress to a value of 480 MPa and elastic modulus to 178.5GPa. The resultant curves for heat-treated sample TiAl2.3 are displayed in Figure 4.41 and the average indentation is displayed in Figure 4.42.

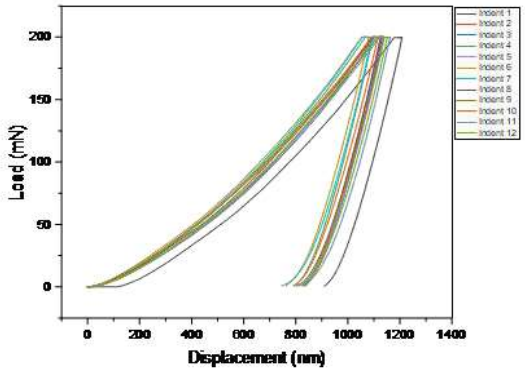


*Figure4.4.39: Relationship between indentation displacement and applied load for twelve indentations on as-produced TiAl 2.3.*

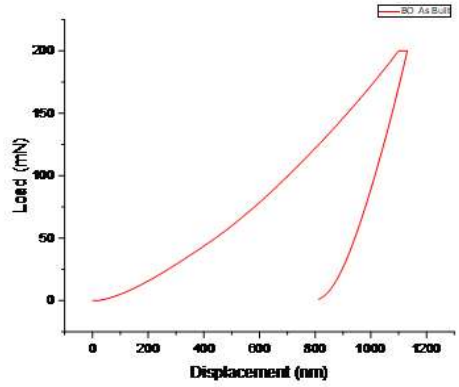


*Figure 4.40: Curve representing average relationship of indentation displacement and applied load for as-produced TiAl 2.3.*

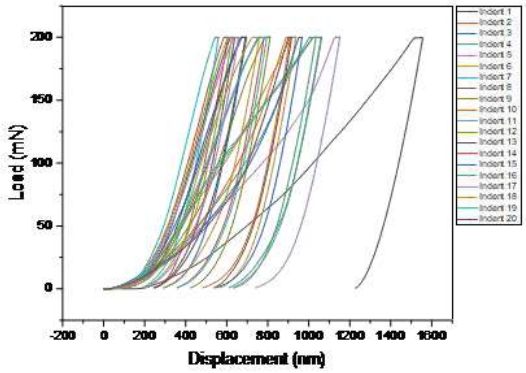


*Figure 4.41: Relationship between indentation displacement and applied load for twenty indentations on heat-treated TiAl 2.3.*

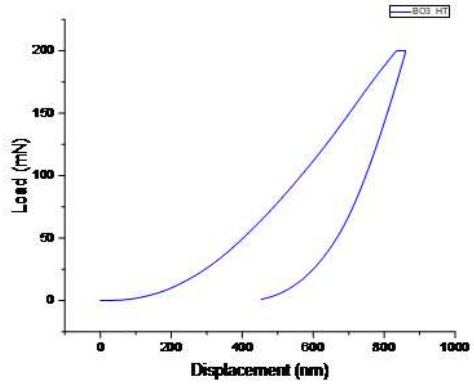


*Figure 4.42: Curve representing average relationship of indentation displacement and applied load for heat-treated TiAl 2.3.*

Nanoindentation carried out on as-produced sample TiAl-2.4 led to calculated yield stress of 250MPa and elastic modulus of 109.5GPa. The relationship between indentation displacement and applied load for as-produced TiAl 2.4 are illustrated in Figures 4.43 and 4.44, where various indentations are displayed in Figure 4.43 and a curve representing the overall average is illustrated in Figure 4.44. Heat-treatment led to an increase in yield stress to a value of 220MPa and elastic modulus to 129.3GPa. The resultant curves for heat-treated sample TiAl2.4 are displayed in Figure 4.45 and the average indentation is displayed in Figure 4.46.

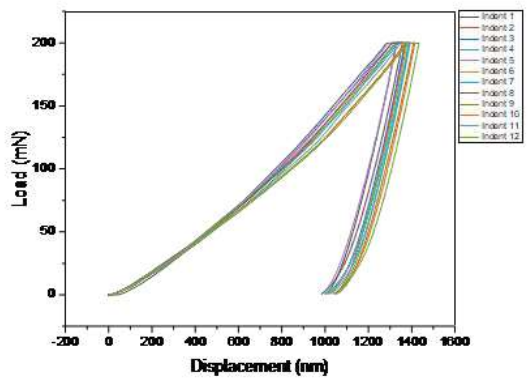


*Figure 4.43: Relationship between indentation displacement and applied load for twelve indentations on as-produced TiAl 2.4.*

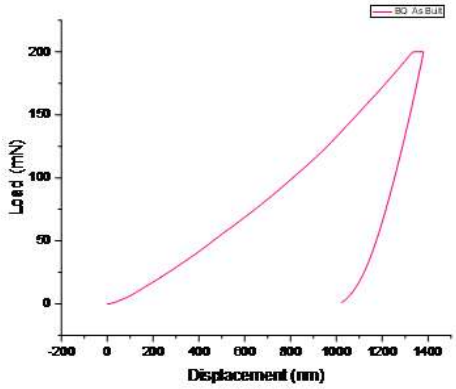


*Figure 4.44: Curve representing average relationship of indentation displacement and applied load for as-produced TiAl 2.4.*

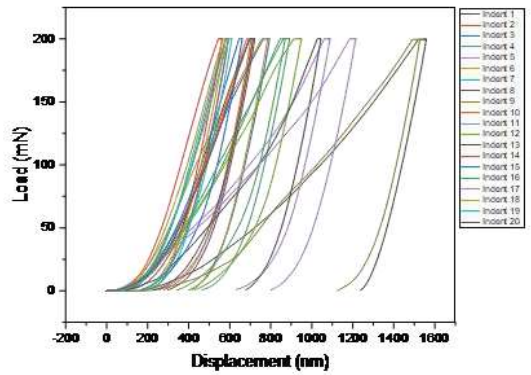


*Figure 4.45: Relationship between indentation displacement and applied load for twenty indentations on heat-treated TiAl 2.4.*

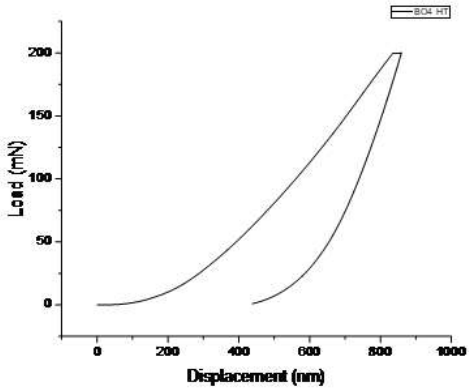


*Figure 4.46: Curve representing average relationship of indentation displacement and applied load for heat-treated TiAl 2.4.*

### 4.1.8 Thermogravimetric analysis (TGA) of TiAl alloys

Figure 4.47 displays mass loss due oxidation as a function of time. It was observed that as-produced TiAl-2.4 underwent initial mass loss in the first 60 minutes at a rate of 0.0235404mg/min. This mass loss was followed by mass gain which continued at a rate of 0.017000mg/min for 83 minutes. The mass gain was followed by a drastic reduction in mass gain rates to 0.00088308mg/min, oxidation at this rate continued for 112 minutes. Oxidation then led to mass gain at a rate of 0,0128304mg/min the last for 85 minutes of the experiment.

Heat-treated TiAl-2.4 underwent initial mass loss in the first 60 minutes at a rate of 0.019431mg/min. This mass loss was followed by mass gain which continued at a rate of 0.021810mg/min for 78 minutes. The mass gain was followed by a drastic reduction in mass

gain to a rate of 0.003400mg/min, for 117 minutes into the experiment. Oxidation led to mass gain at a rate of 0,008981268mg/min for the last 85 minutes of the experiment.

Parabolic rate constants $(k = \frac{\Delta m}{\sqrt{t}})$ for isothermal oxidation for as-produced TiAl-2.4 was -0.07050mg/min$^{1/2}$ and 0.086772mg/min$^{1/2}$ for heat treated TiAl-2.4. The drastic mass loss rate reduction between 140 minutes and 255 minutes in both as-produced and heat-treated TiAl-2.4 is indicative of the formation of a protective oxide film prior to that oxidation stage.

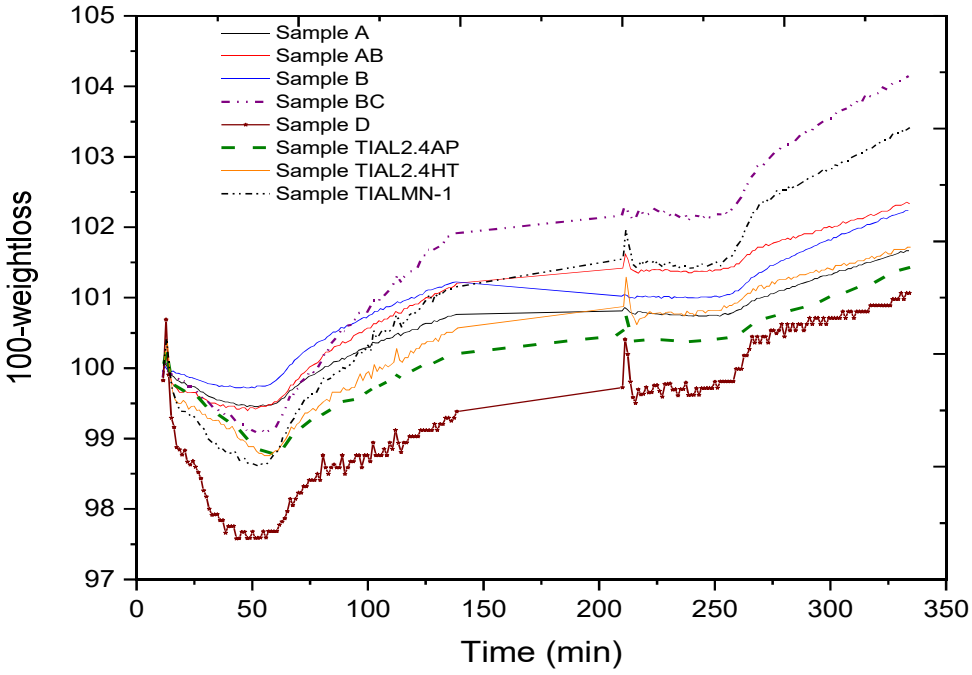


*Figure 4.47: Mass loss as a function of time for as-produced and heat-treated TiAl-2.4 oxidation behaviour.*

Figure 4.48 displays mass loss as a function of temperature. It was observed that mass loss occurred during the heating stages of the experiment and mass gain occurred between 800°C and 900°C. This coincided with mass loss in the first 60 minutes followed by mass gain which continued until the end of the experiment.

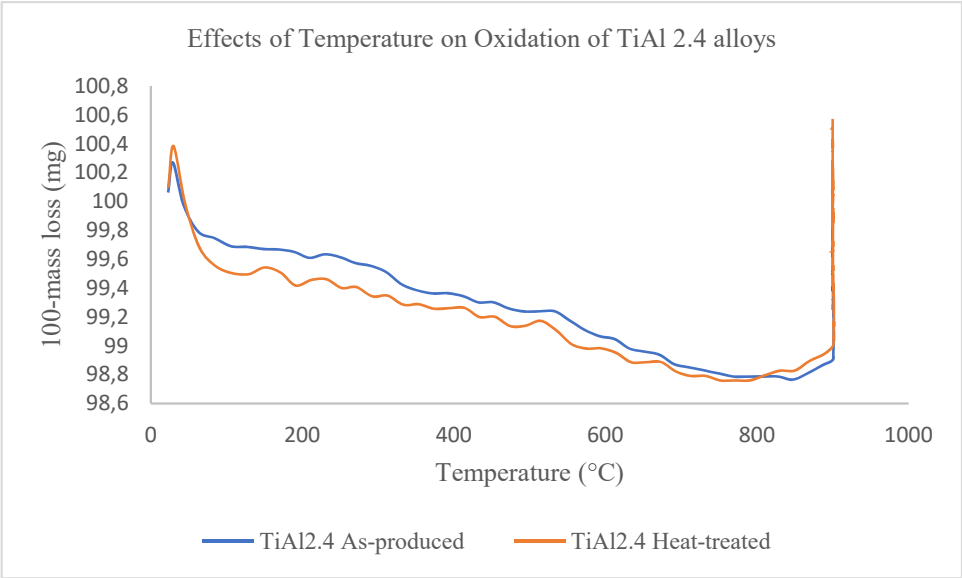


*Figure 4.48: Mass loss as a function of temperature for as-produced and heat-treated TiAl-2.4*

The thickness of the oxide film of as-produced TiAl-2.4 ranged from 29.66µm to 249.6µm as observed in Figure 4.49 where it was also observed that oxidation also took place on the post process thermal cracks. Figure 4.50 displays various layers of the oxide scale. The outer layer was comprised of $TiO_2$ (grey SEM-BSD contrast) which was approximately 14.26µm thick. The first inner layer right below the outer layer was comprised of $Al_2O_3$ (dark grey SEM-BSD contrast) with a thickness that ranged from 4.439µm to 21.16µm. Below the $Al_2O_3$ was another $TiO_2$ layer which contained veins of $Al_2O_3$. Below this layer was another $Al_2O_3$ which was situated directly on the $\alpha_2+\gamma$ equiaxed lamellar grain microstructure. These layers of the oxide film are displayed in Figure 4.50 and the microstructure of the main sample in Figure 4.51. The compositions of each phase of the oxide film are displayed in EDX patterns shown from Figures 4.52 and 4.53. These phases were confirmed by XRD.

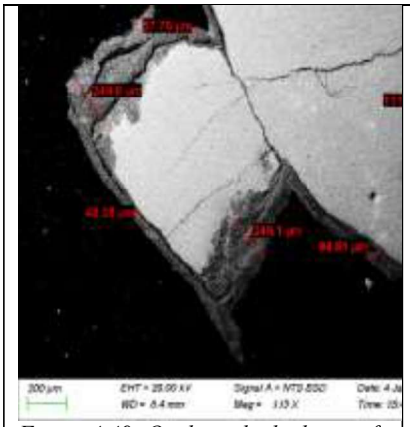

*Figure 4.49: Oxide scale thickness of as-produced TiAl-2.4*

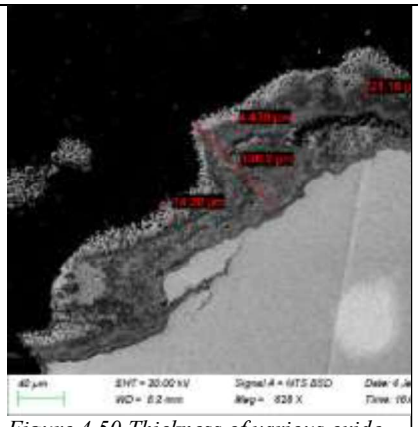

*Figure 4.50 Thickness of various oxide layers of as-produced TiAl-2.4*

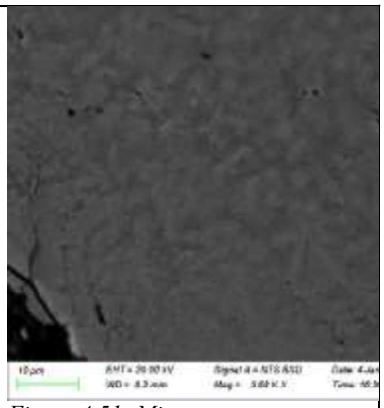

*Figure 4.51: Microstructure underneath oxide scale of as-produced TiAl-2.4*

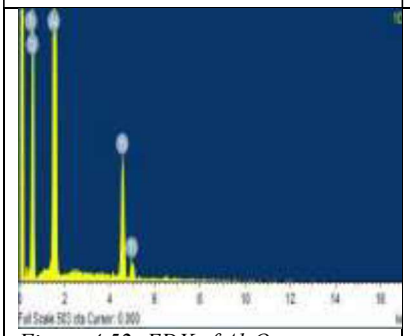

*Figure 4.52: EDX of $Al_2O_3$- 67.62(at%O); 28.34(at%Al); 4.04(at%Ti)*

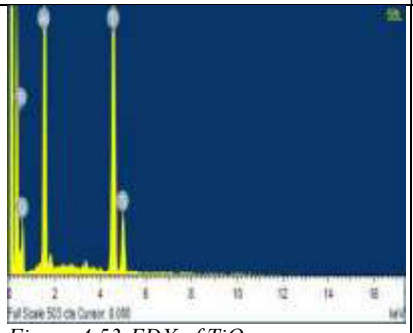

*Figure 4.53:EDX of $TiO_2$- 51.22(at%O); 27.72(at%Ti); 21.06(at%Al)*

The thickness of the oxide film of heat treated TiAl2.4 was smaller than the as-produced sample with a thickness ranging from 27.45µm to 70.54µm as observed in Figure 4.54. $TiO_2$ layers were approximately 21.48µm thick and $Al_2O_3$ layer was approximately 4.311µm thick as observed in Figure 4.55. The microstructure of the heat treated oxidised TiAl-2.4 remained the same as the microstructure prior to oxidation as displayed in Figure 4.56.

The stratified oxide scale microstructures of both as-produced and heat-treated TiAl-2.4 were similar and appear to have developed in similar ways. Although oxidation rates of as-produced sample were lower than that of the heat-treated sample, the oxide scale of the as-produced were thicker. The larger thickness of the oxide scale of as-produced samples could be accredited to the lower initial mass loss which occurred at a lower rate than of the heat-treated sample in the first 60 minutes.

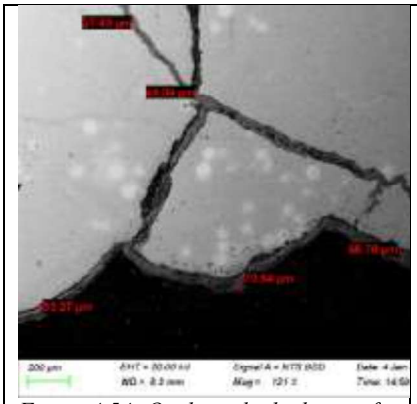

*Figure 4.54: Oxide scale thickness of heat-treated TiAl-2.4*

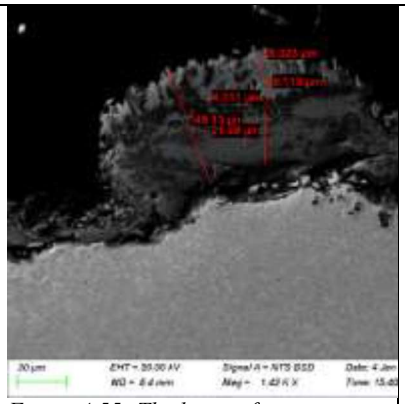

*Figure 4.55: Thickness of various oxide layers of heat-treated TiAl-2.4*

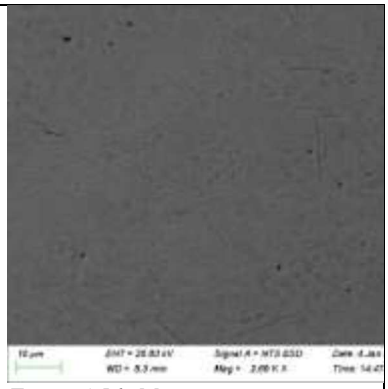

*Figure 4.56: Microstructure underneath oxide scale of heat treated TiAl-2.4*

The correlation of SEM micrographs and thermographs indicate that the outer $TiO_2$ layer, which developed in the first 60 minutes leading to mass loss since it was exposed and did not have a protective oxide scale, which also led to the porosity observed in the outer layer. The formation of the $Al_2O_3$ layer formed between 60 and 140 minutes and led to mass gain. The mass gain coincides with temperatures between 800°C and 900°C. $Al_2O_3$ is only protective below 800°C (Chang, 2007) and is responsible for the drastic reduction in mass gain rate and spallation between 140 and 255 minutes, keeping the sample mass constant. However, as soon as the temperature of the sample exceeded 800°C at 255 minutes, oxidation and spallation proceeded leading to the formation of $TiO_2$ layer with inclusions of $Al_2O_3$ veins. These oxide films were similar to those reported by (Chang, 2007). Thicker $Al_2O_3$ in as-produced sample led to lower mass losses of the oxide film compared to the heat-treated sample which led to a generally thicker oxide film. Compounds in oxide scales were confirmed using XRD and EDX.

## 4.2. Binary TiMn

### 4.2.1 Microstructures of As-produced TiMn alloys

Laser power used to produce all binary TiMn alloys was altered which altered the LEPUL (Gu *et al.,* 2015). TiMn alloys produced using LEPUL of 417.730J/cm produced microstructures which comprised largely of α ductile (labelled i in Figure 4.57) and refined (labelled ii in Figure 4.57) primary dendrites within a β matrix phase (labelled iii in Figure 4.57). These microstructures are illustrated in SEM micrographs displayed in Figures 4.57 to 4. 62. At low Mn feed rates of 0.3rpm, Mn in the general overall composition was low at 13.57at%Mn – Figure 4.57. As the Mn feed rate was increased to 0.5 rpm, the precipitation of $Mn_{0.52}Ti_{0.48}$(s) on α equiaxed grain boundaries (which were situated within the β matrix and α dendrite grain boundaries proceeded as observed in Figures 4.58. These changes in the microstructure were

accompanied by an increase in the Mn in the overall general composition to 31.78at%Mn. As the Mn feed rates were increased further from 0.7, to 0.9, 1.1 and 1.3rpm, the nucleation and precipitation of $Mn_{0.52}Ti_{0.48}$(s) on α equiaxed and dendritic grain boundaries increased (labelled iv in Figure 4.59). The stages of progression of these microstructures as Mn feed rates were increased are observed in Figures 4.59 to 4.62. It was observed that the α primary dendrites dissolved as the Mn feed rates were increased, while the volume proportion of $Mn_{0.52}Ti_{0.48}$(s) phase in the structure appeared to increase. The volume phase proportions were obtained using ImageJ and are included in the image captions.

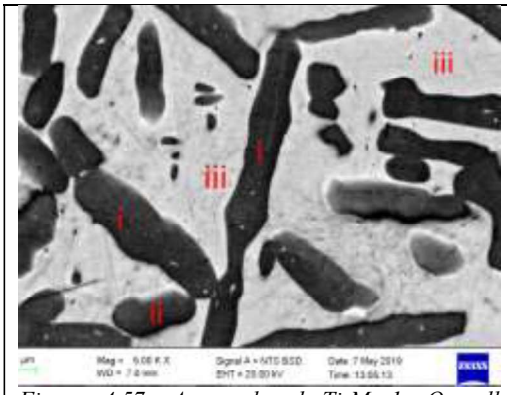


*Figure 4.57: As produced Ti-Mn-1. Overall Composition: 86.43at%Ti 13.57at%Mn (41.27%α and 58.73%β)*

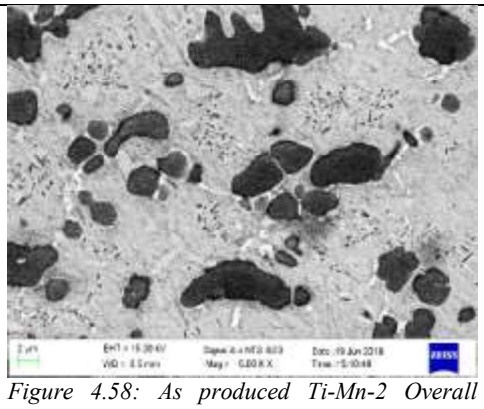

*Figure 4.58: As produced Ti-Mn-2 Overall composition: 78.22at%Ti 31.78at%Mn (25.12%α, 73.49%β and 1.39% $Mn_{0.52}Ti_{0.48}$)*

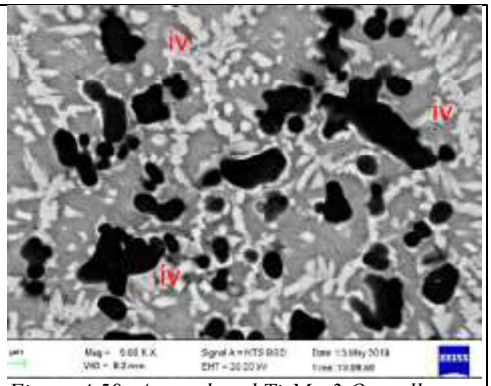


*Figure 4.59: As produced Ti-Mn-3 Overall composition: 76.11at%Ti 23.90at%Mn (20.44%α, 62.29%β and 17.27% $Mn_{0.52}Ti_{0.48}$)*

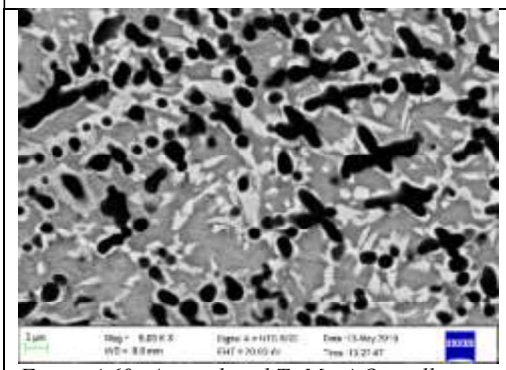

*Figure 4.60: As produced Ti-Mn-4 Overall composition: 71.83at%Ti 27.17at%Mn (14.91%α, 38.43%β and 46.66% $Mn_{0.52}Ti_{0.48}$)*

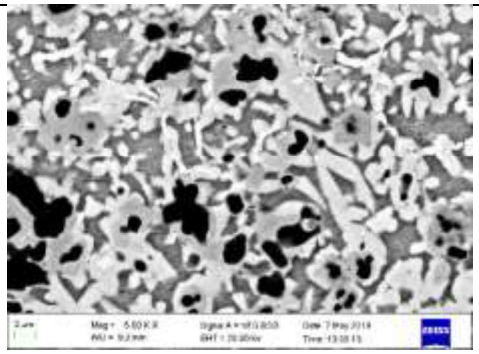

*Figure 4.61: As produced Ti-Mn-5 Overall composition: 71.59at%Ti 18.41at% Mn(9.01%α, 33.93%β and 57.07 $Mn_{0.52}Ti_{0.48}$)*

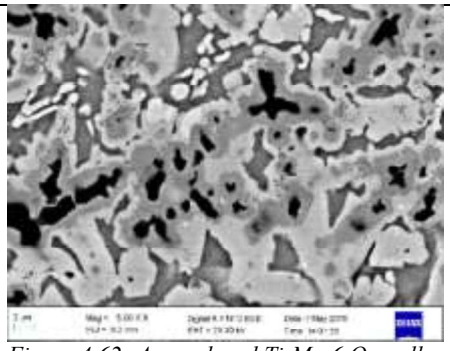

*Figure 4.62: As produced Ti-Mn-6 Overall composition: 64.36at%Ti 35.64at%Mn (2.92%α, 17.91%β and 79.17% $Mn_{0.52}Ti_{0.48}$)*

*Figures 4.57 to 4.62: SEM micrographs taken with BSD mode, EHT set at 20.0kV and the magnification of x500 (2μm) illustrating as produced TiMn alloys produced with LEPUL= 417.730J/cm*

Decreasing LEPUL to 375.605J/cm, coupled with increasing Mn feed rates to 0.9, 1.1 and 1.3rpm. The resulting microstructures had compositions ranging from 28.00at%Mn to 37.60at%Mn, where Mn was high as demonstrated in Figures 4.63 to 4.65. These microstructures had limited traces of α primary dendrites and were comprised largely of

$Mn_{0.52}Ti_{0.48}$(s) phase within the β matrix. The volume proportions of $Mn_{0.52}Ti_{0.48}$(s) phase increased with increasing Mn feed rates while α and β phase decreased.

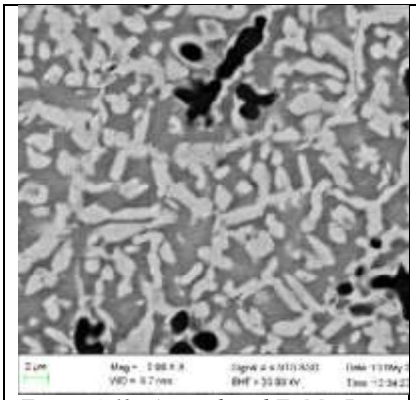

*Figure 4.63: As produced Ti-Mn-7 Overall Composition: 72.00at%Ti 28.00at%Mn(13.62%α, 41.60%β and 44.78% $Mn_{0.52}Ti_{0.48}$)*

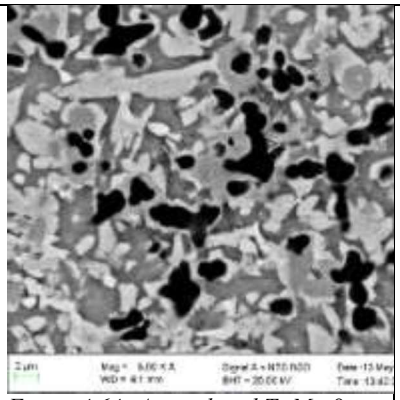

*Figure 4.64: As produced Ti-Mn-8 Overall composition: 66.43at%Ti 33.57at%Mn (12.10%α, 40.75%β and 47.15% $Mn_{0.52}Ti_{0.48}$)*

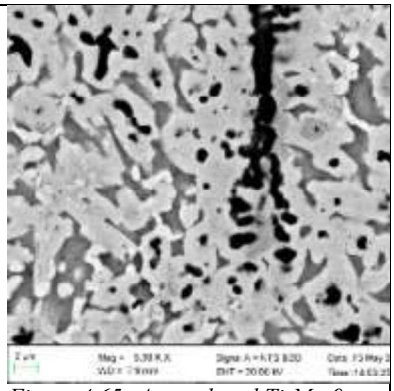

*Figure 4.65: As produced Ti-Mn-9 Overall composition: 62.40at%Ti 37.60at%Mn (5.89%α, 30.50%β and 63.61% $Mn_{0.52}Ti_{0.48}$)*

*Figures 4.63 to 4.65: SEM micrographs taken with BSD mode, EHT set at 20.0kV and the magnification of x500 (2μm) illustrating as produced TiMn alloys produced with LEPUL=375.605J/cm*

Increasing the LEPUL to 459.072J/cm initially at low Mn feed rates (0.3 and 0.5 rpm) produced microstructures which comprised of large Ti rich α primary dendrites within a β matrix as displayed in Figures 4.66 and 4.67. It was also observed that the sizes of the dendrites reduced with increased Mn feed rates. Which is consistent with the reduction in α phase volume proportion as Mn increased. The overall compositions ranged from 8.01at%Mn to 12.58at%Mn as seen in Figures 4.66 and 4.67. As the Mn feed rates were increased further to 0.7rpm, which led to an overall composition of 19.54at%Mn, the nucleation and precipitation of small amounts of $Mn_{0.52}Ti_{0.48}$(s) on α grain boundaries occurred as observed in Figure 4.68

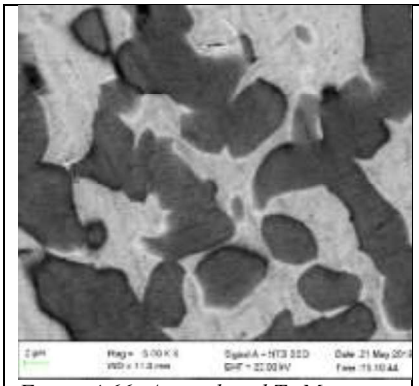

*Figure 4.66: As produced Ti-Mn-10Overall composition: 91.99at% Ti8.01at%Mn(52.95%α, 47.05%β and 0.00% $Mn_{0.52}Ti_{0.48}$)*

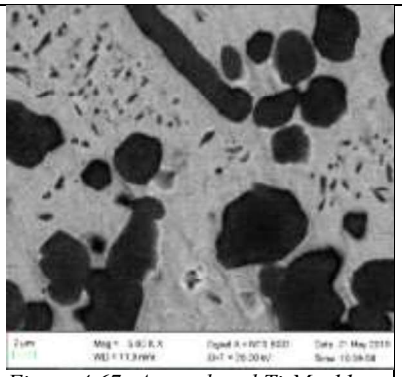

*Figure 4.67: As produced Ti-Mn-11. Overall composition: 87.42at%Ti 12.58at%Mn. (32.49%α, 67.51%β and 0.00% $Mn_{0.52}Ti_{0.48}$)*

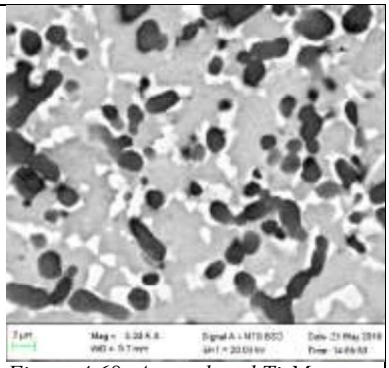

*Figure 4.68: As produced Ti-Mn-12Overall composition: 80.46at%Ti 19.54at%Mn (28.17%α, 62.01%β and 9.82% $Mn_{0.52}Ti_{0.48}$)*

*Figures 4.66 to 4.68: SEM micrographs taken with BSD mode, EHT set at 20.0kV and the magnification of x500 (2µm) illustrating as produced TiMn alloys produced with LEPUL=459.072J/cm*

Further increasing LEPUL to 500.806J/cm and decreasing Mn feed rates to 0.3, 0.5 and 0.7 rpm, produced microstructures displayed in Figures 4.69 to 4.71. These microstructures were dominated by α primary dendrites which were situated within a β matrix phase which had a significantly lower volume proportion as observed in Figure 4.69. The volume proportion of β increased as Mn in the composition increased from 9.87at% to 15.51at% and 18.52at% which was evident in Figures 4.70 and 4.71. However, the formation of $Mn_{0.52}Ti_{0.48}$(s) did not occur for these feed rates and LEPUL.

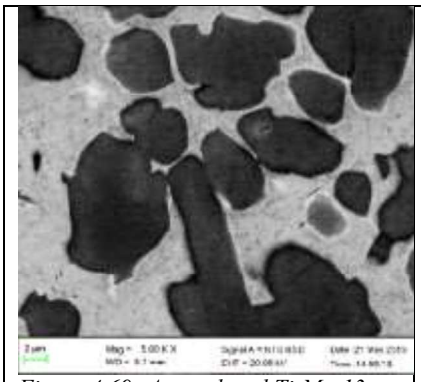

*Figure 4.69: As produced Ti-Mn-13. Overall composition: 90.13at%Ti 9.87at%Mn (55.90%α, 44.10%β and 0.00% $Mn_{0.52}Ti_{0.48}$)*

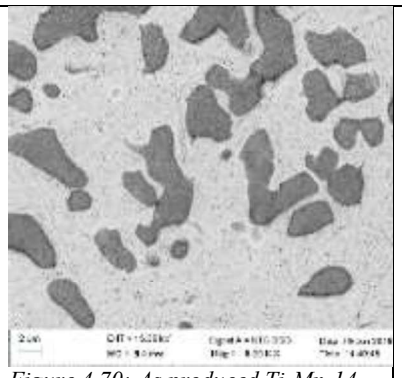

*Figure 4.70: As produced Ti-Mn-14. Overall composition: 84.49at%Ti 15.51at%Mn (34.08%α, 65.92%β and 0.00% $Mn_{0.52}Ti_{0.48}$)*

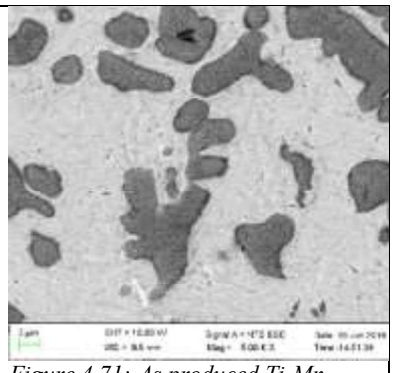

*Figure 4.71: As produced Ti-Mn-15.Overall composition: 81.48at%Ti 18.52at%Mn (26.28%α, 71.9%β and 0.00% $Mn_{0.52}Ti_{0.48}$)*

*Figures 4.69 to 4.71: SEM micrographs taken with BSD mode, EHT set at 20.0kV and the magnification of x500 (2µm) illustrating as produced TiMn alloys produced with LEPUL=500.806J/cm*

Reducing LEPUL to 459.072J/cm and increasing Mn feed rates to 0.9, 1.1 and 1.3rpm, produced microstructures displayed in Figures 4.72 to 4.74. These microstructures contained an extremely limited amount of α dendrites. At 0.9rpm, the microstructure was dominated by the β matrix phase -Figure 4.72. As Mn in the composition increased, the volume of $Mn_{0.52}Ti_{0.48}$(s) increased while α and β phase reduced -Figures 4.73 and 4.74.

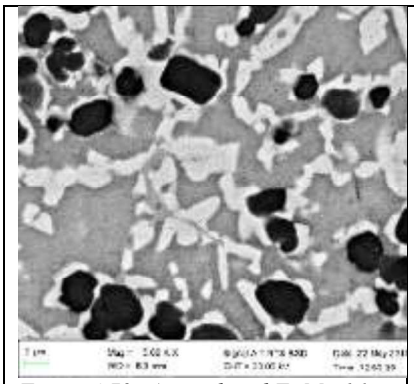

*Figure 4.72: As produced Ti-Mn-16 Overall composition: 71.87at%Ti 28.13atMn (20.09%α, 50.41%β and 28.69% $Mn_{0.52}Ti_{0.48}$)*

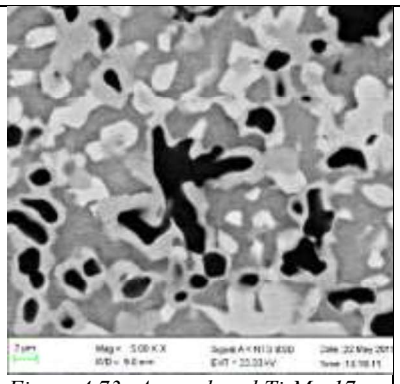

*Figure 4.73: As produced Ti-Mn-17 Overall composition: 21.43at%Ti 78.19at%Mn (11.90%α, 47.14 %β and 40.96% $Mn_{0.52}Ti_{0.48}$)*

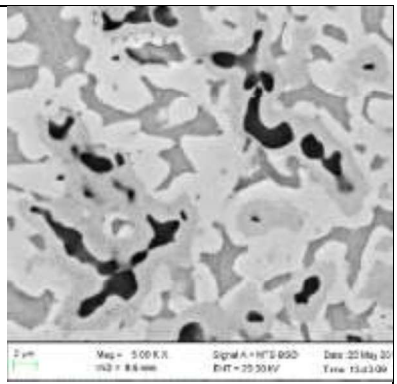

*Figure 4.74: As produced Ti-Mn-18 Overall composition: 67.02at%Ti 32.98at%Mn (6.46%α, 36.76%β and 56.78% $Mn_{0.52}Ti_{0.48}$)*

*Figures 4.72 to 4.74: SEM micrograhs taken with BSD mode, EHT set at 20.0kV and the magnification of x500 (2μm) illustrating as produced TiMn alloys produced with LEPUL=459.072J/cm*

The compositions of as-produced microstructural features are given in Table 4.6. It was observed that α dendrites were Ti rich while β and $Mn_{0.52}Ti_{0.48}$(s) were Mn rich. It was observed that the β phase was most stable at Mn feed rates of 0.3 and 0.5rpm, where the formation of $Mn_{0.52}Ti_{0.48}$(s) was avoided at lower LEPUL

*Table 4.6: Microstructural features of as produced TiMn alloys and their compositions.*

| Microstructure | Description | BSD Contrast | at% Ti | at% Mn | Phases |
|---|---|---|---|---|---|
| Primary dendrites within matrix phase | Primary dendrites | Black | 85.86 -98.18 | 1.82 – 14.14 | α |
| | Matrix | Grey | 64.79 – 83.73 | 16.27 – 35.21 | β |
| Precipitation on primary dendrite grain boundaries and matrix | Precipitates | White | 45.68 – 78.38 | 21.62 – 54.32 | $Mn_{0.52}Ti_{0.48}$(s) |

.

### 4.2.2 Microstructures of Heat-Treated Ti-Mn alloys

Microstructures of Heat Treated TiMn alloys:

Heat-treatment was initially attempted at 1300°C, which resulted in the liquifying of higher Mn samples. This led to the decision of reducing the heat-treatment temperature to 950°C.

At low Mn feed rates, the sizes of the α dendrites increased in size. This led to the use of lower magnifications to take SEM micrographs. Thus, SEM micrographs of the as-produced microstructures taken at a magnification of 2 μm while the magnification was reduced to 10μm to enable viewing of the structure with microstructural features that have increased in size.

The microstructures of heat-treated samples produced using the same LENS parameters yielded unchanged compositions as those found in the as-produced samples.

In Figure 4.75, microstructure of heat-treated sample produced using low Mn feed rate (0.3rpm) and LEPUL= 417.730J/cm contained α primary dendrites within a β matrix, similar to structures that were studied in the as-produced state. Mn in the overall compositions increased according to compositions listed previously in Figures 4.57 to 4.74. As Mn increased, α dendrites dissolved into the β matrix and $Mn_{0.52}Ti_{0.48}$(s) precipitates during heat-treatment as observed from Figure 4.76 to 4.78. Figure 4.79 displays a sample which oxidised during heat-treatment and it could be observed that the dissolution of α primary dendrites was less. Figure 4.80 displays heat-treated microstructures which were produced with a Mn feed rate of 1.3rpm and this structure has similar behaviour to samples in Figures 4.76 to 4.78 where α dendrites dissolved during heat-treatment. This behaviour during heat-treatment led to an increase of Ti in matrix and precipitates. Due to increased Ti, grain boundary precipitates underwent phase transformation reaction (Kostov and Živković, 2008) in Equation 4.1:

$$Mn_{0.52}Ti_{0.48}(s) \rightarrow MnTi(s) \qquad (4.1)$$

MnTi appeared more uniformly distributed than $Mn_{0.52}Ti_{0.48}$(s). As Mn was increased, the dissolution of α dendrites and formation of MnTi continued, leading to increased volume proportions of MnTi(s) phase, situated on α dendrite grain boundaries. The transformation of this microstructure is observed in Figures 4.75 to 4.78 and 4.80. However, in Figure 4.79, the sample oxidised during heat treatment which led to reduced dissolution of α phase and increased MnTi(s) and extremely limited β matrix phase.

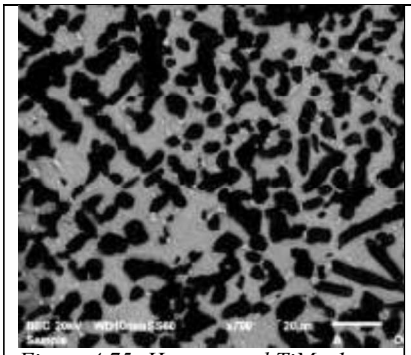

*Figure 4.75: Heat-treated TiMn-1*

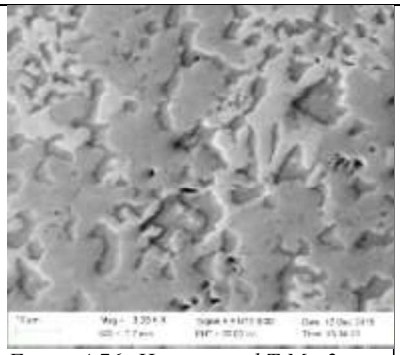

*Figure 4.76: Heat-treated TiMn-2*

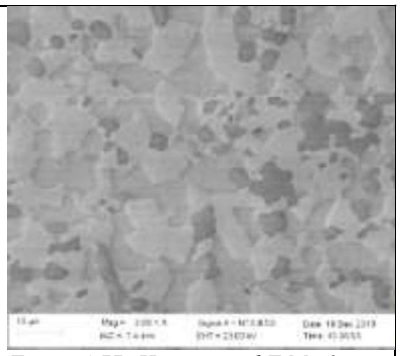

*Figure 4.77: Heat-treated TiMn-3*

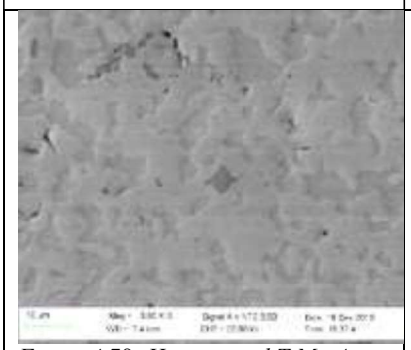

*Figure 4.78: Heat-treated TiMn-4*

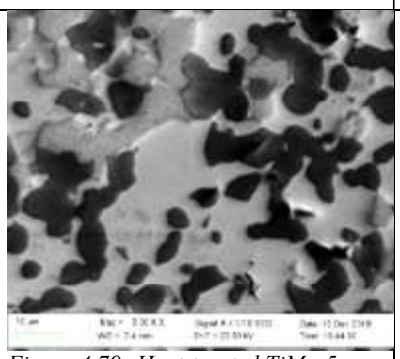

*Figure 4.79: Heat-treated TiMn-5*

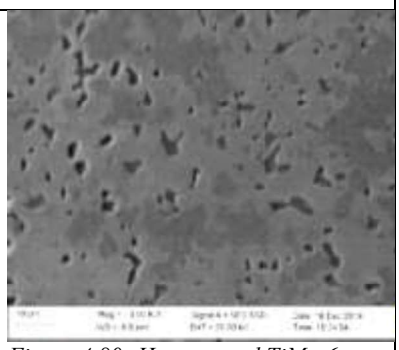

*Figure 4.80: Heat-treated TiMn-6*

*Figures 4.75 to 4.80: SEM micrographs taken with BSD mode, EHT set at 20.0kV and the magnification of x3000 (10µm) illustrating heat-treated TiMn alloys produced with LEPUL=417.730J/cm*

At decreased LEPUL of 375.605J/cm, and increased Mn feed rates (0.9rpm, 1.1rpm and 1.3rpm), heat-treated samples were comprised of MnTi in the shape of previously present dendrites, within a β matrix phase. α dendrites were absent from these microstructures as can be observed in Figures 4.81 and 4.82. These microstructures resulted from the complete dissolution of α dendrites into precipitates MnTi and β matrix.

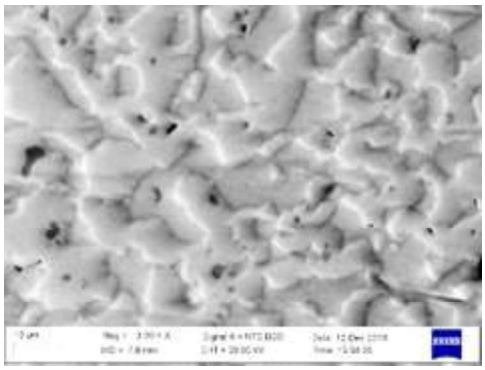

*Figure 4.81: Heat-treated TiMn-7*

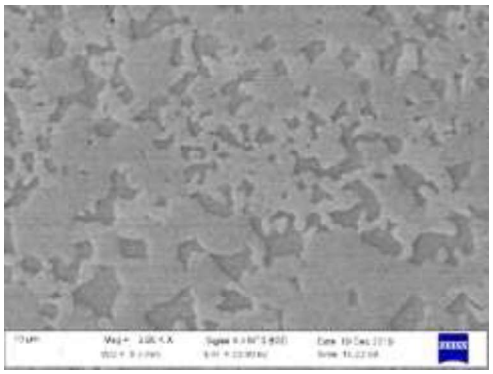

*Figure 4.82: Heat-treated TiMn-8*

*Figures 4.81 to 4.82: SEM micrographs taken with BSD mode, EHT set at 20.0kV and the magnification of x3000 (10µm) illustrating heat-treated TiMn alloys produced with LEPUL=375.605J/cm*

TiMn alloys produced using higher LEPUL=459.072J/cm and low Mn feed rate (0.3rpm) were heat-treated to 950°C, phase segregation mechanisms occurred leading to the increase of primary dendrite sizes.

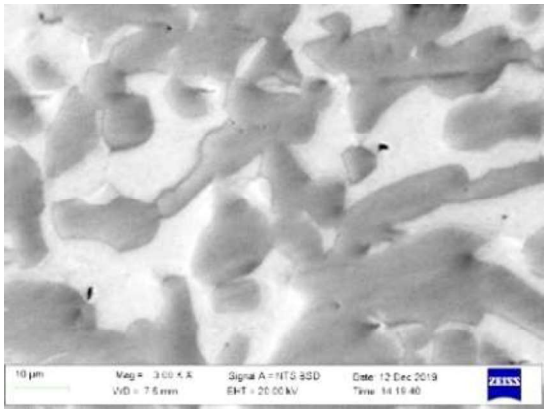

*Figure 4.83: Heat-treated TiMn-10*

Heat-treatment conducted at 1300°C on samples produced with Mn feed rate of 0.5rpm, produced microstructures with elongated α equiaxed grains (also known as blades) with extended lengths within β matrix phase as observed in Figures 4.84. Heat-treatment conducted at 950°C on samples produced with a Mn feed rate of 0.7rpm, led to precipitates undergoing the phase transformation reaction in Equation 4.1 as shown in Figure 4.85. It was observed that $Mn_{0.52}Ti_{0.48}(s)$ dissolved into β matrix at 1300°C but remained in solution in the form of MnTi after heat-treatment was conducted at 950°C as observed in Figures 4.84 and 4.85.

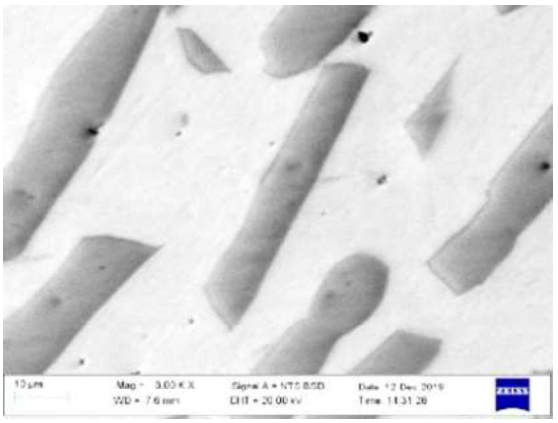

*Figure 4.84: Heat-treated TiMn-11*

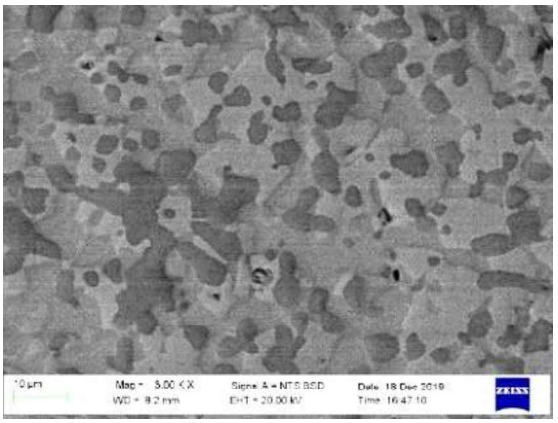

*Figure 4.85: Heat-treated TiMn-12*

*Figures 4.84 to 4.85: SEM micrographs taken with BSD mode, EHT set at 20.0kV and the magnification of x3000 (10μm) illustrating heat-treated TiMn alloys produced using LEPUL=459.072J/cm*

Heat-treated microstructures produced using LEPUL= 500.806J/cm and low Mn feed rates (0.3rpm, 0.5rpm and 0.7rpm) are displayed in Figures 4.86 to 4.88. Figure 4.86 indicates that

the microstructure underwent similar phase segregation as TiMn-10 (Figure 4.83) during heat-treatment at 950°C, which led to an increase in α dendrite sizes. Figure 4.87 displays a microstructure also heat-treated at 1300°C which comprised of α equiaxed grains within β matrix phase (Ankem *et al.,* 1989). $Mn_{0.52}Ti_{0.48}$(s) and MnTi(s) are both absent from this structure, similar to Figure 4.84 (also heat-treated at 1300°C). Figure 4.88 shows the dissolution of α dendrites into β matrix during heat-treatment of increased Mn sample at 950°.

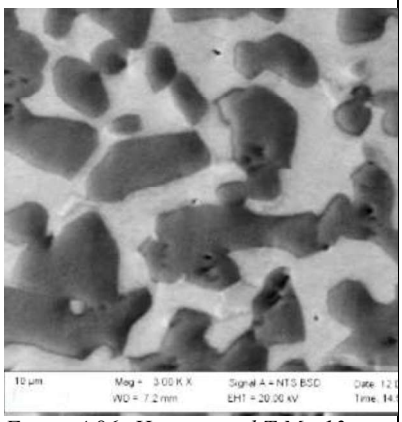

*Figure 4.86: Heat-treated TiMn-13*

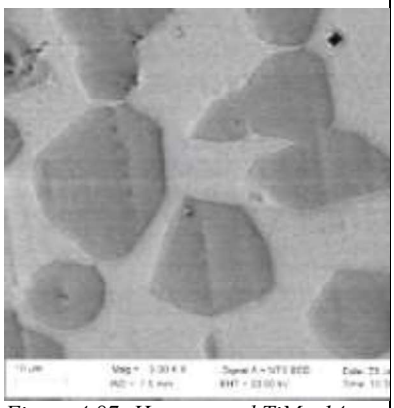

*Figure 4.87: Heat-treated TiMn-14*

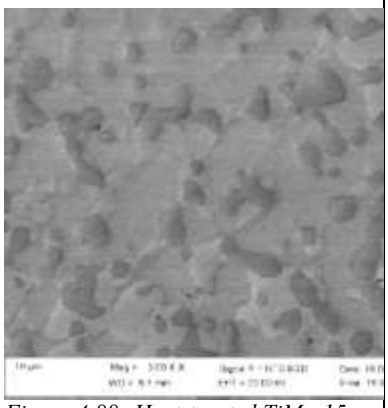

*Figure 4.88: Heat-treated TiMn-15*

*Figures 4.86 to 4.88: SEM micrographs taken with BSD mode, EHT set at 20.0kV and the magnification of x3000 (10μm) illustrating heat-treated TiMn alloys produced using LEPUL=500.806J/cm*

Heat-treated samples produced using LEPUL of 459.72J/cm and high Mn feed rates, appeared to have phase transformation behaviour like heat-treated samples displayed at Figures 4.81 and 4.82, where α dendrites were dissolved and precipitates underwent phase transformation reaction in Equation 4.1 as observed in Figures 4.89 to 4.91.

Although α dendrites dissolved during heat-treatment at high Mn, the extremely Ti rich (at%Ti>99%) dendrites, remained undissolved during heat-treatment. Mn rich $Mn_{0.52}Ti_{0.48}$(s) (at%Mn greater than 40%) precipitates also remained undissolved. These features can be observed in Figure 4.89.

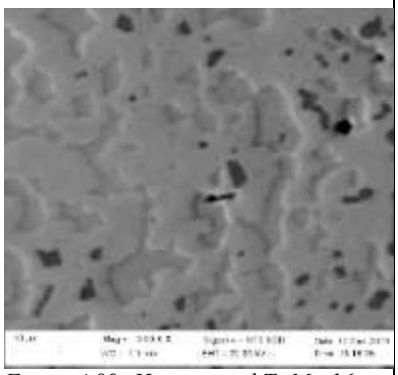

*Figure 4.89: Heat-treated Ti-Mn-16*

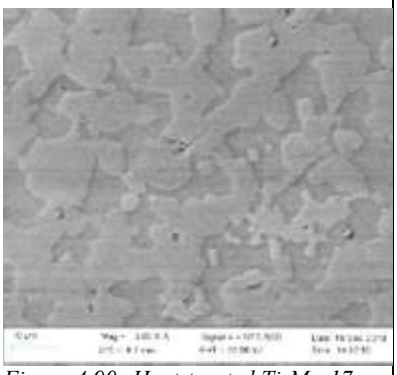

*Figure 4.90: Heat-treated Ti-Mn-17*

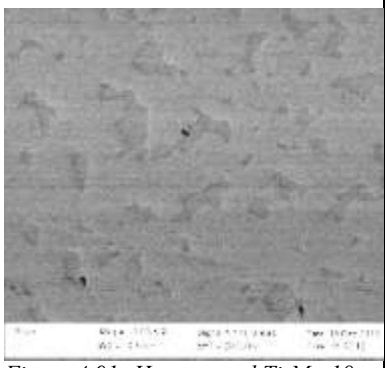

*Figure 4.91: Heat-treated Ti-Mn-18*

*Figures 4.89 to 4.91: SEM micrographs taken with BSD mode, EHT set at 20.0kV and the magnification of x3000 (10μm)illustrating heat treated Ti-Mn alloys produced using LEPUL=459.72J/cm.*

The compositions of the afore mentioned microstructural features of heat-treated TiMn alloys are given in Table 4.7. It is observed that α dendrites and equiaxed grains were Ti rich while $Mn_{0.52}Ti_{0.48}$(s) and MnTi phase were Mn rich. However, α dendrites produced at 950°C were more saturated with Ti than α equiaxed grains produced at 1300°C.

*Table 4.7: Compositions of microstructural features of heat treated TiMn alloys*

| **Description** | **BSD contrast** | **Mn at%** | **Ti at%** | **Phase** |
|---|---|---|---|---|
| Primary dendrites and Equiaxed grains | Black | 0.74 – 12.59 | 99.26 – 87.41 | α |
| Matrix | Grey | 17.56 – 22.57 | 82.44 – 77.43 | β |
| Precipitates | Light grey | 41.80 – 47.00 | 58.20 – 53.00 | $Mn_{0.52}Ti_{0.48}$ |
| Precipitates | Dark grey | 21.76 – 39.38 | 78.24 – 60.62 | MnTi |

Figures 4.92 to 4.97 illustrate the grain size increase of dendrites due to heat-treatment of builds produced at feed rate of 0.3 rpm at various LEPUL values at 950°C. α Dendrite dimensions were measured using Image J software.

SEM micrographs of as-produced structures and heat-treated samples were taken at the magnification of X700 (10-30μm). As-produced sample microstructures were captured in Figures 4.92 to 4.94 and heat-treated sample microstructures were captured from Figures 4.95 to 4.97. The grain dimensions of the elongated α-primary dendrites (ductile dendrites) which included length and width were measured. The grain dimensions of the spherical like α-primary dendrites (refined dendrites) (Arora *et al.,* 2014) which comprised of a diameter were also measured. Average values were obtained according to approximately 7 measurements of

ductile dendrite dimensions and 7 measurements of refined dendrite dimensions. The measurements are included in the captions of the SEM micrographs.

Grain dimensions increased as LEPUL increased from 417.30 J/cm to 459.072J/cm in the as-produced structures, dendrites increased in size as displayed Figures 4.92 and 4.93, from average length and width of 45,83µm and 3,54µm to 78,54µm and 5,63µm but increasing the LEPUL further to 500.806J/cm led to a reduction in dendrite lengths from 78,54µm to 35,21µm with an increase in width and refined dendrite diameters from 7,29µm to 8,33µm shown in Figure 4.94. Dendrites increased in size during heat-treatment at 950°C as observed in captions of Figures 4.95 to 4.97. The grain size dimensions appeared to be increasing with increasing LEPUL in a similar fashion to as-produced state even post heat-treatment. Dendrite lengths increased to averages of 70,49µm, 108µm and 53,53µm and widths to averages of 8,15µm, 8,80µm and 9,12µm during heat-treatment as shown in Figures 4.95, 4.96 and 4.97.

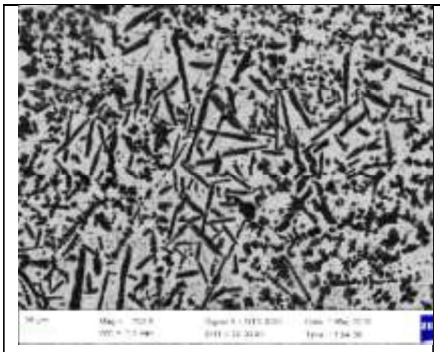

*Figure 4.92: As produced Ti-Mn-1 Average grain width 3,54µm, Average grain length 45,83µm for ductile dendrites; Average diameter 5,63µm for refined dendrites*

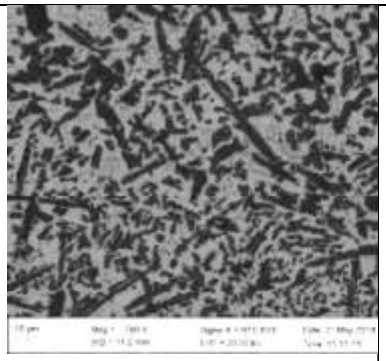

*Figure 4.93: As produced Ti-Mn-10 ; Average grain width 5,63µm, Average grain length 78,54µm for ductile dendrites; Average diameter 7,29µm for refined dendrites.*

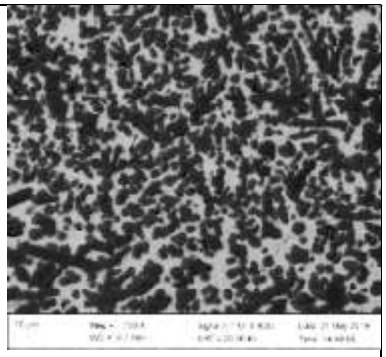

*Figure 4.94: As produced Ti-Mn-13 ; Average grain width 7,08µm, Average grain length 35,21µm for ductile dendrites; Average diameter 8,33µm for refined dendrites.*

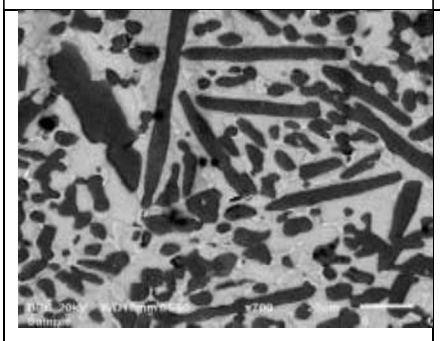

*Figure 4.95: Heat-treated Ti-Mn-1 ; Average grain width 8,15µm , Average grain length 70,49µm for ductile dendrites; Average diameter 9,51µm for refined dendrites.*

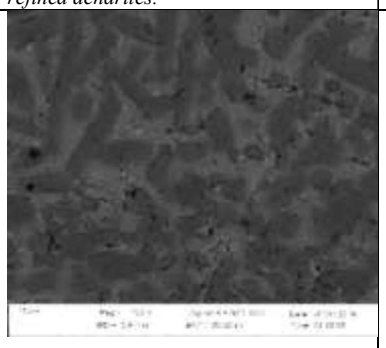

*Figure 4.96: Heat-treated Ti-Mn-10 ; Average grain width 8,80µm for ductile dendrites; Average diameter for refined dendrites 10,80µm.*

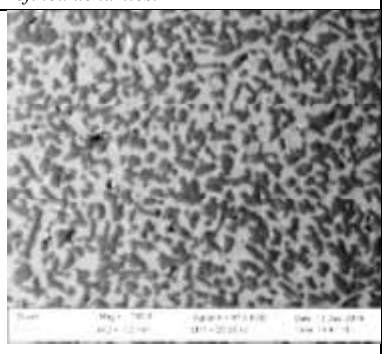

*Figure 4.97: Heat-treated Ti-Mn-13 ; Average grain width 9,12µm, Average grain length 53,53µm for ductile dendrites; Average diameter 13,82µm.*

*Figures 4.92 to 4.97: SEM micrographs displaying grain size increase in samples produced using 0.3rpm Mn feed rate due to heat treatment at 950°C where images were taken at magnification of x700 (10µm).*

### 4.2.3 X-ray diffraction (XRD) for TiMn alloys

According to EVA software α-Ti with a hexagonal crystal orientation and β-$Ti_{17}Mn_3$ with a cubic crystal orientation was produced during laser deposition of TiMn-10 and TiMn-11. The effects of increasing Mn feed rates on crystal structures were observed in TiMn-11. Figures 4.98 and 4.99 display XRD patterns generated from as-produced samples TiMn-10 and TiMn-11.

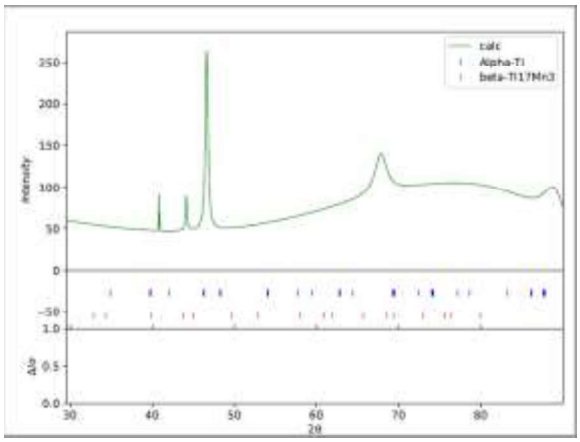


*Figure 4.98: Rietveld refinement of as produced TiMn10 XRD data*

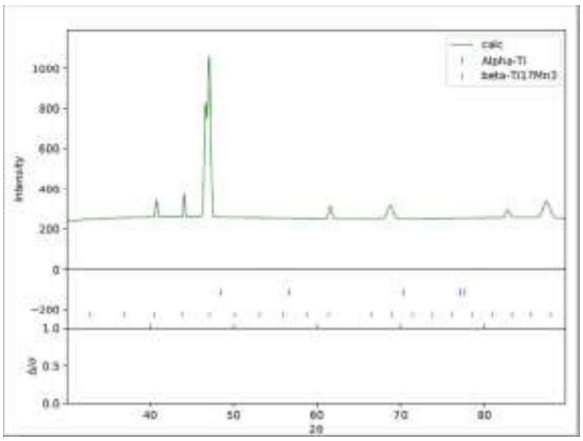


*Figure 4.99: Rietveld refinement of as produced TiMn11 XRD data*

Increasing Mn led to a reduction in hexagonal lattice parameters $a_\alpha$ and $c_\alpha$ from 4.79187Å and 6.50513Å to 3.86376Å and 1.36555Å which is displayed in Figures 4.100 and 4.101.This resulted in reduced d-spacing and reduced hexagonal lattice volume from 129.359$Å^3$ to 17.655$Å^3$ due to Mn addition.

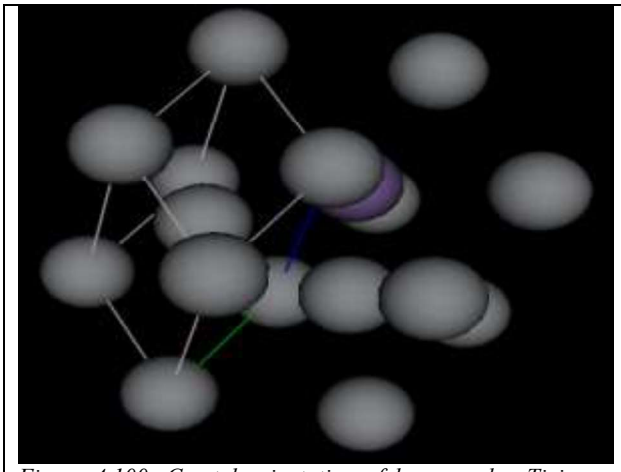

*Figure 4.100: Crystal orientation of hexagonal α-Ti in as produced TiMn10 with lattice parameters: a=4.79187Å ; c=6.50513Å*

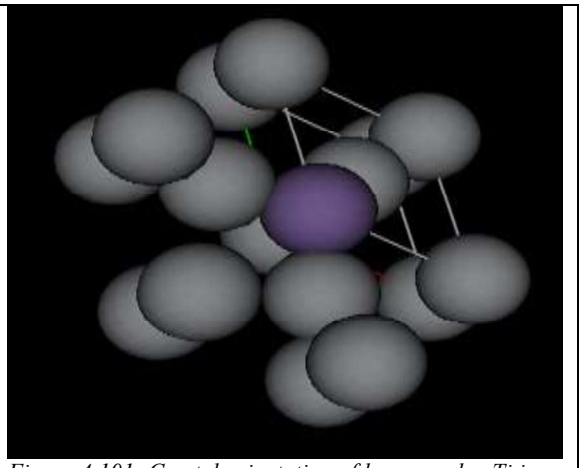

*Figure 4.101: Crystal orientation of hexagonal α-Ti in as produced TiMn11 with lattice parameters: a=3.86376Å ; c=1.36555Å*

Lattice parameter $a_\beta$ in cubic crystal orientation of β-$Ti_{17}Mn_3$ decreased from 8.24423Å to 8.23881Å shown in Figures 4.102 and 4.103. This led to a slight reduction in lattice volume from 560.339Å$^3$ to 559.234Å$^3$. The general reduction in d-spacings are displayed in Table 4.8

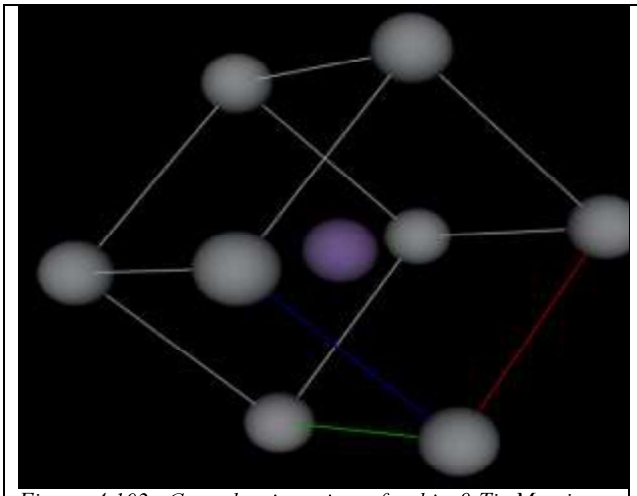

*Figure 4.102: Crystal orientation of cubic β-$Ti_{17}Mn_3$ in as produced TiMn10 with lattice parameters : a=b=c=8.24423Å*

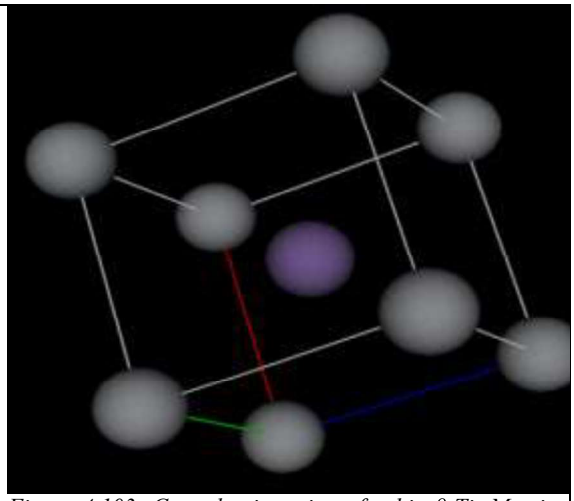

*Figure 4.103: Crystal orientation of cubic β-$Ti_{17}Mn_3$ in as produced TiMn11 with lattice parameters: a=b=c=8.23881Å*

*Table 4.8: Effects of Mn addition on d-spacing of cubic crystal orientation*

| d-spacing | TiMn-10 | TiMn-11 |
|---|---|---|
| $d_{(3\,2\,1)}$ | 2.20336Å | 2.20192Å |
| $d_{(4\,0\,0)}$ | 2.06106Å | 2.05970Å |
| $d_{(4\,1\,1)}$ | 1.94318Å | 1.94191Å |
| $d_{(4\,4\,2)}$ | 1.37404Å | 1.37313Å |

During heat-treatment of TiMn-11 at 1300°C, ω-Ti with a hexagonal orientation was produced along with β-$Ti_{0.9}Mn_{0.1}$ also with a cubic orientation which was observed in the patterns illustrated in Figures 4.104.

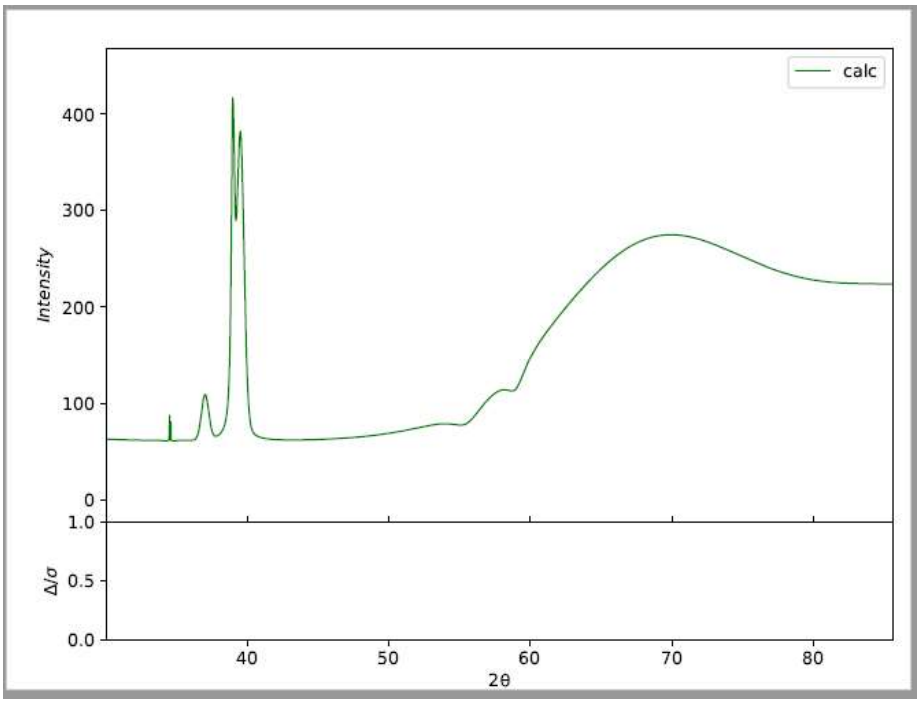


*Figure 4.104: XRD patterns for heat treated TiMn-11*

Heat-treatment also led to an increase in lattice parameter $a_\alpha$ and $c_\alpha$ of hexagonal crystal lattice to 5.60523Å and 4.06776Å -Figure 4.105. Hexagonal lattice volume increased from 17.655Å$^3$ to 110.681Å$^3$ due to heat treatment and re-orientation of the structure. Heat treatment also led to an increase in cubic crystal lattice parameter $a_\beta$ to 9.63481Å-Figure 4.106 and crystal lattice volume increased to 894.394Å$^3$.

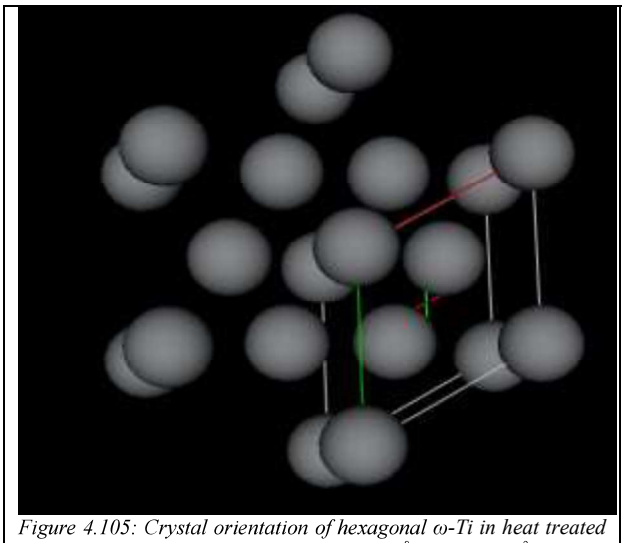

*Figure 4.105: Crystal orientation of hexagonal ω-Ti in heat treated TiMn11 with lattice parameters: a=5.60523Å; c=4.06776Å*

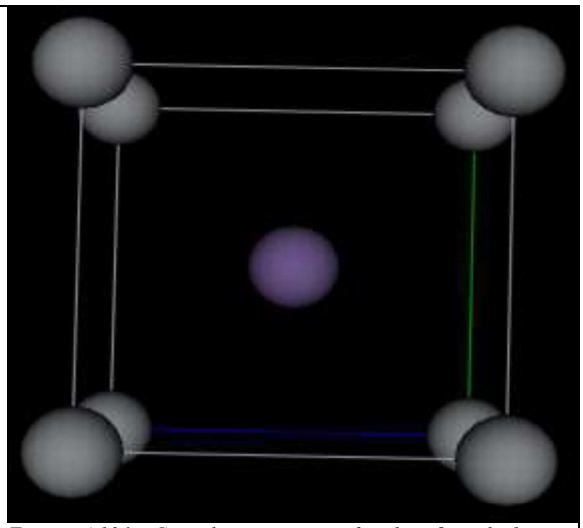

*Figure 4.106: Crystal orientation of cubic β with lattice parameters: a=b=c=9.63481Å*

Figure 4.107 and 4.108 display the peak broadening plots of as produced TiMn10 and TiMn11 while Figure 4.109 displays the peak broadening plot of heat treated TiMn11.

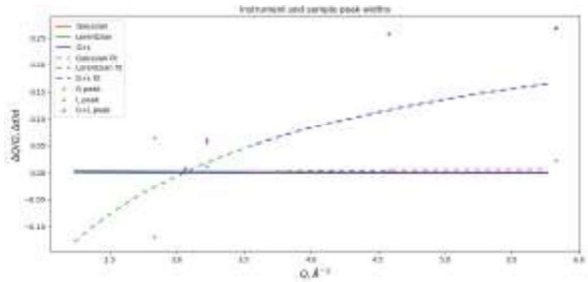

*Figure 4.107: Plot illustration peak broadening of as produced TiMn10.*

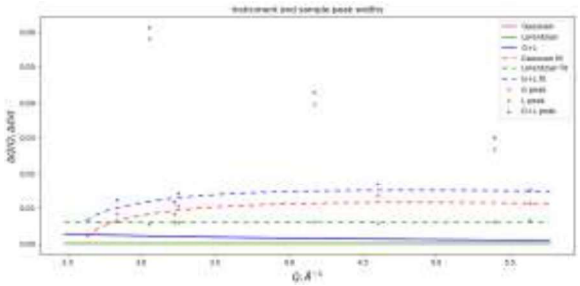

*Figure 4.108: Plot illustrating peak broadening of as produced TiMn11.*

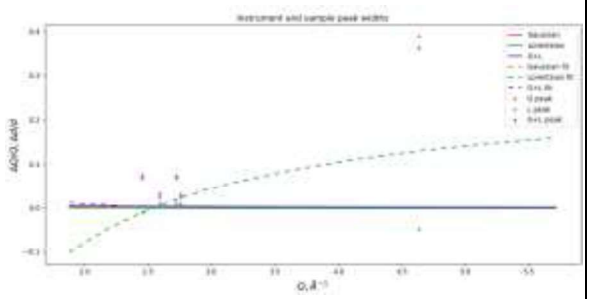

*Figure 4.109: Plot illustrating peak broadening of heat treated TiMn-11.*

Table 4.9 indicates an increase in Mn led to an increase of fractional site occupancy and a decrease in dislocation density. Heat treatment of higher Mn alloy led to reduced dislocation density. Burgers vectors for dislocations: $\frac{1}{2}a\,[1\,1\,1]$ for cubic structures; $\frac{1}{3}a\,[1\,1\,\underline{2}\,0]$ for hexagonal structures along close packed planes $(1\,0\,1)_{\beta}\,||\,(0\,0\,0\,1)_{\alpha}$ (Tong *et al.*, 2017)

*Table 4.9: dislocation densities of TiMn alloys*

| **Sample** | **Phase** | **Dislocation density (x10$^{-4}$ Å$^{-2}$)** |
|---|---|---|
| TiMn 10 as produced | α-Ti | **104,78** |
| | β-$Ti_{17}Mn_3$ | |
| TiMn 11 as produced | α-Ti | **79,58** |
| | β-$Ti_{17}Mn_3$ | |
| TiMn 11 heat treated | ω-Ti | **57,44** |
| | $Ti_{0.9}Mn_{0.1}$ | |

According to DIFFRAC.EVA, TiMn-8 comprised of $Mn_{0.52}Ti_{0.48}$ and β-$Ti_{17}Mn_3$. The broad scattering of the peaks observed in Figure 4.110 indicated the presence of possible amorphous phases or extremely fine particles.

Figure 4.110 displays XRD peaks for high Mn alloys (33.57at%Mn) -TiMn-8, where the XRD peaks corresponded with α and $Mn_{0.52}Ti_{0.48}$(s).

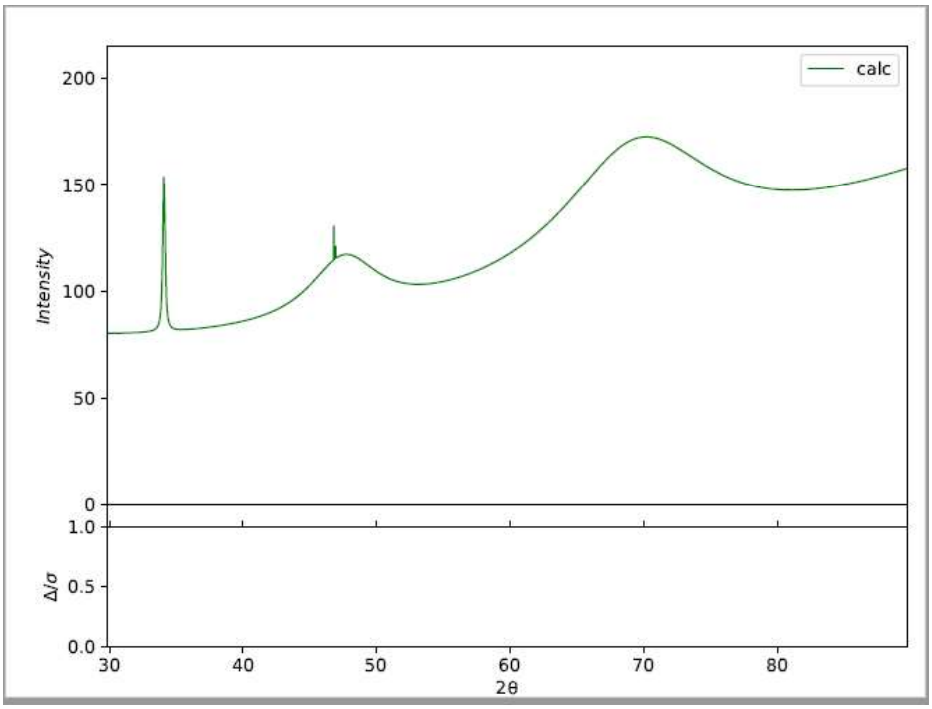


*Figure 4.110: Rietveld refinement of heat treated TiMn8*

. **4.2.4 Electron Back Scatter Diffraction of Ti-Mn alloys**

Samples which yielded the least number of post processing thermal cracks were studied further through EBSD analysis. These samples include as-produced TiMn-10 and heat-treated TiMn-11. Figures 4.111 to 4.114 alongside Table 4.10 display EBSD and SEM-BSD analysis taken on the same spot in as-produced TiMn-10. Table 4.10 alongside. Figure 4.111 display the colour coding and phase distribution of as-produced TiMn-10. It was observed that as-produced TiMn-10 comprised of 41.31vol%α phase and 58.59vol%β phase. Figure 4.112 alongside Table 4.10 displays the elemental distribution in both α and β phase in the SEM-BSD image. It was observed that α phase was Ti rich, while β phase was Mn rich. Figure 4.113 shows that various crystal orientations were detected within the β matrix phase while crystal orientations within individual α primary dendrites appeared uniform. Figure 4.114 displays different grain boundaries within the microstructure of as-produced TiMn-10. The mean, maximum and minimum grain sizes measured in equivalent circle diameter (ECD-µm) are displayed in Table 4.10. The mean grain size of the β phase is larger than that of the α phase. However, the maximum grain size of the α phase is larger than that of the β phase.

*Table 4.10: Numerical documentation of EBSD and SEM-BSD analysis of as produced TiMn-10*

| Phases | α-Ti | β-$Ti_{17}Mn_3$ |
|---|---|---|
| EBDS colour codes | | |
| Phase distribution (vol%) | 41.31 | 58.59 |
| SEM-BSD contrast | Black | Grey |
| Average Ti (at%) | 98.3 | 1.7 |
| Average Mn (at%) | 84.9 | 15.13 |
| Average grain size-ECD(µm) | 6.13 | 7.51 |
| Maximum grain size-ECD(µm) | 24.33 | 19.59 |
| Minimum grain size- ECD(µm) | 3.09 | 3.09 |
| Microstructural Features | Dendrites | matrix |

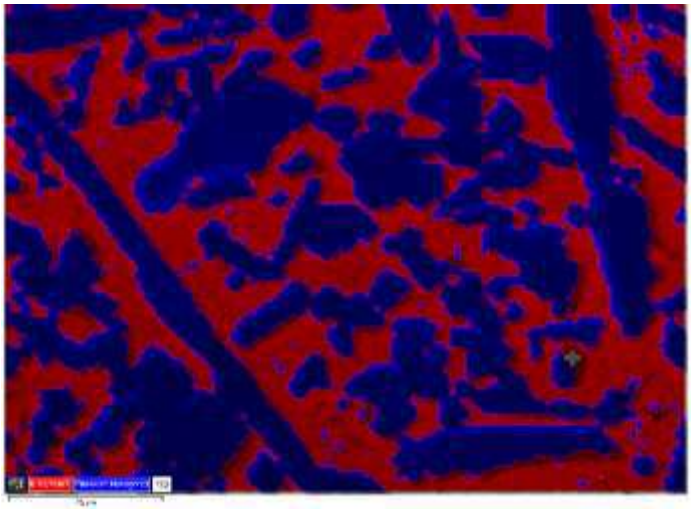

*Figure 4.111: Phase distribution of β and α phases*

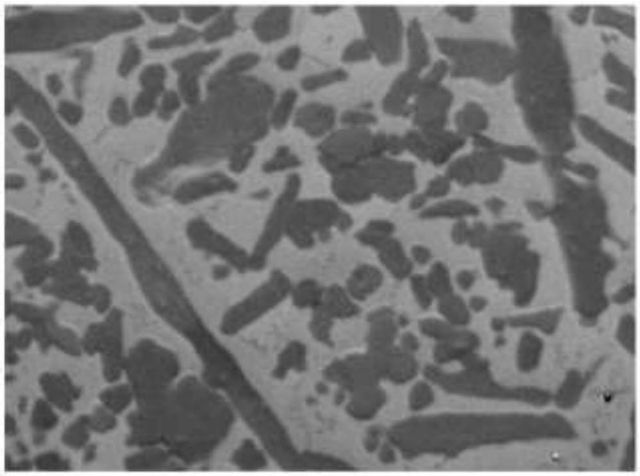

*Figure 4.112: Backscatter diffraction Scanning Electron Micrograph (BSD-SEM) image displaying elemental distribution*

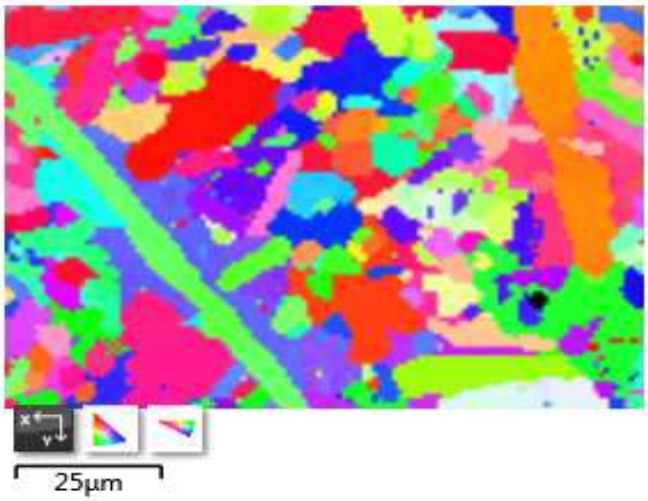


*Figure 4.113: Inverse Polar Figure-Z (IPF-Z) displaying crystal orientation of different grains relative to z-axis*

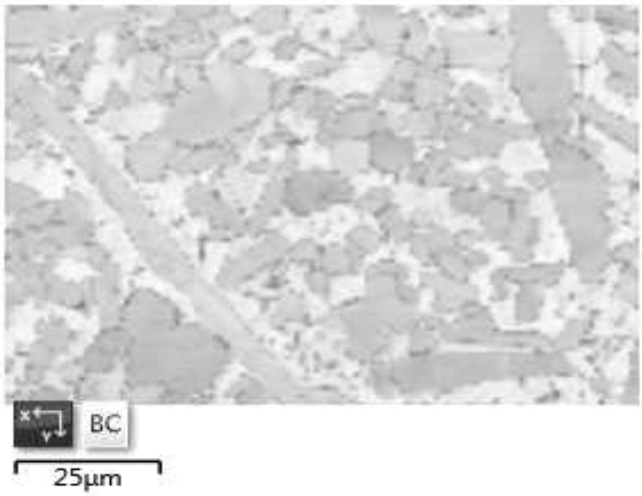


*Figure 4.114: Band contrast image displaying grain boundaries.*

*Figure 4.111 to 4.114: Electron Backscatter Diffraction (EBSD) images of as produced TiMn-10*

Table 4.11 alongside Figures 4.115 to 4.118 display EBSD and SEM-BSD analysis of heat-treated TiMn-11 numerically and visually. The colour coding and phase distribution of heat treated TiMn-11 are displayed in Table 4.11 and Figure 4.115 where it was observed that heat-treated TiMn-11 comprised of 40.47vol%ω+α and 59.51vol%β phase. Figure 4.116 depicts the elemental distribution of the same spot which was captured in the SEM-BSD where the compositions of each phase are shown in Table 4.11. It was observed that both ω+αTi and β-$Ti_{0.85}Mn_{0.15}$ phase had increased Mn. In Figure 4.117 it was observed that the crystal orientations of the β matrix phase grains were generally more uniform, while the crystal orientations of individual equiaxed ω+α grains were uniform but differed from one grain to

another. Grain boundaries of this microstructure are depicted in brand contrast image in Figure 4.118 and it is seen in Table 4.11 that there had been a significant increase in grain size compared to as produced TiMn-10 since in grain sizes averages and maximum grain sizes have increased. However, in this microstructure the hexagonal ω+α grains were larger than the β grains.

*Table 4.11: Numerical illustration of EBSD and SEM-BSD analysis of heated treated TiMn-11*

| Phases | ω -Ti | β-$Ti_{0.85}Mn_{0.15}$ |
|---|---|---|
| EBDS colour codes | | |
| Phase distribution (vol%) | 40.47 | 59.51 |
| SEM-BSD contrast | Black | Grey |
| Average Ti (at%) | 87.41 | 79.05 |
| Average Mn (at%) | 12.59 | 20.95 |
| Average grain size-ECD(µm) | 15.03 | 12.80 |
| Maximum grain size-ECD(µm) | 35.86 | 25.95 |
| Minimum grain size- ECD(µm) | 3.08 | 3.64 |
| Microstructural Features | Dendrites | matrix |

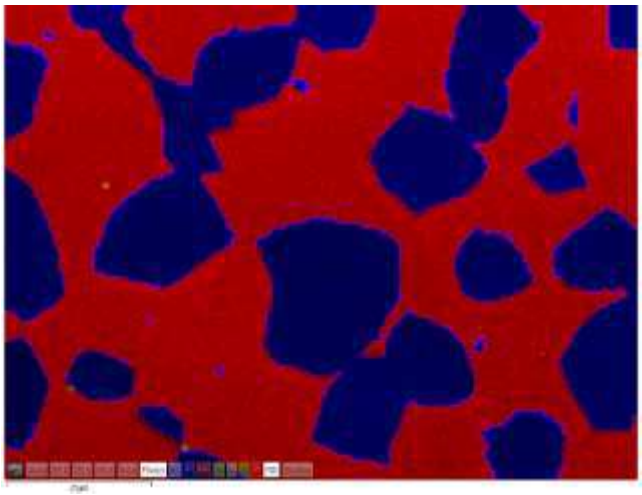

*Figure 4.115: phase distribution of ω and β*

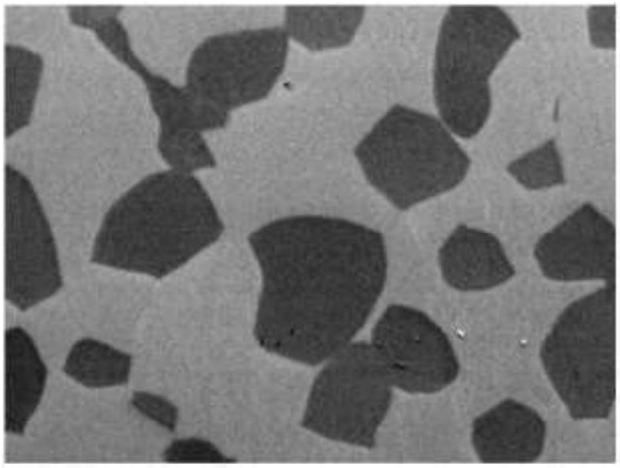

*Figure 4.116: SEM-BSD image displaying elemental distribution*

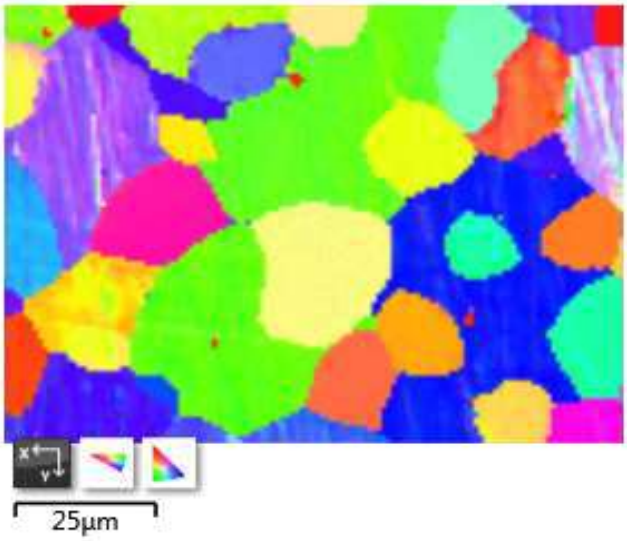


*Figure 4.117: IPF-Z displaying crystal orientations of different grains*

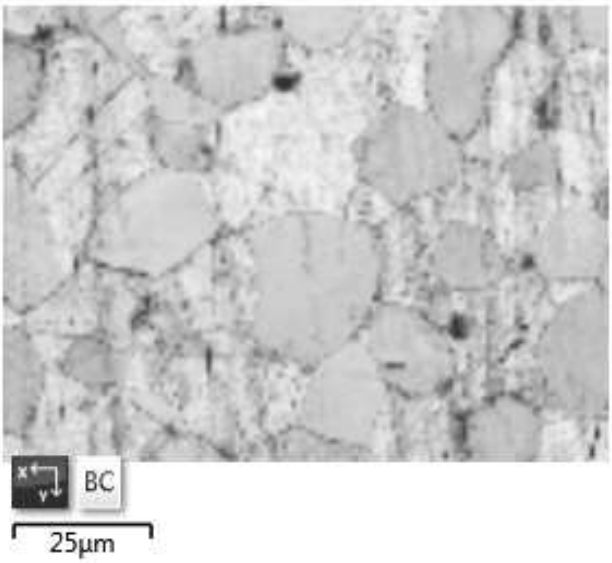


*Figure 4.118: Band contrast image displaying different grain boundaries of heat treated TiMn-11.*

*Figure 4.115 to 4.118: EBSD images of heat-treated TiMn-11*

*Pole Figures*

The highest number of crystal orientations of each phase in both as-produced TiMn-10 and heat-treated TiMn-11 are illustrated in pole figures on standard projections for both cubic and hexagonal systems displayed in Figures 4.119 to 4.122 where the Z-axis comes out of the page. Crystal orientations for cubic β-$Ti_{17}Mn_3$ phase in as-produced TiMn-10 are illustrated in {1 1 0} pole figure in Figure 4.119 where 252 orientations were counted using Image J software. Crystal orientations for hexagonal α+ω-Ti are depicted in $\{1\ 0\ \underline{1}\ 0\}$ pole figure in Figure 4.120 where 306 orientations were counted. Figure 4.121 shows that the crystal orientations detected in cubic β-$Ti_{0.85}Mn_{0.15}$ phase in heat-treated TiMn-11 were more concentrated in certain regions of the stereographic projection for a cubic system and 140 orientations were counted, while Figure 4.122 shows that the orientation detected for the hexagonal ω+α-Ti phase were fewer than in Figure 4.120 and 105 orientations were counted. These findings are also confirmed by observations made in the inverse polar figures in Figures 4.113 and 4.117.

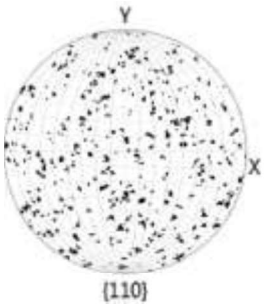


*Figure 4.119: 252 crystal orientations of β phase in as produced TiMn-10 detected by EBSD on {1 1 0} standard projection of cubic system*

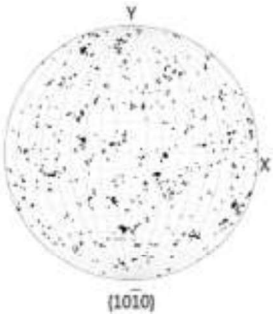


*Figure 4.120: 306 crystal orientations of α phase in as produced TiMn-10 detected by EBSD on $\{10\underline{1}0\}$ standard projection of hexagonal system*




*Figure 4.121: 140 crystal orientations of β phase in heat treated TiMn-11 detected by EBSD on {1 1 0} standard projection of cubic system*

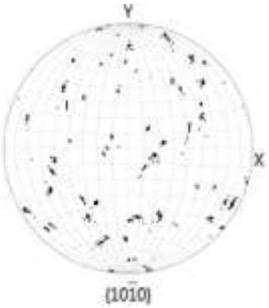


*Figure 4.122: 105 crystal orientations of ω phase in heat treated TiMn-11 detected by EBSD on $\{10\underline{1}0\}$ standard projection of hexagonal system.*

*Figure 6.119 to 4.122: Pole figures displaying crystal orientations of phases*

*Texture measurements*

Texture measurements of phases were measured according to their crystal orientations and outcomes were displayed on standard stereographic projections for cubic and hexagonal systems as shown in Figure 4.123 to 4.126. The texture measurements were carried out in multiples of uniform distribution (MUD)(Creuziger *et al*., 2014). Texture measurements for β-$Ti_{17}Mn_3$ phase in as-produced TiMn-10 are shown in Figure 4.123 where the maximum MUD was 8.52 and the distribution of texture on detected crystal orientations is displayed in standard {1 0 0} cubic system. Figure 4.124 indicates that α-Ti hexagonal orientations in as-produced TiMn-10 had higher texture measurements of up to 15.54MUD as depicted in the {0 0 0 1} standard hexagonal system. Figure 4.125 illustrates the texture measurements and distribution of β-Ti17Mn3 phase in heat-treated TiMn-11, where higher texture of 11.12MUD was detected in this alloy compared to β-$Ti_{17}Mn_3$ phase in as-produced TiMn-10. Figure 4.125 also indicates that higher texture measurements as high as 26.61MUD were also detected on hexagonal ω+α-Ti orientation compared to those in as-produced TiMn-10.

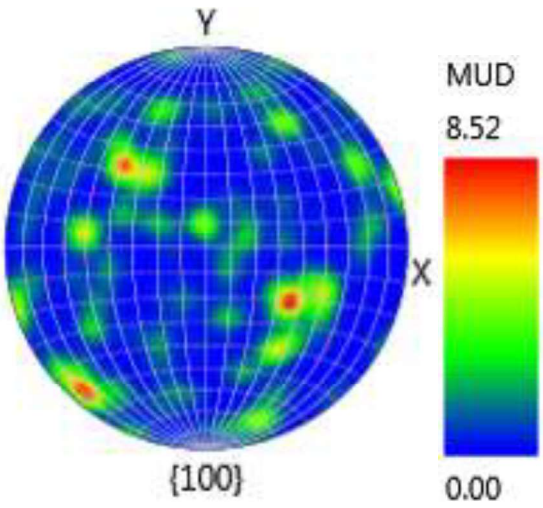


*Figure 4.123:texture distribution of β phase in as produced TiMn-10 detected by EBSD on {1 0 0} standard projection of cubic system*

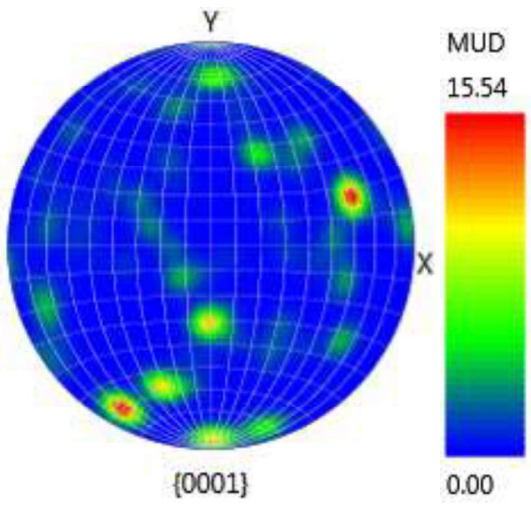


*Figure 4.124:texture distribution of α - phase in as produced TiMn-10 detected by EBSD on {0 0 0 1} standard projection of hexagonal system*

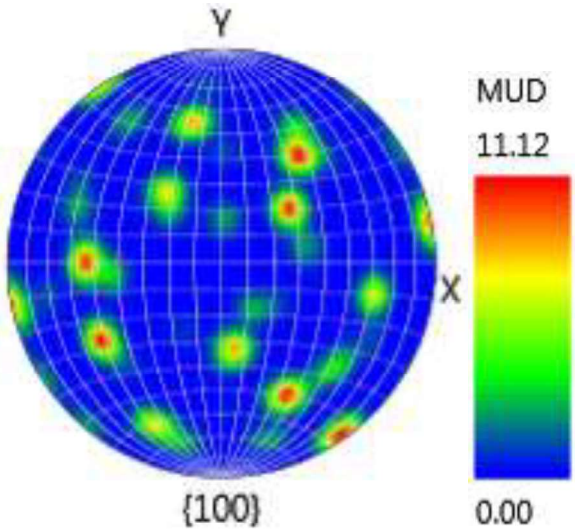


*Figure 4.125:texture distribution of β phase in heat-treated TiMn-11 detected by EBSD on {1 0 0} standard projection of cubic system*

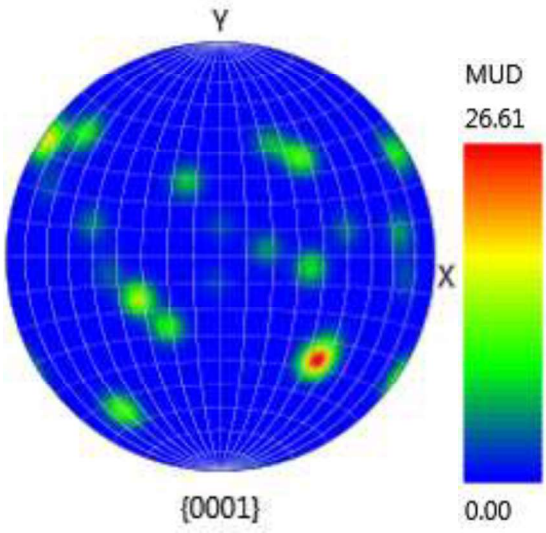


*Figure 4.126: texture distribution of ω - phase in heat-treated TiMn-11 detected by EBSD on {0 0 0 1} standard projection of hexagonal system.*

*Figure 4.123 to 4.126: distribution of crystal textures of various orientations detected measured in MUD for TiMn alloys*

Figure 4.127 displays the alternate co-ordinate system used to describe hexagonal orientations in both XRD and EBSD systems which accommodates 3 co-ordinates.

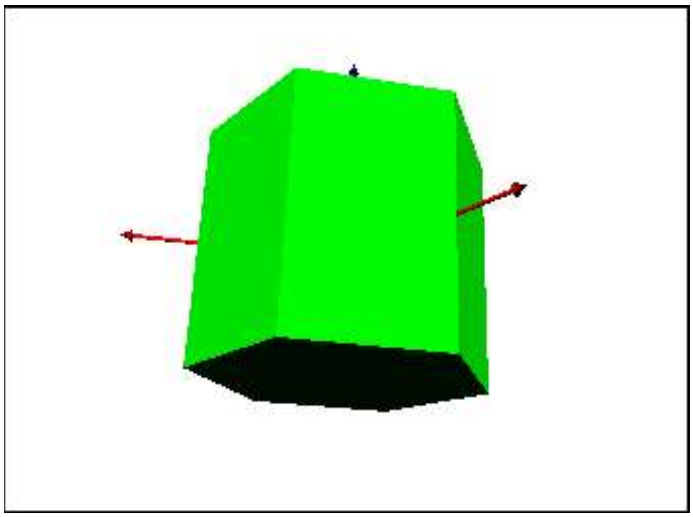

*Figure 4.127: Coordinate system of HCP crystal*

After the microstructures were studied, the mechanical properties were determined by studying microhardness behaviour, crack lengths and calculations of fracture stress.

### 4.2.5 Microhardness of TiMn Alloys

Microhardness of as-produced Ti-Mn alloys:

The effects of altering LEPUL and Mn feed rates on microhardness of the produced structures are displayed in a line graph in Figure 4.128. The microhardness of TiMn alloys produced with LEPUL=417.730J/cm ranged from 531,7739 HV to 667,206 HV and have an average of 601,344HV. Increasing LEPUL to 375.605 J/cm led to microhardness values increase to a range from 582,044HV to 690,7684HV and an average of 641,534HV. Increasing LEPUL to 459.072J/cm led to microhardness values dropping to a range from 506,661HV to 687,737HV with an average of 580,216HV. As the LEPUL was increased further to 500.806 J/cm, microhardness reduced to values ranging from 509,9273HV to 573,993HV with an average value of 535,852HV. This behaviour was observed in the graph (Figure 4.128) where it could also be seen that lower Mn alloys had lower hardness values compared to higher Mn alloys. Alloys produced using a Mn feed rate of 0.5rpm yielded the lowest average microhardness value of 516,120HV which had the highest volume proportion of β phase (67.51%β*)* and absent $Mn_{0.52}Ti_{0.48}$(s). Using high Mn feed rates of 1.3rpm yielded microhardness values with an average value of 681,903HV, the sample had the highest volume proportion of $Mn_{0.52}Ti_{0.48}$(s) (63.61% $Mn_{0.52}Ti_{0.48}$). It was observed that the microhardness increased with increasing Mn

feed rates except for build produced with Mn feed rates of 0.5rpm. Microhardness patterns are illustrated in APPENDIX A.

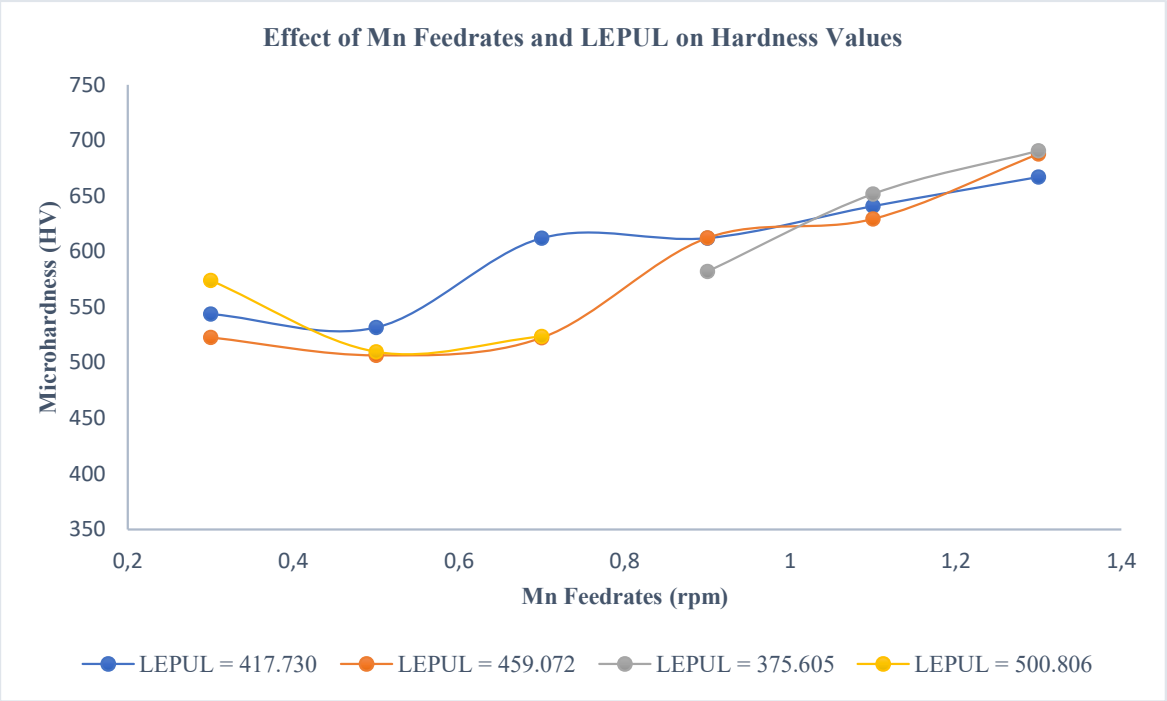


*Figure 4.128: Microhardness of as produced TiMn alloys*

Microhardness of heat-treated TiMn alloys:

The effects of altering Mn feed rates and LEPUL on microhardness for heat-treated samples is displayed in the plot in Figure 4.129. Heat-treated microstructures produced with LEPUL of 417.730J/cm had microhardness values ranging from 583,03HV to 807,64HV with a general average of 675,53HV. Microhardness values increased as LEPUL was decreased to 375.072J/cm at high Mn feed rates, to values ranging from 620,93HV to 711,95HV with a general average of 666,44HV. When LEPUL was increased to 459.072J/cm, hardness values ranged from 509,49HV to 686,57HV with a general average of 602,49HV. Lastly, it was also observed that increasing the LEPUL further to 500.806J/cm at low Mn feed rates, yielded microhardness values range from 511,82HV to 578,21HV, with an average of 549,46HV. Heat-treated samples produced with Mn feed rate (0.5rpm) yielded the lowest average microhardness value of 577,73HV among all Mn feed rates studied. Microhardness generally increases with increasing Mn feed rates too.

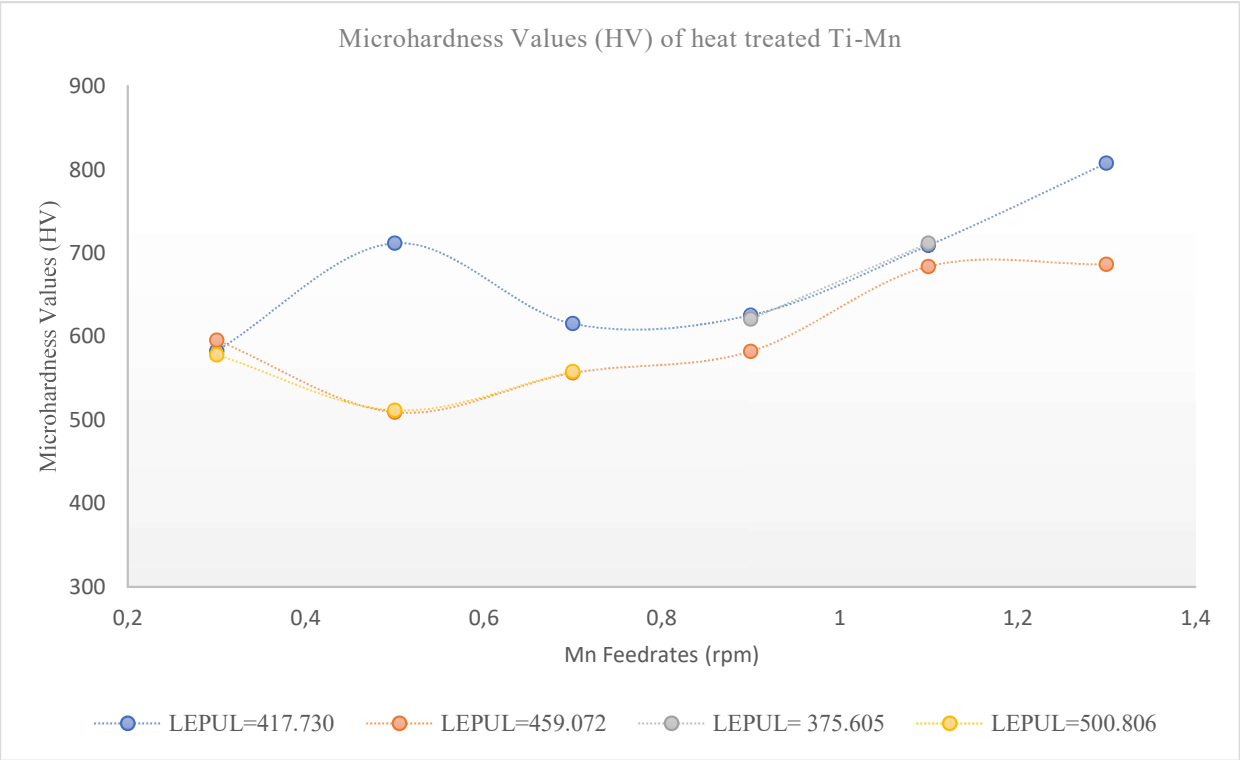


*Figure 4.129: Microhardness of heat treated TiMn alloys*

### 4.2.6 Fracture stress of TiMn alloys

As-produced sample TiMn-10 (produced using 0.3rpm at LEPUL=459.072J/cm) had the lowest number of post processing thermal cracks with low average crack length displayed in Figure 4.130. According to numerical calculations (Varin *et al.,* 2001; Voice *et al.,* 2005), the fracture stress of TiMn-10 was $1087.72\ MPa$. Heat-treated TiMn-11 yielded the highest fracture stress since the sample was crack free as observed in Figure 4.131. These samples were studied further to understand the properties contributing to their mechanical behaviour which allowed them to be resistant to failure due to thermal residual stresses.

Figure 4.132 displays the crack lengths of heat treated TiMn-8, which was produced using high Mn and low LEPUL= 375.605J/cm. The crack lengths of sample TiMn-8 were large and accounted for the low calculated fracture stress value of $178.936\ MPa$.

*Figures 4.130 to 4.132: Optical micrographs of crack lengths and calculated ductility*



*Figure 4.130:Optical micrograph of crack length of as produced Ti-Mn-10.*

Average crack length (a)= 5.448 x$10^{-6}$ m ; fracture toughness= 4.50 MPa$\sqrt{m}$

$\sigma_f = \frac{K_{IC}}{\sqrt{\pi a}} = 1087.72\ MPa$

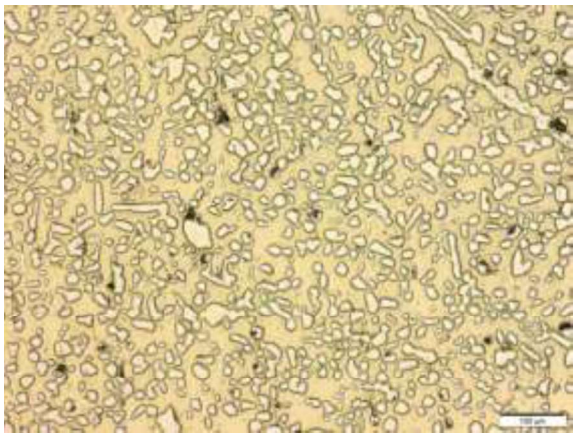

*Figure 4.131: Optical micrograph of crack length of heat treated Ti-Mn-11.*

Ductility is reasonable since the build is crack free.



*Figure 4.132: TiMn-8 contains largest phase proportion of $Mn_{0.52}Ti_{0.48}$(s) in Ti-Mn alloys and is the most brittle TiMn alloys and has lowest calculated ductility.*

Average crack length (a)= 201.3175 x$10^{-6}$ m ; fracture toughness= 4.50 MPa$\sqrt{m}$

$\sigma_f = \frac{K_{IC}}{\sqrt{\pi a}} = 178.936\ MPa$

### 4.2.7 Mechanical Properties of Binary TiMn alloys according to Nanoindentation

Nanoindentations were carried out on dendrites and matrix phase of as produced TiMn-10. The average measured indentation hardness $H_{IT}$ of α dendrites was 3013.2MPa and Vicker's hardness was calculated to be 279.05HV. Maximum measured indentation depth was 1147.67nm. The measured indentation Young's Modulus $E_{IT}$ was 640,88GPa, calculated plane strain Young's modulus E* was 704.27GPa and measured stiffness was 2.833mN/m. The

calculated indentation strain $\varepsilon_{IT}$ was 0.220376881 (22.0377%) which led to calculated yield stress of 141 235,1358MPa.

The average measured indentation hardness $H_{IT}$ of the β matrix was 103280MPa and Vicker's hardness was calculated to be 9565.2HV. The maximum measured indentation depth was 359.04nm. The measured indentation elastic modulus $E_{IT}$ was 590.31GPa, calculated plane strain Young's modulus E* was 648.69GPa and measured stiffness was 0.4774nN/nm. The calculated indentation strain $\varepsilon_{IT}$ was 0.376842105 (37.6842%) which led to calculated yield stress of 222 453,6627MPa. Curves obtained from nanoindentations depicting the relationship between indentation depth and load in as produced TiMn10 are illustrated in Figure 4.133.

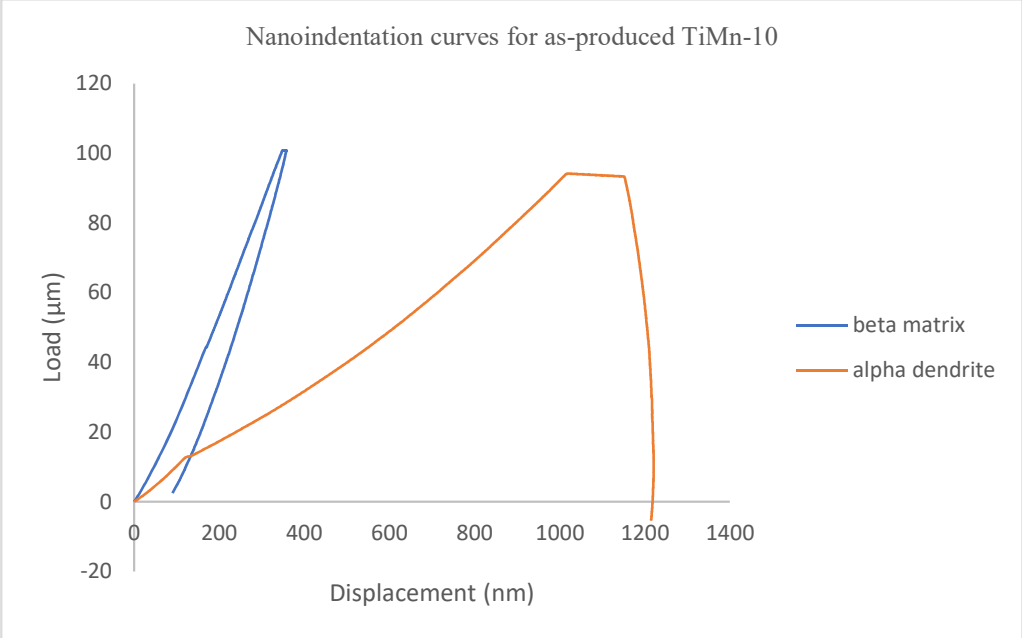


*Figure 4.133: Relationship between indentation depth and load of β and α obtained from nanoindentation.*

Indentations were also carried out on α+ω equiaxed grains and matrix phase of heat treated TiMn11. The average measured indentation hardness $H_{IT}$ of α+ω equi axed was 3718.0MPa and Vicker's hardness was calculated to be 344.33HV. Maximum measured indentation depth was 1110.30nm. The measured indentation elastic modulus $E_{IT}$ was 203.85GPa, calculated plane strain elastic modulus E* was 224.01GPa and measured stiffness was 1.1337mN/m. The calculated indentation strain $\varepsilon_{IT}$ was 0.169461782 (16.9462%) which led to calculated yield stress of 34 544.78MPa.

The average measured indentation hardness $H_{IT}$ of the β matrix was 8762.0MPa and Vicker's hardness was calculated to be 811.45HV. The maximum measured indentation depth was

925.67nm. The measured indentation elastic modulus $E_{IT}$ was 84 GPa , calculated plane strain elastic modulus E* was 93 GPa and measured stiffness was 0.3374nN/nm. The calculated indentation strain $\varepsilon_{IT}$ was 0.196198067 (19.6198%) which led to calculated yield stress of 16 529.491MPa. Curves obtained from nanoindentations depicting the relationship between indentation depth and load for heat treated TiMn11 are illustrated in Figure 4.134.

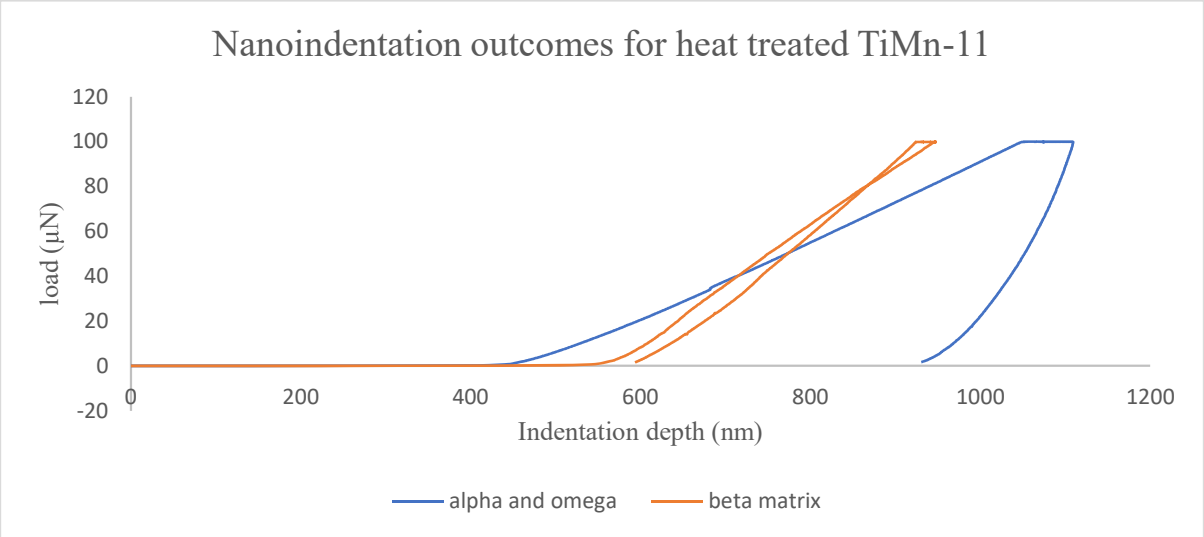


*Figure 4.134: Relationship between indentation depth and load of β and α+ω obtained from nanoindentation.*

### 4.2.8 Thermogravimetric Analysis

Figure 4.135 displays mass loss due oxidation as a function of time. It was observed that as-produced TiMn-10 (labelled SAMPLE-AB on thermograph) underwent initial mass loss in the first 50 minutes at a rate of 0.010625mg/min. This mass loss was followed by mass gain which continued at a rate of 0.01449195mg/min for 90 minutes. The mass of the sample remained unchanged for 115 minutes. Mass gain increased to rates of 0,011333mg/min for the last 85 minutes of the experiment.

As-produced TiMn-11 (labelled SAMPLE-B on thermograph), which had increased Mn, underwent initial mass loss in the first 57 minutes at a rate of 0.004857139 mg/min. This mass loss was followed by mass gain which continued at a rate of 0.0185455mg/min until 138 minutes into the experiment. The mass loss was followed by a minimal mass loss at rate of 0.002236836mg/min, oxidation at this rate continued until 250 minutes into the experiment. These minimal mass loss rates were followed by increased mass gain rates at 0,017000 mg/min and mass gain continued at this rate until the end of the experiment which took a total of 340 minutes.

Heat-treated TiMn-11 (labelled SAMPLE-A on thermograph) underwent initial mass loss in the first 45 minutes at a rate of 0.01457159mg/min. This mass loss was followed by mass gain which continued at a rate of 0.0193500mg/min until 140 minutes into the experiment. The mass gain was followed by a drastic reduction in mass gain rates and the sample mass remained constant until 255 minutes into the experiment. These reduced mass change rates were followed by increased mass gain rates at 0,013852mg/min and mass gain continued at this rate until the end of the experiment which took a total of 340 minutes.

Parabolic rate constants $(k = \frac{\Delta m}{\sqrt{t}})$ for isothermal oxidation for as-produced TiMn-10 was 0.075926mg/min$^{1/2}$ , 0.124735mg/min$^{1/2}$ for as-produced TiMn-11 and 0.111177mg/min$^{1/2}$ for heat treated TiMn-11. The drastic mass gain rate reduction between 140 minutes and 255 minutes in as-produced TiMn-10 and both as-produced and heat treated TiMn-11 were indicative of the formation of a protective oxide film prior to that oxidation stage.

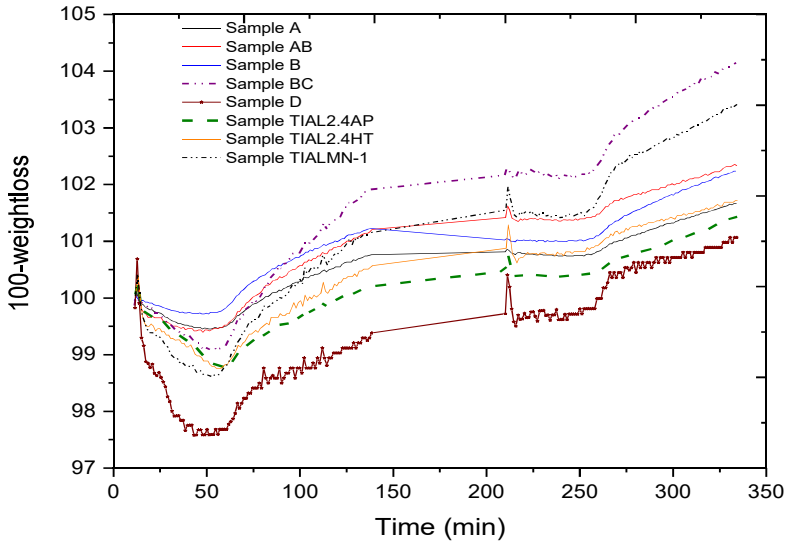


*Figure 4.135: Mass loss as a function of time for as-produced TiMn-10 (SAMPLE AB), as-produced TiMn-11 (SAMPLE B) and heat-treated TiMn-11 (SAMPLE A) oxidation behaviour.*

Figure 4.136 display the effects of temperature on mass loss and gain during oxidation of selected TiMn alloys. It was observed that as-produced TiMn experienced the lowest mass losses before 600°C and gained the most mass between 600°C and 900°C. As-produced TiMn-10 and heat treated TiMn11 oxidised in a similar fashion with respect to temperature but had higher mass losses and lower mass gains compared to as-produced TiMn-11 respectfully.

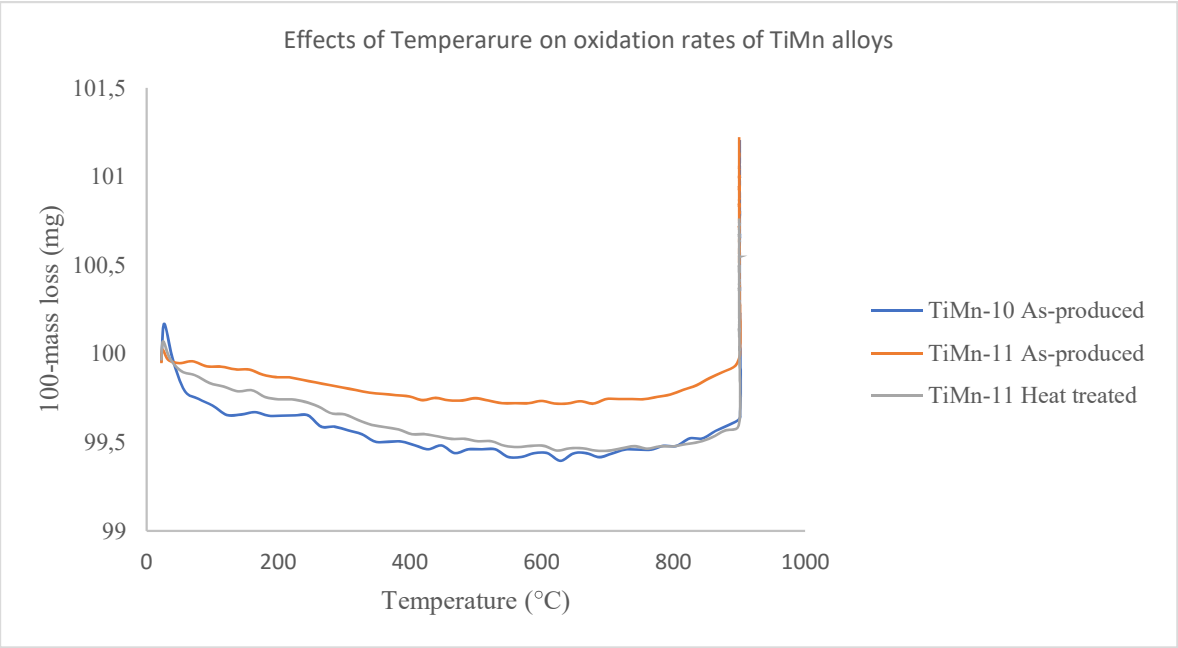


*Figure 4.136: Mass loss as a function of temperature for TiMn alloys*

The thickness of the oxide film of as-produced TiMn-10 ranged from 44.64µm to 111.06 µm as observed in Figure 4.137. Figure 4.138 displays various layers of the oxide scale. The outer layer was comprised of $MnO_2$ (light grey SEM-BSD contrast) with a thickness ranging from approximately 3.066µm to 3.485µm. The first inner layer right below the outer layer was comprised of $TiO_2$ (grey SEM-BSD contrast) with a thickness of approximately 27.61µm. This layer was porous and contained large pores which were outlined with $Mn_3Ti_3O$.The layer closest to the surface of the bulk sample was also comprised of porous $TiO_2$ with smaller pores which did not have $Mn_3Ti_3O$ and had a thickness of approximately 32.37µm. The microstructure beneath the oxide film did not change from being oxidised as displayed in Figure 4.139. The EDX displaying phase detected in the oxide scale are demonstrated in Figures 4.140 to 4.142. These phases were confirmed using XRD.

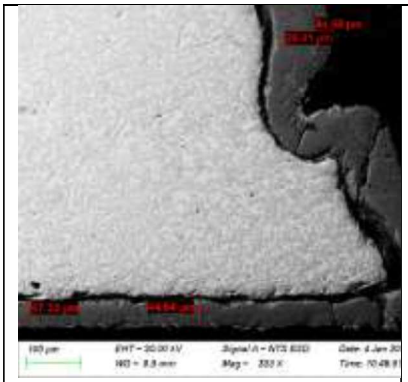

*Figure 4.137:Oxide scale thickness of as-produced TiMn-10.*

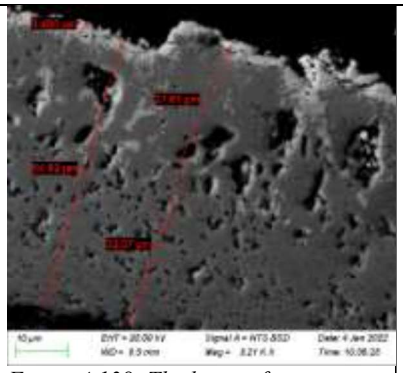

*Figure 4.138: Thickness of various layers of oxide scale of as-produced TiMn-10*

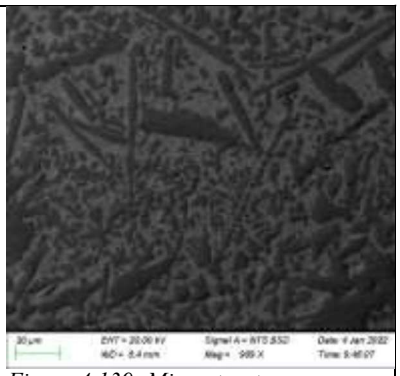

*Figure 4.139: Microstructure underneath oxide scale of oxidised as-produced TiMn-10.*

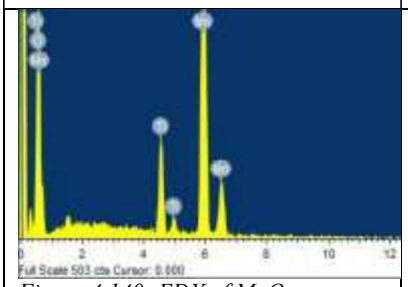

*Figure 4.140: EDX of $MnO_2$ - 69.20(at%O); 26.36(at%Mn); 4.44(at%Ti)*

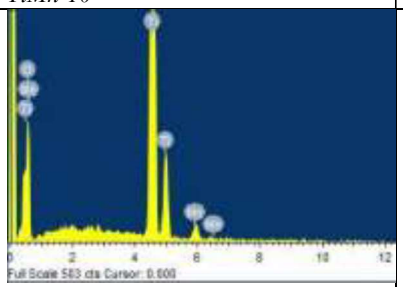

*Figure 4.141: EDX of $TiO_2$- 72.01(at%O); 27.19(at%Ti); 0.80(at%Mn)*

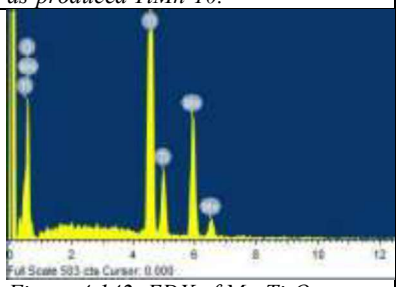

*Figure 4.142: EDX of $Mn_3Ti_3O$- 68.28(at%O); 23.06(at%Ti); 8.66(at%Mn)*

The thickness of the oxide film of as-produced TiMn-11 ranged from 30.96µm to 43.86µm as observed in Figure 4.143. Figure 4.144 displays various layers of the oxide scale. The outer layer was comprised of $TiO_2$ with a thickness of approximately 10.65µm. This layer was porous and contained large pores which were outlined with $Mn_3Ti_3O$. The layer closest to the surface of the bulk sample was also comprised of porous $TiO_2$ with smaller pores which did not have $Mn_3Ti_3O$ and had a thickness of approximately 7.969 µm. The microstructure beneath the oxide film (displayed in Figure 4.145) had the precipitation of $Mn_3Ti_3O$ on α grain boundaries approximately 107.7µm within the bulk sample from the base of the oxide film as displayed in Figure 4.145.

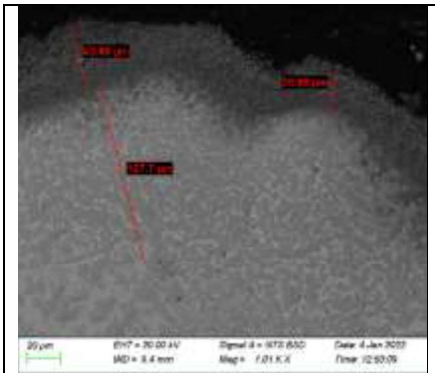

*Figure 4.143: Oxide scale thickness of as-produced TiMn-11.*

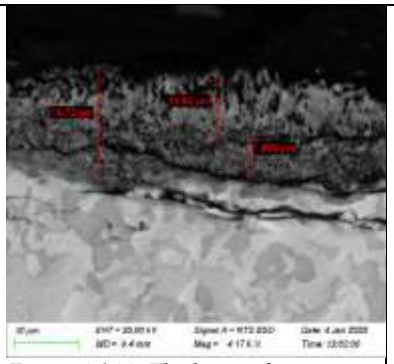

*Figure 4.144: Thickness of various layers of oxide scale of as-produced TiMn-11*

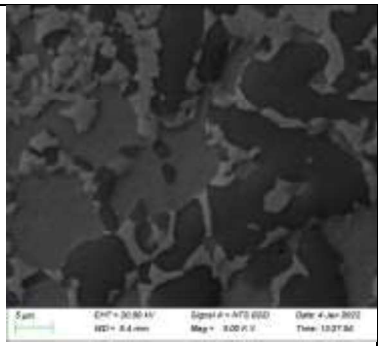

*Figure 4.145: Microstructure underneath oxide scale of oxidised as-produced TiMn-11.*

The thickness of the oxide film of heat-treated TiMn-11 ranged from 36.30µm to 105.7µm as observed in Figure 4.146. Figure 4.147 displays various layers of the oxide scale. The outer layer was comprised of $MnO_2$ with a thickness of 3.154µm. The first inner layer right below the outer layer was comprised of $TiO_2$ with a thickness of approximately 43.35µm. This layer was porous and contained large pores which were outlined with $Mn_3Ti_3O$. The layer closest to the surface of the bulk sample was also comprised of porous $TiO_2$ with smaller pores which did not have $Mn_3Ti_3O$ and had a thickness of approximately 24.90µm. The microstructure beneath the oxide film did not change from being oxidised as displayed in Figure 4.148. The microstructure beneath the oxide film (displayed in Figure 4.148) had the precipitation of $Mn_3Ti_3O$ on α grain boundaries. $Ti(NO_3)_4$ (composition in Figure 4.149) can also be observed on the microstructure within the sample as displayed in Figure 4.149.

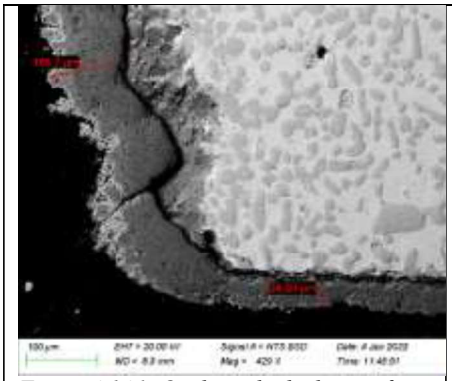

*Figure 4.146: Oxide scale thickness of heat-treated TiMn-11.*

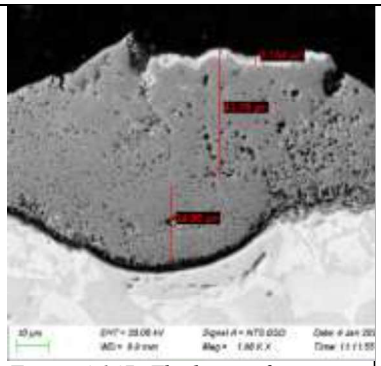

*Figure 4.147: Thickness of various layers of oxide scale of heat-treated TiMn-11*

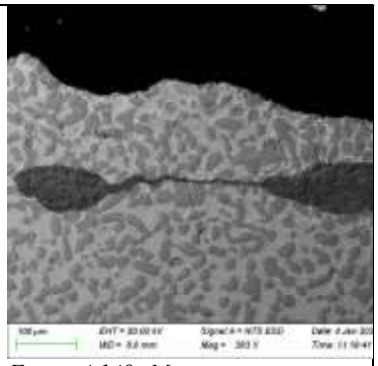

*Figure 4.148: Microstructure underneath oxide scale of oxidised heat-treated TiMn-11.*

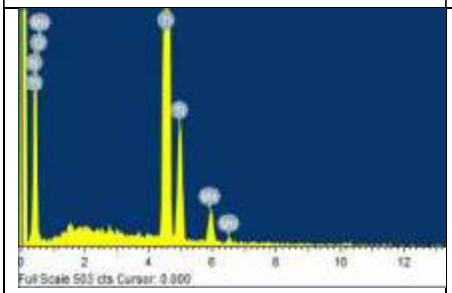

*Figure 4.149: EDX of $Ti(NO_3)_4$- 41.87(at%Ti); 46.48(at%N); 9.31(at%O); 2.34(at%Mn).*

A correlation between thermographs and the structures of the oxide films lead to a conclusion the $MnO_2$ outer layer develops first in the first 50 minutes followed by a mixture of $TiO_2$ and $Mn_3Ti_3O$ between 50 and 140 minutes and serve as a protective oxide film by minimizing oxidation between 140 and 255minutes. However this protective layer becomes non-protective 255 minutes into the experiment. This behaviour applied to selected TiMn alloys. Phase and compounds in the oxide scale were confirmed using XRD and EDX.

## 4.3. Ternary TiAlMn

### 4.3.1 Microstructures of As produced TiAlMn alloys

Microstructures:

Microstructures of as-produced TiAlMn alloys comprised of agglomerated $\alpha_2$ globules (labelled i) within β matrix phase (labelled ii) which contained platelets of γ (labelled iii) (Li *et al.,* 2018a) displayed in Figures 4.150 to 4.152. The development of these microstructures during the addition of Al from 1.39at%Al to 25.39at%Al to 29.20at%Al are displayed in Figures 4.150, 4.151 and 4.152. The Al feed rates were altered alongside Laser Power from 500W at 1.0rpm, to 550W at 1.5rpm and 2.0rpm. Increasing Al feed rates increased Al in the compositions. This also led to an increase in γ phase as observed when comparing Figures 4.150 to 4.151 to 4.152 where the sizes of γ platelets and lamellae increased in length from an approximate average from 1.400μm to 1.840μm to 6.540μm within the β matrix. The increase in γ was also driven by the increasing LEPUL.

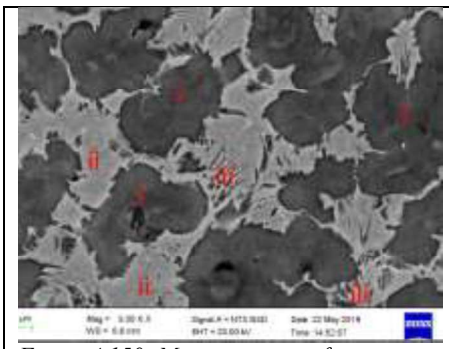

*Figure 4.150: Microstructure of as produced TiAlMn-1.Overall composition: 1.39at%Al 88.50at%Ti 10.12at%Mn. Laser Power: 500W*

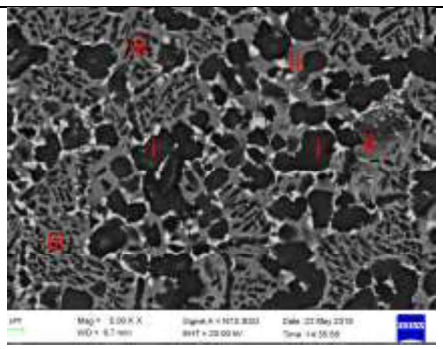

*Figure 4.151: Microstructure of as produced TiAlMn-2.Overall composition: 25.39at%Al 67.95at%Ti 6.66at%Mn. Laser Power: 550W*

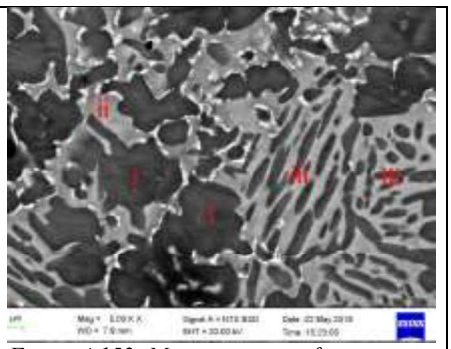

*Figure 4.152: Microstructure of as produced TiAlMn-3.Overall composition: 29.20at%Al 61.18at%Ti 9.62at%Mn. Laser Power: 550W*

*Figure 4.150 to 4.152: SEM micrographs taken with BSD mode, EHT set at 20.0kV and the magnification of x5000 (2μm)*

The compositional ranges of microstructural features illustrated in Figures 4.150 to 4.152 are given in Table 4.12. From Table 4.12, it can be observed that β matrix was Mn rich, $\alpha_2$ globules were Ti rich and γ phase was Al rich.

*Table 4.12: Microstructural features and compositions of TiAlMn alloys obtained through EDS/EDX.*

| Microstructure | Description | BSD contrast | at%Ti Range | at%Al Range | at%Mn Range | Phase |
|---|---|---|---|---|---|---|
| Globulars | Within grain | Black | 73.67 – 98.76 | 1.71 – 22.32 | 0.00 – 4.01 | $\alpha_2$ |
| Matrix | Grain boundary | Light grey | 63.03 – 84.04 | 0.69 – 23.23 | 13.74 – 20.33 | β |
| Dark Grey | Within matrix | Dark grey | 67.14 – 88.90 | 3.47 – 25.16 | 6.96 – 9.54 | γ |

### 4.3.2 Microstructures of Heat Treated TiAlMn Alloys:

Microstructures:

All ternary TiAlMn alloys were heat-treated at 950°C. Heat-treated TiAlMn-1 comprised of agglomerated and equiaxed $\alpha_2$ within β matrix with traces of γ on $\alpha_2$ globular and equiaxed grain boundaries as observed in Figure 4.153. In Figure 4.154 it was observed that γ phase lamellae within the matrix developed into grains during heat treatment. In Figure 4.155, it was observed that the microstructure had transformed into a fully lamellar microstructure where γ lamellae occupied the equiaxed grain and $\alpha_2$ globules the grain boundaries.

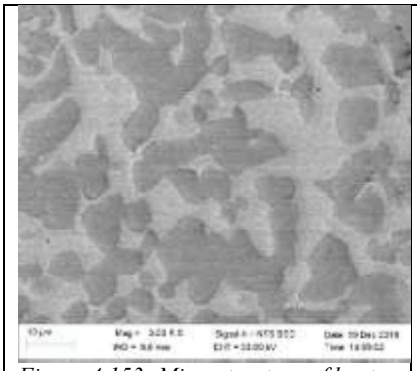

*Figure 4.153: Microstructure of heat treated TiAlMn-1*

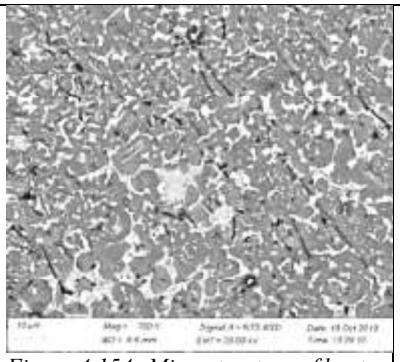

*Figure 4.154: Microstructure of heat treated TiAlMn-2*

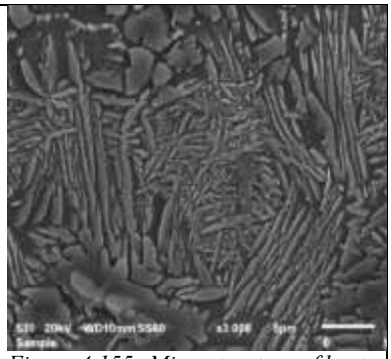

*Figure 4.155: Microstructure of heat treated TiAlMn-3*

*Figure 4.153 to 4.155: SEM micrographs taken with BSD mode, EHT set at 20.0kV and the magnification of x3000 (2μm) illustrating heat treated TiAlMn alloys*

.

### 4.3.3 X-ray Diffraction of TiAlMn alloys

$Al_{2.91}Mn_{1.09}$ with an orthorhombic crystal orientation was produced on Mn addition during laser deposition. $\alpha_2$-$TiMn_{1.20}Al_{0.80}$ with a hexagonal crystal orientation was also produced during deposition along with γ-TiAl with a tetragonal crystal orientation and β-$Ti_{17}Mn_3$ with a cubic crystal orientation (Figure 4.156). $\alpha_2$-$Ti_{0.965}Al_{0.035}$ also with a hexagonal crystal orientation was produced during heat-treatment along with γ-$TiAl_2$ with a tetragonal crystal orientation and β-$Ti_{0.85}Mn_{0.15}$ with a cubic orientation (Figure 4.157).

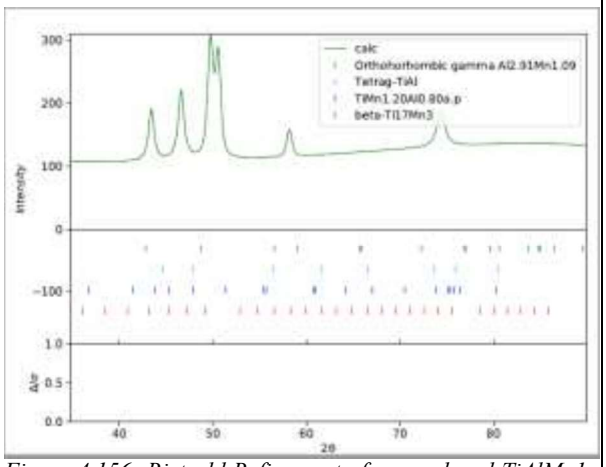


*Figure 4.156: Rietveld Refinement of as produced TiAlMn1 XRD data*

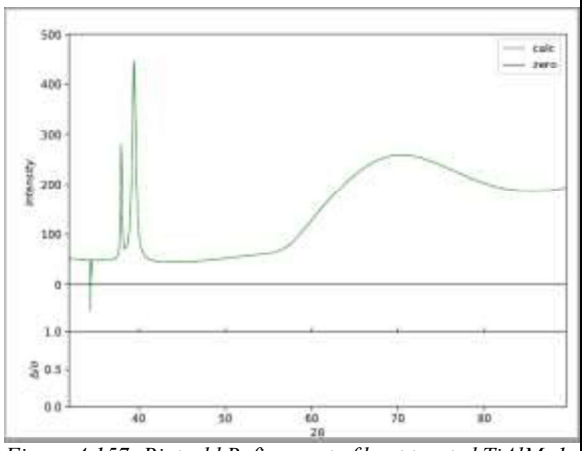


*Figure 4.157: Rietveld Refinement of heat treated TiAlMn1 XRD data*

Tetragonal TiAl lattice parameter $a_\gamma$ reduced to 2.48789Å and $c_\gamma$ increased to 7.32984Å on Mn addition (Figure 4.158).

Tetragonal crystal lattice parameter $a_\gamma$ decreased from 2.48789Å to 2.48079Å and $c_\gamma$ increased from 7.32984Å to 8.16362Å during heat-treatment (Figure 4.159). Lattice volume reduced to 45.37Å$^3$ on Mn addition and increased to 50.24Å$^3$ during heat treatment. (Figure 4.158 and 4.159)

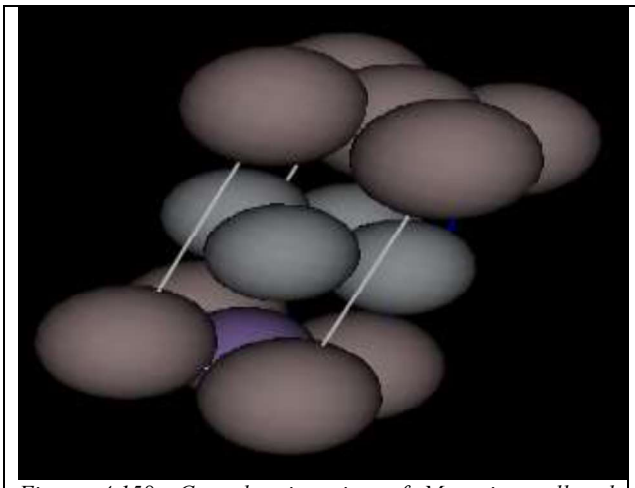

*Figure 4.158: Crystal orientation of Mn micro alloyed tetragonal TiAl with lattice parameters: a=b=2.48789Å ; c=7.32984Å*

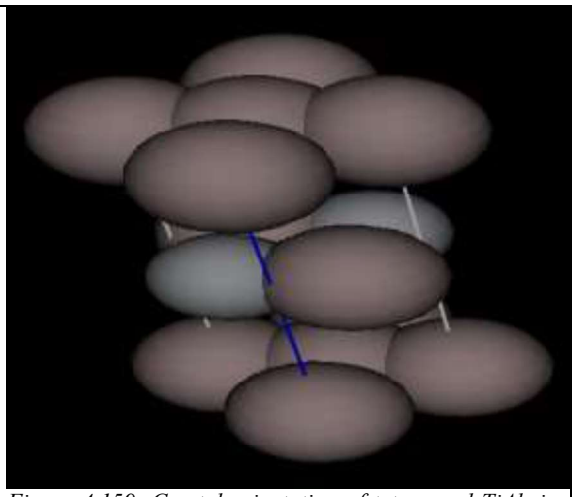

*Figure 4.159: Crystal orientation of tetragonal $TiAl_2$ in heat treated TiAlMn-1 with lattice parameters: a=b=2.48079Å ; c=8.16362Å.*

While hexagonal lattice parameter $a_{\alpha 2}$ increased from 3.89761Å to 4.73510Å and $c_{\alpha 2}$ decreased from 4.71199Å to 3.68838Å during heat treatment as observed in Figures 4.160 and 4.161. Lattice volume increased from 61.99Å$^3$ to 71.62Å$^3$ during heat treatment.

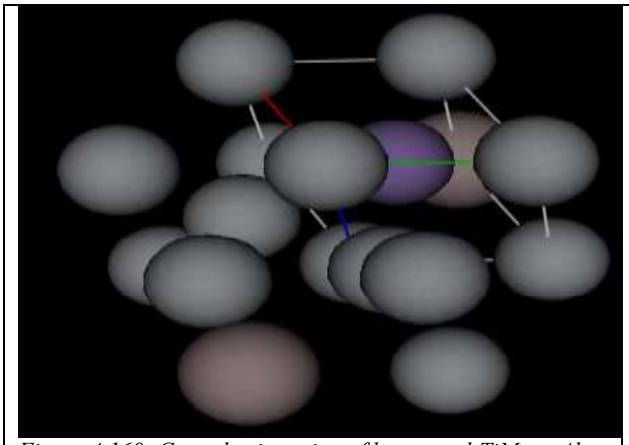

*Figure 4.160: Crystal orientation of hexagonal $TiMn_{1.20}Al_{0.80}$ in as produced TiAlMn1 with lattice parameters: a=3.89761Å; c=4.71199Å*

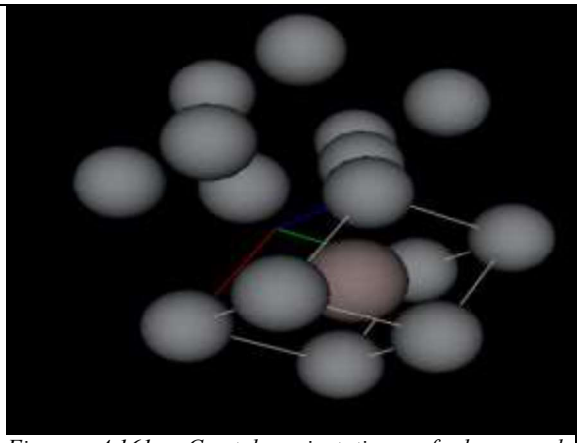

*Figure 4.161: Crystal orientation of hexagonal $Ti_{0.965}Al_{0.035}$ in heat treated TiAlMn1 with lattice parameters: a=4.73510Å ; c=3.68838Å*

Cubic lattice parameter $a_\beta$ increased from 9.36638Å to 9.65303Å (Figures 4.162 and 4.163) and lattice volume increased from 821.704Å$^3$ to 894.394Å$^3$ during heat treatment.

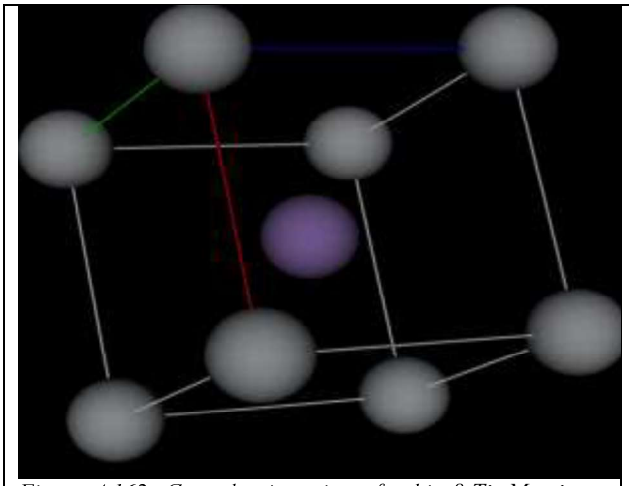

*Figure 4.162: Crystal orientation of cubic $\beta$-$Ti_{17}Mn_3$ in as produced TiAlMn1 with lattice parameter: a=b=c=9.36638Å*

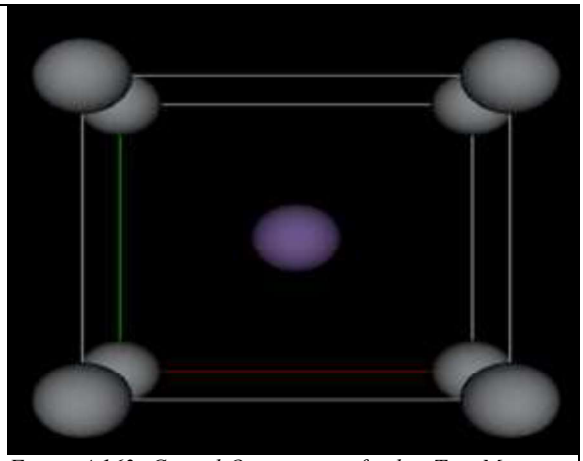

*Figure 4.163: Crystal Orientation of cubic $Ti_{0.85}Mn_{0.15}$ in heat treated TiAlMn1 with lattice parameter: a=b=c=9.65303Å.*

Orthorhombic crystal lattice parameters *a* and *c* of as produced $Al_{2.91}Mn_{1.09}$ increased from 3.17246Å and 3.60870Å to 3.24097Å and 4.39517Å, while *b* decreased from 4.71166Å to 3.48005Å during heat treatment -Figures 4.164 and 4.165. Lattice volume reduced from 53.94Å$^3$ to 49.57Å$^3$ during heat treatment.

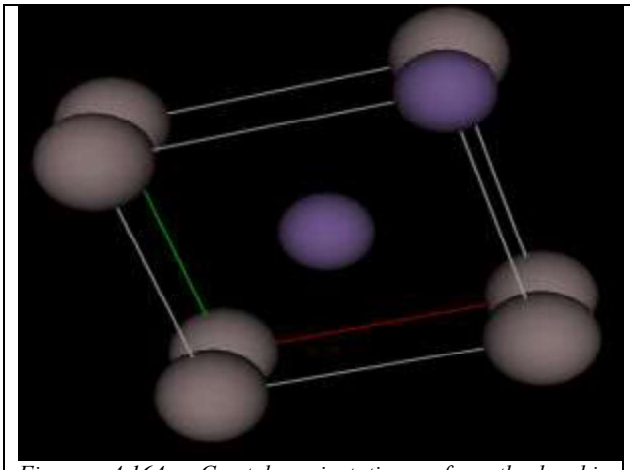

*Figure 4.164: Crystal orientation of orthorhombic $Al_{2.91}Mn_{1.09}$ in as produced TiAlMn1 with lattice parameters: a=3.17246Å; b=4.71166Å; c=3.60870Å*

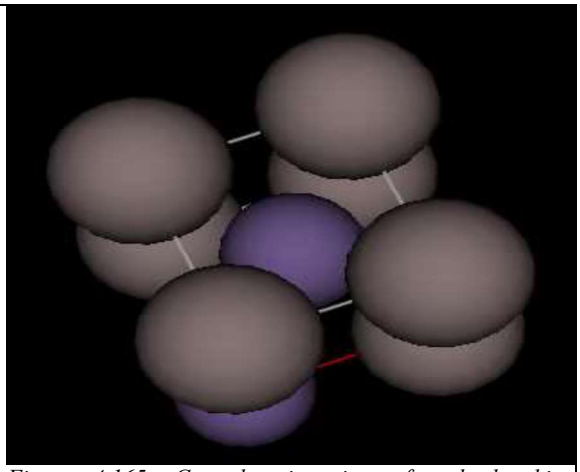

*Figure 4.165: Crystal orientation of orthorhombic $Al_{2.91}Mn_{1.09}$ in heat treated TiAlMn1 with lattice parameter: a=3.24097Å ; b= 3.48005Å ; c=4.39517Å*

Figures 4.166 and 4.167 illustrate the peak broadening of as produced and heat treated TiAlMn1.

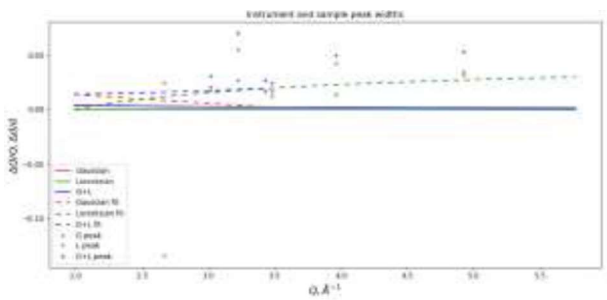

*Figure 4.166: Plot illustrating peak width broadening of as produced TiAlMn1.*

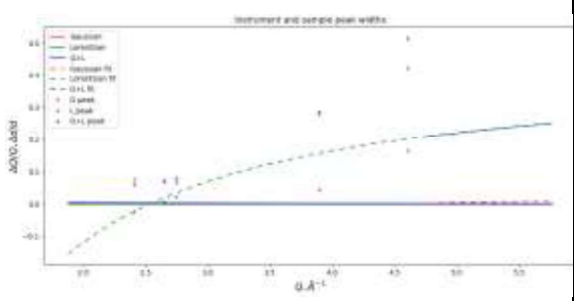

*Figure 4.167: Plot illustrating peak broadening of heat treated TiAMn1.*

In Table 4.13, it was observed that the dislocation densities increased significantly during heat treatment. Dislocations have burger's vectors: $\frac{1}{3}a\,[1\,1\,\underline{2}\,0]$ for hexagonal structure; $\frac{1}{2}a < \underline{1}\,1\,0]$; $\frac{1}{2}a < \underline{1}\ \underline{1}\,2]$; $< 0\,\underline{1}\,1]\ and < 1\,0\,\underline{1}]$ for tetragonal structure; $\frac{1}{2}a\,[1\,1\,1]$ for cubic structures along close packed planes along close packed planes$(1\,1\,1)_{\gamma}||(0\,0\,0\,1)_{\alpha}$ ; $(1\,1\,0)_{\gamma}||(1\,1\,2\,0)_{\alpha}$ (Appel et al., 2011a) and $(1\,0\,1)_{\beta}||(0\,0\,0\,1)_{\alpha}$ (Tong *et al.*, 2017).

*Table 4.13: Dislocation densities of TiAlMn Alloys*

| **Sample** | **Phase** | **Dislocation density ($\times 10^{-4}$ nm$^{-2}$)** |
|---|---|---|
| | | **3,25** |
| TiAlMn1 as produced | TiAl | |
| | $TiMn_{1.20}Al_{0.80}$ | |
| | $\beta$-$Ti_{17}Mn_3$ | |
| | $Al_{2.91}Mn_{1.09}$ | |
| TiAlMn1 heat treated | $TiAl_2$ | **140,86** |
| | $Ti_{0.965}Al_{0.035}$ | |
| | $Ti_{0.85}Mn_{0.15}$ | |
| | $Al_{2.91}Mn_{1.09}$ | |

### 4.3.4 Electron Backscatter Diffraction (EBSD) for TiAlMn alloys

Samples which yielded the least number of post processing thermal cracks were studied further by EBSD analysis. These samples include as-produced and heat-treated TiAlMn-1. Table 4.14 alongside Figure 4.168 display the colour coding and phase distribution of as-produced TiAlMn-1. It was observed that the Mn rich β-$Ti_{17}Mn_3$ phase comprised the matrix while the globules were comprised of the Ti rich $\alpha_2$-Ti phase. This elemental distribution can be observed in the SEM-BSD diagram in Figure 4.169 which was captured on the same spot as the EBSD in Figure 4.168, which is clarified numerically in Table 4.14. However, the γ-phase which comprised 0.01vol% of the alloy was observed within the matrix phase in Figure 4.168, but could not be observed in the SEM-BSD diagram in Figure 4.169. The distribution of the crystal orientations within different grains which comprise both globules and the matrix are displayed in the Inverse Polar Figure-Z (IPF-Z) in Figure 4.170. A variety of crystal orientations with respect to the Z axis were observed within both $\alpha_2$ globules and β matrix. The larger variety in the matrix phase was accredited to the presence of γ-phase within the matrix. Figure 4.171 displays grain boundaries while average, maximum and minimum grain sizes of different phases are stated in Table 4.14 as equivalent circle diameter (ECD-μm). It can be observed that β phase has larger grains than $\alpha_2$ phase, while it became extremely challenging to measure the sizes of γ grains since they were oriented within the matrix phase and globules as platelets.

*Table 4.14: Microstructural features of as-produced TiAlMn-1 detected by EBSD and SEM*

| Phases | $\alpha_2$-Ti | β-$Ti_{17}Mn_3$ | γ- TiAl |
|---|---|---|---|
| EBDS colour codes | | | |
| Phase distribution (vol%) | 44.66 | 55.07 | 0.01 |
| SEM-BSD contrast | Black | Grey | Dark grey |
| Average Ti (at%) | 95.69 | 80.49 | 88.90 |
| Average Mn (at%) | 3.500 | 16.38 | 7.63 |
| Average Al (at%) | 2.350 | 3.127 | 3.47 |
| Average grain size-ECD(μm) | 4.49 | 5.64 | - |
| Maximum grain size | 10.61 | 14.16 | - |
| Minimum grain size | 3.08 | 3.08 | - |
| Microstructural Features | globules | matrix | platelets |

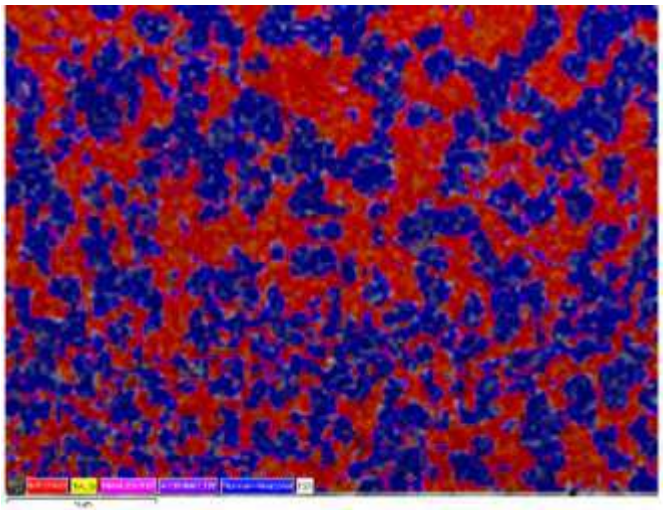

*Figure 4.168: Phase distribution of β, $\alpha_2$ and γ phases*

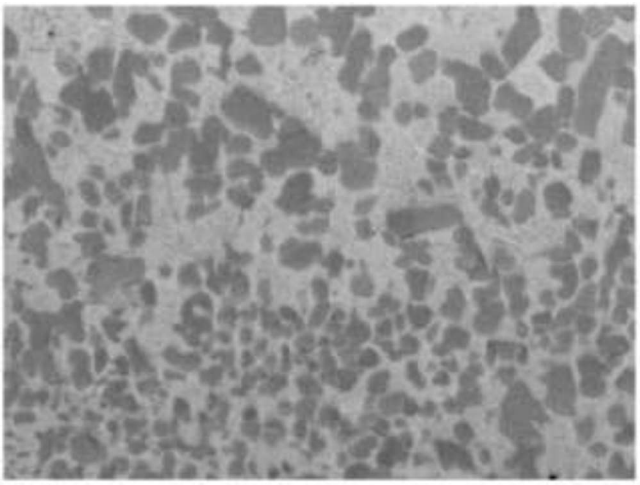

*Figure 4.169: Backscatter diffraction Scanning Electron Micrograph (BSD-SEM) image displaying elemental distribution*

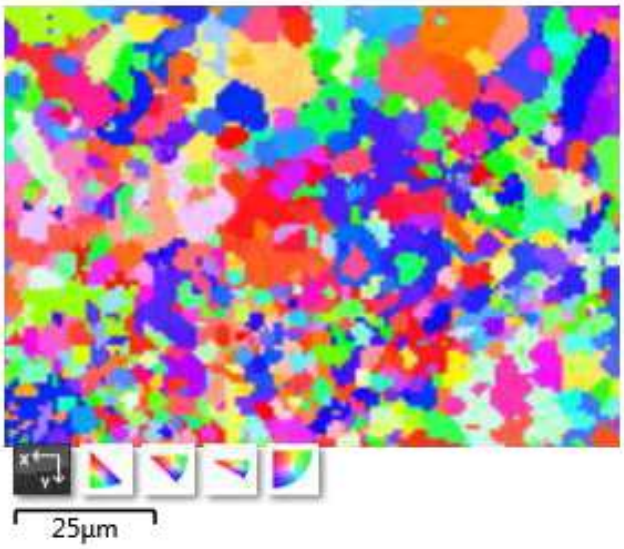


*Figure 4.170: Inverse Polar Figure-Z (IPF-Z) displaying crystal orientation of different grains relative to z-axis*

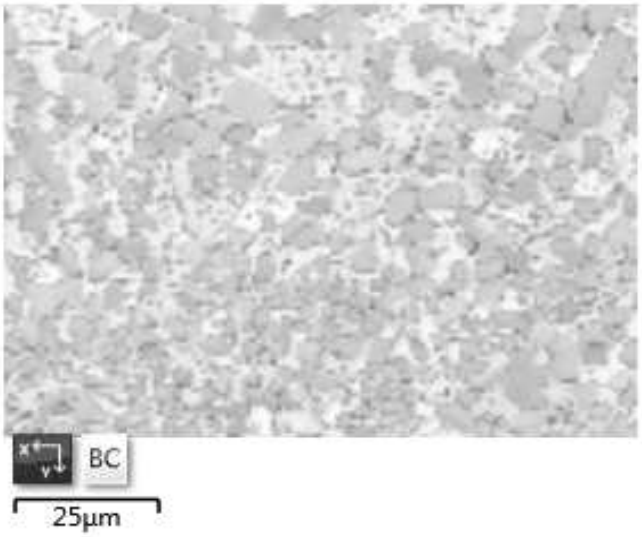


*Figure 4.171: Band contrast image displaying grain boundaries.*

*Figure 4.168 to 4.171: Electron Backscatter Diffraction (EBSD) images of as produced TiAlMn-1*

Table 4.15 alongside Figure 4.172 display the colour coding and phase distribution of heat-treated TiAlMn-1. It was observed that heat-treatment at 950°C led to an increase in $\alpha_2$ phase and a decrease in β-phase. The elemental distribution among these phases is visually observed in Figure 4.173 and numerically observed in Table 4.15. It was seen that heat-treatment has led to the segregation of Ti from the β-phase to $\alpha_2$ and γ phase and the segregation of Mn to β phase. Figure 4.174 display an IPF-Z diagram where it can be observed that in comparison to the as-produced state (Figure 4.170), the crystal orientation within each grain was more

uniform. In Figure 4.175 are the grain boundaries. It was observed in Table 4.15 that heat treatment led to a reduction of β grain sizes and an increase in $\alpha_2$ grains sizes.

*Table 4.15: Microstructural features of heat-treated TiAlMn-1 detected by EBSD and SEM-BSD*

| Phases | $\alpha_2$-Ti | β-$Ti_{0.85}Mn_{15}$ | γ-$TiAl_2$ |
|---|---|---|---|
| EBDS colour codes | | | |
| Phase distribution (vol%) | 71.61 | 27.45 | 0.09 |
| SEM-BSD contrast | Black | Grey | Dark grey |
| Average Ti (at%) | 95.91 | 76.44 | 92.15 |
| Average Mn (at%) | 2.99 | 21.74 | 6.38 |
| Average Al (at%) | 1.10 | 1.830 | 1.47 |
| Average grain size-ECD(µm) | 6.06 | 5.33 | - |
| Maximum grain size | 22.30 | 10.18 | - |
| Minimum grain size | 3.07 | 3.07 | - |
| Microstructural features | Equiaxed grains | Matrix | Grain boundaries |

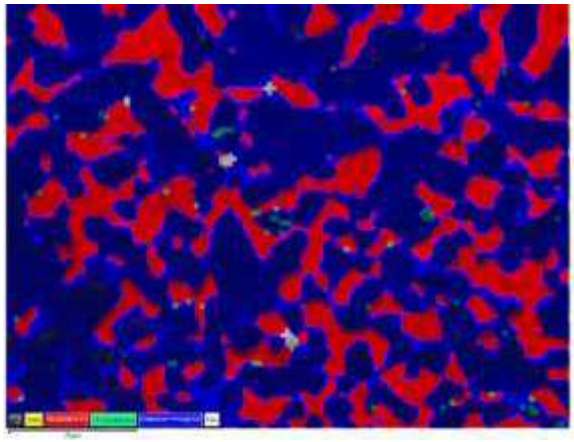

*Figure 4.172: phase distribution of $\alpha_2$, $\beta$, $Ti_{0.965}Al_{0.035}$ and $TiAl_2$*

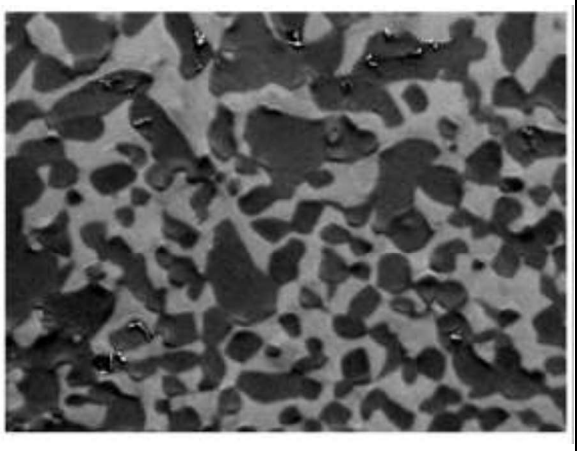

*Figure 4.173: SEM-BSD image displaying elemental distribution*

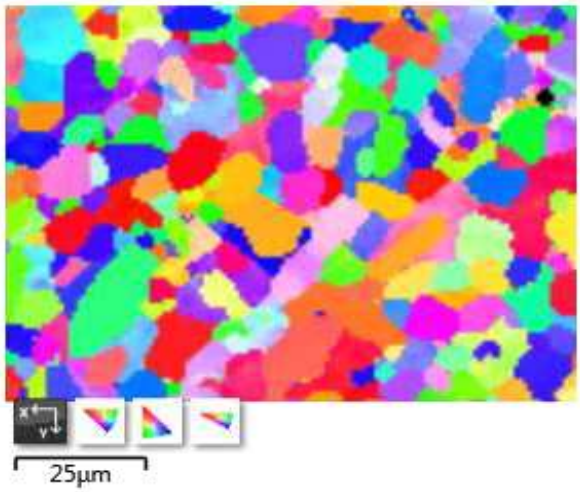


*Figure 4.174: IPF-Z displaying crystal orientations of different grains.*

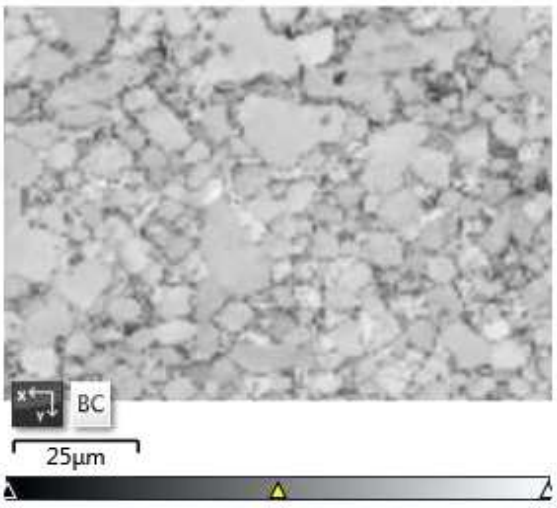


*Figure 4.175: Band contrast image displaying different grain boundaries of heat treated TiAlMn-1.*

*Figure 4.172 to 4.175: EBSD images of heat-treated TiAlMn-1*

*Pole Figures*

Figures 4.176, 4.177 and 4.178 display crystal orientations detected by EBSD in as-produced TiAlMn-1 in pole figures where the Z-axis comes out of the page. Figure 4.176 displays crystal orientations for β-$Ti_{17}Mn_3$ detected on {1 1 0} standard projection for cubic system, where 396 orientations were counted using Image J software. Figure 4.177 displays $\alpha_2$ orientations detected on $\{1\,0\,\underline{1}\,0\}$ standard projection for hexagonal system which amounted to 635 orientations. Figure 4.178 for γ-TiAl detected on {1 1 1} standard projection for a tetragonal system where orientations were too minimal to count. Figures 4.179, 4.180 and 4.181 display crystal orientations detected by EBSD in heat-treated TiAlMn-1. It was observed in Figure 4.179 that β cubic orientations were more concentrated towards orientations with symmetry folds (Widjaja and Marks, 2008) compared to the as-produced state displayed in Figure 4.176,

although 309 orientations were counted in Figure 4.179. It was also observed in Figure 4.180 that the heat-treated state had a reduced number of orientations for hexagonal-$\alpha_2$ crystals compared to the as-produced state in Figure 4.177 and the number of these orientations counted amounted to 480. Figure 4.181 shows that heat-treatment led to increased crystal orientations for the tetragonal $\gamma$-$TiAl_2$ compared to the as-produced state in Figure 4.178 and the number of orientations counted totalled to 18.

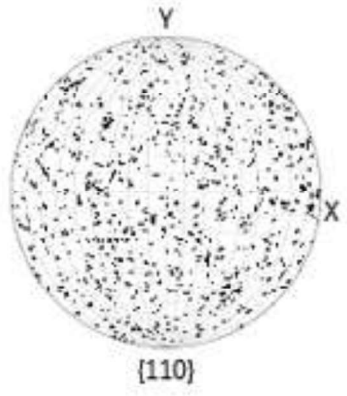


*Figure 4.176: 396 crystal orientations of β phase in as produced TiAlMn-1 detected by EBSD on {1 1 0} standard projection of cubic system*

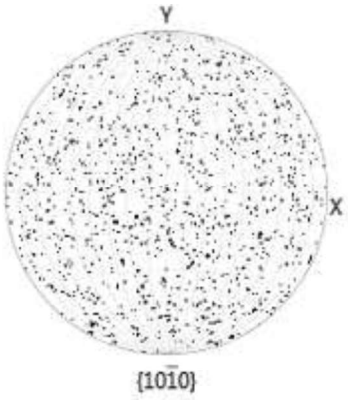


*Figure 4.177: 635 crystal orientations of $\alpha_2$ phase in as produced TiAlMn-1 detected by EBSD on $\{10\underline{1}0\}$ standard projection of hexagonal system*

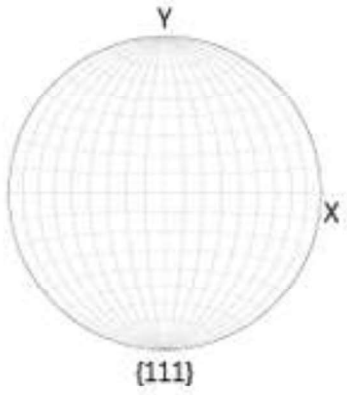


*Figure 4.178: crystal orientations of γ phase in as produced TiAlMn-1 detected by EBSD on {1 1 1} standard projection of cubic system*

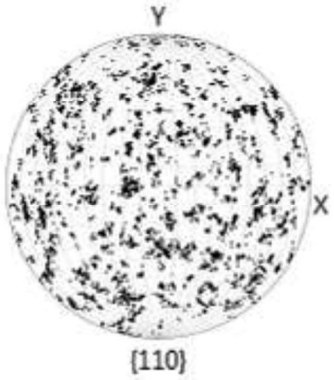


*Figure 4.179: 309 crystal orientations of β phase in heat treated TiAlMn-1 detected by EBSD on {1 1 0} standard projection of cubic system*

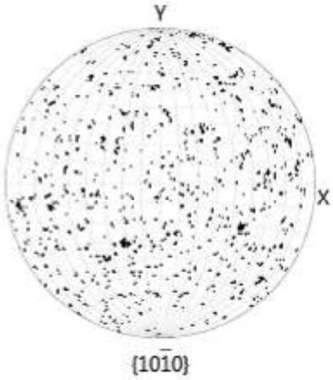


*Figure 4.180: 480 crystal orientations of $\alpha_2$ phase in heat treated TiAlMn-1 detected by EBSD on $\{10\underline{1}0\}$ standard projection of hexagonal system*

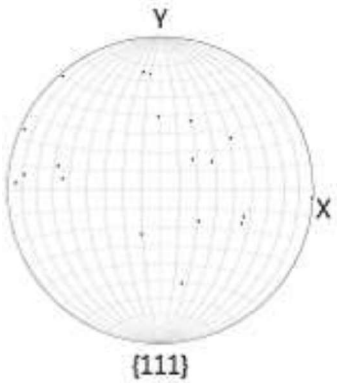


*Figure 4.181:18 crystal orientations of γ phase in heat treated TiAlMn-1 detected by EBSD on {1 1 1} standard projection of cubic system*

*Figure 4.176 to 4.181: Pole figures displaying crystal orientations of phases*

### *Texture measurements*

Texture measurements of various crystal orientations were carried out using EBSD on standard cubic and hexagonal projections using multiples of uniform distribution (MUD). MUD is equivalent to the ratio of a given orientation to the relative weight of the same orientation in a uniform texture distribution (Creuziger *et al.*, 2014). Figures 4.182, 4.183 and 4.184 display

the texture measurements of as-produced TiAlMn-1. Figures 4.185, 4.186 and 4.187 display texture measurements of heat treated TiAlMn-1. Figure 4.182 displays the texture of β orientations in a standard {1 0 0} projection for cubic system where it was observed that the maximum MUD was 6.33. Figure 4.183 shows the texture of hexagonal crystal orientations on standard {0 0 0 1} projection for hexagonal system where maximum MUD was 4.20. Figure 4.184 displays the texture of γ-TiAl orientations on {0 0 1} standard projection for tetragonal system where the orientations were extremely limited but had the maximum texture measurement of 180.27MUD. Figure 4.185 indicates that heat-treatment led to a reduction of maximum texture measurement to 4.54MUD. However, Figure 4.186 indicates that heat-treatment led to maximum increased texture measurements of 11.30MUD in hexagonal structure. Similar to β phase, heat-treatment led to a reduction in texture in tetragonal γ-$TiAl_2$ to MUD of 38.33 as displayed in Figure 4.187.

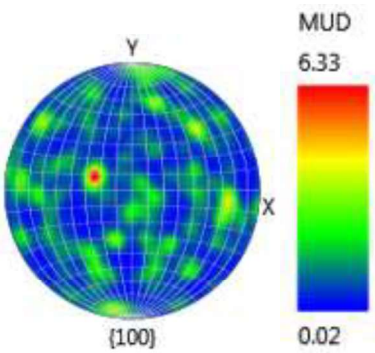


*Figure 4.182: texture distribution of β phase in as produced TiAlMn-1 detected by EBSD on {1 0 0} standard projection of cubic system.*

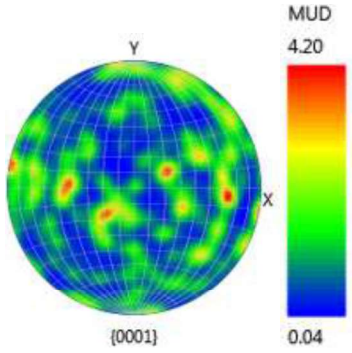


*Figure 4.183: texture distribution of $\alpha_2$ - phase in as produced TiAlMn-1 detected by EBSD on {0 0 0 1} standard projection of hexagonal system.*

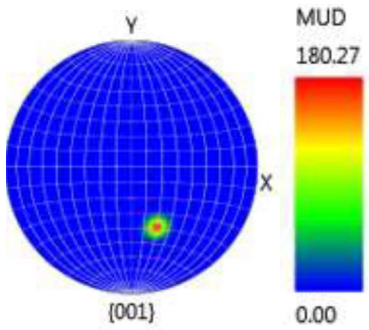


*Figure 4.184: texture distribution of γ phase in as produced TiAlMn-1 detected by EBSD on {0 0 1} standard projection of cubic system.*

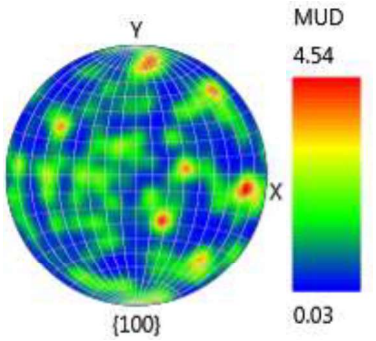


*Figure 4.185: texture distribution of β phase in heat treated TiAlMn-1 detected by EBSD on {1 0 0} standard projection of cubic system.*

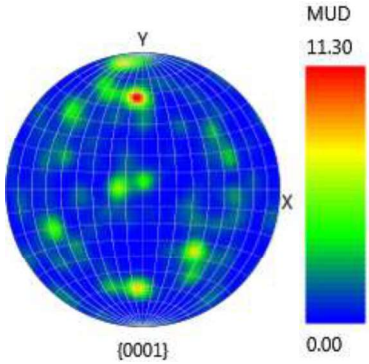


*Figure 4.186: texture distribution of $\alpha_2$ - phase in heat treated TiAlMn-1 detected by EBSD on {0 0 0 1} standard projection of hexagonal system.*

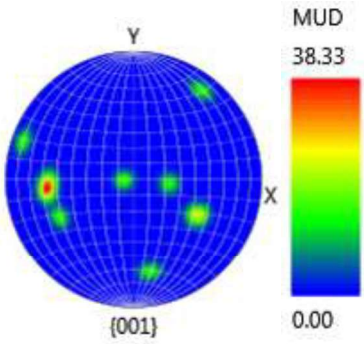


*Figure 4.187: texture distribution of γ phase in heat treated TiAlMn-1 detected by EBSD on {0 0 1} standard projection of cubic system.*

*Figure 4.182 to 4.187: distribution of crystal textures of various orientations detected measured in MUD*

### 4.3.5 Microhardness of TiAlMn alloys

The microhardness values of as-produced TiAlMn ranged from 569,20HV to 602,20HV with an average of 590,02HV. Microhardness increased with increasing LEPUL and Al feed rates as observed in graphical representation displayed in Figure 4.188.

Microhardness of heat-treated TiAlMn structures ranged from 582,92HV to 590,02HV with an average of 585,44HV. The effects of altering Al compositions on microhardness are displayed in Figure 4.97. The microhardness of high Al alloys reduced during heat-treatment.

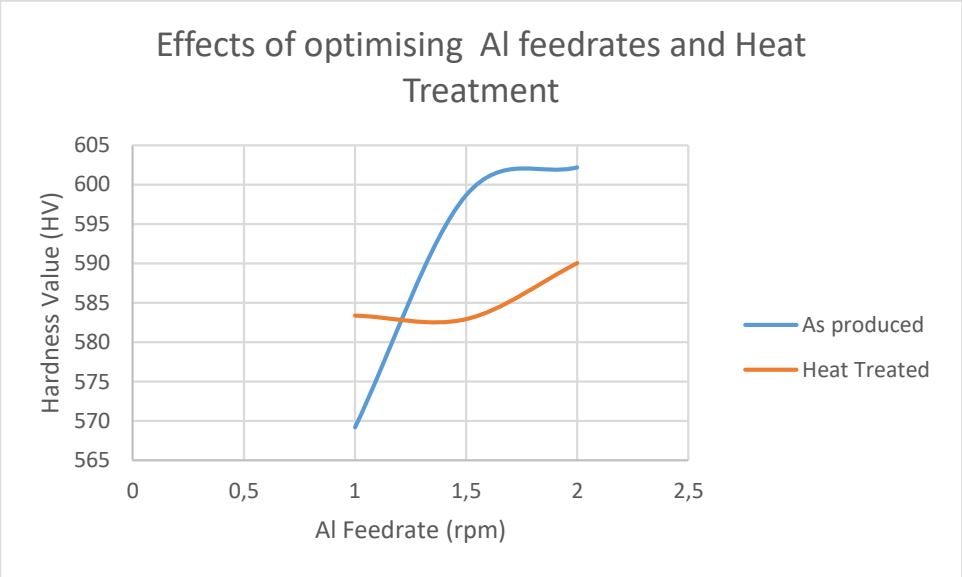


*Figure 4.188: Average microhardness values for as produced and heat treated Ti-Al-Mn alloys*

### 4.3.6 Fracture stress of TiAlMn alloys

Low Al TiAlMn alloys had reduced crack lengths compared to binary TiAl alloys (Figures 4.37 and 4.38) and high Mn binary TiMn (Figure 4.132). These reduced crack lengths displayed in Figures 4.189 and 4.190 indicated improved fracture stress due to Mn addition. However, when the Al was increased to 25.39at%Al and 29.20at%Al, samples became brittle and were friable when attempts to remove them from the Ti-6Al-4V substrate were made. As-produced and heat-treated TiAlMn-1 (1.39at%Al) cracks had calculated fracture stress of 695.69 MPa and 348.612 MPa as displayed in Figures 4.189 and 4.190.

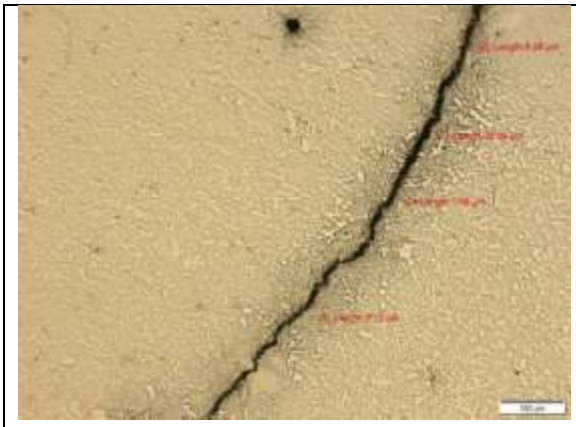

*Figure 4.189: Optical micrographs displaying crack lengths of as produced TiAlMn-1*

Average crack length (a)= 10.523 x$10^{-6}$ m ; fracture toughness= 4.0 MPa$\sqrt{m}$

$\sigma_f = \frac{K_{IC}}{\sqrt{\pi a}} = 695.69\ MPa$



*Figure 4.190: Optical micrographs displaying crack lengths of heat treated TiAlMn-1*

Average crack length (a)= 41.907 x$10^{-6}$ m; fracture toughness=4.0 MPa$\sqrt{m}$

$\sigma_f = \frac{K_{IC}}{\sqrt{\pi a}} = 348.612\ MPa$

*Figures 4.189 and 4.190: Optical micrographs displaying cracks*

### 4.3.7 Thermogravimetric Analysis

Figure 4.191 displays mass loss due oxidation as a function of time. As-produced TiAlMn-1 (labelled SAMPLE-TIALMN-1 on thermograph) underwent initial mass loss in the first 34 minutes at a rate of 0.0127496mg/min. This mass loss was followed by mass gain which continued at a rate of 0.03029104mg/min for 104 minutes. A reduction in mass gain rates to 0.0031315707mg/min then occurred for 112 minutes. Mass gain rates increased to 0,021760122mg/min for the remaining duration of the experiment.

Heat-treated TiAlMn-1 (labelled SAMPLE-BC) underwent initial mass loss in the first 57 minutes at a rate of 0.009272424mg/min. This mass loss was followed by mass gain which continued at a rate of 0.034618333mg/min for 81 minutes. The mass gain was followed by a drastic reduction in mass gain rates to 0.003131571mg/min, oxidation at this rate continued for 112 minutes. Oxidation continued and the sample gain mass at a rate of 0,02244013mg/min for 90 minutes until the experiment was complete.

Parabolic rate constants ($k = \frac{\Delta m}{\sqrt{t}}$) for isothermal oxidation for as-produced TiAlMn-1 was -0.189814mg/min$^{1/2}$ and 0.2115072mg/min$^{1/2}$ for heat-treated TiAlMn-1. The drastic mass loss

rate reduction between 138 minutes and 250 minutes in both as-produced and heat-treated TiAlMn-1 is indicative of the formation of a protective oxide film prior to the oxidation stage.

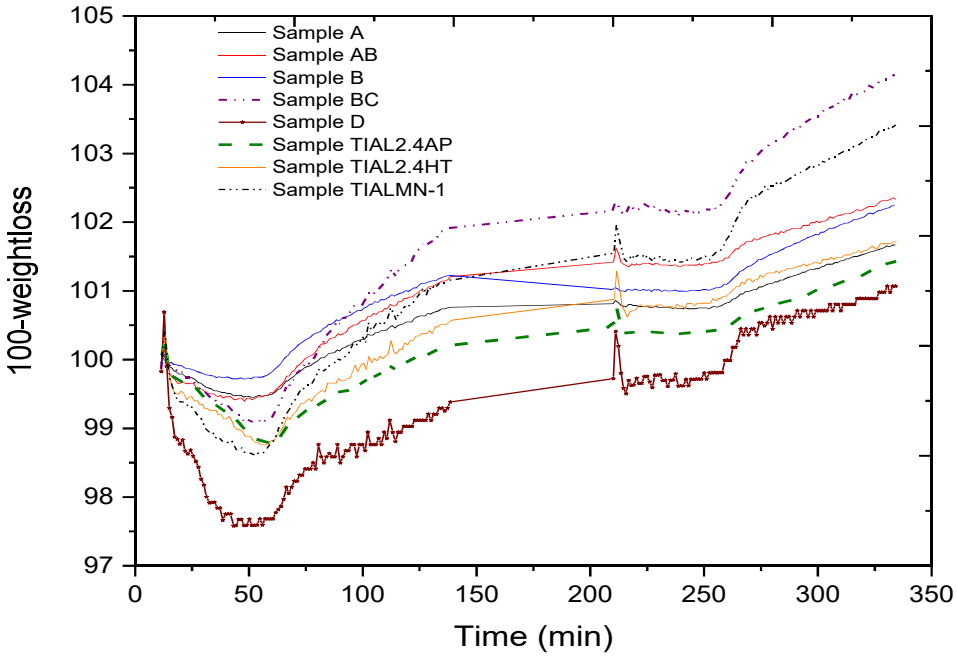


*Figure 4.191: Mass loss as a function of time for as-produced (labelled SAMPLE TIALMN-1) and heat-treated (labelled SAMPLE-BC) TiAMn-1.*

Figure 4.192 display the effects of temperature on mass loss and gain during oxidation of selected TiAlMn alloys. It was observed that as-produced TiAlMn-1 experienced the higher mass losses before 700°C and gained the least mass between 700°C and 900°C. The oxidation behaviour of heat-treated TiAlMn-1 was similar to as-produced TiAlMn-1 but temperature affected the oxidation of heat-treated TiAlMn-1 less than the as-produced sample.

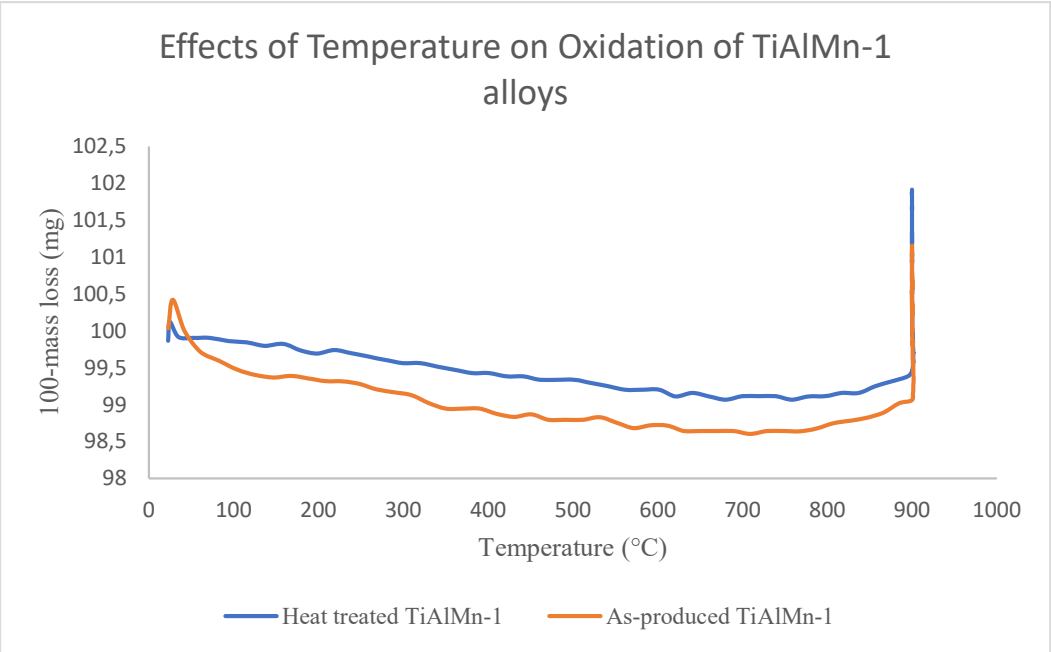


*Figure 4.192: Mass loss as a function of temperature for as-produced and heat-treated TiAlMn-1*

Thickness of the oxide scale of oxidised as-produced TiAlMn-1 ranged from 101.5µm to 244.5µm as displayed in Figure 4.193. The oxide scale contained three distinct layers as observed in Figure 4.194. The outer layer was comprised of $MnO_2$ (light grey BSD contrast) and ranged from 6.461µm to 11.05µm. Beneath the $MnO_2$ layer lied a $TiO_2$ (grey BSD contrast) layer with a thickness of 34.96µm followed by another $TiO_2$ layer which was porous and was 45.22µm thick and contained $MnO_2$ veins. Oxidation led to the precipitation of $MnO_2$ on $\alpha_2$ grain boundaries of the microstructure underneath the oxide scale as displayed on Figure 4.195 but remained unchanged towards the centre of the sample. The compositions of phases which were present in the oxide scale are shown in Figures 4.196 and 4.197 where EDX outcomes are displayed. These phases were confirmed using XRD.

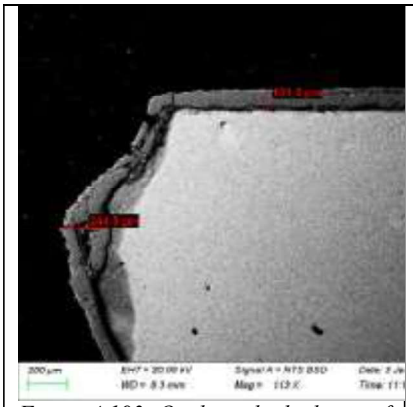

*Figure 4.193: Oxide scale thickness of as-produced TiAlMn-1.*

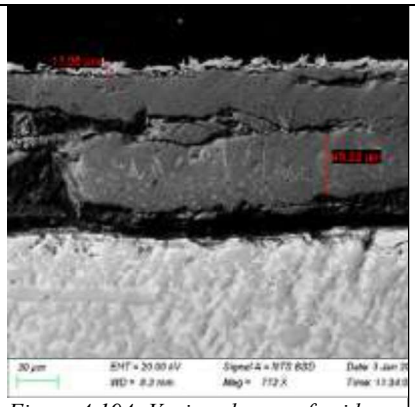

*Figure 4.194: Various layers of oxide scale thickness of as-produced TiAlMn-1.*

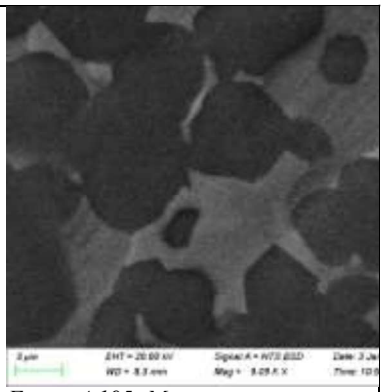

*Figure 4.195: Microstructure underneath oxide scale of as-produced TiAlMn-1.*

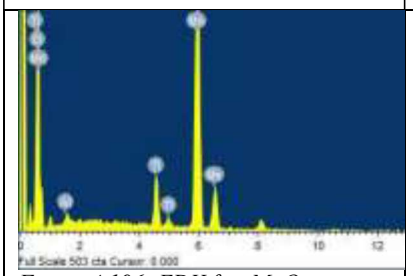

*Figure 4.196: EDX for $MnO_2$ - 64.64(at%O); 31.56 (at%Mn); 3.27(at%Ti); 0.53(at%Al)*

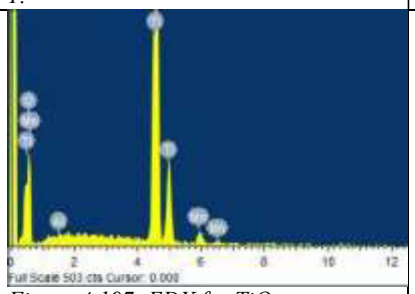

*Figure 4.197: EDX for $TiO_2$- 68.40(at%O); 30.49(at%Ti); 0.93(at%Mn); 0.17(at%Al)*

The thickness of the oxide scale of oxidised heat-treated TiAlMn-1 was approximately 109.9µm as displayed in Figure 4.198. The outer layer was 49.95µm thick and the inner layer was approximately 47.58µm thick. Both layers were comprised of $TiO_2$ (grey BSD contrast) but the inner layer was more porous than the outer layer. Both layers contained extremely small layers of $Al_2O_3$ (black SEM-BSD contrast) towards the top which was observed in Figure 4.199. Oxidation led to the precipitation of $Mn_3O_4$ (light grey SEM-BSD contrast) on $\alpha_2$ grain boundaries of the microstructure underneath the oxide scale as displayed on Figure 4.200 but remained unchanged towards the centre of the sample. The composition of each phase is displayed in EDX patterns shown from Figures 4.201 to 4.203. These phases were confirmed using XRD.

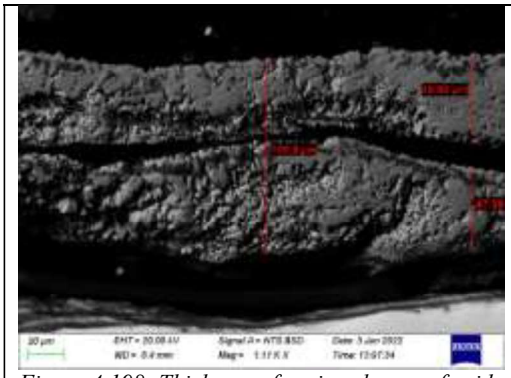

*Figure 4.198: Thickness of various layers of oxide scale of heat-treated TiAlMn-1.*

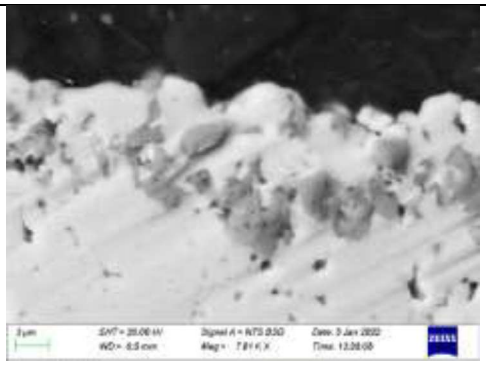

*Figure 4.199: Protective oxide scale of heat-treated TiAlMn-1.*

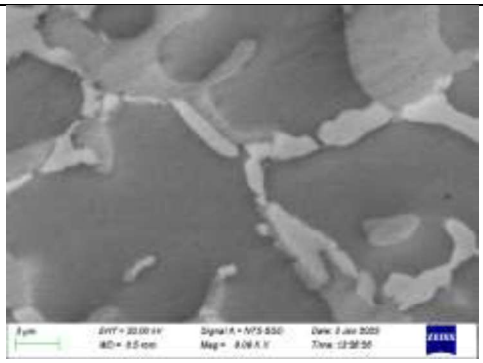

*Figure 4.200 Microstructure underneath oxide scale of oxidised heat-treated TiAlMn-1.*

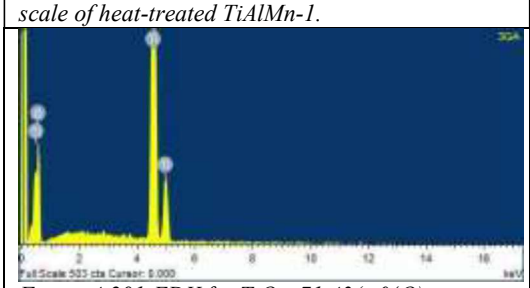

*Figure 4.201:EDX for $TiO_2$ -71.43(at%O); 28.57(at%Ti)*

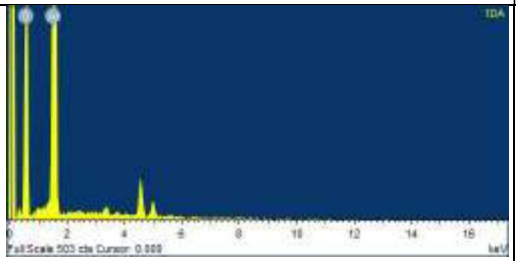

*Figure 4.202: EDX for $Al_2O_3$- 64.17(at%O); 35.83(at%Al)*

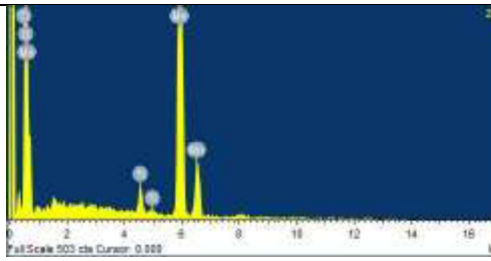

*Figure 4.203: EDX for $Mn_3O_4$ - 63.58(at%O); 33.82(at%Mn); 2.28(at%Ti); 0.32(at%Al)*

### 4.3.8 Mechanical Properties of Ternary TiAlMn alloys according to Nanoindentation

A sample was taken from the large ternary TiAlMn alloy and the total of 16 nanoindentations were carried out on the sample and yielded curves displayed in Figure 4.204. The average measured indentation hardness $H_{IT}$ was 64023,056MPa and average Vicker's hardness was calculated to be 5929,24HV. Average maximum measured indentation depth was 1025,160667nm. The average measured indentation elastic modulus $E_{IT}$ was 463,426GPa, calculated plane strain elastic modulus E* was 522,834GPa and measured stiffness was 1,0352125mN/m. The calculated average indentation strain $\varepsilon_{IT}$ was 0,204182013 (20,41820134%) which led to calculated 0.2% offset yield stress of 105366,1719MPa.

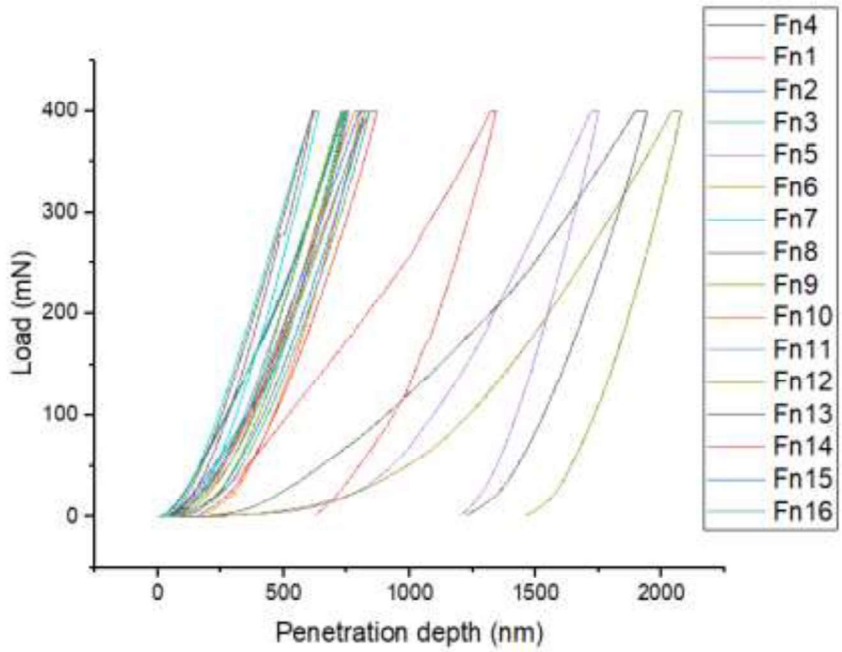


*Figure 4.204: Relationship between indentation depth and load obtained from nano indentations on ternary TiAlMn alloy.*

Vickers hardness was plotted against calculated indentation 0.2% offset yield stress (Equation 3.) and displayed in Figure 4.205. The trendline in the plot indicates a relationship of direct proportionality between Vicker's hardness and calculated yield stress which is also evident in the trendline included.

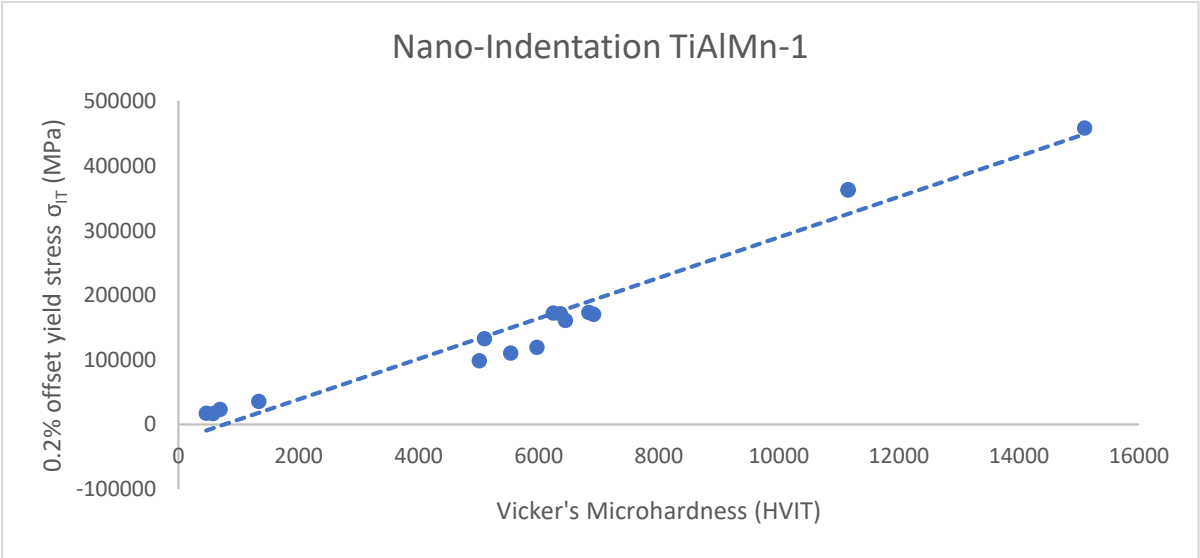


*Figure 4.205: Relationship between Vickers's Hardness and calculated indentation 0,2% offset yield stress.*

Vickers's hardness was again plotted against calculated indentation strain (Equation 3.14) as displayed in Figure 4.206, where a relationship of direct proportionality can be observed also evident in the trendline included.

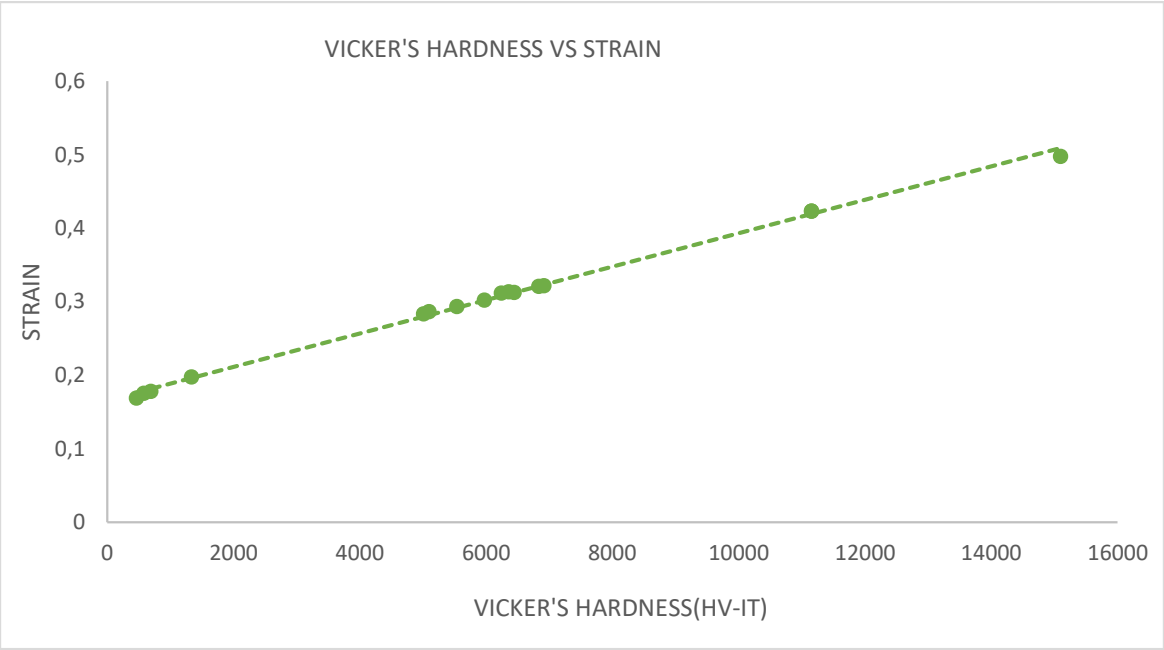


*Figure 4.206: Relationship between Vicker's Hardness and calculated indentation strain.*

Calculated indentation strain was plotted against calculated indentation 0.2% offset yield stress as displayed in Figure 4.207 where a typical stress-strain relationship of the directly proportional elastic region can be observed. The maximum strain calculated from this nano indentation was 49.76%.

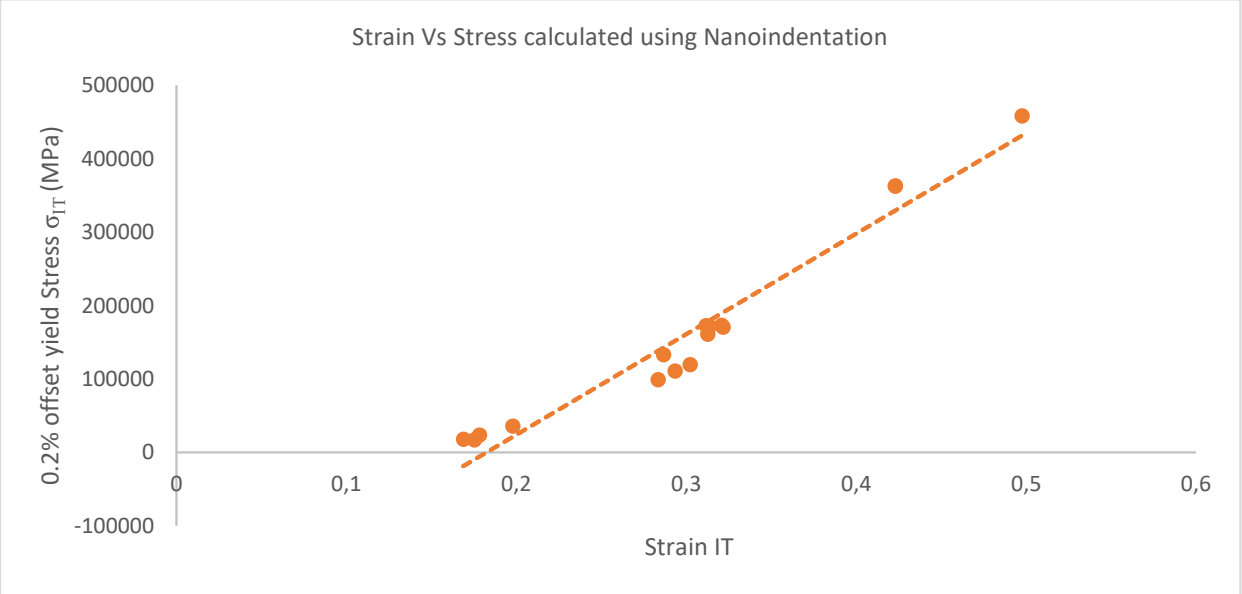


*Figure 4.207: Relationship between calculated indentation stress and strain.*

### 4.3.9 Gleeble Testing

Table 4.16 and Figure 4.209 display the elevated temperature flow stress values vs strain reduction of TiAlMn alloy. From the unrefined gleeble compression stress vs strain graph displayed in Figure 4.208, it was observed that maximum stress values ranging from 101.642MPa to 114.812MPa were required to overcome elastic deformation at high temperatures before the plastic deformation was initiated at lower stress values. These stress values are displayed in Table 4.16. 46.50% strain yielded the lowest strain hardening coefficient (n) while 34.58% yielded the highest stress.

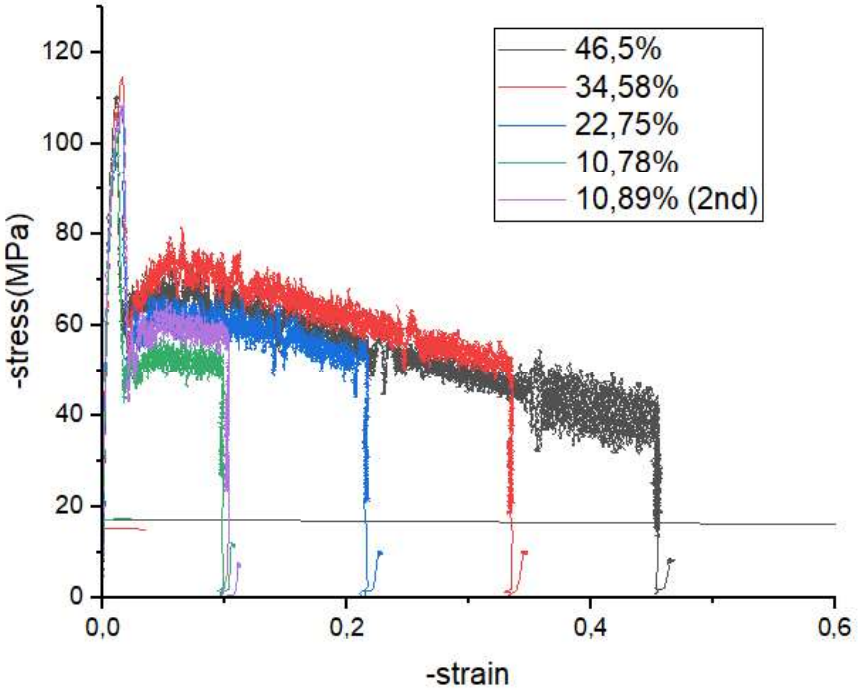


*Figure 4.208: Unrefined gleeble compression stress-strain curves*

*Table 4.16: Strain and Stress values attained from Gleeble testing*

| Strain Reduction | Maximum Stress (MPa) | Average Stress (MPa) | Strain hardening coefficient *-n* | Yield stress (MPa) |
|---|---|---|---|---|
| 46.50% | 110.608 | 40.999 | 0.00995 | 58.732 |
| 34.58% | 114.812 | 43.323 | 0.01009 | 67.825 |
| 22.75% | 108.153 | 36.100 | 0.01005 | 52.613 |
| 10.89% | 101.642 | 25.549 | 0.01000 | 51.953 |
| 10.78% | 109.172 | 25.483 | 0.01007 | 46.492 |

When the stress strain curves in Figure 4.208 were refined and smoothed using Origins Software, curves plotted in Figure 4.209 were yielded. Average stresses are displayed in Figure 4.209 and Table 4.16. It was determined that compression flow stress and yield stress values

increased with increasing strain reduction values until 34.58% strain. This indicates a simultaneous improvement of ductility and material strength until 34.58% strain reduction where the average flow stress value was 43.323MPa and yield stress 58.732MPa. However, at 46.50% strain reduction, the flow stress reduced to an average of 40.999MPa and yield stress to 58.732MPa, indicating reduced strength with increased ductility, since lower average flow stress was required to deform the alloy to a higher strain value. An increase in strain reduction from 10.78% to 10.89% showed the effects of small strain reduction changes and it confirmed that strain reduction increased with flow stress at low strain values. Flow stress increased from an average of 25.483MPa to 25.549MPa. At 46.5% strain, the lowest strain hardening coefficient was yielded and at 34.58% strain, the highest strain hardening coefficient was yielded.

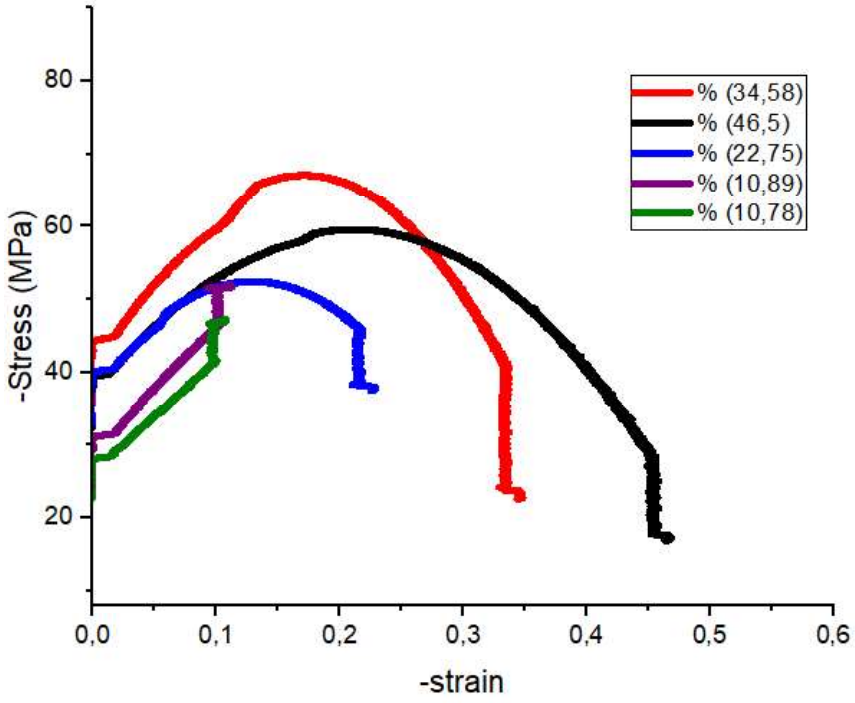


*Figure 4.209: Refined gleeble compression stress-strain curves*

Microhardness tests were conducted to examine the effects of strain on microhardness. From the plot in Figure 4.210, the undeformed sample had the highest microhardness value of 623,235HV. The microhardness of hot deformed samples decreased to values ranging from 553,506HV to 561,712HV with an average of 560,953HV. This indicated that hot deformation of TiAlMn led to strain softening due stress relief resulting from the 3 minutes holding time before compression. The sample with the highest flow stress value had the highest

microhardness values among the deformed samples while the sample with the highest strain value had the lowest microhardness.

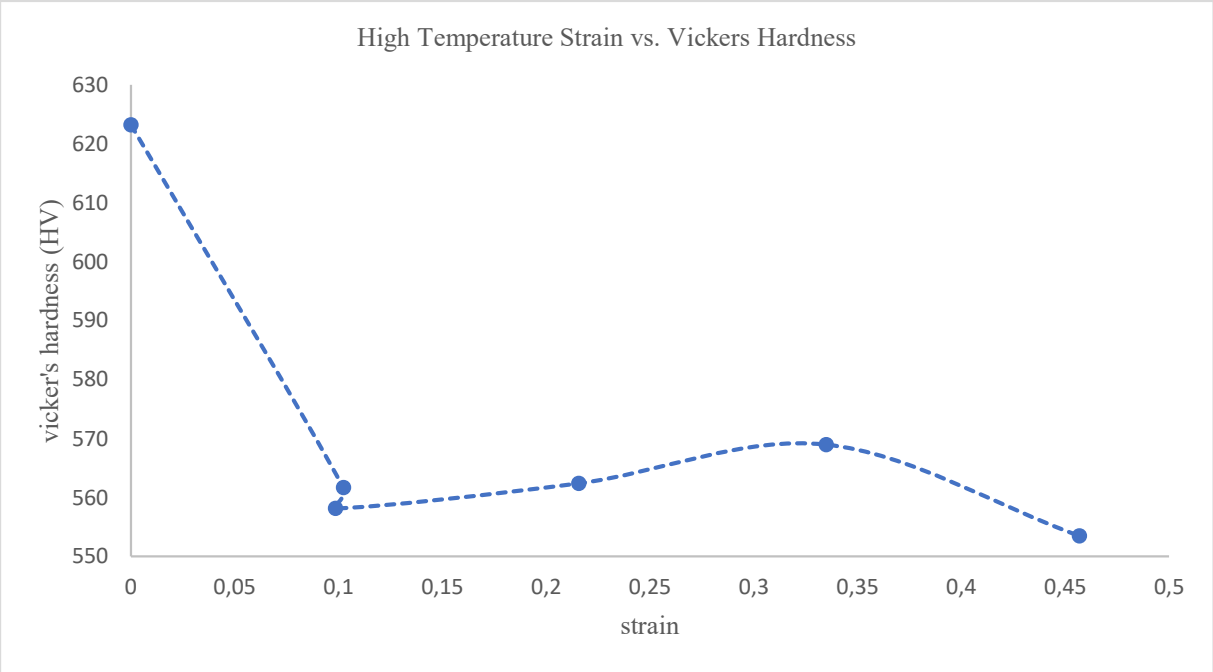


*Figure 4.210: Graphical representation of the effect of strain reduction of microhardness*

Figure 4.211 displays the microstructure of an undeformed TiAlMn. The volume proportion of β phase was estimated to be 22.37% using image J as displayed in Figure 4.212. Figure 4.213 shows the microstructure at higher magnification, and it was seen that the microstructure was dominated by singular and agglomerated $\alpha_2$ globules (labelled i) which had grain diameters ranging from 5.5µm to 12µm. The matrix was comprised of β phase labelled (ii) and within the matrix are smaller γ lamellar grains with grain lengths ranging from 2µm to 4µm and widths ranging from 0.300µm to 1.000µm labelled (iii).

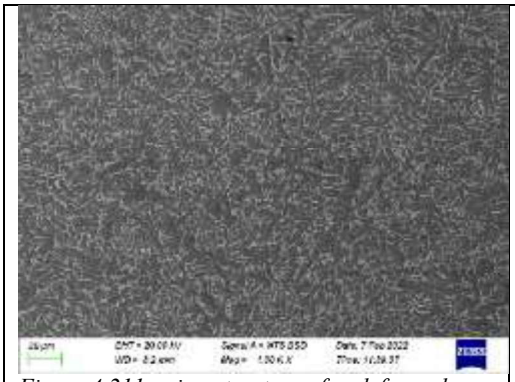

*Figure 4.211: microstructure of undeformed TiAlMn sample taken at Magnification of 20µm (x1000).*

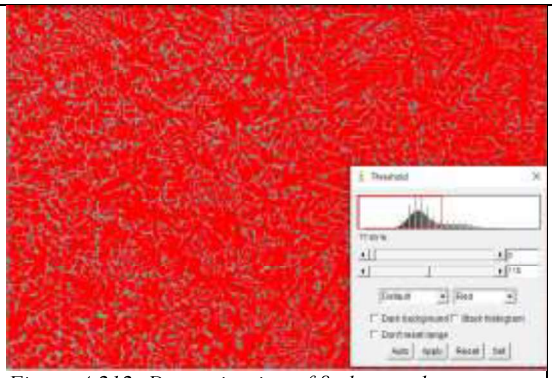

*Figure 4.212: Determination of β phase volume proportion (22.37%) using Image J for undeformed TiAlMn sample.*

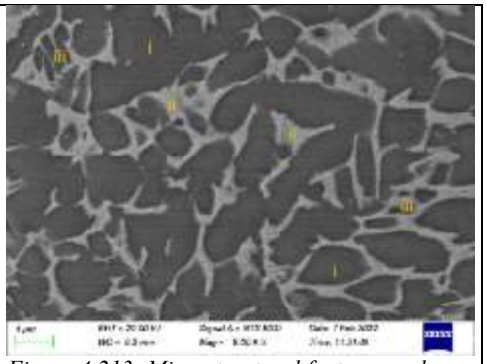

*Figure 4.213: Microstructural features and grain boundaries of undeformed TiAlMn sample taken at magnification of 4µm (x1000).*

Figure 4.214 displays the microstructure along the tensile axis of TiAlMn deformed at 1000°C and compressed at 10.78% strain reduction. The volume proportion of β phase was estimated to be 39.51% using image J as displayed in Figure 4.215. Figure 4.216 shows the microstructure at higher magnification and it was seen that the microstructure was comprised with more singular and less agglomerated $\alpha_2$ globules (labelled i) which had grain diameters ranging from 3μm to 4μm. The matrix was comprised of β phase (labelled ii) and within the matrix were smaller γ lamellar grains with lengths ranging from 2.000μm to 3.700μm and widths ranging from 1.000μm to 1.500μm (labelled iii). Figures 4.217 to 4.219 display the microstructure, phase proportions and high magnification microstructure of sample deformed at 10.89% strain. Microstructural features and grain parameters of this sample were similar to those deformed with 10.78% strain with a slightly higher β proportion of 41.14%, but structure appeared to have slightly more buckling along the tensile axis.

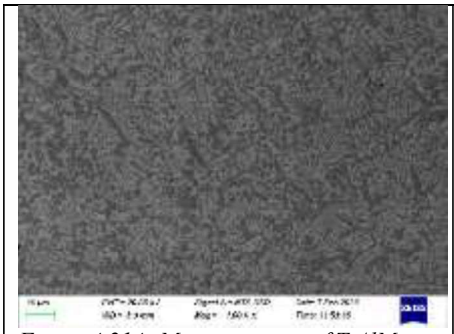

*Figure 4.214: Microstructure of TiAlMn sample deformed to 10.78% strain reduction taken at Magnification of 20μm (x1000).*

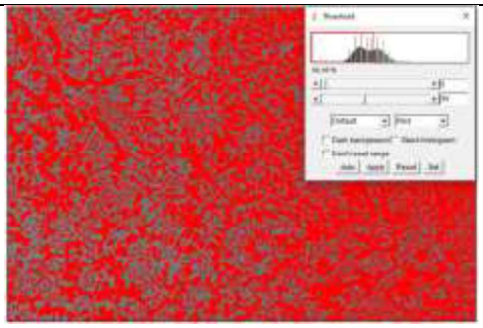

*Figure 4.215: Determination of β phase volume proportion (39.51%) using Image J for TiAlMn sample deformed to 10.78% strain reduction.*

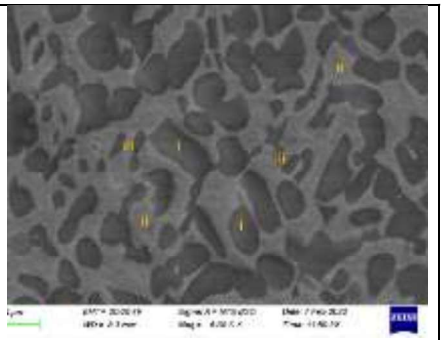

*Figure 4.216: Microstructural features and grain boundaries of TiAlMn sample deformed to 10.78% strain reduction taken at magnification of 4μm (x1000).*

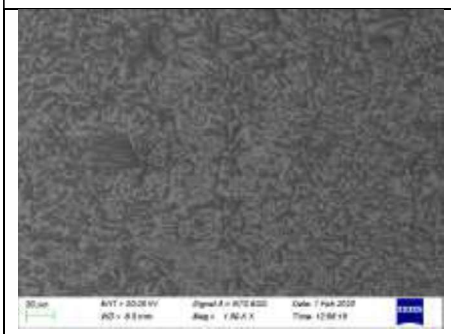

*Figure 4.217: Microstructure of TiAlMn sample deformed to 10.89% strain reduction taken at Magnification of 20μm (x1000).*

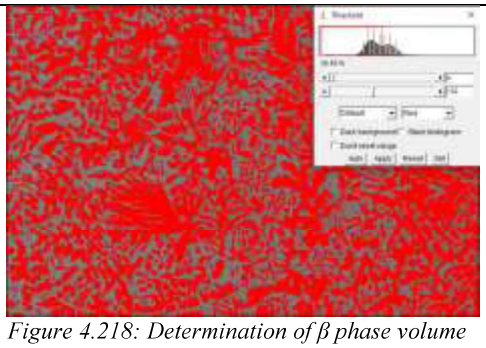

*Figure 4.218: Determination of β phase volume proportion (41.14%) using Image J for TiAlMn sample deformed to 10.89% strain reduction.*

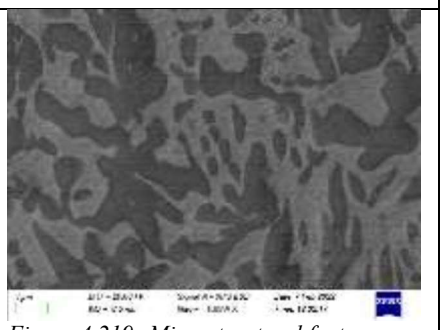

*Figure 4.219: Microstructural features and grain boundaries of TiAlMn sample deformed to 10.89% strain reduction taken at magnification of 4μm (x1000).*

Figure 4.220 displays the microstructure along the tensile axis of TiAlMn deformed at 1000°C and compressed at 22.75% strain reduction. The volume proportion of β phase was estimated to be 50.46% using image J as displayed in Figure 4.221. Figure 4.220 shows the microstructure

at higher magnification, and it was seen that the microstructure was also comprised with less $\alpha_2$ globules which have grain diameters ranging from 3µm to 4µm. The γ phase within the matrix increased in proportion and had lamellar grain lengths ranging from 3.000µm to 8.443µm and widths ranging from 0.971µm to 1.684µm. Further buckling was evident in the structure.

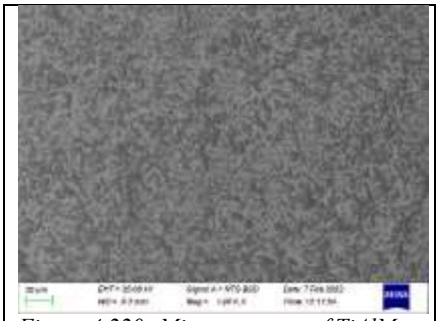

*Figure 4.220: Microstructure of TiAlMn sample deformed to 22.75% strain reduction taken at Magnification of 20µm (x1000).*

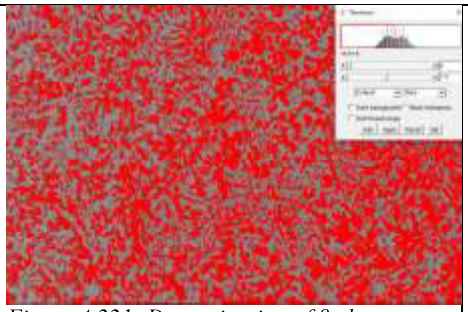

*Figure 4.221: Determination of β phase volume proportion (50.46%) using Image J for TiAlMn sample deformed to 22.75% strain reduction.*

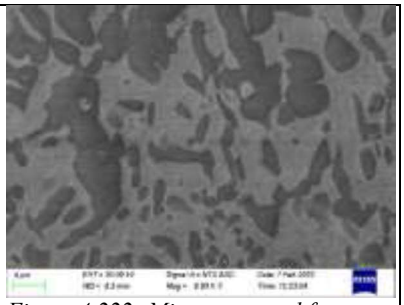

*Figure 4.222: Microstructural features and grain boundaries of TiAlMn sample deformed to 22.75% strain reduction taken at magnification of 4µm (x1000).*

Figure 4.223 displays the microstructure along the tensile axis of TiAlMn deformed at 1000°C and compressed at 34.58% strain reduction. The volume proportion of β phase was estimated to be 44.34% using image J as displayed in Figure 4.224. Figure 4.225 shows the microstructure at higher magnification, and it was seen that the microstructure was also comprised with even less $\alpha_2$ globules which have grain diameters ranging from 3µm to 4µm. The γ phase within the matrix increased in proportion reducing the β phase proportion and had lamellar grain lengths ranging from 2.5µm to 8.443µm and widths ranging from 0.890µm to 1.145µm. Further buckling was also evident in the structure along the tensile axis.

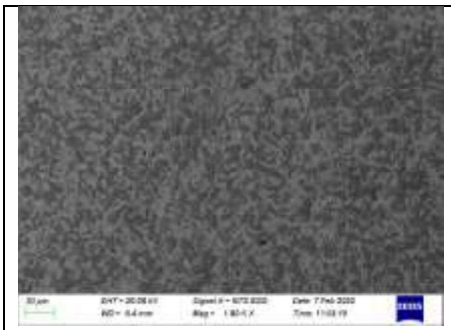

*Figure 4.223: Microstructure of TiAlMn sample deformed to 34.58%strain reduction taken at Magnification of 20µm (x1000).*

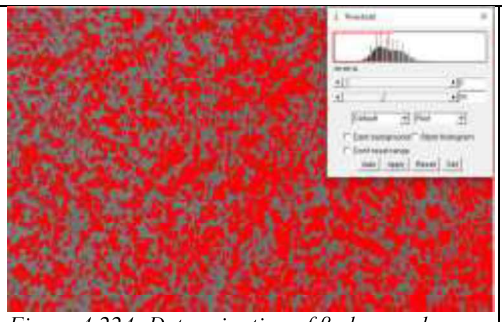

*Figure 4.224: Determination of β phase volume proportion (44.34%) using Image J for TiAlMn sample deformed to 34.58% strain reduction.*

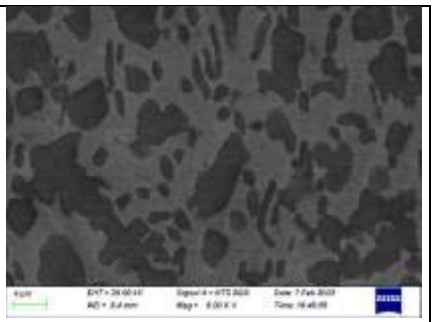

*Figure 4.225: Microstructural features and grain boundaries of TiAlMn sample deformed to 34.58% strain reduction taken at magnification of 4µm (x1000).*

Figure 4.226 displays the microstructure along the tensile axis of TiAlMn deformed at 1000°C and compressed at 46.50% strain reduction. The volume proportion of β phase was estimated to be 51.84% using image J as displayed in Figure 4.227. Figure 4.228 shows the microstructure at higher magnification and a reduction in $\alpha_2$ globules was evident which still had grain diameters ranging from 3µm to 4µm. The γ phase within the matrix increased in proportion and had lamellar grain lengths ranging from 4.440µm to 8.617µm and widths ranging from 0.971µm to 1. 684µm. Further buckling of the structure was also evident along the tensile axis.

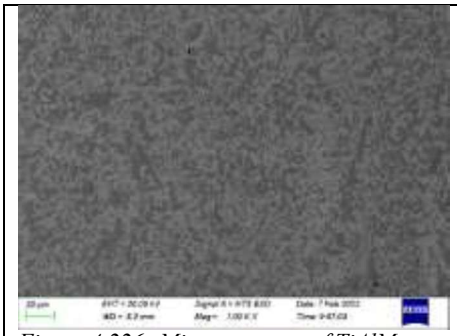

*Figure 4.226: Microstructure of TiAlMn sample deformed to 46.50% strain reduction taken at Magnification of 20µm (x1000).*

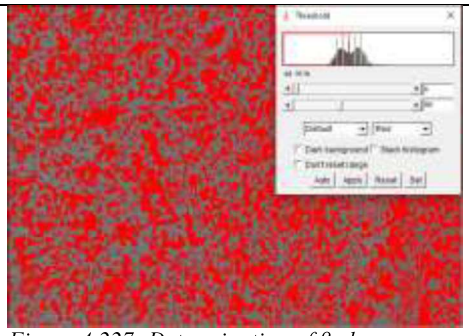

*Figure 4.227: Determination of β phase volume proportion (51.84%) using Image J for TiAlMn sample deformed to 46.50% strain reduction.*

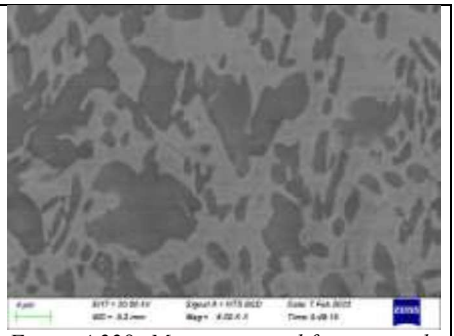

*Figure 4.228: Microstructural features and grain boundaries of TiAlMn sample deformed to 46.50% strain reduction taken at magnification of 4µm (x1000).*

The β phase was comprised of an average of 84.57at%Ti, 7.79at%Al and 7.64at%Mn. The $\alpha_2$ globules were comprised of 93.59at%Ti, 5.09at%Al and 1.32at%Mn. γ lamellae was comprised of 91.27at%Ti, 6.90at%Al and 1.83at%Mn. These compositions were obtained from EDX.

Figure 4.229 shows the effects of strain reduction on lattice parameters of different phases. Between 10.89% and 10.78%, cubic lattice parameter $a_\beta$ reduced due to buckling of the structure also observed in SEM micrographs (Figures 4.216 and 4.219). However, at 22.75% strain reduction, lattice parameter $a_\beta$ increased with an increase in β phase volume proportion. At 34.58% and 46.50% strain reduction, $a_\beta$ continued to reduce due to buckling.

Hexagonal lattice parameter $a_\alpha$ remained unchanged under all strain reductions, but $c_\alpha$ increased between 10.78%, 10.89% and 22.75% and was followed by reduction at 34.58% and 46.50%.

Tetragonal lattice parameter $a_\gamma$ increased gradually with an increase in γ phase as strain reduction increased. While tetragonal lattice parameter $c_\gamma$ increased rapidly at strain reductions 10.78% and 10.89% and continued to reduce at 22.75%, 34.58% and 46.50%.

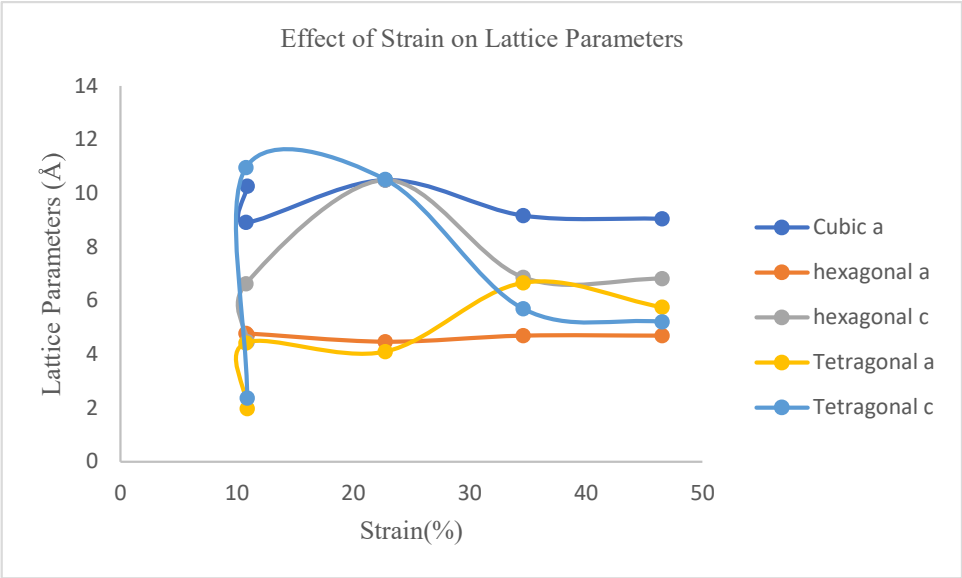


*Figure 4.229: Effects of strain Reduction on Lattice Parameters*

Figure 4.230 indicates that $\alpha_2$ and $\gamma$ phase had similar lattice volumes under all compression strains tested while $\beta$ had significantly higher lattice volumes which were affected both by phase volume proportions and buckling of the structure.

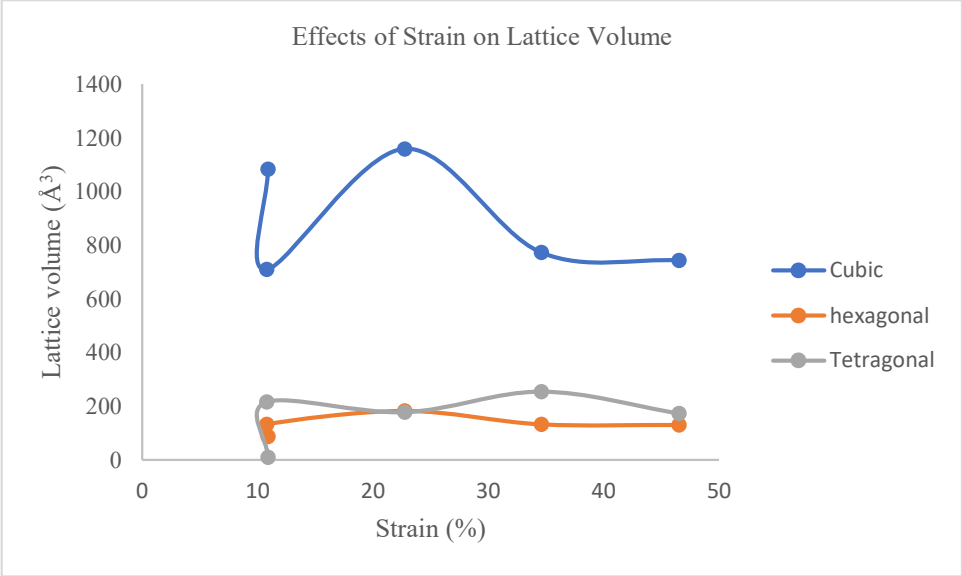


*Figure 4.230: Effects of Strain Reduction on Lattice Volume*

Figure 4.231 indicates that dislocation densities increased with increasing strain until 34.58% strain reduction, then decreased at 46.50%. The dislocation densities increased in a similar fashion to the stress and strain where yield stress increased with strain until 34.58% reduction (Figure 4.209). At 46.50% the yield stress decreased. Microhardness behaved in a similar fashion where microhardness increased with strain until 34.58% reduction and reduced at 46.50% reduction (Figure 4.211). As c/a ratio reduces, dislocation densities increase with strength.

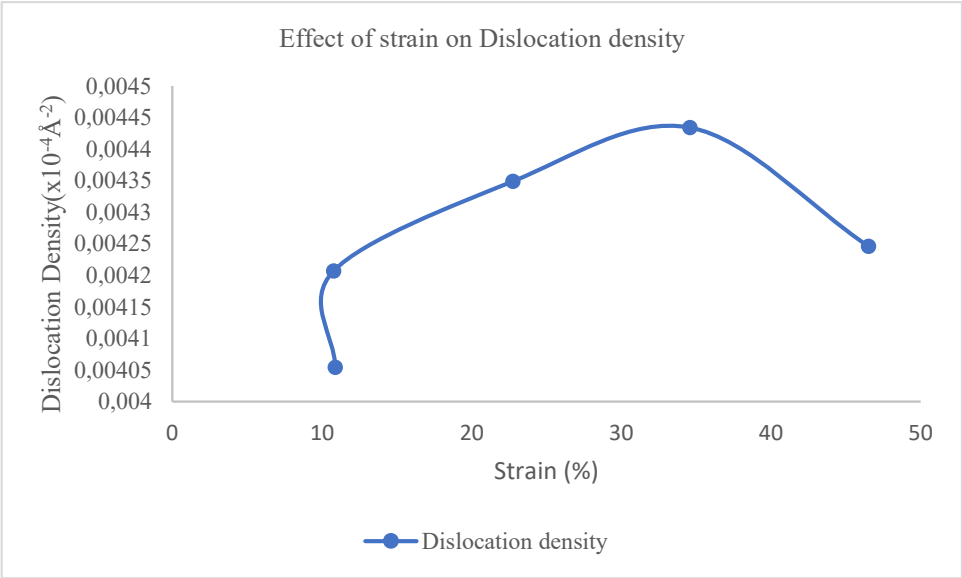


*Figure 4.231: Effects of strain reduction on dislocation density*

In Figure 4.232 it was observed that the most favourable combination of ductility and strength were achieved at a hexagonal c/a ratio of 1,4625 and a tetragonal c/a ratio of 0,85413. These ratios favoured dislocation motion which favoured good yield stress values but also favour ductility as strain increases. However, at higher strain, dislocation densities reduce due to restriction.

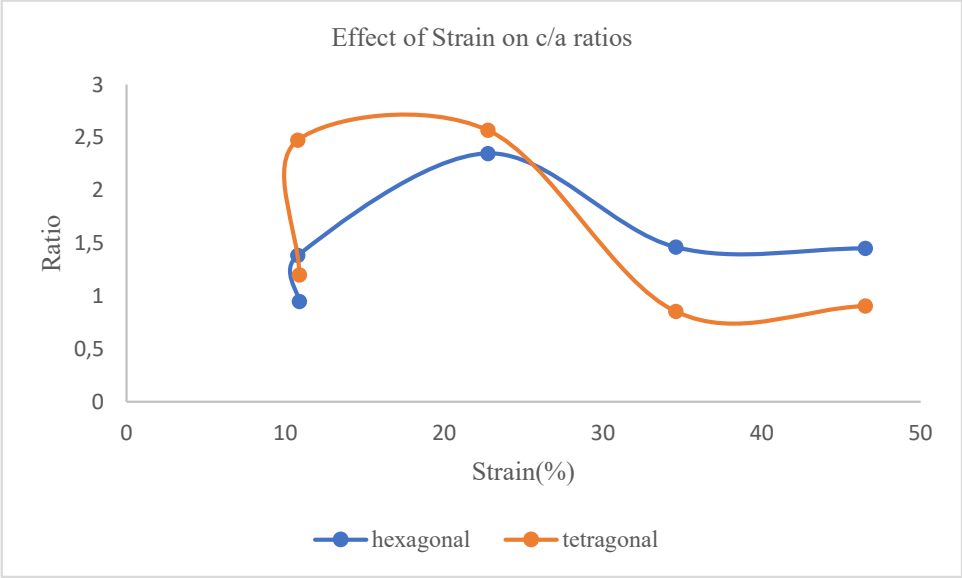


*Figure 4.232: Effect of strain on c/a lattice ratios*

## 4.4. Numerical Modelling

After conducting the above experiments, it was pertinent to delve deeper into the aforementioned findings using the numerical modelling approach. Tlotleng (2019) and Guangyu *et al.* (2016) stated that a single deposited unit length of printed product, subjected to laser power, experiences melting and solidification twice during printing. The initial melting

and solidification are experienced when the unit length is deposited from the nozzle, and the second melting and solidification is experienced when another unit length is deposited on top of the previously deposited unit length. This is experienced repeatedly by subsequent layers, until the intended build (in this case a cube) is completed. This process of re-melting is accounted for by the thermal conductivity of the intermetallic alloys, which allows for the conduction of adequate heat energy from the melt pool to be transferred to the previously deposited layer during deposition (Guangyu *et al.,* 2016; Tlotleng, 2019). Total thermal energy transferred from the laser to a single unit length of deposited length is displayed in Equation 4.2:

$$\Delta H = 2.304 \times LEPUL \tag{4.2}$$

Where LEPUL is the Laser Energy Per Unit Length (Gu *et al.,* 2015). The LEPUL was calculated using Equation 4.3:

$$LEPUL = \frac{Laser\ Power\ (\frac{J}{s})}{Scanning\ Speed\ (\frac{cm}{s})} \tag{4.3}$$

In addition, the total amount of heat energy absorbed by a single deposited unit length, during LENS deposition, is the product of the integral of the specific heat with respect to temperatures speed, and the moles of Ti in the resultant phases. The moles of Ti are used since Ti had the highest melting point temperature when considering elements used in this study. Thus, the minimum energy required to facilitate melting of deposited metal powders must be high enough to melt Ti powder (Sciammarella and Salehi Najafabadi, 2018; Valencia and Quested, 2013) Heat energy can be calculated as displayed in Equation 4.4:

$$\Delta H = n_{Ti} \times C_p \Delta T \tag{4.4}$$

Heat energy can also be calculated as displayed as in Equation 4.5:

$$\Delta H = n_{Ti} \times \int_{298}^{T_M} C_p \ dT \tag{4.5}$$

Where n is the total amount of Ti moles (Sciammarella and Salehi Najafabadi, 2018) in the build, $C_p$ is the specific heat (J/mol-K) and T is the temperature velocity (K/cm) since deposition nozzle moves at a velocity (Bontha *et al.,* 2006; Sciammarella and Salehi Najafabadi, 2018). The temperature values of the specific heat $C_p$ for various phases are displayed in Table 4.17:

*Table 4.17: Specific Heat values for various phases with respect to Temperature*

| **$C_P$ (T) (J/mol-K)** | **Temperature Range (K)** | **References** |
|---|---|---|
| $C_{P(Ti,\alpha)} = 5.28 + 2.4x10^{-3}T$ | 298 – 1155 | (Mills, 2002; Smithells and Brandes, 1992) |
| $C_{P(Ti,\beta)} = 4.74 + 1.9x10^{-3}T$ | 1155 – 1350 | (Mills, 2002; Smithells and Brandes, 1992) |
| $C_{P(Ti,l)} = 11.042$ | 1943 | (Mills, 2002; Smithells and Brandes, 1992) |
| $C_{P(Ti,\gamma)} = 47.32 + 5.568x10^{-3}T - 1.549x10^{-5}T^2 + 2.223x10^{-8}T^3$ (value could not be used since it was measured under different conditions) | 673 - 1703 | (Egry *et al.,* 2007) |

Phases were determined through the correlation of literature (including phase diagrams- Figure 2.7), SEM micrographs (Figures 4.57 to 4.74) and EDS results (Table 4.12). According to SEM-EDX, the amount of Ti in α and β was also influenced by thermal gradients which governed phase segregation mechanisms. Larger thermal gradients and slower cooling rates led to the segregation of Ti to α grains. The microstructures and phases obtained in the as produced builds indicated the occurrence of phase transformation reactions as displayed in Table 4.18.

*Table 4.18: Phase transformation reactions in various alloys.*

| **Alloy** | **Phase Transformation Reactions** | **References** |
|---|---|---|
| Ti-Mn | $L \rightarrow L + \beta \rightarrow \beta$<br>$L \rightarrow L + \beta \rightarrow \beta \rightarrow \beta + \alpha \rightarrow \alpha$ | (Croat *et al.,* 1999; Kamara *et al.,* 2014; Shen *et al.*, 2016) |
| | $L \rightarrow \alpha$ (net transformation) – dendrites<br>$L \rightarrow \beta$ (net transformation)<br>$L \rightarrow \beta \rightarrow \alpha$ (net transformation) – equiaxed grains | |
| Ti-Al | $L \rightarrow L + \beta \rightarrow \beta \rightarrow \beta + \alpha \rightarrow \alpha$ | (Appel *et al.,* 2011a; Imayev *et al.,* 2007) |
| | $L \rightarrow \alpha \rightarrow \alpha + \gamma \rightarrow \alpha_2 + \gamma$ (net transformation) | |
| Ti-Al-Mn | $L \rightarrow L + \beta \rightarrow \beta$<br>$L \rightarrow \beta$ (net transformation)<br>$L \rightarrow L + \beta \rightarrow \beta + \alpha_2 \rightarrow \alpha_2$<br>$L \rightarrow \beta \rightarrow \alpha_2$ (net transformation)<br>$L \rightarrow L + \beta \rightarrow \beta \rightarrow \beta + \gamma \rightarrow \gamma$<br>$L \rightarrow \beta \rightarrow \gamma$ (net transformation) | (Li *et al.,* 2018a) |

Equations listed in Table 4.17 were substituted into Equations 4.6 to 4.9 in accordance with the phase transformation reactions listed in Table 4.18. This was done to calculate the unknown solidification temperature velocities depicted as $T_S$ (K/cm) (Sciammarella and Salehi Najafabadi, 2018; Zheng *et al.,* 2008). The values for $T_S$ were obtained on Microsoft EXCEL using SOLVER. Below are equations used to solve for $T_S$:

For various builds, $T_S$ is obtained by solving equations 5 to 8 for $T_S$

$$\Delta H_{L\to\beta} = n_{Ti}\left[\int_{TS}^{1943} C_{p(Ti,l)}\ dT + \int_{\beta(1350)}^{TS} C_{p(Ti,\beta)}\, dT + \int_{298(RT)}^{T_{\beta(1350)}} C_{p(Ti,\beta)}\ dT\right] \quad (4.6)$$

$$\Delta H_{L\to\beta\to\alpha(equiiaxed)} = n_{Ti}\left[\int_{T_S}^{1943} C_{p(Ti,l)}\ dT + \int_{T_{\beta(1350)}}^{T_S} C_{p(Ti,\beta)}\ dT + \int_{T_{\alpha(1155)}}^{T_{\beta(1350)}} C_{p(Ti,\beta)}\ dT + \int_{298(RT)}^{T_{\alpha(1155)}} C_{p(Ti,\alpha)}\ dT\right] \quad (4.7)$$

$$\Delta H_{L\to\alpha\ (dendrites)} = n_{Ti}\left[\int_{T_S}^{1943} C_{p(Ti,l)}\, dT + \int_{298(RT)}^{T_S} C_{p(Ti,\alpha)}\, dT\right] \quad (4.8)$$

$$\Delta H_{L\to\beta\to\gamma} = n_{Ti}\left[\int_{T_S}^{1943} C_{p(Ti,l)}\ dT + \int_{T_{\beta(1350)}}^{T_S} C_{p(Ti,\beta)}\ dT + \int_{298(RT)}^{T_{\gamma(1350)}} C_{p(Ti,\gamma)}\ dT\right] \quad (4.9)$$

It was assumed that the minimum temperature required from the laser should be high enough to melt Ti powder. Thus, $T_M$= 1943K (Murray, 1981; Schuster and Palm, 2006) was used. Values obtained for $T_S$ allowed for the calculations of the cooling rates per unit length during deposition until solidification was complete. These numerical models could be depicted in Figure 4.233.

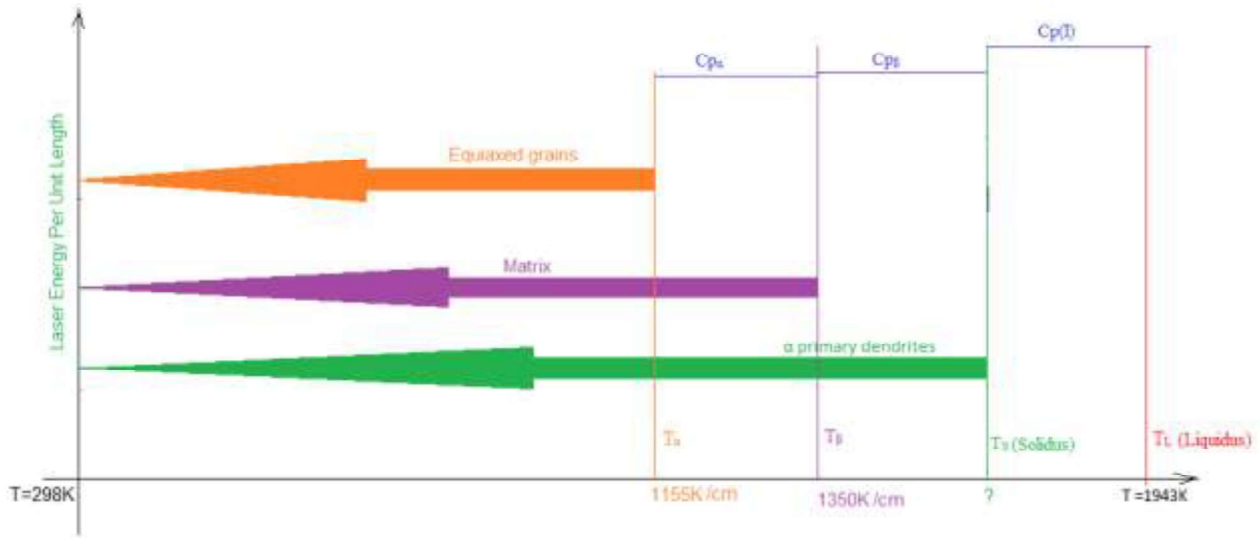


*Figure 4.233: Visual presentation of phase transformation processes during laser deposition.*

Thermal gradient of a singular deposited unit length until the completion of solidification with respect to time is displayed in equation 4.10 as the derivative of temperature with respect to time which is inversely proportional to cooling rates and solidification rates as displayed in Equation 4.11 (Bontha *et al.,* 2006).

$$\frac{\partial T}{\partial t} = \frac{|T_M - T_S|}{t_M - t_S} = \frac{|T_M - T_S|}{\Delta t}\ \alpha \frac{1}{cooling\ rates} \quad (4.10)$$

$$R = \frac{1}{G}\frac{\partial T}{\partial t} \quad (4.11)$$

Where Δt is the time taken to deposit a single unit length, R depicts solidification rates and G depicts thermal gradients.

The thermal gradient with respect to unit length deposited can be expressed as a derivative of temperature with respect to unit length Δx as displayed in equation 4.12.

$$\frac{dT}{dx} = \frac{|T_M - T_S|}{\Delta x} \quad (4.12)$$

Thermal gradients:

Thermal gradients to which the α phase and the β phase are subjected were calculated using the afore mentioned numerical models. The effects of altering Mn feed rates and LEPUL on calculated thermal gradients $\frac{dT_\alpha}{dx}$ and $\frac{dT_\beta}{dx}$ are graphically displayed in Figures 4.234 and 4.235. The calculations and EXCEL spread sheet is presented in APPENDIX B. In both Figures, it was observed that thermal gradients $\frac{dT}{dx}$ increased with increasing LEPUL. However, $\frac{dT_\alpha}{dx}$ (Figure 4.234) was not affected by Mn feed rates but $\frac{dT_\beta}{dx}$ (Figure 4.235) increased with increasing Mn feed rates.

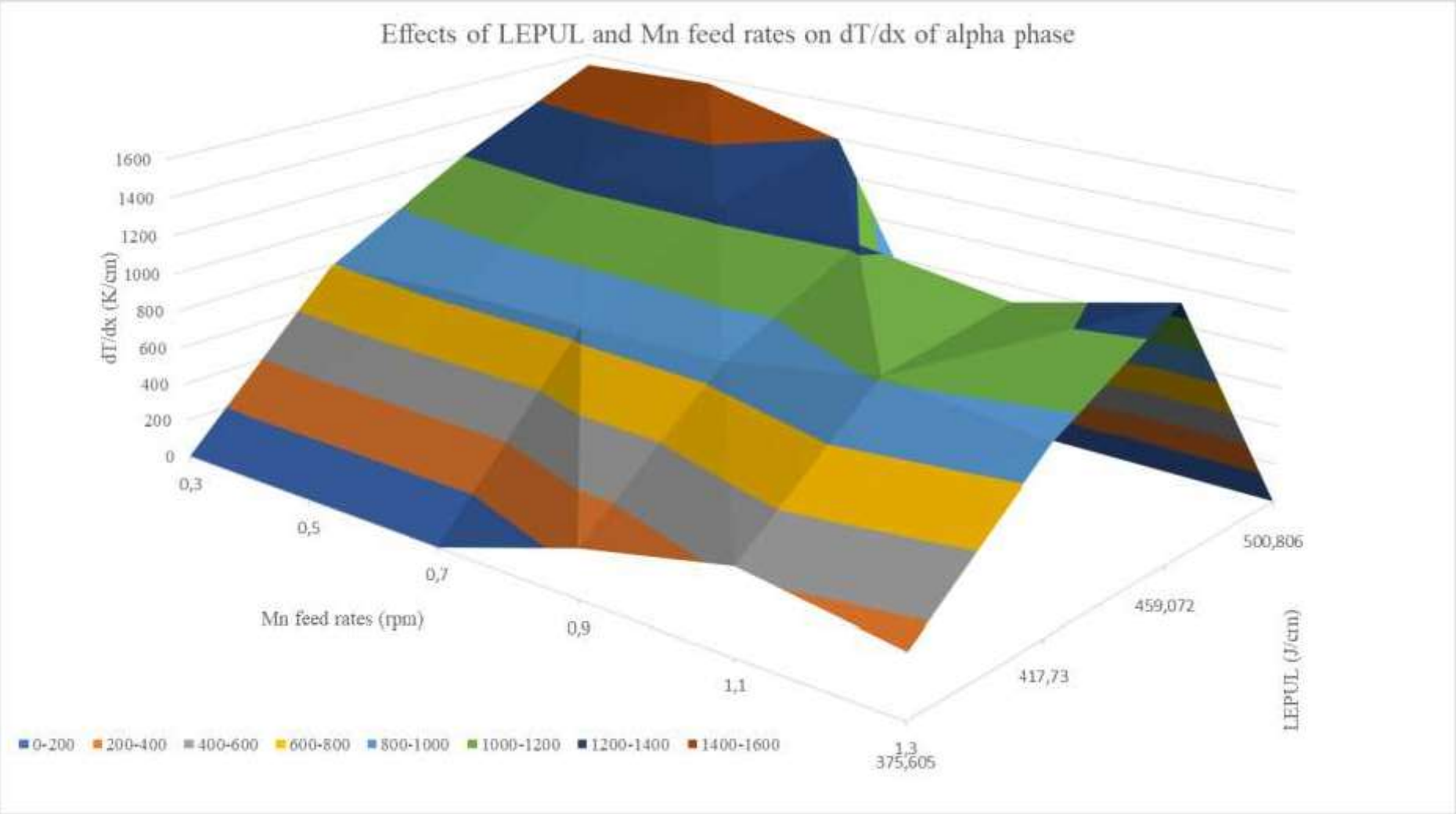


*Figure 4.234: Influence of Mn feed rates and LEPUL on thermal gradients with respect to the x dimension of Ti-α phase.*

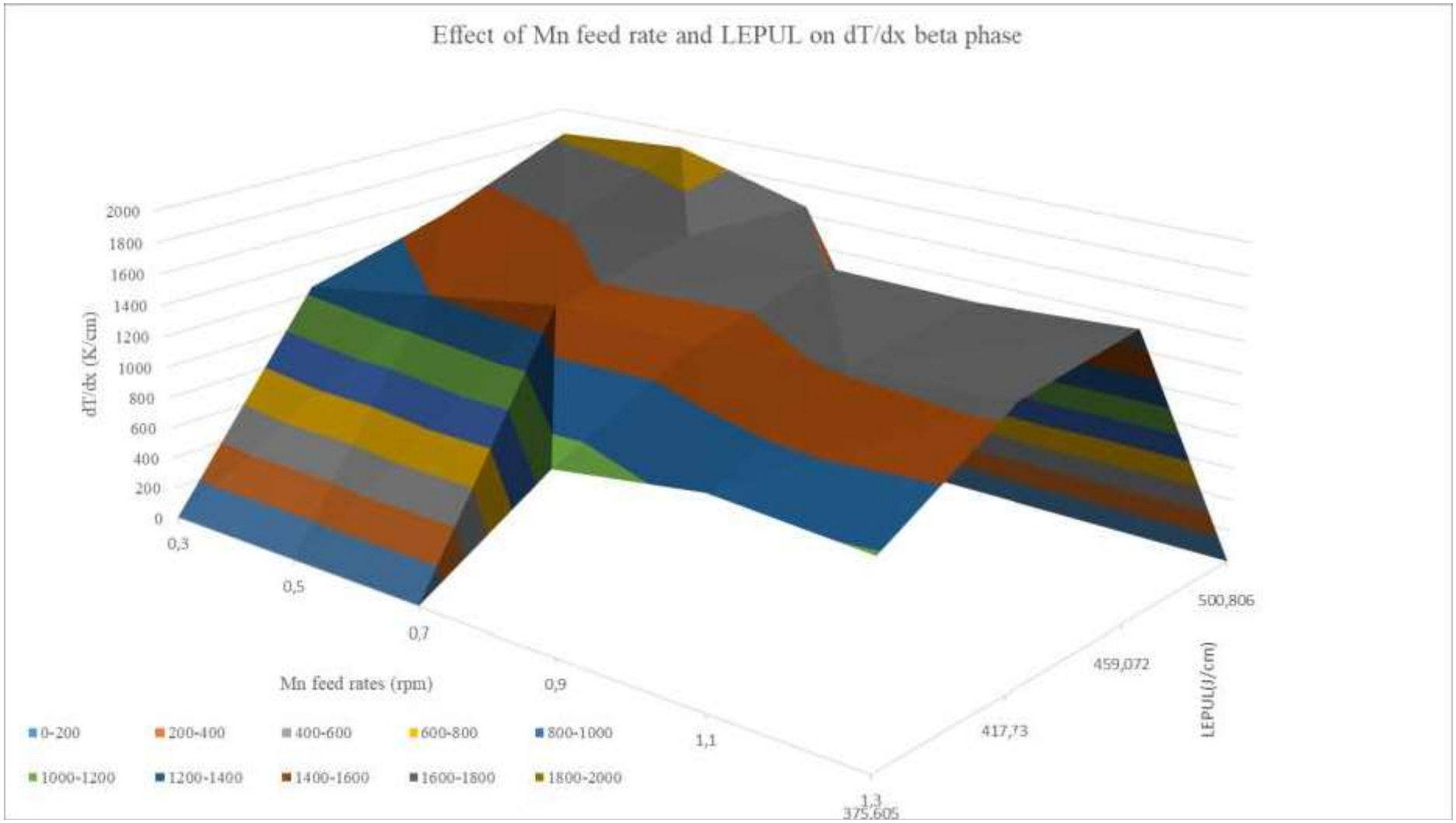


*Figure 4.235: Influence of Mn feed rates and LEPUL on thermal gradients of Ti-β phase.*

## 4.5. Densification

Density measurements on as produced samples studied further were carried out and compared to calculated densities which were based on the arial compositions determined by EDS/EDX. This allowed for the densification of samples during fabrication to be determined. For this study, the densification of the TiMn and TiAl alloys exceeded 100%, while the densification for TiAlMn alloys was lower than 100%. These outcomes are displayed in Table 4.19.

*Table 4.19: Theoretical Density alongside measured density*

| Sample | Calculated bulk density ($g/cm^3$) | Measured density | %Densification |
|---|---|---|---|
| TiAl 2.3 | 3,76704 | | |
| TiAl 2.4 | 3,71106 | 4.05653 | 109.309 |
| TiMn-10 | 4,766044 | 5.52253 | 115.872 |
| TiMn-11 | 4,914888 | 5.05905 | 102.933 |
| TiAlMn1 | 4.771946 | 4.39700 | 92.144 |

# Chapter 5: Discussions

After the experimental procedures were undertaken and results were obtained, various analogies were made and are discussed in this section. The effects of increasing Ar carrier gas flowrates, Mn addition, adjusting laser power during laser deposition and applying post process heat-treatment, on microstructure, crystal orientations, dislocation densities and microhardness were discussed, and conclusions were drawn from these analyses. Focus was also placed on how varied LENS parameters and their effected on post processing thermal cracking.

Binary TiAl Alloys

The findings which resulted from altering Al feed rates and Ar gas flowrates on microstructures and mechanical behaviour are discussed in this section. This section also discusses the effects of heat treatment on microstructures and mechanical properties of binary TiAl alloys.

Ar gas allows for the conservation of thermal energy, similar to He which is also an inert gas (Ogino and Hirata, 2015; Traidia *et al.,* 2011). This conservation of heat energy influenced by Ar gas conductivity enhances higher ratios of convective heat transfer of Ar gas to radiative heat transfer at melt free solidified surfaces during laser deposition (Li *et al.,* 2011). This enabled higher radiative heat transfer to melt free surface which enable solid state phase reactions (Appel et al., 2011a) on melt free surface post laser deposition. This led to the formation of nearly lamellar and fully lamella microstructures which form through solid state phase transformation reactions (Appel, 2010). As Ar gas flow rates increased, it became easier to blow the gas on the solid melt free surface, which increased heat transfer ratios (Li *et al.,* 2011).

At low Al concentrations (45 – 49at%Al) which resulted from low Al feed rates (1.5rpm), solidification took place through recrystallization of the β dendrites from melt, followed by the peritectic formation of α phase *(McCullough et al.,* 1989; Schuster and Palm, 2006) upon cooling. The development of these microstructures as Ar gas flowrates were increased were evident in microstructures observed in as-produced state as Ar gas flow rates were increased. These microstructures provided evidence that increase Ar gas flow rates allowed peritectic phase reaction: $\beta \rightarrow \beta + \alpha \rightarrow \alpha$ where α plates were formed and while Ti segregated to remaining β ribs (Küstner *et al.,* 2003). As Ar gas flow rates were increased further, γ lamellae precipitated within α plates forming α+γ nearly lamellar or basket weave structure through the

following solid state phase transformation reactions: $\alpha \rightarrow \alpha + \gamma$ (Küstner *et al.,* 2003; McCullough *et al.,* 1989).

At higher Al concentrations above 49at%Al, α columnar dendrites recrystalized from melt and later transformed to γ phase through solid state phase transformation reaction: $\alpha \rightarrow \alpha + \gamma \rightarrow \alpha_2 + \gamma$ on cooling leading to fully lamellar equiaxed microstructure produced (McCullough *et al.,* 1989). These microstructural developments were observed as Ar gas flow rates were increased. This confirmed that increasing Ar gas volumetric flow rates allowed for solid state transformation reactions which produced equiaxed granular structures (Küstner *et al.,* 2003) and enhanced the production of γ phase.

Increasing Ar carrier gas flowrates also led to a decrease in tetragonal lattice parameters and volume. Which also led to reduced interplanar spacings in tetragonal lattices. However, the hexagonal lattice parameter *a* decreased while *c* increased. This led to a slight increase in hexagonal lattice volumes. The increase in hexagonal lattice parameter *c* was accredited to Ar interstitial atoms which occupy the lattice along the *c*-axis. This forced the lattice to increase in size along the c-axis to accommodate the Ar atoms (Khojier *et al.,* 2013). Since hexagonal structure is the brittle and hard phase due to its complexity which restricts dislocation motion during microhardness indentation (Appel and Wagner, 1998; Gebhard *et al.*, 2009; Kim *et al*., 2014), thus increased hexagonal lattice volume led to a slight increase in microhardness in TiAl alloys as Ar gas flowrates increased. A significant reduction in dislocation densities due to increased Ar carrier gas flowrates was also observed.

Heat treating at 950°C caused low Al concentration builds to produce fully lamellar $\alpha_2$+γ equiaxed grain microstructures (Appel, 2010), while higher Al concentrations (above 49at%Al) produced uniform duplex γ fine grained microstructures (Kim, 1994). According to Schuster and Palm, (2006), phases produced during heat treatment are generally thermodynamically favourable at 950°C.

At low Al concentrations as Ar carrier gas flow rates were increased, the equiaxed microstructure appeared coarser in the heat-treated state. This indicated a reduction in cooling rates as Ar gas flow rates were increased since grain growth and coarsening were enhanced by slower cooling rates (Gil *et al.*, 2001).

When heat treatment was carried out on TiAl alloys, it led to an increase in dislocation densities, which were accompanied by a significant reduction in microhardness values. This further validated that increased dislocation densities lead to reduced microhardness in binary

TiAl alloys (Appel, 2010). However, binary TiAl alloys were severely cracked indicating low fracture stress even through their microhardness values were low. These outcomes further support the findings by (Kim, 1994) which reported the existing imbalance between ambient temperature ductility and mechanical strength.

$\alpha_2+\gamma$ had higher microhardness than uniform $\gamma$ (Gebhard *et al.,* 2009). Uniform $\gamma$ microstructures had significantly lower microhardness due to the absence of $\alpha_2$ phase (Kuang *et al.,* 2002). However, uniform $\gamma$ had a higher number of post processing thermal cracks than $\alpha_2+\gamma$ since thermal cracks were initiated at $\gamma$ phase and propagated rapidly in a cleavage fashion through the microstructure. While in two phase $\alpha_2+\gamma$ microstructure, $\alpha_2$ which is harder, served as crack initiation sites and prevented rapid crack propagation during thermal strain. These two-phase microstructures allowed cracks to propagate on $\alpha_2$ in a ligament fashion, hindering rapid crack propagation during thermal stress to which materials were subjected. In $\alpha_2+\gamma$ structures, the $\alpha_2/\gamma$ interfaces allow for dislocation motion during fracture which prevented stress concentrations on $\alpha_2/\gamma$ interfaces, which also prevents brittle fracture behaviour and lowers fracture stress. Uniform duplex $\gamma$ led to stress concentrations on $\gamma/\gamma$ interfaces which accelerated fracture and led to brittle behaviour of the structure (S.-W. Kim *et al.,* 2014). These stress concentration on $\gamma/\gamma$ interfaces also led to reduced fracture stress. This mechanical behaviour is similar to outcomes reported by Kuang *et al.*, 2002 where microhardness and tensile properties reduced simultaneously and the study was concluded by stating that although $\alpha_2$ is harder than $\gamma$, it has the ability to to improve the both strength and ductility since it enables dislocation glide relaxation.

When nanoindentations were carried out on TiAl alloys both on the heat-treated and as-produced states, extremely low ambient temperature tensile strength was calculated. This further validated the low fracture stress calculated from post processing thermal crack lengths. This means that the brittle behaviour of the alloys was accredited by low yield stress and fracture stress, even though the microhardness values were low.

When oxidation behaviour of TiAl was studied using thermogravimetric analysis, it could be observed that TiAl alloys had the lowest mass gains but also had the thickest oxide films recorded when microstructures were studied. This behaviour was due to the low density of TiAl alloys and its oxides. It was also observed that the formation of the $Al_2O_3$ served as a protective scale which delayed oxidation of the material after its formation but became less effective over time and as temperature increased. These findings were similar to findings by (Chang, 2007).

Binary TiMn Alloys

As LEPUL increased, the melt pool dimensions (length and penetration depth) during laser deposition increased (Assuncao et al., 2012). This led to an increased temperature drop from liquidus ($T_L$) and solidus ($T_S$) resulting in increased$\frac{dT}{dx}$. $\frac{dT}{dx}$ Increases with increasing LEPUL and reducing cooling and solidification rates (Bontha *et al.*, 2006). These solidification mechanisms are attributed to convective heat transfer, which was highly dependent on thermal diffusivity and surface temperature coefficients. High thermal diffusivity and lower temperature coefficients enabled heat transfer by conduction during deposition (Rai *et al.,* 2007)

These thermophysical mechanisms were evident in the microstructural development of TiMn alloys. As LEPUL was increased in low Mn alloys, α dendrites increased in size and quantity. This is the result of the increased drop from $T_L$ to $T_S$, which allowed further crystallization of α dendrites before the completion of solidification. This also allows for the segregation of Ti to the α phase and Mn to the β phase.

As Mn content increased, β phase increased and α phase decreased. This occurred because Mn is a β phase stabilizer (Holden *et al.,* 1954; Murray, 1981) while the solubility of Mn in α phase is highly limited (Murray, 1981). This leads to the nucleation and precipitation of Mn on α grain boundaries in the form of $Mn_{0.52}Ti_{0.48}$(s) (Croat *et al.*, 1999) as Mn was increased further. $Mn_{0.52}Ti_{0.48}$(s) is a brittle phase since it led to increased microhardness (Keryvin *et al.,* 2009), post processing thermal crack density and low fracture stress.

When LEPUL was increased at low Mn, the ductility improved which is observed by reduction in microhardness and post processing thermal cracking, and increased fracture stress. $\frac{dT_\beta}{dx}$ increased with increasing microhardness as Mn in the composition increased, while $\frac{dT_\alpha}{dx}$ remained unaffected by Mn compositions.

When Mn was increased and LEPUL was decreased, the production of $Mn_{0.52}Ti_{0.48}$(s) was enhanced. The increased microhardness was due to the self-diffusion rates of Mn being higher than those of Ti (Polmear *et al.,* 2017). This led to the β phase having diffusion rates with magnitudes three times faster than α phase (Polmear *et al.,* 2017). This enables β to store higher magnitudes of energy within alloy surfaces which led to smaller microhardness indentations and higher microhardness values due to more energy working against forces applied by the microhardness indenter.

Heat treatment of all TiMn alloys led to increased self-diffusion of Mn due to the energy injection resulting from heating (Polmear *et al.*, 2017). This enhanced the self-diffusivity of the TiMn alloys and led to increased stored energy within the surface of the alloy which increased microhardness values post heat treatment. The microhardness values of TiMn are high compared to TiAl, which is accounted by the self-diffusion rates (Polmear *et al*., 2017). The diffusion rates of Mn are higher than Al.

During heat treatment at 950°C, Ti in low Mn alloys underwent α grain boundary segregation which resulted in larger and more Ti saturated α primary dendrites and more Mn rich β phase. Heat treating at 1300°C led to the re-ordering of α dendrites into ω+α equiaxed grains.

Increasing Mn in low Mn alloys led to reduced hexagonal and cubic lattice parameters which led to reduced interplanar spacing. This led to slightly reduced microhardness, dislocation densities and surface cracks. Unlike binary TiAl, reduced dislocation density led to reduced microhardness only in these low Mn alloys studied. This indicates that although the dislocation densities were lower in TiMn11, the dislocations had a greater ability to cross glide between close packed planes and move faster than crack propagation during thermal strain, leading to less stress build up on α/β interfaces which increases fracture stress and resulted in crack free surfaces due to increased fracture stress. These outcomes are due to Mn atoms having smaller radii than Ti atoms, thus substitution of Mn on Ti sublattices led to lattice and interplanar spacing reduction (Kim *et al*., 2016; Shu *et al*., 2012; Wang *et al.,* 2018).However, with the exception of low Mn alloys, TiMn alloys generally had higher microhardness values compared to TiAl alloys and had lower dislocation densities. This further supports that increased dislocation densities reduce microhardness and increased ductility (Appel *et al.*, 2011b). This theory was further supported by increased microhardness and reduced dislocation densities due to heat treatment.

Comparing as-produced TiMn-10 which has one crack to crack free heat-treated TiMn-11 through EBSD analysis it could be observed that the cubic and hexagonal phase distributions were similar. However as produced TiMn-10 contained hexagonal α while heat treated TiMn-11 contained hexagonal α+ω phase. It could also be observed that heat treated TiMn-11 had more homogenous crystal orientations, which is evident in the inverse polar figures and the lower number of orientations counted in the pole figures. The homogeneity of the crystal orientations resulted in lower dislocation densities but higher texture measurements (Li and Rajapakse, 2007; Widjaja and Marks, 2008). The aforementioned factors all contribute to the

crack free surface of TiMn-11 and the α+ω phase contributes to lower microhardness value and improved fracture stress of heat treated TiMn-11 (Santos *et al*., 2015).

When nanoindentation was carried out on TiMn samples, it revealed that α dendrites had low Vicker's hardness but yielded low calculated yield stress and strain compared to β phase which had higher Vickers's hardness values and resulted in higher calculated yield stress and strain values. This also indicates that reduced Vickers's hardness leads to reduced strength, which are findings similar to those of TiAl alloys. However, the α phase had higher stiffness than the β phase. Thus as-produced TiMn-10 and heat-treated TiMn-11 had a good balance of α and β phase which led to a good balance between ductility and mechanical strength which limited post process thermal cracking. Because β phase had higher calculated yield stress, this indicated more dislocation motion during strain, which was further supported by crystal orientations with symmetry folds which have the ability to activate additional appropriate dislocation systems during strain compared to the more complex hexagonal structure (Shu *et al.*, 2012; Wang *et al.*, 2018).

The phase transformation reaction $\alpha \rightarrow \omega$ requires high pressure (P) as displayed in the model demonstrated in Equation 5.1

$$P_{(\omega \rightarrow \alpha)} < P_0 < P_{\alpha \rightarrow \omega} \qquad 5.1$$

According to the Ideal Gas Law displayed in Equation 5.2, the change in temperature (ΔT) during heat treatment in the presence of encapsulated Ar gas, leads to increased pressure, since volume remains constant in this setting (Zarkevich and Johnson, 2016).

$$\Delta PV = nR\Delta T \qquad 5.2$$

Where V depicts volume, n number of moles of gas, R Avogadro's constant. However, Equation 5.3 to 5.5 display that increased pressure and enthalpy (H) results in ideal conditions to facilitate the phase transformation reaction $\alpha \rightarrow \omega$ at 1300°C which is not possible at 950°C because ΔT is not high enough.

$$H = E + PV \qquad 5.3$$

$$H = E + \Delta PV \qquad 5.4$$

$$H = E + nR\Delta T \qquad 5.5$$

When the oxidation of TiMn alloys was conducted, it was observed that TiMn was subjected to higher mass gain than TiAl alloys although they had thinner oxide scales. This was again accredited to the higher density of TiMn alloys. However, it was also observed that $Mn_3Ti_3O$ serves as a protective film which loses its effect over time. It was also established that heat treatment of TiMn at 1300°C slows down oxidation leading to reduced mass loss over time and temperature increase.

Ternary TiAlMn Alloys

Mn addition to TiAl alloys led to a reduction in tetragonal lattice parameters *a* and increased *c* (increased *c/a* ratio) and a reduction in d-spacings (Shu *et al.,* 2012). This led to a reduction in tetragonal lattice volume due to the substitution of Mn atom (which has a smaller radius) on Al sub lattices (which has a larger radius).

However, hexagonal lattice volume increased due to Mn addition to TiAl. These changes in lattice parameters led to a reduction in dislocation densities but increased microhardness values. Increased microhardness and reduced post process thermal cracking can possibly be accredited by reduced dislocation densities and twinning induced plasticity (Inui *et al*., 1992; Jiao *et al.,* 2016; Yoo and Fu, 1998) which led to work hardening and improved strength (fracture stress). The mechanism involved included the repulsive forces between dislocation twin boundaries and atoms leading to the storage of energy within the surface which increased microhardness values. Although microhardness values had increased, the number of cracks in the sample reduced. Since the interplanar spacings between $\alpha_2/\gamma$ interfaces were smaller, this led to higher dislocation cross glide speeds which exceeded crack propagation speeds during thermal strain and resulted in fewer cracks (Appel, 2010; Appel *et al.,* 2011a; Appel and Wagner, 1998; Shu *et al.,* 2012).

Heat treatment of ternary TiAlMn-1 alloy led to an increase in microhardness values and dislocation densities. Increased microhardness values were accounted by the diffusion rates of Mn which are higher than those of Al and Ti (Polmear *et al.*, 2017) and the enhancement of twinning induced plasticity (Jiao *et al.*, 2016). This means that during heat treatment, Mn atoms absorbed energy which resulted in larger amounts of energy being stored within the surface which work against the microhardness indenter during microhardness indentation leading to increased microhardness values and strength (Jiao *et al.*, 2016; Yoo and Fu, 1998). Lattice parameters of tetragonal, hexagonal and cubic structures increased during heat treatment due to thermal expansion, which also led to increased dislocation density. This indicated that

although dislocation densities increased, they were restricted in motion compared to the as-produced state of TiAlMn-1 since the heat-treated sample also indicated a reduction in fracture stress.

Orthohormbic $Al_{2.91}Mn_{1.09}$ lattice parameters decreased during heat treatment. The fractional site occupancy of this phase was 1 which indicated that dislocations were not mobile within this phase.

The increase in Al feed rates led to an increase in volume of γ phase in the microstructure. This again confirms that Al addition is a γ phase stabilizer. The production of γ phase is favourable at lower temperatures (Schuster and Palm, 2006) and slower cooling rates are required to facilitate solid state phase transformation reactions to produce γ phase. These slower cooling rates are favoured by increased Laser Energy per unit length (LEPUL)(Bontha *et al.*, 2006). As LEPUL increased, the sizes of γ platelets within the β matrix increased which led to brittle behaviour (increased hardness and reduced fracture stress).

However, low Al (1.39at%Al) TiAlMn-1 structures which contained minimal γ, yielded increased microhardness and reduced post process thermal cracks. These post processing thermal cracks were smaller than those observed in binary TiAl alloys. The reduction in crack lengths occurred simultaneously with reduction in interplanar spacing between close packed planes. A similar observation was made when crack length increased with increasing d-spacing in heat treated TiAl-2.4 and TiAlMn-1. Reduced interplanar spacings allow dislocations the ability to cross glide easily between planes to enable dislocation glide relaxation during thermal strain, which allows dislocations the ability to move at speeds closer to those of crack propagation during fracture, which led to reduced crack lengths (Shu *et al.*, 2012; Wang *et al.*, 2018).

As-produced high Al (25.39at%Al,10.12at%Mn and 29.20at%Al,6.66at%Mn) ternary alloys were extremely brittle and had the highest microhardness. Both the brittle behaviour and high microhardness is accounted by thermal residual stresses caused by thermal gradients during deposition, leading to higher post processing thermal cracking and microhardness values (Sharman *et al.,* 2018).

Heat-treated high Al (25.39at%Al and 29.20at%Al) samples were fully lamellar $\alpha_2+\gamma$ which had reduced microhardness compared to as-produced state. Although the samples had lower microhardness, they were still extremely friable. This was due to microstructural features not having the appropriate parameters that enable ductility, such as correct interlamellar spacings

and lamellar boundary angle to the tensile axis (Kim *et al.,* 2014; Yamaguchi *et al.,* 2000). Increasing Al in ternary TiAlMn alloys leads to solid state transformation reaction $\beta \rightarrow \gamma$ as displayed in the image in Figure 5.1 (Li *et al.*, 2018b). The presence of the β matrix phase known to have strength three times higher than α phase (Holden *et al.,* 1954), which is absent in the heat-treated state could contribute to high microhardness and low fracture stress

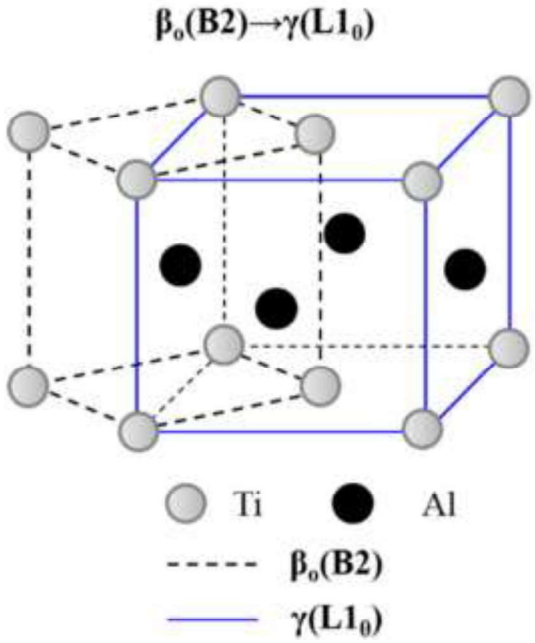


*Figure 5.1: Phase transformation due to Al addition (Li et al., 2018b)*

As-produced and heat-treated TiAlMn-1 underwent EBSD analysis. From the EBSD analysis it could be observed that heat treatment led to orientations of β phase to be concentrated along the symmetry folds of the {1 1 0} standard projection for a cubic system(Widjaja and Marks, 2008). This led to increased symmetry in crystal orientations (Nolze and Winkelmann, 2020), which resulted in the activation additional dislocation glide systems (Shu *et al.,* 2012) which was evident in increased dislocation densities post heat treatment. Although the volume proportion of hexagonal $\alpha_2$ phase increased due to heat treatment, fewer crystal orientations were detected, which indicated homogeneity within the phase. Dislocation motion is highly limited in $\alpha_2$ phase due to the complexity of the crystal structure (Kim *et al.,* 2014). Heat treatment also led to increased tetragonal orientations, which allow dislocations to glide along $\alpha_2/\gamma$ interfaces (Kim *et al.,* 2014). Heat treatment also led to a reduction in texture measurements of cubic β and tetragonal γ orientations but increased texture in $\alpha_2$ orientations. All these mechanisms led to increased microhardness values and reduced fracture stress.

Increased microhardness in TiAlMn-1 values post heat treatment can be accredited by increased $\alpha_2$ phase which restricted dislocation motion during microhardness indentation, leading to a stress build up within the phase (Kim *et al.,* 2014), thus more stresses working against the microhardness indenter during testing. Since $\alpha_2$ has higher microhardness than $\gamma$ phase (Gebhard *et al.,* 2009), the reduction of $\gamma$ phase volumes and increase in $\alpha_2$ volumes during heat treatment led to increased microhardness values post heat treatment.

When the oxidation behaviour of TiAlMn alloy was studied, it could be observed that Mn addition increased the oxidation of TiAl-based alloy According to the thermographs, TiAlMn alloys underwent the high mass gain during TGA, followed by TiMn alloys and then by TiAl alloys which had the lowest mass gain. However, according to SEM measurements, TiAl alloys had the thickest oxide scales, followed by TiAlMn alloys and then TiMn alloys having the thinnest oxide scales. The contradiction between the thermograph findings and SEM thickness measurements was due to the $MnO_2$ having higher density than $Al_2O_3$ which led to more mass gain even where oxide scales were thinner. Self-diffusion rates and coefficient of Mn are higher than those of Ti and Al (Polmear *et al.,* 2017). Oxidation rates of alloys during TGA are highly dependent on self-diffusivity of the elements in alloys, since the diffusion of oxidant molecules through oxide films is proportional to gas pressure. Thus higher diffusivity of Mn added to TiAl, led to increased oxidation rates in TiAlMn in this study since the gas pressure in the TGA furnace was kept constant as a variable. Increased oxidation rates were accredited to high self-diffusion of Mn (Rossi, 2015).

Gleeble compression tests were conducted to analyse high temperature mechanical behaviour of ternary TiAlMn. It was observed that the best combination of high temperature ductility and yield strength occurred at 34.58i strain. This value also appeared to have the highest strain hardening coefficient which was validated by the highest microhardness values among hot deformed samples. The material appears to have good toughness at this strain.

Based on the transformation of the microstructure during hot deformation it could be determined that $\beta$ phase was responsible for high temperature strength since yield stress increased with $\beta$ phase volume proportion (Holden *et al.*, 1954). However, at 46.50% strain it was observed that a large portion of the $\beta$ matrix had transformed to $\gamma$ grains and this has the implication that $\gamma$ phase was responsible for high temperature ductility (Appel *et al.*, 2011a). These $\gamma$ grains result from the dissolution of $\alpha_2$ globules into the $\beta$ matrix and the phase

transformation of β to γ as observed in Figure 5.1. These solid-state phase transformation reactions can be summarized as follows:$\alpha_2 \rightarrow \beta \rightarrow \gamma$.

It was also observed that a reduction in hexagonal and tetragonal lattice parameters along the *c* axis during strain favoured both yield strength and ductility because it led to a reduction in the *c/a* ratio, which indicated increased lattice symmetry which activated additional dislocation systems. This was evident in the increase in dislocation densities achieved at the highest yield stress and ductility at 34.58%. These outcomes support findings reported by (Shu *et al*., 2012) and (Wang *et al.*, 2018).

As ductility increased further, yield stress and strain hardening reduced, this further validated the imbalance between mechanical strength and ductility (Kim, 1994).

# Chapter 6: Conclusions and Recommendations

## 6.1 Conclusions

The effects of LENS parameters on microstructures and mechanical properties were investigated by producing TiAl, TiMn and TiAlMn alloys using various settings. The resulting microstructures were used to analyse the laser deposition mechanisms during LENS operation. The effects of Mn addition to TiAl were also studied using a variety of characterization methods. After analysing the effects of altering Al and Mn feed rates, Ar gas flowrates and LEPUL, followed by heat treatment on microstructures and mechanical properties, the following conclusions were made.

1. Adjusting Ar carrier gas flowrates insulates melt free surfaces during LENS deposition and preserves heat energy required to facilitate solid state phase transformation reactions which take place at lower temperatures reached during slow cooling. Thus increasing Ar gas flowrates reduces cooling rates of melt free surfaces.
2. Increasing Ar gas flowrates also leads to the occupation of Ar interstitial atoms on $\alpha_2$ crystal lattices along the c-axis which leads to a reduction of dislocation densities and increased microhardness.
3. Heat-treatment of binary TiAl alloys increases dislocation densities and reduces microhardness and fracture stress.
4. Increasing laser power increases thermal gradient and slows down solidification and cooling rates enabling phase segregation to take place.
5. Increasing Mn feed rates beyond 0.5rpm and reducing laser power leads to the formation of the undesirable $Mn_{0.52}Ti_{0.48}$(s) phase which is brittle.
6. Heat treating low Mn TiMn alloys leads to reduced dislocation densities and increased microhardness.
7. Lattice reduction in low Mn TiMn alloys increases fracture stress.
8. Mn addition to TiAl increases fracture stress and microhardness.
9. Heat treatment of low Al TiAlMn alloys lead to increased and dislocation densities which are favoured by lattice symmetry.
10. The best combination of high temperature ductility and yield strength (toughness) can be obtained at 34.58% strain.
11. Low Mn feed rates and higher laser power is favourable for fracture stress of Ti-based builds.

12. The optimal ternary alloy has composition of Ti-6.33at%Al-5.17at%Mn.
13. The ideal ternary alloy is comprised of $\gamma+\alpha_2$ +44.34%$\beta$.
14. Mn addition is detrimental to the oxidation resistance of TiAl.
15. The best combination of LENS parameters include Al feed rate of 1.0rpm and Argon carrier gas flowrate of 6L/min; Mn feed rate of 0.3rpm and Argon carrier gas flowrate of 1.2L/min; Ti feed rate of 2.5rpm and Argon gas flowrate of 3.0L/min.

## 6.2 Recommendations

1. It is recommended that fully lamella ternary $\alpha_2+\gamma$ microstructure be adjusted to have the correct microstructural parameters which will allow for improved ductility.
2. It should be explored further as to why dislocation densities increased with increasing microhardness when ternary TiAlMn-1 was heat treated, since that behaviour contradicts literature and the behaviour of binary Ti alloys. Transmission Electron microscopy should be carried out to see if the peak broadening on the samples were due to dislocation densities or possible amorphous metallic phases.
3. It is also recommended that possible coatings to slow down oxidation at high temperatures should be researched further.

# 7. References


Ahmadi, M., Hosseini, S.R., Hadavi, S.M.M., 2016. Effects of heat treatment on microstructural modification of as-cast gamma-TiAl alloy. Journal of Materials Engineering and Performance 25, 2138–2146.

Ankem, S., Margolin, H., 1983. Alpha-beta interface sliding in Ti-Mn alloys. Metallurgical Transactions A 14, 500–503.

Ankem, S., Shyue, J., Vijayshankar, M., Arsenault, R., 1989. The effect of volume per cent of phase on the high temperature tensile deformation of two-phase TiMn alloys. Materials Science and Engineering: A 111, 51–61.

Appel, F., 2010. TiAl Intermetallics. Encyclopedia of Aerospace Engineering.

Appel, F., Paul, J.D.H., Oehring, M., 2011a. Gamma titanium aluminide alloys. Wiley Online Library.

Appel, F., Paul, J.D.H., Oehring, M., 2011b. Gamma titanium aluminide alloys. Wiley Online Library.

Appel, F., Wagner, R., 1998. Microstructure and deformation of two-phase γ-titanium aluminides. Materials Science and Engineering. 22, 187–268.

Arora, H.S., Mridha, S., Grewal, H.S., Singh, H., Hofmann, D.C., Mukherjee, S., 2014. Controlling the length scale and distribution of the ductile phase in metallic glass composites through friction stir processing. Science and Technology of Advanced Materials. 15, 1-7.

Assuncao, E., Williams, S., Yapp, D., 2012. Interaction time and beam diameter effects on the conduction mode limit. Optics and Lasers in Engineering 50, 823–828.

Attar, H., Ehtemam-Haghighi, S., Kent, D., Wu, X., Dargusch, M.S., 2017. Comparative study of commercially pure titanium produced by laser engineered net shaping, selective laser melting and casting processes. Materials Science and Engineering: A 705, 385–393.

Austin, C.M., Kelly, T.J., Huang, S.-C., 1996. Titanium aluminide alloy with improved temperature capability.

Bartels, A., Schillinger, W., 2001. Micromechanical mechanism of texture formation in γ-TiAl. Intermetallics 9, 883–889.

Basu, S., Moseson, A., Barsoum, M.W., 2006. On the determination of spherical nanoindentation stress–strain curves. Journal of Materials Research 21, 2628–2637.

B.H Toby, R.B Von Dreele, J. Appel Cryst, 2013. GSAS2 46, 544–549.

Bontha, S., Klingbeil, N.W., Kobryn, P.A., Fraser, H.L., 2006. Thermal process maps for predicting solidification microstructure in laser fabrication of thin-wall structures. Journal of Materials Processing Technology 178, 135–142.

Boyer, R., Briggs, R., 2005. The use of β titanium alloys in the aerospace industry. Journal of Materials Engineering and Performance 14, 681–685.

Brossmann, U., Würschum, R., Badura, K., Schaefer, H.-E., 1994. Thermal formation of vacancies in TiAl. Physical Review B 49, 6457.

Bunaciu, A.A., UdriŞTioiu, E.G., Aboul-Enein, H.Y., 2015. X-ray diffraction: instrumentation and applications. Critical Reviews in Analytical Chemistry 45, 289–299.

Cahoon, J., Broughton, W., Kutzak, A., 1971. The determination of yield strength from hardness measurements. Metallurgical Transactions 2, 1979–1983.

Campbell, J., Ritchie, R., Rao, K.V., 1999. The effect of microstructure on fracture toughness and fatigue crack growth behavior in γ-titanium aluminide based intermetallics. Metallurgical and Materials Transactions A 30, 563–577.

Carneiro, Í., Simões,S., 2020. Recent advances in EBSD characterization of metals. Metals 10, 1097.

Chandler, H., 1999. Introduction to hardness testing. Hardness testing. USA: ASM International 1–13.

Chang, S., 2007. The isothermal and cyclic oxidation behavior of a titanium aluminide alloy at elevated temperature. Journal of Materials Engineering and Performance 16, 508–514.

Chesnutt, J.C., 1992. GE Aircraft Engines One Neumann Way 45212–6301.

Clemens, H., Bartels, A., Bystrzanowski, S., Chladil, H., Leitner, H., Dehm, G., Gerling, R., Schimansky, F.P., 2006. Grain refinement in γ-TiAl-based alloys by solid state phase transformations. Intermetallics 14, 1380–1385.

Creuziger, A., Syed, K., Gnäupel-Herold, T., 2014. Measurement of uncertainty in orientation distribution function calculations. Scripta Materialia 72, 55–58.

Croat, T., Kelton, K., Holland-Moritz, D., Rathz, T., Robinson, M., 1999. Containerless Solidification Studies of the 1/1 Phase in Ti-(Mn, Cr, Fe)-Si-O Alloys. Presented at the Material Research Society Symposium Proceedings. Materials Research Society, pp. 43–48.

Dai, J., Zhu, J., Chen, C., Weng, F., 2016. High temperature oxidation behavior and research status of modifications on improving high temperature oxidation resistance of titanium alloys and titanium aluminides: A review. Journal of Alloys and Compounds 685, 784–798.

Ding, R., Li, H., Hu, D., Martin, N., Dixon, M., Bowen, P., 2015. Features of fracture surface in a fully lamellar TiAl-base alloy. Intermetallics 58, 36–42.
Egry, I., Brooks, R., Holland-Moritz, D., Novakovic, R., Matsushita, T., Ricci, E., Seetharaman, S., Wunderlich, R., Jarvis, D., 2007. Thermophysical properties of γ-Titanium Aluminide: the European Impress project. International Journal of Thermophysics 28, 1026–1036.
Essienubong, I.A., Ikechukwu, O., Ebunilo, P.O., Ikpe, E., 2016. Material selection for high pressure (HP) turbine blade of conventional turbojet engines. American Journal of Mechanical and Industrial Engineering 1, 1–9.
Fantozzi, G., Esnouf, C., Benoit, W., Ritchie, I., 1982. Internal friction and microdeformation due to the intrinsic properties of dislocations: The Bordoni relaxation. Progress in Materials Science 27, 311–451.
Froes, F., Suryanarayana, C., Eliezer, D., 1992. Synthesis, properties and applications of titanium aluminides. Journal of Materials Science 27, 5113–5140.
Gebhard, S., Pyczak, F., Göken, M., 2009. Microstructural and micromechanical characterisation of TiAl alloys using atomic force microscopy and nanoindentation. Materials Science and Engineering: A 523, 235–241.
Gil, F., Ginebra, M., Manero, J., Planell, J., 2001. Formation of α-Widmanstätten structure: Effects of grain size and cooling rate on the Widmanstätten morphologies and on the mechanical properties in Ti6Al4V alloy. Journal of Alloys and Compounds 329, 142–152.
Gintalas, M., Rivera-Diaz-del-Castillo, P.E., 2022. Advanced Electron Microscopy: Progress and Application of Electron Backscatter Diffraction. Journal: Encyclopedia of Materials: Metals and Alloys 648–661.
Gouda, M.K., Nakamura, K., Gepreel, M.A.H., 2016. Effect of Mn-Content on the deformation behavior of binary Ti-Mn alloys. Presented at the Key Engineering Materials, Trans Tech Publ, pp. 214–218.
Griffith, M., Keicher, D., Atwood, C.L., 1996. Free form fabrication of metallic components using laser engineered net shaping (LENS). Sandia National Labs., Albuquerque, NM (United States).
Gu, D., 2015. Laser additive manufacturing of high-performance materials. Springer.
Gu, D., Shen, Y., 2007. Balling phenomena during direct laser sintering of multi-component Cu-based metal powder. Journal of Alloys and Compounds 432, 163–166.
Gu, D., Wang, H., Dai, D., Chang, F., Meiners, W., Hagedorn, Y.-C., Wissenbach, K., Kelbassa, I., Poprawe, R., 2015. Densification behavior, microstructure evolution, and wear property of TiC nanoparticle reinforced AlSi10Mg bulk-form nanocomposites prepared by selective laser melting. Journal of Laser Applications 27, S17003.
Guangyu, Y., Wenpeng, J., Pei, Z., Liang, J., Nan, L., Jian, W., Huiping, T., 2016. Microstructures of as-fabricated and post heat treated Ti-47Al-2Nb-2Cr alloy produced by selective electron beam melting (SEBM). Rare Metal Materials and Engineering 45, 1683–1686.
Heinrich, C., Waas, A., Wineman, A., 2009. Determination of material properties using nanoindentation and multiple indenter tips. International Journal of Solids and Structures 46, 364–376.
Holden, F., Ogden, H., Jaffee, R., 1954. Heat treatment, structure, and mechanical properties of Ti-Mn alloys. JOM 6, 169–184.
Hu, D., 2001. Effect of composition on grain refinement in TiAl-based alloys. Intermetallics 9, 1037–1043.
Imayev, R., Imayev, V., Oehring, M., Appel, F., 2007. Alloy design concepts for refined gamma titanium aluminide based alloys. Intermetallics 15, 451–460.
Inui, H., Oh, M., Nakamura, A., Yamaguchi, M., 1992. Room-temperature tensile deformation of polysynthetically twinned (PST) crystals of TiAl. Acta Metallurgica et Materialia 40, 3095–3104.
Jafari, S., Nikolaidis, T., 2018. Thermal management systems for civil aircraft engines: Review, challenges and exploring the future. Applied Sciences 8, 2044.
Jiao, Z., Luan, J., Liu, C., 2016. Strategies for improving ductility of ordered intermetallics. Progress in Natural Science: Materials International 26, 1–12.
Kainuma, R., Fujita, Y., Mitsui, H., Ohnuma, I., Ishida, K., 2000. Phase equilibria among α (hcp), β (bcc) and γ (L10) phases in Ti–Al base ternary alloys. Intermetallics 8, 855–867.
Kamara, A., Marimuthu, S., Li, L., 2014. Finite element modeling of microstructure in laser-deposited multiple layer Inconel 718 parts. Materials and Manufacturing Processes 29, 1245–1252.
Karaoglanli, A.C., Ogawa, K., Turk, A., Ozdemir, I., 2013. Thermal shock and cycling behavior of thermal barrier coatings (TBCs) used in gas turbines. Progress in gas turbine performance 237–260.
Kasap, S.O., 2006. Principles of electronic materials and devices. Tata McGraw-Hill.
Kawabata, T., Fukai, H., Izumi, O., 1998. Effect of ternary additions on mechanical properties of TiAl. Acta Materialia 46, 2185–2194.
Kelly, T.J., Weimer, M.J., Austin, C.M., London, B., Larson Jr, D.E., Wheeler, D.A., 2001. Heat treatment of gamma titanium aluminide alloys.
Keryvin, V., Hoang, V., Shen, J., 2009. Hardness, toughness, brittleness and cracking systems in an iron-based bulk metallic glass by indentation. Intermetallics 17, 211–217.

Khalili, S., Soleimanian, V., Mokhtari, A., 2016. Developing a method for the evaluation of dislocation parameters from the Rietveld refinement procedure. Powder Diffraction 31, 198.
Khojier, K., Savaloni, H., Shokrai, E., Dehghani, Z., Dehnavi, N.Z., 2013. Influence of argon gas flow on mechanical and electrical properties of sputtered titanium nitride thin films. Journal of Theoretical and Applied Physics 7, 1–6.
Kim, J.-W., Hwang, M.-J., Han, M.-K., Kim, Y.-G., Song, H.-J., Park, Y.-J., 2016. Effect of manganese on the microstructure, mechanical properties and corrosion behavior of titanium alloys. Materials Chemistry and Physics 180, 341–348.
Kim, M., Oh, M., Lee, J., Inui, H., Yamaguchi, M., Wee, D.-M., 1997. Composition and growth rate effects in directionally solidified TiAl alloys. Materials Science and Engineering: A 239, 570–576.
Kim, S.-W., Na, Y.-S., Yeom, J.-T., Kim, S.E., Choi, Y.S., 2014. An in-situ transmission electron microscopy study on room temperature ductility of TiAl alloys with fully lamellar microstructure. Materials Science and Engineering: A 589, 140–145.
Kim, Y.-W., 1994. Ordered intermetallic alloys, part III: gamma titanium aluminides. The Journal of Minerals, Metals and Materials Society, 46, 30–39.
Kim, Y.-W., Dimiduk, D.M., 1991. Progress in the understanding of gamma titanium aluminides. Journal of Minerals, Metals and Materials Society 43, 40–47.
Kim, Y.-W., Smarsly, W., Lin, J., Dimiduk, D., Appel, F., 2014. Gamma Titanium Aluminide Alloys 2014: A Collection of Research on Innovation and Commercialization of Gamma Alloy Technology. John Wiley & Sons.
Koçak, A., Karasu, B., 2018. General evaluations of nanoparticles. El–Cezeri Journal of Science and Engineering (EJCSE) 5, 191–236.
Kostov, A.I., Živković, D.T., 2008. Thermodynamic calculations in ternary titanium-aluminium-manganese system. Journal of the Serbian Chemical Society 73, 499–506.
Kothari, K., Radhakrishnan, R., Wereley, N.M., 2012. Advances in gamma titanium aluminides and their manufacturing techniques. Progress in Aerospace Sciences 55, 1–16.
Krishna, S.C., Gangwar, N.K., Jha, A.K., Pant, B., 2013. On the prediction of strength from hardness for copper alloys. Journal of Materials, 1–6.
Kuang, J., Harding, R., Campbell, J., 2002. Microstructures and properties of investment castings of γ-titanium aluminide. Materials Science and Engineering: A329, 31–37.
Kumpfert, J., 2001. Intermetallic alloys based on orthorhombic titanium aluminide. Advanced Engineering Materials 3, 851–864.
Kung, S.-C., 1990. High-temperature coating for titanium aluminides using the pack-cementation technique. Oxidation of metals 34, 217–228.
Küstner, V., Oehring, M., Chatterjee, A., Güther, V., Brokmeier, H., Clemens, H., Kim, Y., Clemens, H., Rosenberger, A., 2003. Gamma titanium aluminides.
Lapin, J., 2009. TiAl-based alloys: Present status and future perspectives. Presented at the Conference proceedings METAL, p. 2009.
Li, F., Rajapakse, R., 2007. Analytical saturated domain orientation textures and electromechanical properties of ferroelectric ceramics due to electric/mechanical poling. Journal of Applied Physics 101, 054110.
Li, X., Xu, H., Xing, W., Chen, B., Ma, Y., Liu, K., 2018a. Phase transformation behavior of a β-solidifying γ-TiAl-based alloy from different phase regions with various cooling methods. Metals 8, 731.
Li, Z., Liu, L., Ma, W., Kakimoto, K., 2011. Effects of argon flow on heat transfer in a directional solidification process for silicon solar cells. Journal of Crystal Growth 318, 298–303.
Liu, C., Maziasz, P., 1998. Microstructural control and mechanical properties of dual-phase TiAl alloys. Intermetallics 6, 653–661.
Liu, W., DuPont, J., 2002. Fabrication of Titanium Aluminide Matrix Composites by Laser Engineered Net Shaping 124. Presented at the 2002 International Solid Freeform Fabrication Symposium.
Liu, Z., Ning, F., Cong, W., Jiang, Q., Li, T., Zhang, H., Zhou, Y., 2016. Energy consumption and saving analysis for laser engineered net shaping of metal powders. Energies 9, 763.
Loh, N., Sia, K., 1992. An overview of hot isostatic pressing. Journal of Materials Processing Technology 30, 45–65.
Long, M., Rack, H., 1998. Titanium alloys in total joint replacement—a materials science perspective. Biomaterials 19, 1621–1639.
Maruyama, K., Yamamoto, R., Nakakuki, H., Fujitsuna, N., 1997. Effects of lamellar spacing, volume fraction and grain size on creep strength of fully lamellar TiAl alloys. Materials Science and Engineering: A 239, 419–428.
McCullough, C., Valencia, J., Levi, C., Mehrabian, R., 1989. Phase equilibria and solidification in Ti-Al alloys. Acta Metallurgica 37, 1321–1336.

Mercer, C., Soboyejo, W., 1997. Effects of alloying on crack-tip deformation and shielding in gamma-based titanium aluminides. Acta Materialia 45, 961–971.
Mills, K.C., 2002. Recommended values of thermophysical properties for selected commercial alloys. Woodhead Publishing.
Morinaga, M., Saito, J., Yukawa, N., Adachi, H., 1990. Electronic effect on the ductility of alloyed TiAl compound. Acta Metallurgical *et* Materialia 38, 25–29.
Mulder, M., 2016. Synthesis of LiNi0. 5Mn1. 5O4 nanofibers by electrospinning, Bachelor's Thesis, University of Twente.
Murray, J.L., 1981. The Mn− Ti (Manganese-Titanium) system. Bulletin of Alloy Phase Diagrams 2, 334–343.
Nolze, G., Winkelmann, A., 2020. About the reliability of EBSD measurements: Data enhancement. Presented at the IOP Conference Series: Materials Science and Engineering, IOP Publishing, p. 012018.
Ogino, Y., Hirata, Y., 2015. Numerical simulation of metal transfer in argon gas-shielded GMAW. Welding in the World 59, 465–473.
Okura, T., 2015. Materials for Aircraft Engines, Aerospace Engineering, 5063, pp1-14
Pathak, S., Kalidindi, S.R., 2015. Spherical nanoindentation stress–strain curves. Materials science and engineering: R: Reports 91, 1–36.
Polmear, I., StJohn, D., Nie, J.-F., Qian, M., 2017. Light alloys: metallurgy of the light metals. Butterworth-Heinemann.
Prasad, U., Xu, Q., Chaturvedi, M.C., 2002. Effect of cooling rate and manganese concentration on phase transformation in Ti–45 at.% Al based alloys. Materials Science and Engineering: A 329, 906–913.
Rai, R., Elmer, J., Palmer, T., DebRoy, T., 2007. Heat transfer and fluid flow during keyhole mode laser welding of tantalum, Ti–6Al–4V, 304L stainless steel and vanadium. Journal of Physics D: Applied Physics 40, 5753.
Rajendran, R., Venkateshwarlu, M., Petley, V., Verma, S., 2014. Strain hardening exponents and strength coefficients for aeroengine isotropic metallic materials–a reverse engineering approach. Journal of the Mechanical Behavior of Materials 23, 101–106.
Rossi, C., 2015. Al-based energetic nano materials: design, manufacturing, properties and applications. John Wiley & Sons.
Ruiz-Moreno, A., Hähner, P., Fumagalli, F., Haiblikova, V., Conte, M., Randall, N., 2020. Stress− strain curves and derived mechanical parameters of P91 steel from spherical nanoindentation at a range of temperatures. Materials and Design 194, 108950.
Santos, E.C., Shiomi, M., Osakada, K., Laoui, T., 2006. Rapid manufacturing of metal components by laser forming. International Journal of Machine Tools and Manufacture 46, 1459–1468.
Santos, P.F., Niinomi, M., Cho, K., Nakai, M., Liu, H., Ohtsu, N., Hirano, M., Ikeda, M., Narushima, T., 2015. Microstructures, mechanical properties and cytotoxicity of low cost beta Ti–Mn alloys for biomedical applications. Acta Biomaterialia 26, 366–376.
Schuster, J.C., Palm, M., 2006. Reassessment of the binary aluminum-titanium phase diagram. Journal of Phase Equilibria and Diffusion 27, 255–277.
Sciammarella, F.M., Salehi Najafabadi, B., 2018. Processing Parameter DOE for 316L Using Directed Energy Deposition. Journal of Manufacturing and Materials Processing 2, 61.
Sharman, A., Hughes, J., Ridgway, K., 2018. Characterisation of titanium aluminide components manufactured by laser metal deposition. Intermetallics 93, 89–92.
Shen, H.-T., Young, K.-H., Meng, T., Bendersky, L.A., 2016. Clean grain boundary found in C14/body-center-cubic multi-phase metal hydride alloys. Batteries 2, 22.
Shirai, Y., Yamaguchi, M., 1992. Studies of vacancies and dislocations in TiAl by positron annihilation, in: High Temperature Aluminides and Intermetallics, pp. 173–181.
Shu, S., Qiu, F., Xing, B., Jin, S., Wang, Y., Jiang, Q., 2012. Study of effect of Mn addition on the mechanical properties of Ti2AlC/TiAl composites through first principles study and experimental investigation. Intermetallics 28, 65–70.
Smithells, C.J., Brandes, E.A., 1992. Smithells metals reference book.
Soboyejo, W., Mercer, C., Lou, K., Heath, S., 1995. An investigation of the fatigue and fracture behavior of mn-containing gamma titanium aluminides. Metallurgical and Materials Transactions A 26, 2275–2291.
Tlotleng, M., 2019. Microstructural properties of heat-treated LENS in situ additively manufactured titanium aluminide. Journal of Materials Engineering and Performance 28, 701–708.
Tlotleng, M., Pityana, S. 2018. In-Situ Alloyed LENS Additively Manufactured TiAl-Nb Structure
Tong, V., Joseph, S., Ackerman, A.K., Dye, D., Britton, T.B., 2017. Using transmission Kikuchi diffraction to characterise α variants in an α+ β titanium alloy. Journal of Microscopy 267, 318–329.
Traidia, A., Roger, F., Chidley, A., Schroeder, J., Marlaud, T., 2011. Effect of helium-argon mixtures on the heat transfer and fluid flow in gas tungsten arc welding. Journal of Chemistry and Chemical Engineering 5, 854–861.

Tryggvason, G., 1997. Computational Investigation of Atomization (AFOSR-contract FA9620-96-1-0356). Report Documentation, 1001, 150.
Valencia, J.J., Quested, P.N., 2013. Thermophysical properties. ASM Handbook Comitee, 15, 468-481
Varin, R., Zbroniec, L., Wang, Z., 2001. Fracture toughness and yield strength of boron-doped, high (Ti+ Mn) L12 Titanium Tri-Aluminides. Intermetallics 9, 195–207.
Varol, M., Atimtay, A., Bay, B., Olgun, H., 2010. Investigation of co-combustion characteristics of low quality lignite coals and biomass with thermogravimetric analysis. Thermochimica Acta 510, 195–201.
Voice, W.E., Henderson, M., Shelton, E.F., Wu, X., 2005. Gamma titanium aluminide, TNB. Intermetallics 13, 959–964.
Vujic, D., Li, Z., Whang, S.H., 1988. Effect of rapid solidification and alloying addition on lattice distortion and atomic ordering in L1_0 tial alloys and their ternary alloys. Metallurgical Transactions A 19, 2445–2455.
Wang, Q., Ding, H., Zhang, H., Chen, R., Guo, J., Fu, H., 2018. Influence of Mn addition on the microstructure and mechanical properties of a directionally solidified γ-TiAl alloy. Materials Characterization 137, 133–141.
Weisheit, A., Mordike, B., Smarlsy, W., Richter, K., 2000. Laser surface remelting and laser surface gas alloying of an intermetallic TiAl alloy. Lasers in Engineering 10, 63–81.
Widjaja, E., Marks, L., 2008. Models for quasicrystal–crystal epitaxy. Journal of Physics: Condensed Matter 20, 314003.
Woo, W., Ungár, T., Feng, Z., Kenik, E., Clausen, B., 2010. X-ray and neutron diffraction measurements of dislocation density and subgrain size in a friction-stir-welded aluminum alloy. Metallurgical and Materials Transactions A 41, 1210–1216.
Wu, X., Hu, D., 2005. Microstructural refinement in cast TiAl alloys by solid state transformations. Scripta Materialia 52, 731–734.
Yamaguchi, M., Johnson, D., Lee, H., Inui, H., 2000. Directional solidification of TiAl-base alloys. Intermetallics 8, 511–517.
Yoo, M., Fu, C., 1998. Physical constants, deformation twinning, and microcracking of titanium aluminides. Metallurgical and Materials Transactions A 29, 49–63.
Zarkevich, N.A., Johnson, D.D., 2016. Titanium α– ω phase transformation pathway and a predicted metastable structure. Physical Review B 93, 020104.
Zhang, F., Weidmann, A., Nebe, B., Burkel, E., 2009. Preparation of TiMn alloy by mechanical alloying and spark plasma sintering for biomedical applications. Presented at the Journal of Physics: Conference Series, IOP Publishing, p. 012007.
Zhang, Huarui, Tang, X., Zhou, C., Zhang, Hu, Zhang, S., 2013. Comparison of directional solidification of γ-TiAl alloys in conventional Al2O3 and novel Y2O3-coated Al2O3 crucibles. Journal of the European Ceramic Society 33, 925–934.
Zheng, B., Zhou, Y., Smugeresky, J., Schoenung, J., Lavernia, E., 2008. Thermal behavior and microstructural evolution during laser deposition with laser-engineered net shaping: Part I. Numerical calculations. Metallurgical and Materials Transactions A 39, 2228–2236.

# 8. APPENDICES

# APPENDIX A: Microhardness Profiles

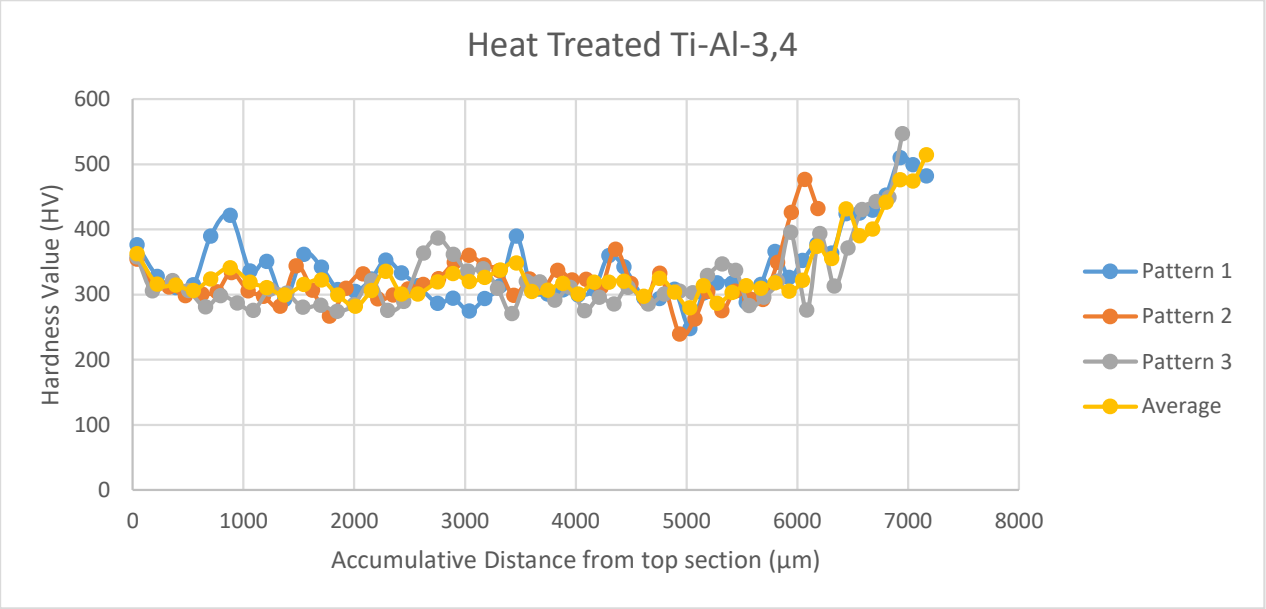


*Figure A1: Microhardness profile of TiAl alloy*

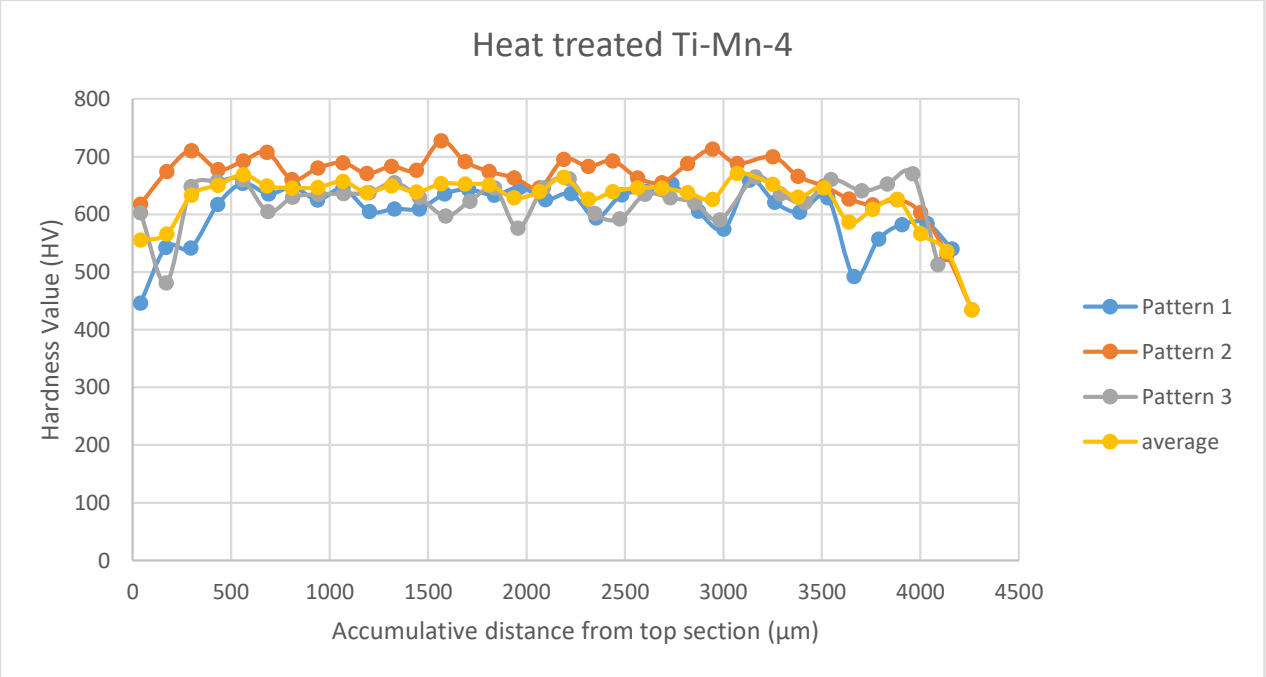


*Figure A-2: Microhardness profile of TiMn alloy*

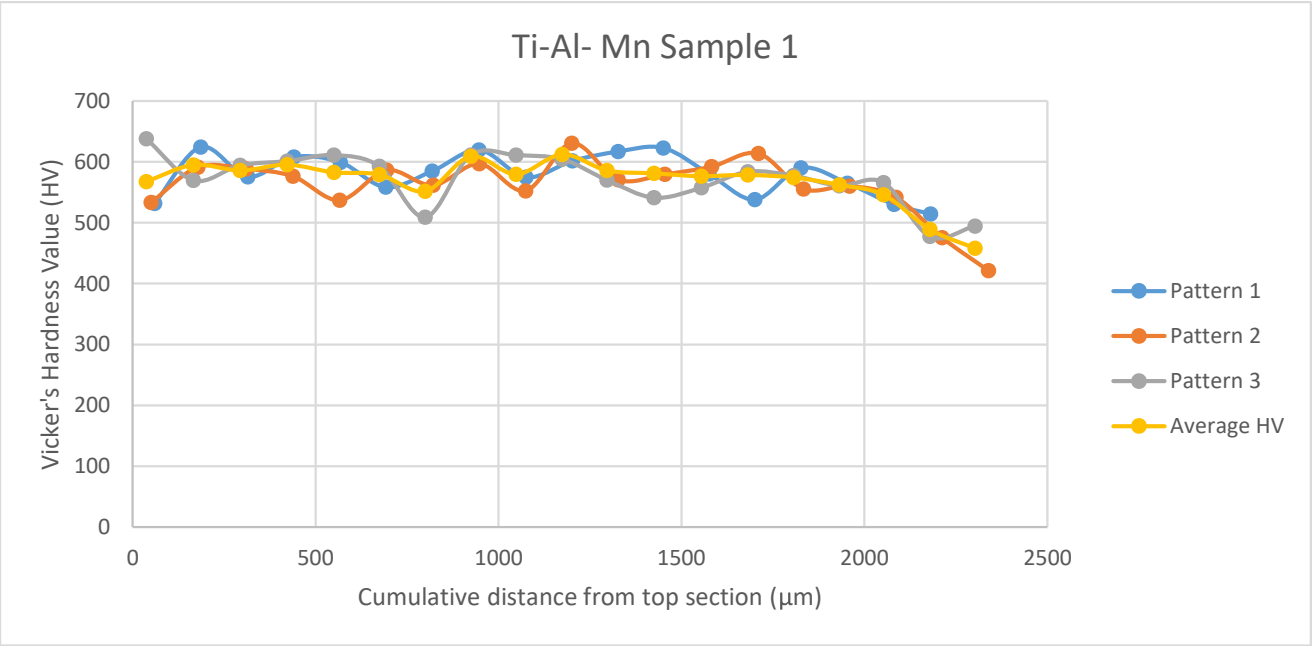


*Figure A-3: Microhardness profile of TiAlMn alloy*

## APPENDIX B: SOLVING FOR $T_S$ ON MICROSOFT EXCEL

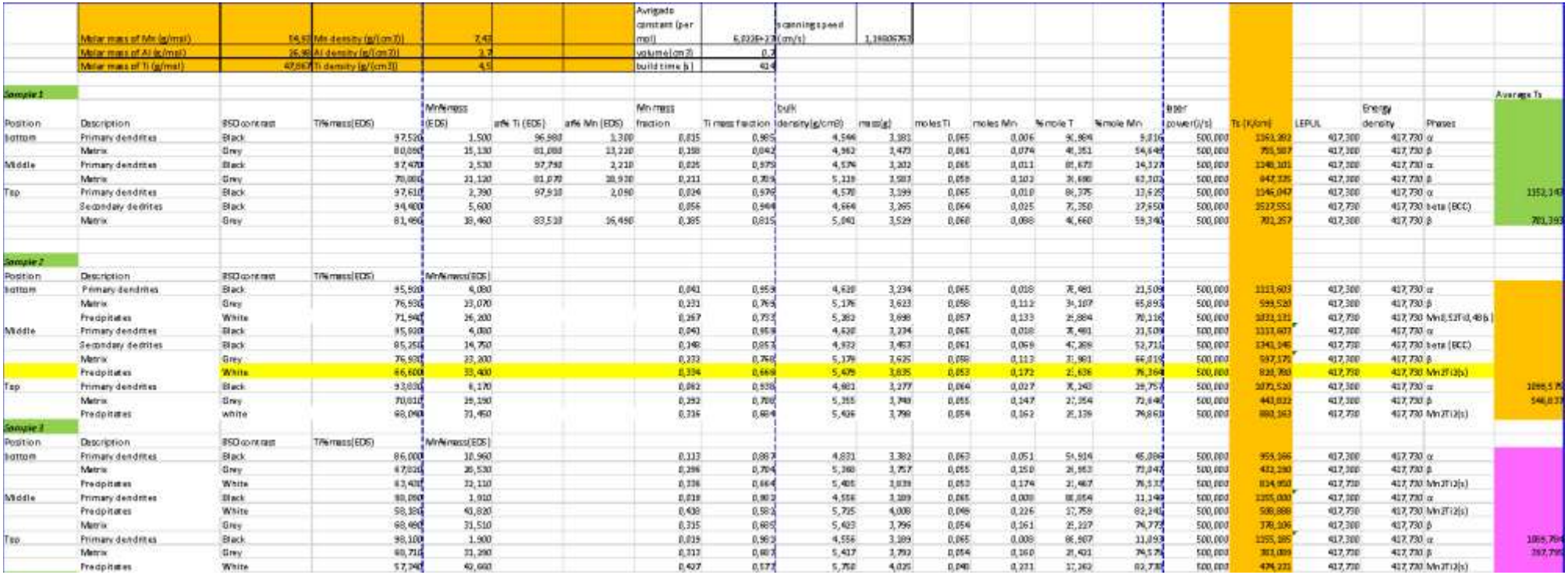

| | | |

| | | | | | | | | | | | | | | | | | | | | |
|---|---|---|---|---|---|---|---|---|---|---|---|---|---|---|---|---|---|---|---|---|
| *Sample 10* | | | | | | | | | | | | | | | | | | | | |
| Position | Description | BSD contrast | Ti%mass (EDS) | | Mn%mass (EDS) | | | | | | | | | | | | | | | |
| bottom | Ductile primiary + secondary dendrites | Black | 97,570 | | 1,770 | | 0,018 | 0,982 | 4,552 | 3,187 | 0,065 | 0,008 | 89,536 | 10,464 | 550,000 | 737,798 | 459,073 | 459,073 α | | |
| | Fine dendites | Black | 97,330 | | 1,850 | | 0,019 | 0,981 | 4,555 | 3,188 | 0,065 | 0,008 | 89,096 | 10,904 | 550,000 | 1211,791 | 459,072 | 459,073 beta (BCC) | | |
| | Matrix | Grey | 83,730 | | 14,940 | | 0,151 | 0,849 | 4,944 | 3,461 | 0,061 | 0,071 | 46,522 | 53,478 | 550,000 | 463,496 | 459,073 | 459,073 β | | |
| middle | Primary dendrites | Black | 98,180 | | 1,820 | | 0,018 | 0,982 | 4,553 | 3,187 | 0,065 | 0,008 | 89,332 | 10,668 | 550,000 | 737,218 | 459,073 | 459,073 α | | |
| | Matrix | Grey | 83,850 | | 16,150 | | 0,162 | 0,839 | 4,973 | 3,481 | 0,061 | 0,076 | 44,626 | 55,374 | 550,000 | 444,431 | 459,073 | 459,073 β | 463,570 | |
| Top | ductile primary dendrites | Black | 98,480 | | 1,520 | | 0,015 | 0,985 | 4,545 | 3,181 | 0,065 | 0,007 | 90,956 | 9,044 | 550,000 | 741,754 | 459,073 | 459,073 α | 738,923 | |
| | Fine primary dendrites | Black | 98,480 | | 1,520 | | 0,015 | 0,985 | 4,545 | 3,181 | 0,065 | 0,007 | 90,956 | 9,044 | 550,000 | 1216,637 | 459,072 | 459,073 beta (BCC) | | |
| | Matrix | Grey | 85,910 | | 14,090 | | 0,141 | 0,859 | 4,913 | 3,439 | 0,062 | 0,065 | 48,624 | 51,376 | 550,000 | 482,783 | 459,073 | 459,073 β | | |
| *Sample 11* | | | | | | | | | | | | | | | | | | | | |
| Position | Description | BSD contrast | Ti%mass (EDS) | | Mn%mass (EDS) | | | | | | | | | | | | | | | |
| bottom | primary dendrites | Black | 89,020 | | 9,280 | | 0,094 | 0,906 | 4,777 | 3,344 | 0,063 | 0,042 | 59,823 | 40,177 | 550,000 | 606,708 | 459,073 | 459,073 α | | |
| | Matrix | Grey | 79,270 | | 17,010 | | 0,177 | 0,823 | 5,018 | 3,512 | 0,060 | 0,084 | 41,974 | 58,026 | 550,000 | 414,695 | 459,073 | 459,073 β | | |
| Middle | Fine primary dendrites | Black | 97,960 | | 2,040 | | 0,020 | 0,980 | 4,560 | 3,192 | 0,065 | 0,009 | 88,171 | 11,829 | 550,000 | 733,862 | 459,073 | 459,073 α | | |
| | Fine primary dendrites | grey | 85,600 | | 14,400 | | 0,144 | 0,856 | 4,922 | 3,445 | 0,062 | 0,067 | 47,990 | 52,010 | 550,000 | 994,381 | 459,072 | 459,073 beta (BCC) | | |
| | Matrix | Grey | 77,130 | | 22,870 | | 0,229 | 0,771 | 5,170 | 3,619 | 0,058 | 0,111 | 34,361 | 65,639 | 550,000 | 302,618 | 459,073 | 459,073 β | 352,595 | |
| Top | Dendrites | Black | 98,000 | | 2,000 | | 0,020 | 0,980 | 4,559 | 3,191 | 0,065 | 0,009 | 88,380 | 11,620 | 550,000 | 734,474 | 459,073 | 459,073 α | 691,682 | |
| | Matrix | Grey | 78,800 | | 21,200 | | 0,212 | 0,788 | 5,121 | 3,585 | 0,059 | 0,102 | 36,587 | 63,413 | 550,000 | 340,354 | 459,073 | 459,073 β | | |
| *Sample 12* | | | | | | | | | | | | | | | | | | | | |
| Position | Description | BSD contrast | Ti%mass (EDS) | | Mn%mass (EDS) | | | | | | | | | | | | | | | |
| bottom | primary dendrites | Black | 94,570 | | 4,710 | | 0,047 | 0,953 | 4,639 | 3,247 | 0,065 | 0,021 | 75,708 | 24,292 | 550,000 | 690,614 | 459,073 | 459,073 α | | |
| | secondary dendrites arms | Black | 95,110 | | 4,040 | | 0,041 | 0,959 | 4,619 | 3,234 | 0,065 | 0,018 | 78,514 | 21,486 | 550,000 | 1179,280 | 459,072 | 459,073 beta (BCC) | | |
| | Precipitates | White | 66,990 | | 30,220 | | 0,311 | 0,689 | 5,411 | 3,788 | 0,055 | 0,158 | 25,600 | 74,400 | 550,000 | 568,476 | 459,072 | 459,073 MnZTi2(s) | | |
| | Matrix | Grey | 74,710 | | 23,350 | | 0,238 | 0,762 | 5,198 | 3,638 | 0,058 | 0,117 | 33,184 | 66,816 | 550,000 | 280,567 | 459,073 | 459,073 β | | |
| Middle | Primary +Seccndary dendrites | Black | 97,300 | | 2,700 | | 0,027 | 0,973 | 4,579 | 3,205 | 0,065 | 0,012 | 84,834 | 15,166 | 550,000 | 725,648 | 459,073 | 459,073 α | | |
| | Precipitates | White | 64,440 | | 35,560 | | 0,356 | 0,644 | 5,542 | 3,879 | 0,052 | 0,186 | 21,953 | 78,047 | 550,000 | 422,487 | 459,072 | 459,073 MnZTi2(s) | | |
| | Matrix | Grey | 73,040 | | 26,960 | | 0,270 | 0,730 | 5,290 | 3,703 | 0,057 | 0,134 | 29,604 | 70,396 | 550,000 | 202,694 | 459,073 | 459,073 β | 224,237 | |
| top | Dendrites | Black | 94,350 | | 5,650 | | 0,057 | 0,943 | 4,666 | 3,266 | 0,061 | 0,025 | 72,161 | 27,839 | 550,000 | 675,300 | 459,073 | 459,073 α | 696,521 | |
| | Matrix | Grey | 72,530 | | 27,470 | | 0,275 | 0,725 | 5,305 | 3,713 | 0,056 | 0,137 | 29,070 | 70,930 | 550,000 | 189,450 | 459,073 | 459,073 β | | |
| *Sample 13* | | | | | | | | | | | | | | | | | | | | |
| Position | Description | BSD contrast | Ti%mass (EDS) | | Mn%mass (EDS) | | | | | | | | | | | | | | | |
| bottom | primary dendrites | Black | 98,090 | | 1,530 | | 0,015 | 0,985 | 4,545 | 3,182 | 0,065 | 0,007 | 90,869 | 9,131 | 600,000 | 406,415 | 500,806 | 500,806 α | | |
| | fine primary dendrites | Black | 88,890 | | 10,380 | | 0,105 | 0,895 | 4,806 | 3,364 | 0,063 | 0,047 | 57,068 | 42,932 | 600,000 | 762,245 | 500,806 | 500,806 beta (BCC) | | |
| | Matrix | Grey | 81,880 | | 17,400 | | 0,175 | 0,825 | 5,014 | 3,509 | 0,060 | 0,083 | 42,211 | 57,789 | 600,000 | 141,943 | 500,806 | 500,806 β | | |
| middle | primary dendrites | Black | 98,090 | | 1,910 | | 0,019 | 0,981 | 4,556 | 3,189 | 0,065 | 0,008 | 88,854 | 11,146 | 600,000 | 401,268 | 500,806 | 500,806 α | 403,842 | |
| | matrix | Grey | 81,120 | | 18,880 | | 0,189 | 0,811 | 5,053 | 3,537 | 0,060 | 0,090 | 40,009 | 59,991 | 600,000 | 114,514 | 500,806 | 500,806 β | 120,469 | |
| Top | Primary Dendrites | Black | 89,160 | | 80,660 | | 0,475 | 0,525 | 5,892 | 4,124 | 0,045 | 0,284 | 14,645 | 85,355 | 600,000 | 0,000 | 402,038 | 500,806 | | |
| | Matrix | Grey | 80,660 | | 19,340 | | 0,193 | 0,807 | 5,067 | 3,547 | 0,060 | 0,092 | 39,297 | 60,703 | 600,000 | 104,950 | 500,806 | 500,806 β | | |
| *Sample 14* | | | | | | | | | | | | | | | | | | | | |
| Position | Description | BSD contrast | Ti%mass (EDS) | | Mn%mass (EDS) | | | | | | | | | | | | | | | |
| bottom | Fine primary dendrites | black | 97,370 | | 1,920 | | 0,019 | 0,981 | 4,557 | 3,190 | 0,065 | 0,008 | 88,728 | 11,272 | 600,000 | 400,940 | 500,806 | 500,806 α | | |
| | Matrix | Grey | 79,070 | | 20,930 | | 0,209 | 0,791 | 5,113 | 3,579 | 0,059 | 0,101 | 36,964 | 63,036 | 600,000 | 70,917 | 500,806 | 500,806 β | | |
| Middle | Primary dendrites | Black | 97,410 | | 2,590 | | 0,026 | 0,974 | 4,576 | 3,203 | 0,065 | 0,011 | 85,376 | 14,624 | 600,000 | 381,739 | 500,806 | 500,806 α | | |
| | Fine Dendrites | Black | 89,000 | | 11,000 | | 0,110 | 0,890 | 4,822 | 3,376 | 0,063 | 0,050 | 55,672 | 44,328 | 600,000 | 752,591 | 500,806 | 500,806 beta (BCC) | | |
| | Matrix | Grey | 76,020 | | 23,980 | | 0,240 | 0,760 | 5,203 | 3,642 | 0,058 | 0,118 | 32,979 | 67,021 | 600,000 | 1,241 | 500,806 | 500,806 β | 51,673 | |
| Top | Primary Dendrites | Black | 93,420 | | 6,580 | | 0,066 | 0,934 | 4,693 | 3,285 | 0,061 | 0,029 | 68,787 | 31,213 | 600,000 | 331,217 | 500,806 | 500,806 α | 374,632 | |
| | secondary dendrites arms | Black | 88,310 | | 11,690 | | 0,117 | 0,883 | 4,843 | 3,390 | 0,063 | 0,053 | 53,972 | 46,028 | 600,000 | 740,113 | 500,806 | 500,806 beta (BCC) | | |
| | Precipitates | White | 78,380 | | 21,620 | | 0,216 | 0,784 | 5,133 | 3,593 | 0,059 | 0,105 | 36,010 | 63,990 | 600,000 | 531,417 | 500,806 | 500,806 MnZTi2(s) | | |
| | Matrix | Grey | 79,620 | | 20,380 | | 0,204 | 0,796 | 5,097 | 3,568 | 0,059 | 0,098 | 37,750 | 62,250 | 600,000 | 82,862 | 500,806 | 500,806 β | | |

# 9. PUBLICATIONS

Materials Today: Proceedings 62 (2022) S163–S175

Contents lists available at ScienceDirect

Materials Today: Proceedings

journal homepage: www.elsevier.com/locate/matpr

# Characterization of Mn micro alloyed TiAl fabricated using Laser Engineered Net Shaping (LENS)

Sibusisiwe Motha [a,*], Nthabiseng Maledi [a], Monnamme Tlotleng [b,c]

[a] School of Chemical and Metallurgical Engineering, University of the Witwatersrand, 1 Jan Smuts Avenue, Johannesburg 2050, South Africa
[b] National Laser Centre, Counsil of Scientific and Industrial Research, Meiring Naude Rd, Brummeria, Pretoria 0001, South Africa
[c] Department of Mechanical Engineering Science, University of Johannesburg, Kingsway Campus, Auckland Park, Johannesburg 2006, South Africa

ARTICLE INFO

*Article history:*
Available online 07 May 2022

*Keywords:*
Powder Metallurgy
Rapid Solidification Microstructure
Laser Processing
Titanium-Aluminide
Manganese
Microstructure

ABSTRACT

This work investigates the effect of micro-alloying in LENS fabricated TiAl alloys with Mn. The effects of altering Al feed rates and laser power on the LENS machine settings were researched alongside the effects of using heat-treatment as a post processing step. It was established that the addition of Mn improved mechanical properties through the reduction of interplanar spacings. It was also observed that increasing Al feed rates and laser power increased the volume proportions of γ-phase both in the as-produced and heat-treated states. It was also determined that alloys containing higher volume proportions of the γ- phase yielded brittle behaviour.
© 2021 The Authors. Published by Elsevier Ltd.
This is an open access article under the CC BY-NC-ND license (https://creativecommons.org/licenses/by-nc-nd/4.0) Selection and peer-review under responsibility of the scientific committee of the International Symposium on Nanostructured and Advanced Materials.

## 1. Introduction

The use of TiAl based alloys in the aero engine manufacturing industry has the potential to reduce fuel consumption and improve the efficiency of aero engines, since TiAl based alloys have the strength of Ni-based superalloys which are currently being used in aero engines, at half the density[1,2]. However, the use of TiAl based alloys is restricted by their poor ambient temperature ductility governed by deformation mechanisms which are attributed to the crystal orientation[3].

Micro alloying of TiAl based alloys with various elements has been applied as a strategy to improve the mechanical properties. These strategies have been incorporated into traditional fabrication methods such as wrought ingot casting [4,5]. Ductility and mechanical strength of Ti-Al alloys have also been improved by micro alloying with various elements including chromium (Cr), niobium (Nb), manganese (Mn), vanadium (V), carbon (C), tungsten (W), thallium (Ta), boron (B) and silicon (Si) [3,4]. Elements such as Hf, Nb, Ta and Zr, which substitute on the Ti sub-lattice sites, enhance strength while elements such as Mn, Ga, Mo, Cr and W, which prefer Al sub-lattice sites, enhance ductility[3,6,7].

The micro alloying of TiAl with Mn at a maximum of 2 (at. %) has been carried out to improve ductility. Mn preferentially substitutes on Al sub-lattice sites, and since Mn has a smaller radius than Al, this leads to lattice shrinkage and a decrease in interplanar spacings. As a result, this allows more dislocations to cross glide between close packed planes [6,8,9]. Lattice shrinkage leads to a reduction in tetragonality of γ and increases the symmetry of the lattices. This further activates additional dislocation glide systems leading to an increase in dislocation multiplication and mobility during dislocation glide relaxion taking place during strain hardening. Dislocation multiplication and mobility improves ductility in the TiAlMn alloy [8].

Lattice shrinkage also leads to grain refinement thereby allowing for intergranular micro-cracking during ductile fracture, which hinders rapid crack propagation. Fine grains have improved ductility since it is only subject to intergranular fracture as opposed to coarse grains which are subjected to both intergranular and intragranular fracture [9]–[13]. The addition of Mn to TiAl also has an electronic effect [14] because it leads to an increase in electron density between Ti atoms and Mn atoms leading to metallic bonding between atoms, which also improves mechanical properties [15].

The use of micro alloying to improve ductility alongside traditional fabrication methods has not mitigated challenges such as

* Corresponding author.
*E-mail address:* Sibusisiwe.Motha@students.wits.ac.za (S. Motha).

https://doi.org/10.1016/j.matpr.2022.04.817
2214-7853/© 2021 The Authors. Published by Elsevier Ltd.
This is an open access article under the CC BY-NC-ND license (https://creativecommons.org/licenses/by-nc-nd/4.0) Selection and peer-review under responsibility of the scientific committee of the International Symposium on Nanostructured and Advanced Materials.

material wastage, high costs and the processes being tedious [16,17]. Thus, the use of Laser Engineered Net Shaping (LENS) as a fabrication method has been proposed to mitigate these challenges faced in traditional fabrication processes. LENS is an additive manufacturing process which prints out three dimensional objects in a layer upon layer fashion according to a computer aided design (CAD) [16,17].

This work investigates the effects of ternary alloying TiAl with Mn to improve ductility and using LENS as a fabrication process to address challenges encountered in traditional manufacturing methods and to control microstructures and mechanical properties.

## 2. Experimental methodology

### 2.1. Materials

Commercially pure spherical powders of titanium (Ti) and aluminium (Al) and irregular shaped pure manganese (Mn) powder with particle size distribution ranges of 45–90 μm for Ti and Al, and 45–75 μm for Mn were used in this study. Both Ti and Al powders were supplied by German-based company, TLS Technik GmbH & Co Spezialpulver while Mn was supplied by a local mining company called Manganese Metal Company (South Africa). Powders were used in their as-received conditions and deposited on titanium alloy grade 5 (Ti-6Al-4 V) base plates. Both binary and ternary alloys of TiAlMn were synthesized using the LENS machine by means of an in-situ alloying synthesis approach.

### 2.2. Synthesis

Synthesis of Ti-Al-Mn alloys on Ti-6Al-4 V substrates were carried out using the Optomec 850-R LENS machine. During synthesis, powders were deposited concurrently into the melt-pool from their independent external hoppers. The powder and laser spots were deposited on the same centre for maximum melting and optimum powder efficiency during deposition. Cubes with size dimensions of $1 \times 1 \times 0.7$ $cm^3$ were printed using process parameters that are reported in Table 1. The Ti feed rate was kept constant at 2.5 rpm with Ar gas flowrates at 3 L/min. LENS head deposition speed of 1.198 cm/s was used during deposition while the carrier gas flowrate for Al (L/min) and Al powder feed rate (rpm) were varied according to parameters listed in Table 1. Experimental setup similar to the one used and reported by Tlotleng *et al.* [19] was used in this study.

### 2.3. Heat-treatment

All samples generated were sectioned into halves. One half was characterised in the as-produced state, and the other half was taken for heat-treatment. For heat-treatment, the cut sample was encapsulated into silica tubes which were filled with Ar gas and sealed to prevent the sample from oxidising during heat-treatment. Nabertherm muffle furnace was used to heat-treat the samples. A heating rate of 3 °C/s was used to ramp the temperature to 950 °C. The samples were held at 950 °C for three hours, followed by furnace cooling to room temperature.

### 2.4. Characterization

The microstructure was studied using Scanning Electron Microscope (SEM), with Backscatter Diffraction (BSD) mode, and Electron High Tension (EHT) set at 20 kV. Compositions of microstructural features were obtained with Energy Dispersive X-Ray Spectroscopy (EDS/EDX). Lattice parameters of the sample structures were identified using XRD BRUKER D2 PHASER. The Cu-$K_\alpha$ ($\lambda$ = 1.54Å) was used as the radiation source at a current of 10 mA, voltage of 30 kV, scan ranging from $2\theta = 5°$ to 90° at a scan speed of 8.5°/min and step increment of 0.026°. Electron Backscatter Diffraction (EBSD) was performed using Zeiss Cross-Beam 540 Scanning Electron Microscope at an electron acceleration voltage of 25 kV and a probe current of 10nA was used to attain the crystal orientations within microstructures. Olympus Optical Microscope (OM) was used to measure and analyse post processing thermal cracks in order to study the mechanical behaviour of the alloys. To study the mechanical properties further, microhardness tests were performed using Future-Tech Micro hardness Tester Model FM-700, with a load of 500 gf and dwell time of 15 s. (See Fig. 1.)

**Table 1**
LENS parameters used to fabricate cubes.

| Sample number | Mn Feed-rates (rpm) | Ar carrier gas flowrates (L/min) | Al Feed-rates (rpm) | Ar carrier gas flowrates (L/min) | Power (W) |
|---|---|---|---|---|---|
| TiAl –2.3 | – | – | 1.5 | 5 | 350 |
| TiAl-2.4 | – | – | 1,5 | 6 | 350 |
| TiAlMn-1 | 0,3 | 1,2 | 1 | 6 | 500 |
| TiAlMn-2 | 0,3 | 1,2 | 1,5 | 6 | 550 |
| TiAlMn-3 | 0,3 | 1,2 | 2 | 6 | 550 |

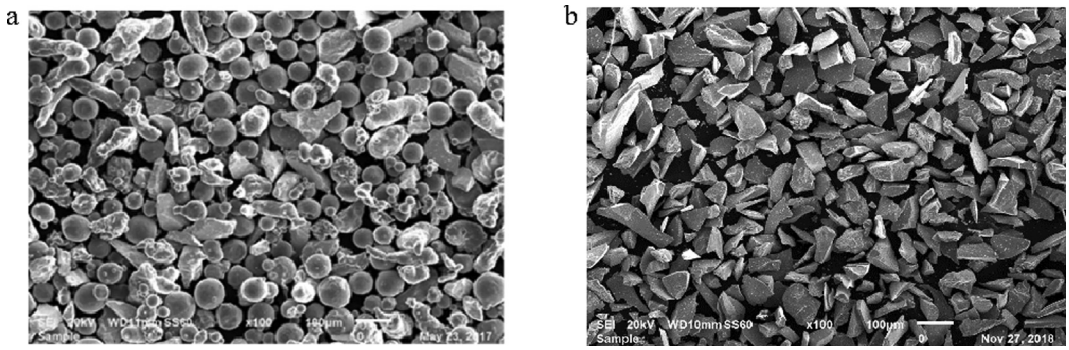


**Fig. 1.** powder metals used as feed stock in LENS machine: (a) spherical TiAl powder [18] (b)irregular shaped Mn powder.

## 3. Results

### 3.1. Microstructure

The effects of Mn addition on TiAl microstructures are displayed in Fig. 2. Microstructure of binary TiAl produced using low Ar carrier gas flowrates (5 L/min) comprised of nearly lamellar α + γ microstructure illustrated in Fig. 2a. The microstructure of binary TiAl alloy produced when the Ar carrier gas flowrates was 6 L/min is displayed in Fig. 2b and it comprises of fully lamella $\alpha_2$ + γ equiaxed grains [3]. The addition of Mn to TiAl led to a microstructure comprising of agglomerated $\alpha_2$ globules within the β-phase matrix with fine γ platelets [20] as displayed in Fig. 2c. As laser power was increased from 500 W to 550 W and Al feed rates from 1 rpm to 2 rpm, larger γ grains within the β matrix were produced, while smaller $\alpha_2$ agglomerated globules were produced as observed in Fig. 2d.

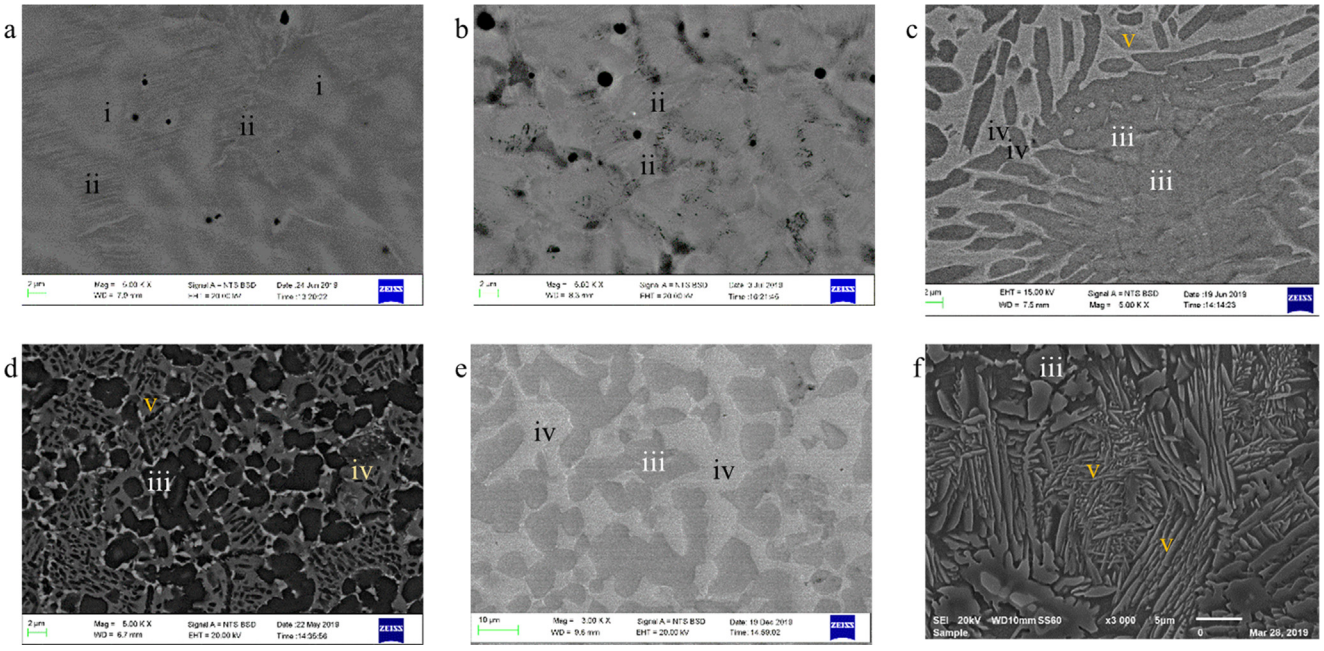


**Fig. 2.** SEM micrographs taken with BSD mode, EHT set at 20.0 kV: (a) as-produced 0.0at%Mn 56.02at%Al 43.98at%Ti- TiAl-2.3 alloy taken at magnification of x5000 (2 μm) (b) as-produced 0.0at%Mn 57.42at%Al 42.58at%Ti alloy taken at magnification of x5000 (2 μm) –(TiAl-2.4) (c) as-produced 1.39at%Al 88.50at%Ti 10.12at%Mn alloy taken at magnification of x5000 (2 μm) – (TiAlMn-1) (d) as-produced 25.39at%Al 67.95at%Ti 6.66at%Mn alloy taken at magnification of x5000 (2 μm) –(TiAlMn-3) (e) heat treated version of sample displayed in Fig. 2 c taken with magnification of x3000 (10 μm) – (TiAlMn-1) (f) heat treated version of sample displayed in Fig. 2 c taken with magnification of x3000 (10 μm)- (TiAlMn-3).

**Table 2**
Microstructural features and compositions of TiAlMn alloys obtained through EDS/EDX.

| Microstructure | Description | BSD contrast | at%Ti range | at%Al range | at%Mn range | Phase | Labels |
|---|---|---|---|---|---|---|---|
| Nearly lamellar | Within equiaxed grains | Light grey | 52.52–69.46 | 30.54–47.48 | 0.00 | $\alpha_2$ | (i) |
| Fully lamellar | Grain boundaries | Dark grey | 56.82 – 58.05 | 41.95–43.18 | 0.00 | $\alpha_2$ + γ | (ii) |
| Globules | Within grain | Black | 73.67 – 98.76 | 1.71 – 22.32 | 0.00 – 4.01 | $\alpha_2$ | (iii) |
| Matrix | Grain boundary | Light grey | 63.03 – 84.04 | 0.69 – 23.23 | 13.74 – 20.33 | β | (iv) |
| Platelets | Within matrix | Dark grey | 67.14 – 88.90 | 3.47 – 25.16 | 6.96 – 9.54 | γ | (v) |

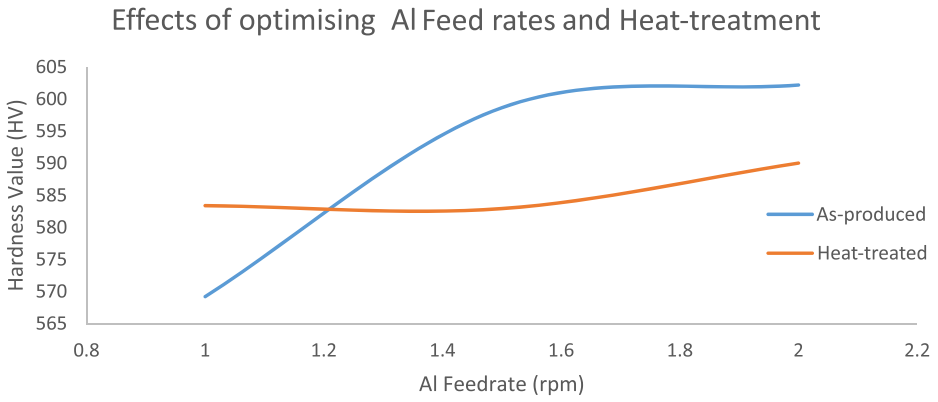


**Fig. 3.** Graphical representation displaying the effects of increasing Al feed rates and heat treatment on average microhardness values of TiAlMn alloys.

Binary TiAl and ternary TiAlMn alloys were heat-treated at 950 °C. Heat-treated binary TiAl alloys contained fully lamellar $\alpha_2$ + $\gamma$ equiaxed grains. TiAlMn-1 comprised of agglomerates of $\alpha_2$-phase within the β-matrix with traces of $\gamma$ on $\alpha_2$ globular grain boundaries as observed in Fig. 2e. In Fig. 2f, it was observed that during heat-treatment the microstructure transformed from $\alpha_2$ globules within β matrix which contained $\gamma$ platelets (Fig. 2d) into a fully lamellar microstructure due to the growth of $\gamma$ lamellae which increased in length from an approximate average of 1.400 μm to 1.840 μm to 6.540 μm within the β matrix. $\gamma$ lamellae occupied the equiaxed grain and $\alpha_2$ globules the grain boundaries. In the compositions of the microstructures displayed in Table 2, it was observed that $\alpha_2$ globules were Ti rich with compositions ranging from 73.67 at% to 98.76 at%, β matrix was Mn rich with compositions ranging from 13.74 at% to 20.33 at% and $\gamma$ phase is Al rich with compositions ranging from 3.47 at% to 25.16 at%. However, when the Al was increased to 25.39 at% and 29.20 at%, samples became brittle and were friable, as a result, the samples were not analysed further.

### 3.2. Microhardness

The microhardness values of as-produced binary TiAl-2.3 and TiAl-2.4 were 522HV and 535HV respectively. The microhardness values reduced to 386HV and 391HV after heat-treatment. The microhardness values of as-produced TiAlMn ranged from 569HV to 602HV with an average of 590HV. Fig. 3 displays the effects of increasing Al feed rates in TiAlMn alloys on microhardness in the as-produced state and heat-treated state.

Microhardness of heat-treated TiAlMn structures ranged from 582HV to 590HV with an average of 585HV. The effects of altering Al compositions on microhardness are displayed in Fig. 3. It can be observed that increasing Al feed rates increased microhardness in both the as-produced state and heat-treated state. However, heat-treatment led to an increase in microhardness in low Al alloys but reduction in microhardness in high Al alloys.

### 3.3. Crack lengths and calculated fracture stress

Furthermore, since thermal gradients induce thermal residual stresses which led to post processing thermal cracking[21]–[23].

**Table 3**
Effects of crack lengths on calculated fracture stress.

| Sample | Crack Length | Fracture toughness | Calculated fracture stress: $\sigma_f = \frac{K_{IC}}{\sqrt{\pi a}}$ [24] |
|---|---|---|---|
| As-produced TiAl-2.4 | 65.293 x$10^{-6}$ *m* | 1.00 MPa $\sqrt{m}$ [3] | 69*MPa* |
| As-produced TiAlMn-1 | 10.523 x$10^{-6}$ *m* | 4.0 MPa $\sqrt{m}$ [25] | 695*MPa* |
| Heat treated TiAlMn-1 | 41.907 x$10^{-6}$ *m* | 4.0 MPa $\sqrt{m}$ | 348*MPa* |

Fracture stress was calculated using crack lengths and fracture toughness with $\sigma_f = \frac{K_{IC}}{\pi a}$, where a depicts crack length; $K_{IC}$ depicts fracture toughness. [24]. Values used to calculate fracture stress are presented in Table 3. TiAlMn-1 alloy had reduced crack lengths compared to binary TiAl alloy (Fig. 4a). These reduced crack lengths indicate improved fracture toughness with a value of 695 MPa due to Mn addition. As-produced and heat-treated TiAlMn-1 (1.39at% Al) cracks and calculated fracture stress are displayed in Fig. 4b and 4c. It is observed that heat-treatment reduced the calculated fracture stress of TiAlMn from 695 MPa to 348 MPa. Further studies were made on TiAlMn-1 since it yielded improved properties compared to TiAlMn-2 and TiAlMn-3.

### 3.4. X-Ray Diffraction

According to EVA software, $Ti_{0.4}Al_{0.6}$ with a cubic orientation was produced during deposition of TiAl-2.3. However, when Rietveld refinement was performed, it was determined that the crystal orientation was tetragonal, shown in Fig. 5a. When heat-treatment was carried out, $Ti_{0.15}Al_{0.85}$ also with a tetragonal crystal orientation was produced- Fig. 5b. Tetragonal lattice parameters *a* and *c* of as-produced TiAl-2.3 increased due to heat-treatment as shown in Table 4. Tetragonal lattice volume increased due to heat-treatment. $Ti_{0.7}Al_{0.3}$ with a hexagonal crystal orientation was also produced during laser deposition and $Ti_3Al$ also with a hexagonal crystal orientation was produced post heat-treatment- displayed in Fig. 5a and 5b. Hexagonal lattice parameter *a* reduced and *c* increased due to heat-treatment as shown in Table 4. When Ar carrier gas flowrate was increased to produce TiAl-2.4, $Ti_{0.25}Al_{0.75}$ with a tetragonal orientation was produced during laser deposition (Fig. 5c) and TiAl with a tetragonal crystal orientation was produced during heat-treatment (Fig. 5d). Tetragonal lattice parameters of TiAl-2.4 *a* and *c* reduced due to heat-treatment. The tetragonal lattice volume reduced during heat-treatment (Table 4). $Ti_{0.6}Al_{0.4}$ with a hexagonal crystal orientation was also produced during laser deposition (Fig. 5c) and $Ti_{19}Al_6$ also with a hexagonal crystal orientation was produced during heat-treatment of TiAl-2.4 displayed in Fig. 5d. Hexagonal lattice of TiAl-2.4 parameters *a* and *c* increased during heat treatment. Hexagonal lattice volume increased - Table 4

$Al_{2.91}Mn_{1.09}$ with an orthorhombic crystal orientation was produced on Mn addition during laser deposition. Orthorhombic crystal lattice parameters *a* and *c* of as-produced $Al_{2.91}Mn_{1.09}$ increased, while *b* decreased during heat-treatment -Fig. 6f. Lattice volume reduced during heat-treatment. $TiMn_{1.20}Al_{0.80}$ with a hexagonal crystal orientation was also produced during deposition along with TiAl with a tetragonal crystal orientation and β-$Ti_{17}Mn_3$ with a cubic crystal orientation (Fig. 5e). $Ti_{0.965}Al_{0.035}$ also with a hexagonal crystal orientation was produced during heat-treatment along with $TiAl_2$ with a tetragonal crystal orientation and $Ti_{0.85}Mn_{0.15}$ with a cubic orientation (Fig. 5f).

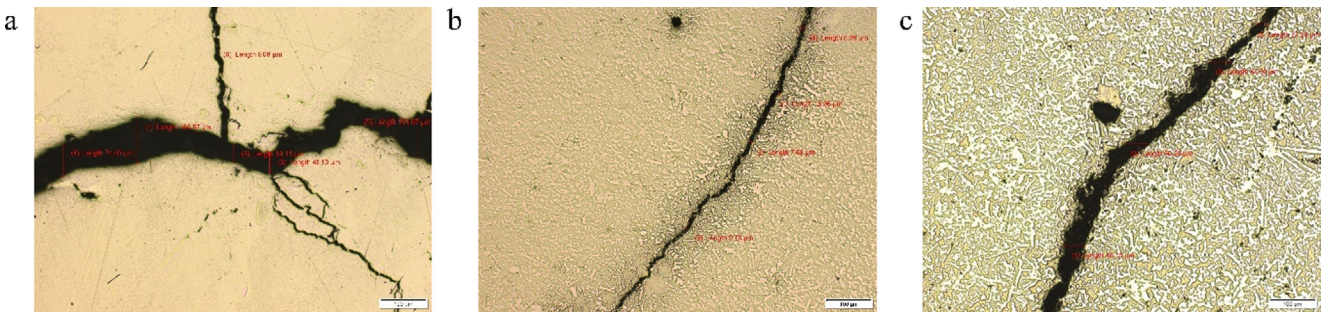


**Fig. 4.** Optical Micrographs and crack measurements of (a) as-produced TiAl alloy (b) as-produced TiAlMn alloy (c) heat-treated TiAlMn alloy.

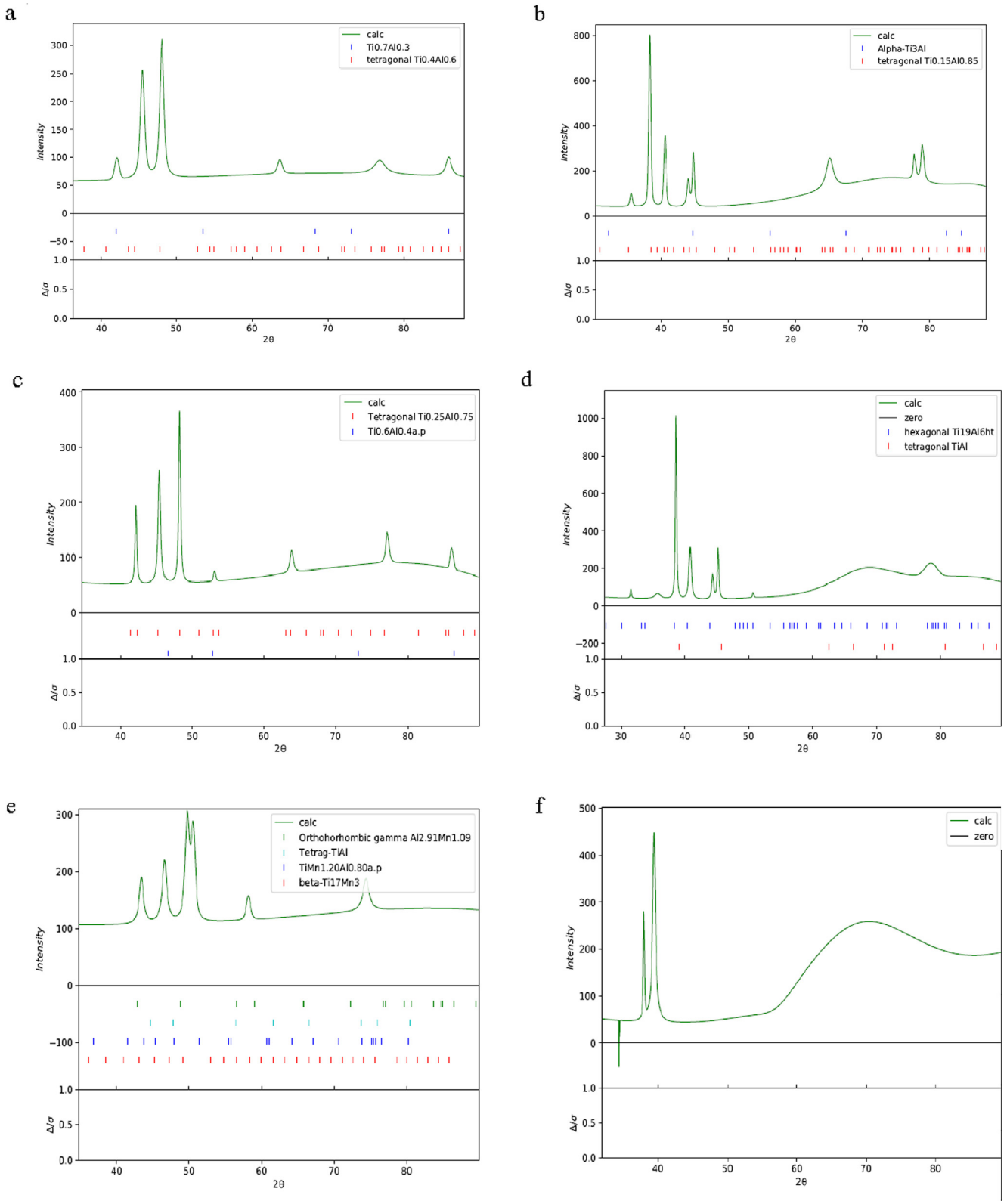


**Fig. 5.** Rietveld refinement performed on GSAS2 for XRD outcomes displaying phases of (a) as-produced TiAl-2.3 (b) heat-treated TiAl-2.3 (c) as-produced TiAl-2.4 (d) heat-treated TiAl-2.4 (e) as-produced TiAlMn-1 (f) heat-treated TiAlMn-1.

Tetragonal TiAl lattice parameter *a* reduced and *c* increased on Mn addition (Fig. 6c).

Tetragonal crystal lattice parameter *a* decreased and *c* increased during heat-treatment. Lattice volume reduced to on Mn addition and increased during heat treatment.

While hexagonal lattice parameter *a* increased and *c* decreased during heat-treatment. Lattice volume increased during heat treatment- Fig. 6d.

Cubic lattice parameter *a* increased (Fig. 6e) and lattice volume increased from to during heat-treatment Table 4.

**Table 4**
Lattice parameters of TiAl based alloys in as produced state and heat-treated state.

| | Phase | Lattice | Lattice parameters As-fabricated | | | Heat-treated | | | |
|---|---|---|---|---|---|---|---|---|---|
| | | | *a* | *b* | *c* | *a* | *b* | *c* | Volume |
| TiAl-2.3 AP and HT | $Ti_{0.4}Al_{0.6}$ | Tetragonal | 5.65844Å | – | 4.27050Å | | | | 136.73Å$^3$ |
| | $Ti_{0.7}Al_{0.3}$ | Hexagonal | 2.48044Å | – | 1.70823Å | | | | 9.10Å$^3$ |
| | $Ti_{0.15}Al_{0.85}$ | Tetragonal | | | | 9.03931Å | – | 4.65872Å | 380.66Å$^3$ |
| | $Ti_3Al$ | Hexagonal | | | | 2.33136Å | – | 2.78449Å | 13.11Å$^3$ |
| TiAl-2.4 | $Ti_{0.25}Al_{0.75}$ | Tetragonal | 5.65642Å | – | 4.25863Å | | | | 136.26Å$^3$ |
| | $Ti_{0.6}Al_{0.4}$ | Hexagonal | 2.47547Å | – | 1.99574Å | | | | 10.56Å$^3$ |
| | TiAl | Tetragonal | | | | 4.02903Å | | 1.31601Å | 21.36Å$^3$ |
| | $Ti_{19}Al_6$ | Hexagonal | | | | 4.14000Å | | 14.07095Å | 208.47Å$^3$ |
| TiAlMn-1 | $Al_{2.91}Mn_{1.09}$ | Orthorhombic | 3.17246Å | 4.71166Å | 3.60870Å | | | | 53.94Å$^3$ |
| | $Al_{2.91}Mn_{1.09}$ | Orthorhombic | | | | 3.24097Å | 3.48005Å | 4.39517Å | 49.57Å$^3$ |
| | $TiMn_{1.20}Al_{0.80}$ | Hexagonal | 3.89761Å | – | 4.71199Å | | | | 61.99Å$^3$ |
| | TiAl | Tetragonal | 2.48789Å | – | 7.32984Å | | | | 45.37Å$^3$ |
| | β-$Ti_{17}Mn_3$ | Cubic | 9.36638Å | | | | | | 821.704Å$^3$ |
| | $Ti_{0.965}Al_{0.035}$ | Hexagonal | | | | 4.73510Å | – | 3.68838Å | 71.62Å$^3$ |
| | $TiAl_2$ | Tetragonal | | | | 2.48079Å | – | 8.16362Å | 50.24Å$^3$ |
| | $Ti_{0.85}Mn_{0.15}$ | Cubic | | | | 9.65303Å | – | – | 894.394Å$^3$ |

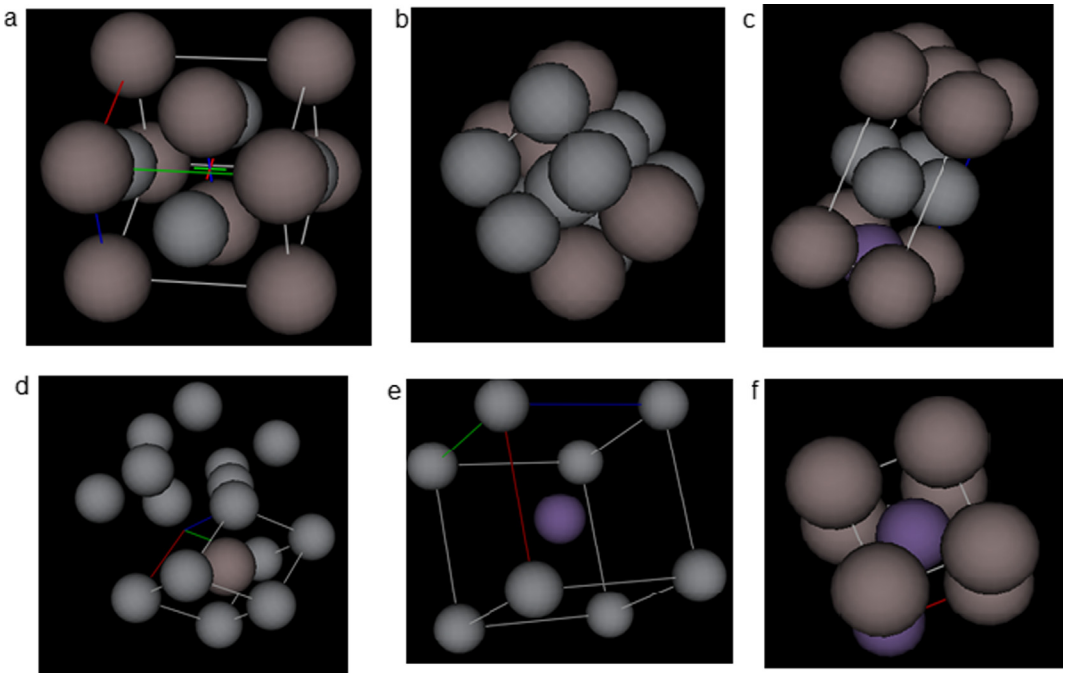


**Fig. 6.** crystal orientations and lattice parameters (a) As-produced tetragonal $Ti_{0.4}Al_{0.6}$ with lattice parameters: $a = b = 5.65844$Å; $c = 4.27050$Å- TiAl-2.3 (b) Heat-treated hexagonal $Ti_3Al$ with lattice parameters: $a = 2.33136$Å ; $c = 2.78449$Å- TiAl-2.3 (c) Crystal orientation of as-produced Mn micro alloyed tetragonal TiAl with lattice parameters: $a = b = 2.48789$Å ; $c = 7.32984$Å (d) Crystal orientation of hexagonal $Ti_{0.965}Al_{0.035}$ in heat-treated TiAlMn-1 with lattice parameters: $a = 4.73510$Å ; $c = 3.68838$Å (e) Crystal orientation of cubic β-$Ti_{17}Mn_3$ in as-produced TiAlMn-1 with lattice parameter: $a = b = c = 9.36638$Å (f) Crystal orientation of orthorhombic $Al_{2.91}Mn_{1.09}$ in heat-treated TiAlMn-1 with lattice parameter: $a = 3.24097$Å ; $b = 3.48005$Å ; $c = 4.39517$Å.

**Table 5**
Details of atoms illustrated in Fig. 6.

| Elements | Al | Mn | Ti |
|---|---|---|---|
| Isotope | Natural Abundance | Natural Abundance | Natural Abundance |
| Number of atoms per cell | 1.7 | 2.8 | 17.5 |
| Atomic weight | 26.982 | 54.938 | 47.900 |
| Bond radii | 1.60 | 1.54 | 1.66 |
| Angle radii | 1.43 | 1.30 | 1.46 |
| Van der Waals radii | 2.05 | 1.70 | 1.70 |
| Default colour | Beige | Purple | Grey |

**Table 6**
Effects of increasing Ar carrier gas flow rates on d-spacings of tetragonal crystal lattices.

| d- spacings – Tetragonal | As-produced TiAl-2.3 | As-produced TiAl-2.4 |
|---|---|---|
| $d_{(2\,2\,0)}$ | 2.00056Å | 1.99985Å |
| $d_{(1\,1\,2)}$ | 1.88379Å | 1.87956Å |
| $d_{(2\,2\,2)}$ | 1.45991Å | 1.45773Å |
| $d_{(2\,1\,3)}$ | 1.24067Å | 1.23794Å |
| $d_{(3\,3\,2)}$ | 1.13118Å | 1.13000Å |

**Table 7**
Effects of increasing Ar carrier gas flow rates on d-spacings of hexagonal crystal lattices.

| d-spacing – Hexagonal | As produced TiAl-2.3 | As produced TiAl-2.4 |
|---|---|---|
| $d_{(1000)}$ | 2.14813Å | 2.14382Å |
| $d_{(0112)}$ | 1.70823Å | 1.99574Å |
| $d_{(0222)}$ | 1.33702Å | 1.46075Å |
| $d_{(0213)}$ | 1.24022Å | 1.23773Å |

Crystal orientations produced are illustrated in Fig. 6 and colour coded in Table 5, where atomic radii are also listed. These diagrams were obtained using GSAS2. Hexagonal $\alpha_2$ and tetragonal $\gamma$ crystal orientations produced in binary TiAl alloys are displayed in Fig. 6a and 6b. While hexagonal $\alpha_2$, tetragonal $\gamma$, cubic $\beta$ and orthorhombic $Al_{2.91}Mn_{1.09}$ produced by ternary TiAlMn alloys are depicted in Fig. 6c, 6d, 6e and 6d.

Increasing Ar carrier gas flowrates led to a reduction in lattice parameters both in the as-produced and heat-treated states of tetragonal crystal lattices. The *d*-spacings along common crystal planes of as produced TiAl-2.3 and TiAl-2.4 reduced as displayed in Table 6.

However, the simultaneous reduction and increase of certain lattice parameters in the hexagonal crystal lattices led to reduction and increase of various d-spacings along common crystal planes when Ar carrier gas flow rates were increased as shown in Table 7. This implies that Ar interstitial atoms occupied the crystal along hexagonal lattice parameter *c* (situated in octahedral interstitial voids), so when the hexagonal lattice makes space to accommodate the Ar atoms, the tetragonal lattice volume was compromised and reduced, which leads to reduction of tetragonal interplanar spacings.

### 3.5. Dislocation densities

Dislocation densities were calculated by performing Rietveld refinement with respect to Lorentzian (HL) and Gaussian (HG) functions [26] to produce plots where $\frac{\Delta Q}{Q}$ was plotted against Q. The broadening of peak widths [27] were calculated using the Equations (1) and (2)

$$\frac{\Delta Q}{Q} = \frac{\Delta d}{d} \tag{1}$$

$$\frac{\Delta d}{d} * Q = \Delta d \tag{2}$$

Where ΔQ and Δd are equivalent to the full width at half maximum (FWHM), also known as ΔK [28]. Δd can then be substituted into the Scherrer formula [29] in Equation (3) to calculate crystal size.

$$D = \frac{K\lambda}{\Delta d * \cos(\theta)} \tag{3}$$

Where D is the crystal size(Å), K is the shape factor and λ the wavelength (Å) of X ray. The crystal size was used to estimate dislocation density using Equation (4)

$$\delta = \frac{1}{D^2} \tag{4}$$

Where δ is the dislocation density ($Å^{-2}$)

Fig. 7a and 7b illustrate the peak broadening of as-produced and heat-treated TiAl-2.3. The peak broadening of as-produced and heat-treated TiAl-2.4 are illustrated in Fig. 7c and 7d. These plots were used to calculate dislocation densities displayed in Table 8.

Dislocation densities of TiAl-2.3, TiAl-2.4 and TiAlMn-1 increased during heat-treatment. Dislocations had burger's vectors: $\frac{1}{3}a[11\bar{2}0]$ for hexagonal structure;$\frac{1}{2}a<\bar{1}10]$;$\frac{1}{2}a<\bar{1}\,\bar{1}2]$; $<0\bar{1}1]$*and* $<10\bar{1}]$ for tetragonal structure [3] along close packed planes $(111)_\gamma \| (0001)_\alpha$ and $(110)_\gamma \| (1120)_\alpha$ [3] ;$\frac{1}{2}a[111]$ for cubic structures along close packed planes $(101)_\beta \| (0001)_\alpha$ [30]**.** Fig. 7e and 7f illustrate the peak broadening of as-produced and heat-treated TiAlMn-1.

### 3.6. Electron Backscatter Diffraction (EBSD) analysis

Samples that yielded the least number of post processing thermal cracks were studied further by EBSD analysis. These samples include as-produced and heat-treated TiAlMn-1. Table 9 alongside Fig. 8a display the colour coding and phase distribution of as-produced TiAlMn-1. From the results, it was observed that the matrix was comprised of Mn rich β-$Ti_{17}Mn_3$ while the agglomerated globules were comprised of the Ti rich $\alpha_2$-Ti phase. This elemental distribution can be observed in the SEM-BSD diagram in Fig. 8b which was captured on the same spot as the EBSD in Fig. 8a. However, the γ-phase which comprised 0.01 vol% was observed within the matrix phase in Fig. 8a but could not be observed in the SEM-BSD diagram in Fig. 8b. The distribution of the crystal orientations within different grains which comprise both globules and the matrix are displayed in the Inverse Polar Figure-Z (IPF-Z) in Fig. 8c. A variety of crystal orientations with respect to the Z axis were observed within both $\alpha_2$ globules and β matrix. The larger variety in the matrix phase was accredited to the presence of γ-phase within the matrix. Fig. 8d displays grain boundaries while average, maximum and minimum grain sizes of different phases are stated in Table 9 as equivalent circle diameter (ECD-μm). It was observed that β phase has larger grains than $\alpha_2$ phase, while it became extremely challenging to measure the sizes of γ grains since they were oriented within the matrix phase and globules as platelets.

Table 10 and Fig. 9a shows the colour coding and phase distribution of heat-treated TiAlMn-1. It was observed that heat-treatment at 950 °C led to an increase in $\alpha_2$-phase and a decrease and slight reorientation of β-phase to β-$Ti_{0.85}Mn_{0.15}$. The elemental distribution among these phases is visually observed in Fig. 9b and numerically presented in Table 10. It can be observed that heat-treatment has led to the segregation of Ti from the β-phase to $\alpha_2$ and γ phase and the segregation of Mn to β phase. Fig. 9c displays an IPF-Z diagram where it can be observed that in comparison to the as-produced state (Fig. 8c), the crystal orientations to the z-axis within each grain are more uniform. In Fig. 9d are the grain boundaries. It can be observed in Tables 9 and 10 that heat-treatment led

### 3.7. Polar Figures

Fig. 10a, b and c display crystal orientations detected by EBSD in as-produced TiAlMn-1 in pole figures. Fig. 10a displays crystal orientations for β-$Ti_{17}Mn_3$ detected on {1 1 0} standard projection for cubic system, where 396 orientations were counted using Image J software. Fig. 10b displays $\alpha_2$ orientations detected on $\{1\ 0\ \bar{1}\ 0\}$ standard projection for hexagonal system which amounted to 635 orientations. Fig. 10c displays γ-TiAl detected on {1 1 1} standard projection for a tetragonal system. Fig. 10d, e and f display crystal orientations detected by EBSD in heat-treated TiAlMn-1. It could be observed in Fig. 10d that β cubic orientations were more concentrated towards orientations with symmetry folds compared to the as produced state displayed in Fig. 10a, although 309 orientations were counted. It was also observed in Fig. 10e that the heat-treated state appeared to have a reduced number of orientations of hexagonal-$\alpha_2$ crystals compared to the as-produced state in Fig. 10b and the number of these orientations counted

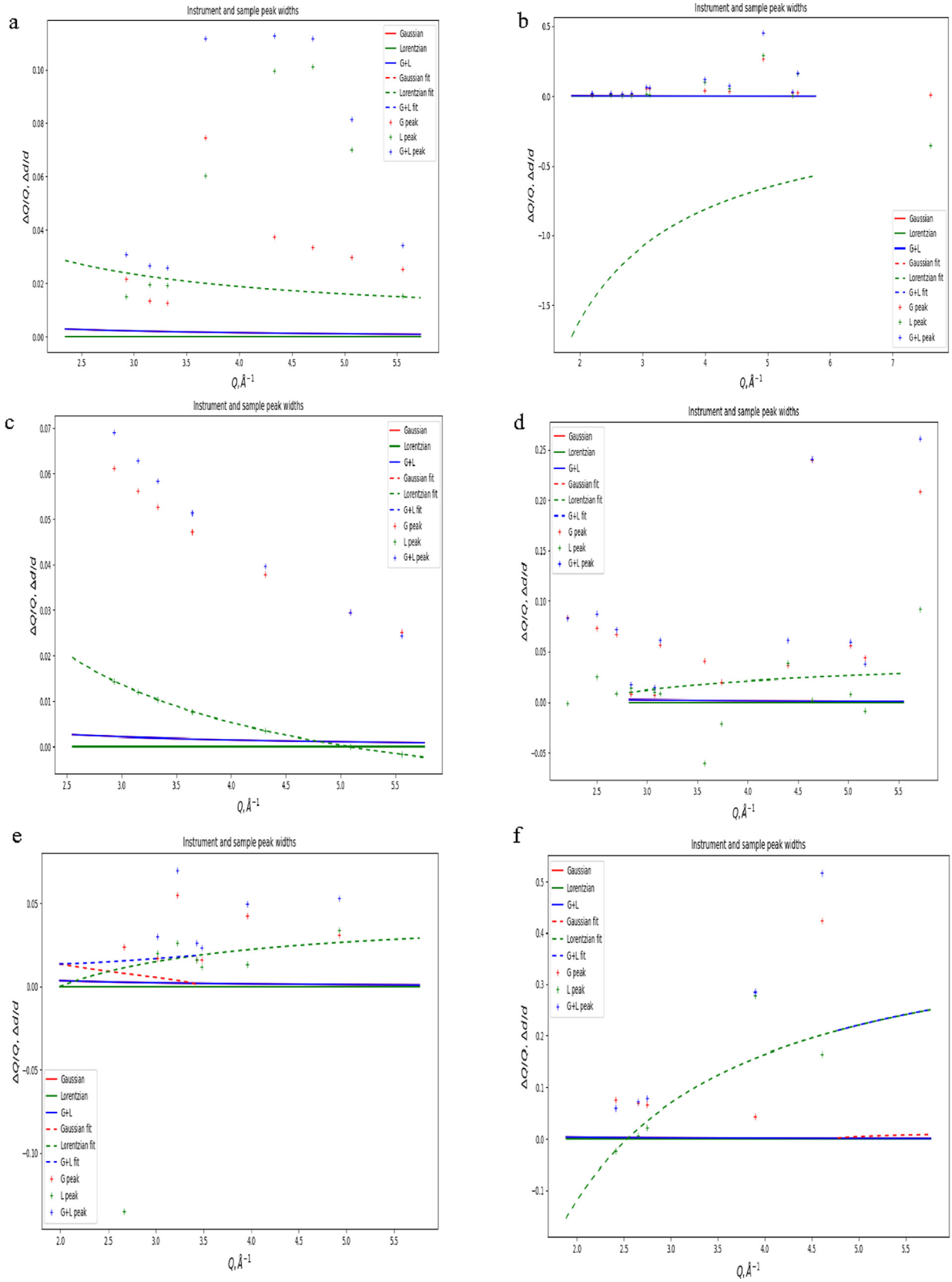


**Fig. 7.** Plots displaying peak width broadening of XRD patterns of (a) as-produced TiAl2.3 (b) heat-treated TiAl-2.3 (c) as-produced TiAl-2.4 (d) heat-treated TiAl-2.4 (e) as-produced TiAlMn-1 (f) heat-treated TiAlMn-1.

**Table 8**
Calculated dislocation densities of TiAl based alloys.

| Sample | Dislocation density (x$10^{-4}$ Å$^{-2}$) (As produced) | Dislocation density (x$10^{-4}$ Å$^{-2}$) (Heat treated) |
|---|---|---|
| TiAl-2.3 | 11,54 | 53,11 |
| TiAl-2.4 | 3,60 | 29,72 |
| TiAlMn-1 | 3,25 | 140,86 |

**Table 9**
Microstructural features of as-produced TiAlMn-1 detected by EBSD and SEM.

| Phases | $\alpha_2$ -Ti | β-$Ti_{17}Mn_3$ | γ- TiAl |
|---|---|---|---|
| EBDS colour codes | Blue | Red | Yellow |
| Phase distribution (vol%) | 44.66 | 55.07 | 0.01 |
| SEM-BSD contrast | Black | Grey | Dark grey |
| Average Ti (at%) | 95.69 | 80.49 | 88.90 |
| Average Mn (at%) | 3.500 | 16.38 | 7.63 |
| Average Al (at%) | 2.350 | 3.127 | 3.47 |
| Average grain size-ECD(μm) | 4.49 | 5.64 | – |
| Maximum grain size | 10.61 | 14.16 | – |
| Minimum grain size | 3.08 | 3.08 | – |
| Microstructural Features | globules | matrix | platelets |

amounted to 480. Fig. 10f shows that heat-treatment led to increased crystal orientations of the tetragonal γ-$TiAl_2$ compared to the as-produced state in Fig. 10f and the number of orientations counted totalled to 18.

### 3.8. Texture measurements

Texture peaks were identified on XRD patterns for both as-produced and heat-treated alloys prior to the performance of Rietveld Refinements [31]. Texture measurements of various crystal orientations were carried out using EBSD on standard cubic and hexagonal projections using multiples of uniform distribution (MUD). MUD is equal to the ratio of a given orientation to the relative weight of the same orientation in a uniform texture distribution[32]. Fig. 11a, b and c display the texture measurements of as-produced TiAlMn-1 while Fig. 11d, e and f display texture measurements of heat-treated TiAlMn-1. Fig. 11a displays the texture of β orientations in a standard {1 0 0} projection for cubic system where it can be observed that the maximum MUD was 6.33. Fig. 11b shows the texture of hexagonal crystal orientations on standard {0 0 0 1} projection for hexagonal system where maximum MUD is 4.20. Fig. 11c displays the texture of γ-TiAl orientations on {0 0 1} standard projection for tetragonal system where the orientations are extremely limited but have the maximum texture measurement of 180.27MUD. Fig. 11d indicates that heat-treatment led to a reduction of maximum texture measurement

**Table 10**
Microstructural features of heat treated TiAlMn-1 detected by EBSD and SEM-BSD.

| Phases | $\alpha_2$-Ti | β-$Ti_{0.85}Mn_{15}$ | γ-$TiAl_2$ |
|---|---|---|---|
| EBDS colour codes | Blue | Red | Yellow |
| Phase distribution (vol%) | 71.61 | 27.45 | 0.09 |
| SEM-BSD contrast | Black | Grey | Dark grey |
| Average Ti (at%) | 95.91 | 76.44 | 92.15 |
| Average Mn (at%) | 2.99 | 21.74 | 6.38 |
| Average Al (at%) | 1.10 | 1.830 | 1.47 |
| Average grain size-ECD(μm) | 6.06 | 5.33 | – |
| Maximum grain size | 22.30 | 10.18 | – |
| Minimum grain size | 3.07 | 3.07 | – |
| Microstructural features | Equiaxed grains | Matrix | Grain boundaries |

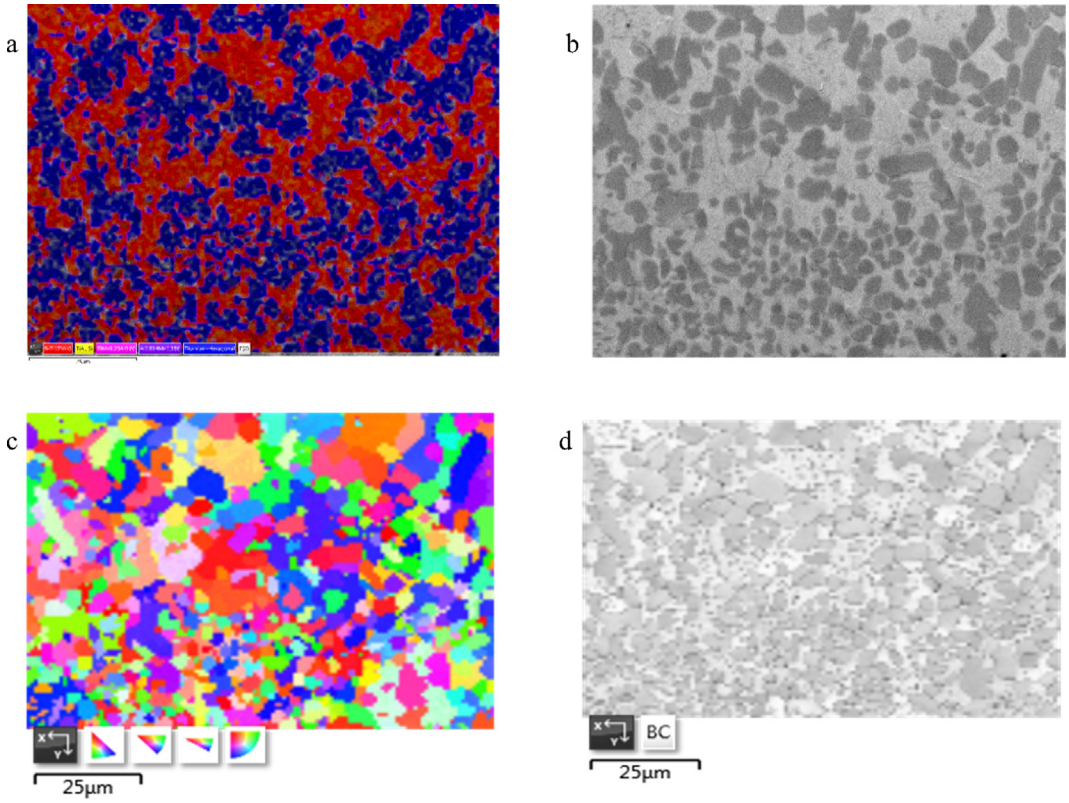


**Fig. 8.** Electron Backscatter Diffraction (EBSD) images of as-produced TiAlMn-1 (a)Phase distribution of β, $\alpha_2$ and γ phases (b) Backscatter diffraction Scanning Electron Micrograph (BSD-SEM) image displaying elemental distribution (c) Inverse Polar Figure-Z (IPF-Z) displaying crystal orientation of different grains relative to z-axis (d) Band contrast image displaying grain boundaries.

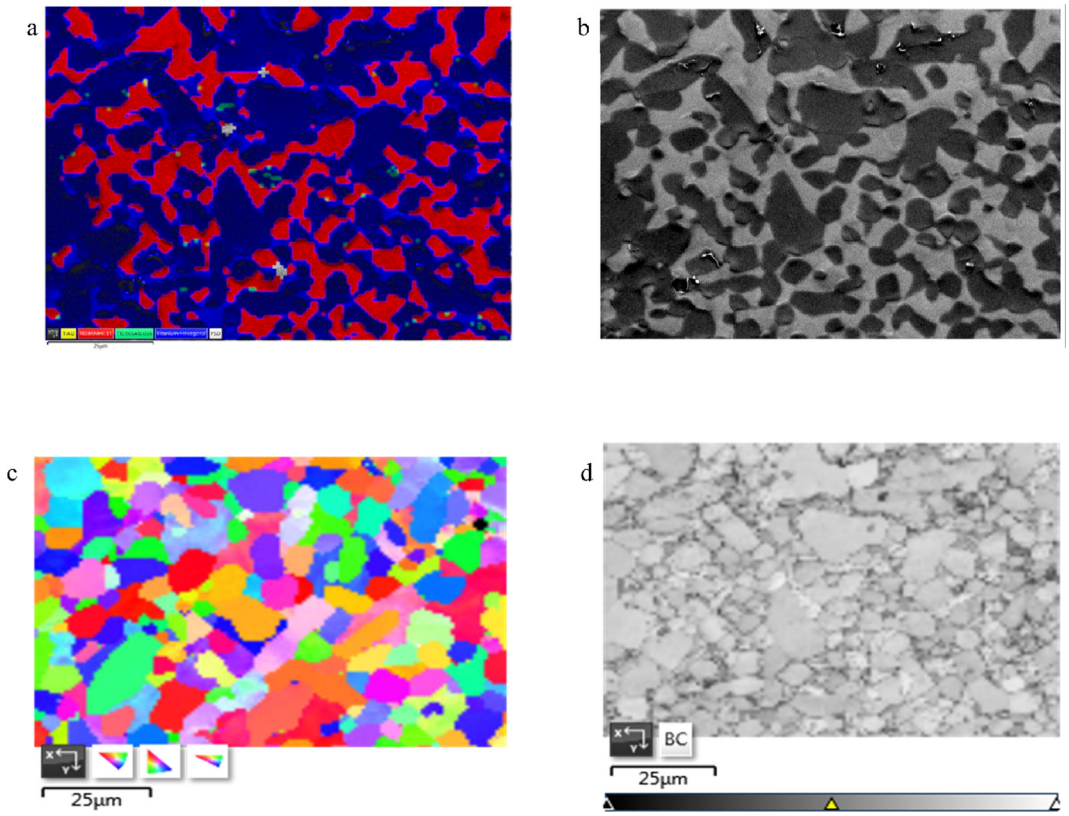


**Fig. 9.** EBSD images of heat-treated TiAlMn-1 (a) phase distribution of $\alpha_2$, β, $Ti_{0.965}Al_{0.035}$ and $TiAl_2$ (b) SEM-BSD image displaying elemental distribution (c) IPF-Z displaying crystal orientations of different grains (d) Band contrast image displaying different grain boundaries of heat-treated TiAlMn-1.

to 4.54MUD for β- $Ti_{0.85}Mn_{0.15}$. However, Fig. 11e indicates that heat-treatment led to maximum increased texture measurements of 11.30MUD. Similar to β phase, heat-treatment led to a reduction in texture in tetragonal γ-$TiAl_2$ to MUD of 38.33 as displayed in Fig. 11f.

## 4. Discussion

After the experimental procedures were undertaken and results were obtained, various analogies were made and are discussed in this section. The effects of increasing Ar carrier gas flowrates, Mn addition and laser power during laser deposition and applying post processing heat-treatment, on crystal orientations, dislocation densities and microhardness were discussed, and conclusions were drawn from these analyses. Focus was also placed on how varied LENS parameters also affected post processing thermal cracking.

Increasing Ar carrier gas flowrates led to a decrease in tetragonal lattice parameters and volume. Which also led to reduced interplanar spacings in tetragonal lattices. However, the hexagonal lattice parameter *a* decreased while *c* increased. This led to a slight increase in hexagonal lattice volumes. The increase in hexagonal lattice parameter *c* was accredited to Ar interstitial atoms which occupy a lattice along the *c*-axis. This forced a lattice to increase in size along the *c*-axis to accommodate the Ar atoms [29]. Since hexagonal structure is the brittle and hard phase due to its complexity which restricts dislocation motion [5,33,34], increased hexagonal lattice volume led to a slight increase in microhardness in TiAl alloys. A significant reduction in dislocation densities due to increased Ar carrier gas flowrates was also observed.

When heat-treatment was carried out on TiAl alloys, it led to an increase in dislocation densities, which were accompanied by a significant reduction in microhardness values. This further validated that increased dislocation densities lead to reduced microhardness in binary TiAl alloys [4]. However, binary TiAl alloys were severely cracked even through their microhardness values were low. Increasing Ar carrier gas flowrates and heat treatment both led to segregation of grain boundary of Al to both tetragonal and hexagonal structures. This observation was made in both XRD and SEM/EDX findings.

Mn addition to TiAl alloys led to a reduction in tetragonal lattice parameters *a* and increased *c* (increased *c/a* ratio) and a reduction in d-spacings [9]. This led to a reduction in tetragonal lattice volume due to the substitution of Mn atom (which has a smaller radius) on Al sub lattices (which has a larger radius).

However, hexagonal lattice volume increased due to Mn addition to TiAl. These changes in lattice parameters led to a reduction in dislocation densities but increased microhardness values. Increased microhardness and reduced post process thermal cracking can possibly be accredited by reduced dislocation densities and twinning induced plasticity [35]–[37] which led to work hardening and improved strength. The mechanism involved included the repulsive forces between dislocation twin boundaries and atoms leading to the storage of energy within the surface which increased microhardness values. Although microhardness values had increased, the number of cracks in the sample reduced. Since the interplanar spacings between α/γ interfaces were smaller, this led to higher dislocation cross glide speeds which exceeded crack propagation speeds during thermal strain and resulted in fewer cracks [3]–[5,9].

Heat treatment of ternary TiAlMn-1 alloy led to an increase in microhardness values and dislocation densities. Increased microhardness values were accounted by the diffusion rates of Mn which are higher than those of Al and Ti [38] and the enhancement of twinning induced plasticity[36]. This means that during heat treat-

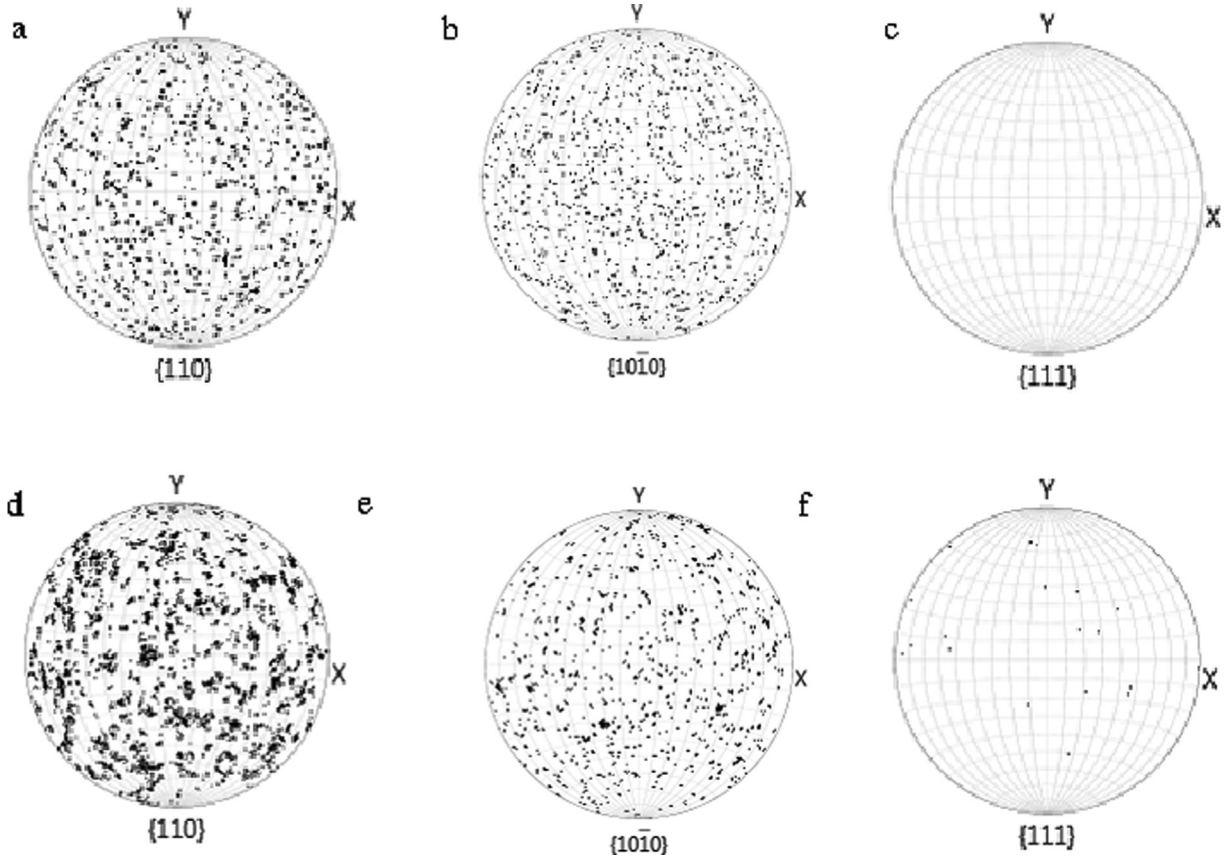


**Fig. 10.** Pole figures displaying crystal orientations of phases (a) 396 crystal orientations of β phase in as-produced TiAlMn-1 detected by EBSD on {1 1 0} standard projection of cubic system (b) 635 crystal orientations of $\alpha_2$ phase in as-produced TiAlMn-1 detected by EBSD on $\{10\bar{1}0\}$ standard projection of hexagonal system (c) crystal orientations of γ phase in as-produced TiAlMn-1 detected by EBSD on {1 1 1} standard projection of cubic system (d) 309 crystal orientations of β phase in heat-treated TiAlMn-1 detected by EBSD on {1 1 0} standard projection of cubic system (e) 480 crystal orientations of $\alpha_2$ phase in heat-treated TiAlMn-1 detected by EBSD on $\{10\bar{1}0\}$ standard projection of hexagonal system (f) 18 crystal orientations of γ phase in heat-treated TiAlMn-1 detected by EBSD on {1 1 1} standard projection of cubic system.

ment, Mn atoms absorbed energy which resulted in larger amounts of energy being stored within the surface which work against the microhardness indenter during microhardness indentation leading to increased microhardness values and strength [36,37]. Lattice parameters of tetragonal, hexagonal, and cubic structures increased during heat treatment due to thermal expansion, which also led to increased dislocation density. This indicated that although dislocation densities increased, they were restricted in motion compared to the as produced state of TiAlMn-1 since the heat-treated sample had more cracks.

Orthorhombic $Al_{2.91}Mn_{1.09}$ lattice parameters decreased during heat treatment. The fractional site occupancy of this phase was 1 which indicated that dislocations were not mobile within this phase.

The increase in Al feed rates led to an increase in volume of γ phase in the microstructure. This again confirms that Al addition is a γ phase stabilizer. The production of γ phase is favourable at lower temperatures [39] and slower cooling rates are required to facilitate solid state phase transformation reactions to produce γ phase. These slower cooling rates are favoured by increased Laser Energy per unit length (LEPUL)[40]. As LEPUL increased, the sizes of γ platelets within the β matrix increased which led to brittle behaviour (increased hardness and friable).

However, low Al (1.39at%Al) TiAlMn-1 structures which contained minimal γ, yielded increased microhardness and reduced post process thermal cracks. These post processing thermal cracks were smaller than those observed in binary TiAl alloys. The reduction in crack lengths occurred simultaneously with reduction in interplanar spacing between close packed planes. A similar observation was made when crack length increased with increasing d-spacing in heat treated TiAl-2.4 and TiAlMn-1. Reduced interplanar spacings allow dislocations the ability to cross glide easily between planes to enable dislocation glide relaxation during thermal strain, which allows dislocations the ability to move at speeds closer to those of crack propagation during fracture, which led to reduced crack lengths [6,9].

As-produced high Al (25.39at%Al,10.12at%Mn and 29.20at% Al,6.66at%Mn) ternary alloys were extremely brittle and had the highest microhardness. Both the brittle behaviour and high microhardness is accounted by thermal residual stresses caused by thermal gradients during deposition, leading to higher post processing thermal cracking and microhardness values[22]. The presence of the β matrix phase known to have strength three times higher than α phase [41], which is absent in the heat-treated state could contribute to high microhardness values.

Heat-treated high Al (25.39at%Al and 29.20at%Al) samples were fully lamellar $\alpha_2$ + γ which had reduced microhardness compared to as-produced state. Although the samples had lower microhardness, they were still extremely friable. This was due to microstructural features not having the appropriate parameters that enable ductility, such as correct interlamellar spacings and lamellar boundary angle to the tensile axis [34,42]. It was observed that the larger the volume of Al in both binary and ternary alloys, yielded lower microhardness values post heat-treatment. This is accredited to stress relief [43] and the slower diffusion rates of Al compared to Ti and Mn, which led to lower storage of energy

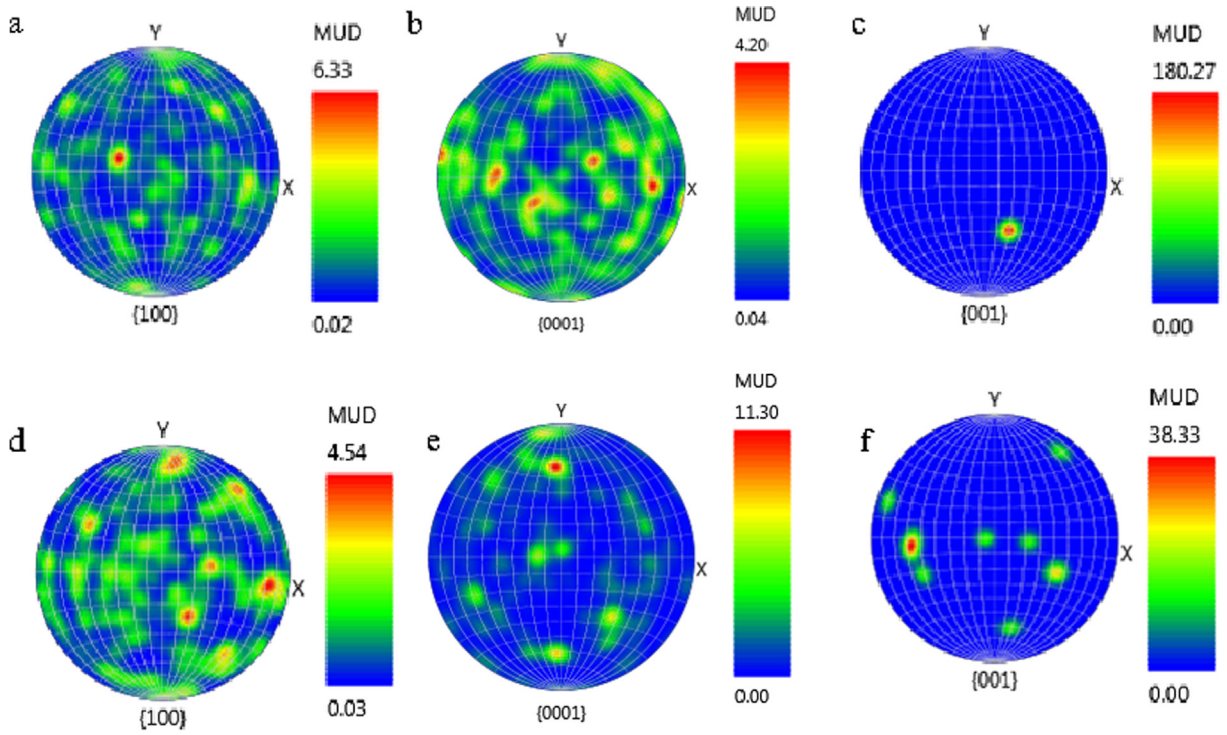


**Fig. 11.** distribution of crystal textures of various orientations detected measured in MUD for: (a) texture distribution of β phase in as-produced TiAlMn-1 detected by EBSD on {1 0 0} standard projection of cubic system (b) texture distribution of $\alpha_2$ - phase in as-produced TiAlMn-1 detected by EBSD on {0 0 0 1} standard projection of hexagonal system (c) texture distribution of γ phase in as-produced TiAlMn-1 detected by EBSD on {0 0 1} standard projection of cubic system (d) texture distribution of β phase in heat treated TiAlMn-1 detected by EBSD on {1 0 0} standard projection of cubic system (e) texture distribution of $\alpha_2$ - phase in heat treated TiAlMn-1 detected by EBSD on {0 0 0 1} standard projection of hexagonal system (f) texture distribution of γ phase in heat treated TiAlMn-1 detected by EBSD on {0 0 1} standard projection of cubic system.

within the surface of the alloys during heat-treatment [38], meaning less energy worked against the microhardness indenter during microhardness testing, yielding lower microhardness values post heat-treatment. Reduced microhardness can also be a result of reduced β matrix phase after heat-treatment [41].

As-produced and heat-treated TiAlMn-1 underwent EBSD analysis. From the EBSD analysis it was observed that heat-treatment led to orientations of β phase to be concentrated along the symmetry folds of the {1 1 0} standard projection for a cubic system[44]. This led to increased symmetry in crystal orientations [45], which resulted in the activation additional dislocation glide systems [9] which was evident in increased dislocation densities post heat-treatment. Although the volume proportion of hexagonal $\alpha_2$ phase increased due to heat-treatment, fewer crystal orientations were detected, which indicated homogeneity within the phase. Dislocation motion is highly limited in $\alpha_2$ phase due to the complexity of the crystal structure[34]. Heat-treatment also led to increased tetragonal orientations, which allow dislocations glide along $\alpha_2/\gamma$ interfaces [34]. Reduced number of crystal orientations counted on pole figures post heat treatment indicated that heat treatment led to microstructures with more homogenous crystal orientation distribution. This is also evident in the inverse polar figures which contain grains which appear more uniform. Heat-treatment also led to a reduction in texture measurements of cubic β and tetragonal γ orientations but increased texture in $\alpha_2$ orientations. All these mechanisms led to increased microhardness values.

Increased microhardness in TiAlMn-1 values post heat-treatment can be accredited by increased $\alpha_2$ phase which restricted dislocation motion during microhardness indentation, leading to a stress build up within the phase[34], thus more stresses working against the microhardness indenter during testing. Since $\alpha_2$ has higher microhardness than γ phase [33], increase in $\alpha_2$ volumes during heat-treatment led to increased microhardness values post heat-treatment.

## 5. Conclusions

Through experimental work, which included fabrication, heat treatment, characterization with XRD, SEM and EBSD, findings obtained led to the following conclusions for this research:

1. The addition of Mn as a ternary alloying element increased microhardness and reduced post processing thermal cracking.
2. Increasing Al feed rates and laser power in TiAlMn alloys increases the volume proportions of γ, which led to alloys being friable post heat treatment, but with lower microhardness values.
3. Mn addition reduces interplanar spacings and reduced dislocation densities. However, heat-treatment increased dislocation densities.
4. Increased dislocation densities in binary TiAl alloys reduces microhardness, but increased dislocation densities in ternary TiAlMn increased microhardness.

## CRediT authorship contribution statement

**Sibusisiwe Motha:** Validation, Formal analysis, Investigation, Data curation, Visualization. **Nthabiseng Maledi:** Conceptualization, Writing – review & editing, Supervision, Project administration, Funding acquisition. **Monnamme Tlotleng:** Methodology, Resources, Writing – review & editing, Supervision, Funding acquisition.

## Declaration of Competing Interest

The authors declare that they have no known competing financial interests or personal relationships that could have appeared to influence the work reported in this paper.

## Acknowledgements

The authors wish to thank Council for Scientific and Industrial Research (CSIR) for providing the facilities to produce the samples for this research and National Research Foundation (NRF), grant number: TTK160527166453 for the Thuthuka Projects and Manufacturing, Engineering and Related Services Sector Education Authority (merSETA) for financial support. Mr Dzara for assisting with glass blowing services, Manganese Metal Company (MMC) for supplying Manganese powder and Dr Clive Oliphants at NMISA for assisting with the EBSD service. A special thanks to Professor Michael Lee from Nelson Mandela University for academic advice.

## References

[1] J. Lapin, 'TiAl-based alloys: Present status and future perspectives', 2009, vol. 19, no. 21.5, p. 2009.
[2] C. M. Austin, T. J. Kelly, and S.-C. Huang, 'Titanium aluminide alloy with improved temperature capability', Aug. 1996.
[3] F. Appel, J.D.H. Paul, M. Oehring, *Gamma titanium aluminide alloys*. Wiley Online, Library (2011).
[4] F. Appel, 'TiAl Intermetallics', *Encyclopedia of Aerospace Engineering*, 2010.
[5] F. Appel, R. Wagner, Microstructure and deformation of two-phase γ-titanium aluminides, Materials science and engineering: r: reports 22 (5) (1998) 187–268.
[6] Q. Wang, H. Ding, H. Zhang, R. Chen, J. Guo, H. Fu, Influence of Mn addition on the microstructure and mechanical properties of a directionally solidified γ-TiAl alloy, Materials Characterization 137 (2018) 133–141.
[7] R. Kainuma, Y. Fujita, H. Mitsui, I. Ohnuma, K. Ishida, Phase equilibria among α (hcp), β (bcc) and γ (L10) phases in Ti–Al base ternary alloys, Intermetallics 8 (8) (2000) 855–867.
[8] D. Vujic, Z. Li, S.H. Whang, Effect of rapid solidification and alloying addition on lattice distortion and atomic ordering in L1 0 tial alloys and their ternary alloys, Metallurgical Transactions A 19 (10) (1988) 2445–2455.
[9] S. Shu, F. Qiu, B. Xing, S. Jin, Y. Wang, Q. Jiang, Study of effect of Mn addition on the mechanical properties of Ti2AlC/TiAl composites through first principles study and experimental investigation, Intermetallics 28 (2012) 65–70.
[13] D. Hu, Effect of composition on grain refinement in TiAl-based alloys, Intermetallics 9 (12) (2001) 1037–1043.
[14] M. Morinaga, J. Saito, N. Yukawa, H. Adachi, Electronic effect on the ductility of alloyed TiAl compound, Acta Metallurgica et Materialia 38 (1) (1990) 25–29.
[15] T. Kawabata, H. Fukai, O. Izumi, Effect of ternary additions on mechanical properties of TiAl, Acta Materialia 46 (6) (1998) 2185–2194.
[16] D. Gu (Ed.), Laser Additive Manufacturing of High-Performance Materials, Springer Berlin Heidelberg, Berlin, Heidelberg, 2015.
[17] D. Gu, Y. Shen, Balling phenomena during direct laser sintering of multi-component Cu-based metal powder, Journal of Alloys and Compounds 432 (1-2) (2007) 163–166.
[18] M. Tlotleng and S. Pityana, 'In-Situ Alloyed LENS ADDITIVELY MANUFACTURED TiAl-Nb STRUCTURE', 2018.
[19] M. Tlotleng, Microstructural properties of heat-treated LENS in situ additively manufactured titanium aluminide, Journal of Materials Engineering and Performance 28 (2) (2019) 701–708.
[20] X. Li, H. Xu, W. Xing, B. Chen, Y. Ma, K. Liu, Phase transformation behavior of a β-solidifying γ-TiAl-based alloy from different phase regions with various cooling methods, Metals 8 (9) (2018) 731.
[21] W. Liu, J. DuPont, Fabrication of Titanium Aluminide Matrix Composites by Laser Engineered Net Shaping 124, presented at the 2002 International Solid Freeform Fabrication Symposium, 2002.
[22] A.R.C. Sharman, J.I. Hughes, K. Ridgway, Characterisation of titanium aluminide components manufactured by laser metal deposition, Intermetallics 93 (2018) 89–92.
[23] A. Weisheit, B. Mordike, W. Smarlsy, K. Richter, Laser surface remelting and laser surface gas alloying of an intermetallic TiAl alloy, Lasers in Engineering 10 (1) (2000) 63–81.
[24] W.E. Voice, M. Henderson, E.F.J. Shelton, X. Wu, Gamma titanium aluminide, TNB, Intermetallics 13 (9) (2005) 959–964.
[25] R.A. Varin, L. Zbroniec, Z.G. Wang, Fracture toughness and yield strength of boron-doped, high (Ti+ Mn) L12 titanium trialuminides, Intermetallics 9 (3) (2001) 195–207.
[26] S. Khalili, V. Soleimanian, A. Mokhtari, Developing a method for the evaluation of dislocation parameters from the Rietveld refinement procedure, Powder Diffraction 31 (3) (2016) 198–204.
[27] B.H Toby, R.B Von Dreele, and J. Appl. Cryst, 'GSAS2', vol. 46, pp. 544–549, 2013.
[28] W. Woo, T. Ungár, Z. Feng, E. Kenik, B. Clausen, X-ray and neutron diffraction measurements of dislocation density and subgrain size in a friction-stir-welded aluminum alloy, Metallurgical and Materials Transactions A 41 (5) (2010) 1210–1216.
[29] K. Khojier, H. Savaloni, E. Shokrai, Z. Dehghani, N.Z. Dehnavi, Influence of argon gas flow on mechanical and electrical properties of sputtered titanium nitride thin films, Journal of Theoretical and Applied Physics 7 (1) (2013) 1–6.
[30] V. Tong, S. Joseph, A.K. Ackerman, D. Dye, T.B. Britton, Using transmission Kikuchi diffraction to characterise α variants in an α+ β titanium alloy, Journal of microscopy 267 (3) (2017) 318–329.
[31] F. Wang, W. Shen, J. Fan, J. Du, K. Chen, J.P. Liu, Strong texture in nanograin bulk Nd–Fe–B magnets via slow plastic deformation at low temperatures, Nanoscale 11 (13) (2019) 6062–6071.
[32] A. Creuziger, K. Syed, T. Gnäupel-Herold, Measurement of uncertainty in orientation distribution function calculations, Scripta Materialia 72 (2014) 55–58.
[33] S. Gebhard, F. Pyczak, M. Göken, Microstructural and micromechanical characterisation of TiAl alloys using atomic force microscopy and nanoindentation, Materials Science and Engineering: A 523 (1–2) (2009) 235–241.
[34] S.-W. Kim, Y.-S. Na, J.-T. Yeom, S.E. Kim, Y.S. Choi, An in-situ transmission electron microscopy study on room temperature ductility of TiAl alloys with fully lamellar microstructure, Materials Science and Engineering: A 589 (2014) 140–145.
[35] H. Inui, M. Oh, A. Nakamura, M. Yamaguchi, Room-temperature tensile deformation of polysynthetically twinned (PST) crystals of TiAl, Acta Metallurgica et Materialia 40 (11) (1992) 3095–3104.
[36] Z. Jiao, J. Luan, C. Liu, Strategies for improving ductility of ordered intermetallics, Progress in Natural Science: Materials International 26 (1) (2016) 1–12.
[37] M. Yoo, C. Fu, Physical constants, deformation twinning, and microcracking of titanium aluminides, Metallurgical and Materials Transactions A 29 (1) (1998) 49–63.
[38] I. Polmear, D. StJohn, J.-F. Nie, M. Qian, Light alloys: metallurgy of the light metals, Butterworth-Heinemann, 2017.
[39] J.C. Schuster, M. Palm, Reassessment of the binary aluminum-titanium phase diagram, Journal of phase equilibria and diffusion 27 (3) (2006) 255–277.
[40] S. Bontha, N.W. Klingbeil, P.A. Kobryn, H.L. Fraser, Thermal process maps for predicting solidification microstructure in laser fabrication of thin-wall structures, Journal of Materials Processing Technology 178 (1–3) (2006) 135–142.
[41] F. Holden, H. Ogden, R. Jaffee, Heat treatment, structure, and mechanical properties of Ti-Mn alloys, JOM 6 (2) (1954) 169–184.
[42] M. Yamaguchi, D. Johnson, H. Lee, H. Inui, Directional solidification of TiAl-base alloys, Intermetallics 8 (5–6) (2000) 511–517.
[43] F. Bassani, Encyclopedia of condensed matter physics, Elsevier acad. press (2005).
[44] E. Widjaja, L. Marks, Models for quasicrystal–crystal epitaxy, Journal of Physics: Condensed Matter 20 (31) (2008) 314003.
[45] G. Nolze, A. Winkelmann, 'About the reliability of EBSD measurements, Data enhancement' 891 (1) (2020) 012018.

## Further Reading

[10] Y.-W. Kim, W. Smarsly, J. Lin, D. Dimiduk, F. Appel, Gamma Titanium Aluminide Alloys 2014: A Collection of Research on Innovation and Commercialization of Gamma Alloy Technology, John Wiley & Sons, 2014.
[11] S. Chubb, D. Papaconstantopoulos, B. Klein, First-principles study of L 1 0 Ti-Al and V-Al alloys, Physical Review B 38 (17) (1988) 12120.
[12] Y.-W. Kim, Ordered intermetallic alloys, part III: gamma titanium aluminides, Jom 46 (7) (1994) 30–39.

# CHARACTERIZATION OF TITANIUM-ALUMINIDE ALLOYS FABRICATED USING LASER ENGINEERED NET SHAPING

**S.N. Motha[1*], N Maledi[2*] & M. Tlotleng[3]**

[1*] Department of Chemical and Metallurgical Engineering, University of the Witwatersrand, South Africa, 378773@students.wits.ac.za

[2] Department of Mechanical Engineering, University of Johannesburg, South Africa, MTlotleng@csir.co.za

## ABSTRACT

The continuous study of Ti-Al based alloys has led to the exploration of Laser Engineered Net Shaping (LENS) as a fabrication process alternative to traditional methods such as ingot casting and hot isostatic pressing. However, the fabrication of Ti-Al based alloys using LENS poses various challenges such as post processing thermal cracking, which is caused by a combination of the brittle nature of Ti-Al based alloys and thermal residual stresses. This work investigates the effects of altering LENS parameters on microstructures, microhardness and post processing thermal cracks. The effects of altering LENS parameters on deposition mechanisms were studied by observing changes in the microstructure. The effects of heat treatment on microstructures were also studied. The resulting microstructures and microhardness revealed that Ar gas flow rates lead to slower cooling rates during laser deposition while post heat treatment lead to the reduction in microhardness.

## 1. INTRODUCTION

There has been a great and growing interest in utilising Ti-Al based alloys as potential replacements for Ni-based superalloys in the aero-engine manufacturing industry. This great interest stems from the unique combination of the material's physical and mechanical properties; which enable high temperature strength as high as that of Ni-based superalloys at half the density [1,2] . The use of Ti-Al based alloys for aero-engine applications has the potential to reduce fuel consumption and increase financial savings in the aviation industry[3]. However, the application of these materials is limited by their imbalance between high temperature creep resistance and ambient temperature ductility. Poor ambient temperature ductility leads to limited processability during manufacturing, This leads to an increase in the production costs when using traditional fabrication methods [4]–[6]. The ambient temperature ductility is attributed to the crystal orientation of γ and $\alpha_2$+γ phases which are arranged in a Burger's Orientation: $(111)_\gamma$ || $(0001)_\alpha$ and $[110]\gamma||1120]\alpha_2$ [4,5].Numerous attempts have been made to improve the ambient temperature ductility of Ti-Al alloys. These attempts encompass methods such as directional solidification, controlling lamella colony sizes and electromagnetic cold crucible directional solidification [4], [5], [9]. Directional solidification findings established that the maximum attainable ductility of Ti-Al alloys was 20% [6,7]. This value is obtained when the angle between the lamella colony boundaries and the tensile axis is 31° [4], [10], [11]. However, this maximum value of ductility is accompanied by the minimal value of creep strength of close to 0.0 MPa [10], [11]. It was also established that the maximum value of strength (400 MPa) occurs when the angle between lamella boundaries and tensile axis is 90° where ductility is at 0% [4], [10]. The best combination of ductility and strength occurs when lamella colony boundaries are parallel to the tensile axis [4], [10].

Microstructural features which include $\alpha_2$-$\alpha_2$ spacing, interplanar spacing and lamella colony sizes have also been adjusted in an attempt to improve ductility [9]. However, in adjusting these microstructural features, it was also established that parameters favourable for the improvement of ductility are detrimental to the creep strength of the $\alpha_2$+γ structure [6], [11]. Deformation mechanisms which account for ductility can also account for microhardness behaviour of Ti-Al since microhardness is inversely proportional to ductility [12], [13].

Strategies to improve the ductility of Ti-Al alloys have been attempted using traditional fabrication methods such as wrought ingot casting where heat treatment or hot isostatic pressing have been used as post processing methods and have been helpful in studying the evolution of microstructures [14]. These strategies have been successful in the improvement of the ambient temperature ductility, but are extremely costly, tedious and time consuming [15], [16]. In attempt to mitigate shortcomings from these strategies, additive manufacturing (AM) is continuously being investigated as a potential manufacturing process to replace these traditional processes. Laser Engineered Net Shaping (LENS) is an AM process that is able to produce components through a layer upon layer fashion according to a computer aided design. LENS machines, in the manufacturing sectors, are used for the free form fabrication and surface repair of metallic components and have the potential to minimize production costs, time and material wastage during production [15], [16].

LENS comprises of a glove box in which process occurs. The laser and powder deposition head are enclosed in this glove box where processing can occur under oxygen depleted environment so that high purity parts can be produced. Typically, argon is used as both the purge and process gas. To this glove box, two external powder hoppers are attached. The set-up is controlled remotely from a central computer station that is installed an Optomec software. It is from this computer station that slice-files and process input parameters can be manipulated during manufacturing without having to stop and start. YAG laser supplied by (IPG PHOTONICS) is used to melt the depositing powder during manufacturing and is also controlled remotely from the computer station.

Adjusting various process parameters when printing from the LENS system during fabrication can affect the microstructure and mechanical properties of the deposited structure. During

deposition, laser heat input (or energy densities) lead to thermal gradients pile-ups which in turn lead to post process thermal cracking in the build [17], [18]. The crack density and sizes can be influenced by the mechanical behaviour of the material and LENS parameters [17], [18]. This work investigates the effects of altering the Al feed rates and Ar carrier gas flowrates, and using heat treatment, as a post processing step, to transform the resulting microstructure of the manufactured part thereby improving their mechanical properties.

## 2. EXPERIMENTAL METHODOLOGY

Ti-Al alloys were synthesised on Ti-6Al-4V substrates using the Optmec 850-R LENS machine. The alloys were synthesised from melting, with a laser beam, commercially pure spherical powders of titanium (Ti) and aluminium (Al). Both powders had an average particle size distribution of 45-90 µm. The mixture of Ti and Al powder are displayed in the SEM micrograph in Figure 1. Both Ti and Al powders were supplied by TLS Technik GmbH & Co Spezialpulver, Germany. Scanning Electron Microscope (SEM) micro-image of the feedstock powder is shown in Figure 1.

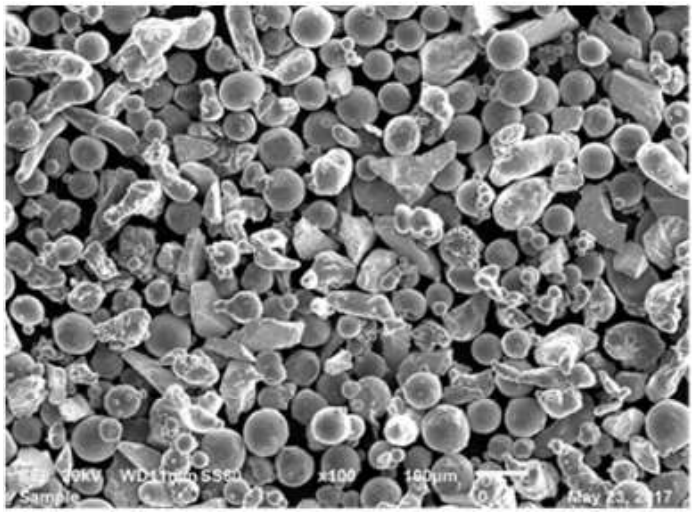

**Figure 1: SEM micrograph of Ti and Al powder feed stock (17)**

The depositing powders were formed into 1 x 1 x 0.7 cm cubes. The depositing powders were processed from their independent hoppers [Hopper-1: Ti and Hopper-2: Al] and injected into the laser melt-pool that was created on the Ti-6Al-4V base plate and upon cool the molten pool, now a mixture of Ti and Al, form into cube sizes of 1 X 1 X 0.7 $cm^3$. Argon was used as a carrier gas and shrouded the melt-pool from being oxidised. The powder feed rates can be manipulated to obtain certain compositions (like in functional grade structures, metal matrix composites and so forth) in the printed component. LENS head deposition speed that was used was 1.198 cm/s while the Ti feed rate was kept constant at 2.5 rpm. Al feed rates and Ar carrier gas flowrates were varied as reported in Table 1.

**Table 1: LENS parameters used during synthesis of cubes.**

| Sample number | Al | | |
|---|---|---|---|
| | **Feed rates (rpm)** | **Ar carrier gas flowrates (L/min)** | Power (W) |
| Ti-Al-2.1 | 1,5 | 3 | 350 |
| Ti-Al-2.2 | 1,5 | 4 | 350 |
| Ti-Al-2.3 | 1,5 | 5 | 350 |
| Ti-Al-2.4 | 1,5 | 6 | 350 |
| Ti-Al-3.1 | 2 | 3 | 350 |
| Ti-Al-3.2 | 2 | 4 | 350 |
| Ti-Al-3.3 | 2 | 5 | 350 |
| Ti-Al-3.4 | 2 | 6 | 350 |

### 2.1 Heat treatment

Ti-Al cubes were sectioned in halves for as-built and heat treatment characterisation. Before heat treatment, samples were encapsulated and purged with Ar gas in silica tubes to prevent them from oxidising during heat treatment. Heat treatment was performed in a Nabertherm muffle furnace where the temperature was ramped up to 950°C at heating rate of 3.33°C/s and held for 3 hours before the sample was allowed to cool inside the furnace overnight.

#### *2.1.1 Characterization*

In order to understand the characteristics of all the samples, Olympus optical microscope (OM) was used to measure the lengths of the post processing thermal cracks. In addition, SEM with a backscatter diffraction (BSD) mode and Electron High Tension (EHT), was used to study the microstructures of all the samples. Energy Dispersive X-Ray Spectroscopy (EDS/EDX) was used to obtain the chemical compositions of the microstructural features that were observed. Samples were removed from the substrates using diamond wire cutting machine in order to study their phases and lattice parameters using BRUKER D2 PHASER X-ray diffraction (XRD). This XRD used a Cu-Kα (λ=1.54Å) radiation source at a current of 10mA, voltage of 30KV, scan range where 2θ=5° to 90° at a scan speed of 8.5°/min and step increment of 0.026°. Phases were identified using DIFFRAC.EVA V.4.2.2 XRD software. Electron Backscatter Diffraction (EBSD) was used to determine the phase proportions and crystal orientations. The influence of microstructure on mechanical properties was studied by performing microhardness tests were 90 microhardness indentations were made using the Future-Tech Micro hardness Tester Model FM-700, with a load of 500 gf and dwell time of 15 seconds.

## 3. RESULTS

### 3.1 Microstructures

Low Al TiAl alloys produced using low Ar carrier gas flowrates (3L/min) produce ß equiaxed dendrites [19] as displayed in Figure 2a. When Ar carrier gas flow rates were increases to 5L/min, an equiaxed α+γ nearly lamellar microstructure was produced as displayed in Figure 2b. Heat treating of the low Al structures lead to an equiaxed $\alpha_2+\gamma$ fully lamellar microstructure [8] which is displayed in Figure 2c. The grain sizes of the heat treated low Al alloys increased with increasing Ar carrier gas flowrates.

High Al alloys produced with low Ar carrier gas flowrates (3L/min) produced α columnar dendrites as displayed in Figure 2d. When Ar carrier gas flowrates were increased to 6L/min, a basket weave α+γ microstructure [20] was produced as displayed in Figure 2e. Heat treating of high Al structures produced uniform γ duplex microstructures [21] as displayed in Figure 2f.

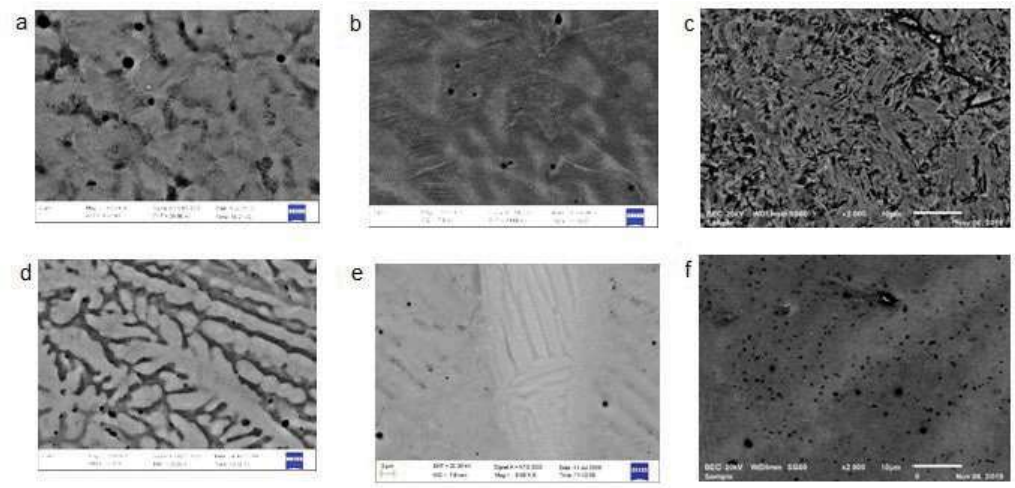


**Figure 2: SEM micrographs taken with BSD mode, EHT set at 20.0kV illustrating microstructures of samples: (a)as produced with Low Al feed rate (1.0rpm)- 42.71at%Al57.29at%Ti and low Ar carrier gas flowrate (3L/min) (b) as produced with low Al feed rate (1.0rpm) -56.02at%Al43.98at%Ti and high Ar carrier gas flowrates (5L/min) (c) heat treated TiAl alloy produced with low Al feed rate (1.0rpm) (d) as produced with high Al feed rate (2.0rpm) - 48.17at%Al51.83at%Ti and low Ar carrier gas flow rate (3L/min) (e) as produced with high Al feed rate (2.0rpm)- 63.22at%Al36.78at%Ti and high Ar carrier gas flow rate (5L/min) (f) heat treated TiAl alloys produced with high Al feed rate (2.0rpm)**

### 3.2 Microhardness

Microhardness values for samples generated at low Al feed rate ( 1.5 rpm) range from 509,056HV to 535,556HV with an average of 523,792HV. These values are wavy (up and down) with the lowest and highest HV value reported for 3 l/min and 6 l/min, respectively. Microhardness values drop when Al feed rates were increased to 2.0 rpm for the same Ar gas flowrate. In fact a significant drop in HV values was achieved for the sample that was produced with hardness was achieved for 4 l/min and was followed with a sharp rise in hardness value with an increase in Ar flowrate. Microhardness values at high Al feed rates drop to values within a range of 464,056HV to 498,889HV and averaged 476,24HV. These was attributed to the difference in the as-produced microstructures. Equiaxed dendritic and nearly lamellar microstructures seemed to be yielding higher microhardness values when compared to microstructures containing columnar dendrites, basket weave structure and fully lamellar equiaxed grain.

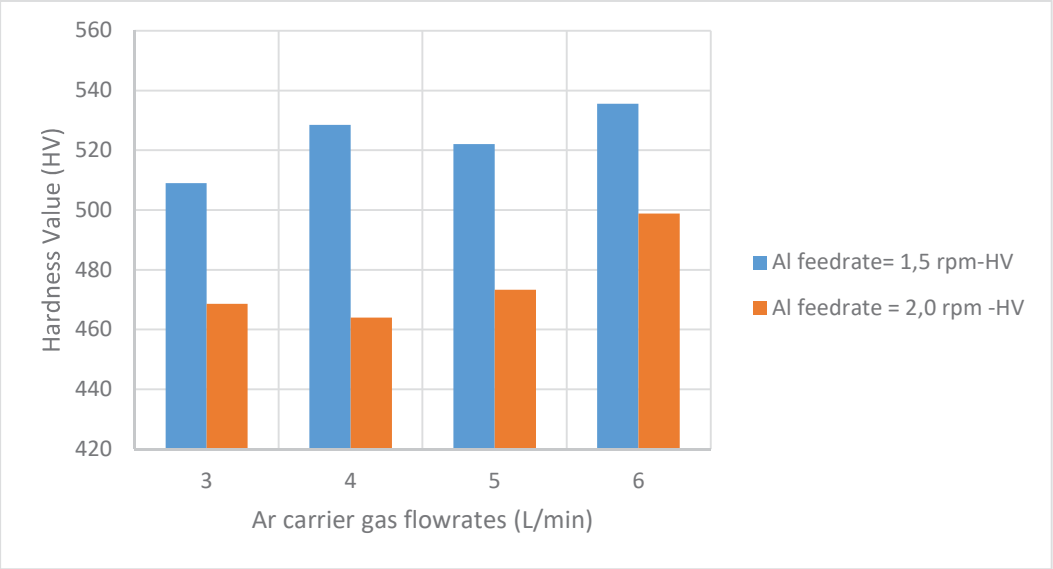


**Figure 3: Graphical representation of the effect of Al feed rates and Ar carrier gas flowrates on microhardness of as produced TiAl alloys**

The micro-hardness values of heat treated Ti-Al samples dropped significantly compared to the as produced alloys as observed in the bar graph illustrated in Figure 4. The microhardness profiles are also wavy. Micro-hardness values of heat treated Ti-Al alloys produced with low Al feed rate (1.5 rpm) dropped to a range from 387 HV to 448 HV and an average of 408 HV. The maximum hardness for these heat treated structures achieved was 447,53HV at 5L/min and the minimum was 386,74HV at 4L/min. It was observed that micro-hardness values increase with grain sizes. Micro-hardness values of heat treated Ti-Al samples produced with Al feed rate of 2.0rpm dropped to a range from 304 HV to 334 HV and an average hardness of 315 HV. The maximum hardness value achieved for these structures was 334,34HV at 6L/min and the minimum value of 304,13HV at 4L/min. This indicates that microstructures that contain the γ-phase yield low hardness.

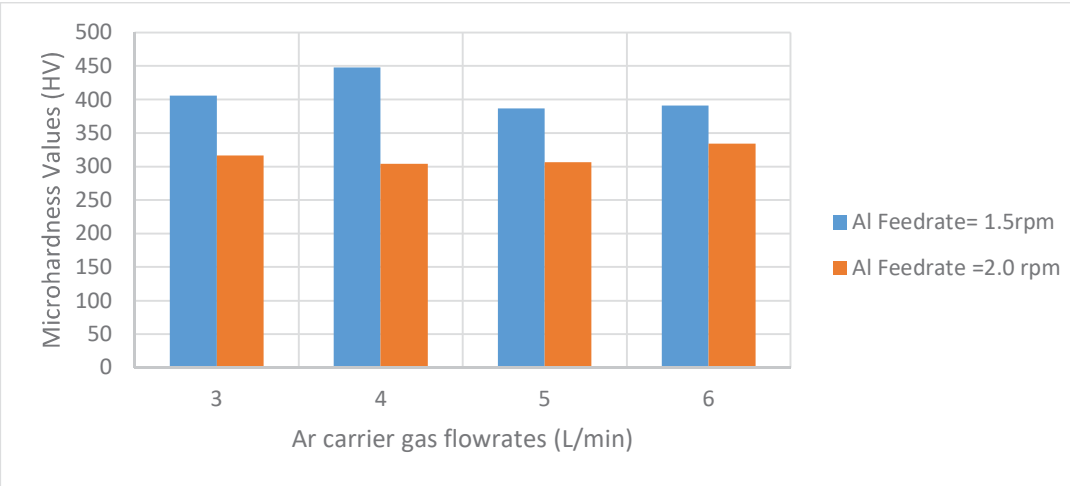


**Figure 4: Microhardness of Heat treated TiAl alloys**

### 3.3 Crystal structure

Since as produced and heat treated TiAl 2.3 sample number had the lowest crack density and lengths among all samples studied, further investigations regarding their behaviour was carried out by performing XRD. XRD confirmed the presence of γ phase with a [1 1 1] close packed plane as can be observed in Figure 5 alongside Table 2. It is observed that the as produced TiAl 2.3 sample number had XRD peaks from crystallographic planes that include [1 1 1]$_\gamma$, [2 2 0 ]$_\gamma$ and [ 2 1 1 ]$_\beta$. The d-spacing d(Å) of the close packed planes [1 1 1] was calculated to have had increased from 2.139Å to 2.517Å and the lattice parameter increased from 3.705A to 4.359A during heat treatment. The XRD peaks from different crystallographic planes which include [2 0 0]$_\gamma$, [2 1 0]$_\alpha$, [3 2 0]$_\alpha$ and [3 2 1]$_\beta$ were detected on heat treated samples. These peaks revealed various d-spacings and lattice parameter as observed in Table 2. Heat treatment also led to the broadening of the peaks which indicated strain distribution according to Stephen's Model [22]. Bragg's Equation for diffraction was used to calculate lattice parameters $n\lambda_{Cu\,K\alpha} = 2 * d_{[hkl]} sin\theta_{(hkl)}^{BRAGG}$ [23].

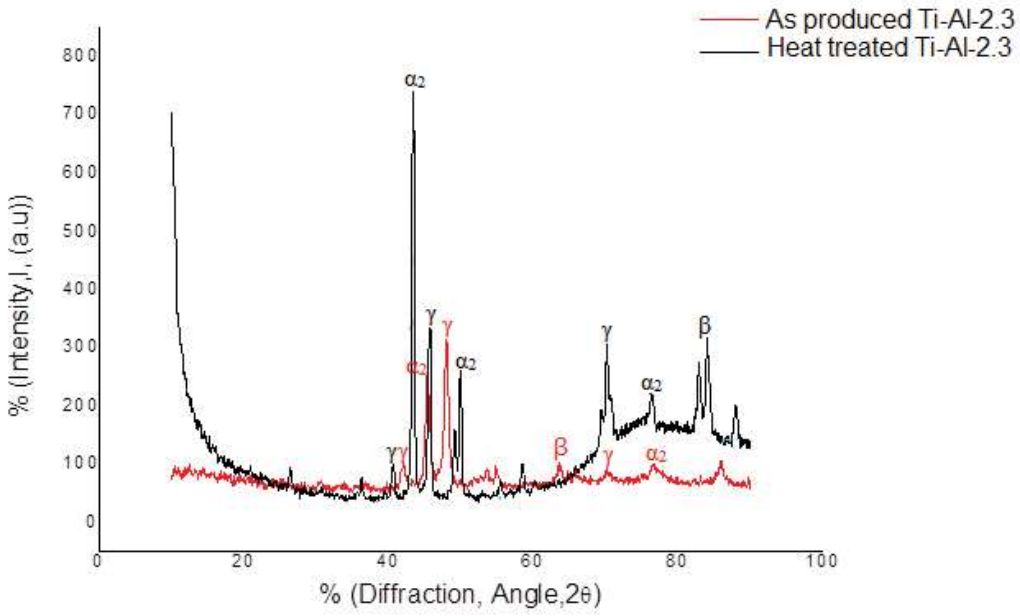


**Figure 5: XRD patterns (a) As produced and heat treated TiAl-2.3**

**Table 2: XRD peaks and lattice parameters calculated**

| 2θ(˚)-peaks | Miller Indices [h k l] | Crystal structure/ Reflections present | $d(\text{Å}) = \frac{\lambda_{Cu\,K\alpha}}{2 * sin\theta}$ | $a = d_{hkl} * \sqrt{h^2 + k^2 + l^2}$ | Phase |
|---|---|---|---|---|---|
| 42.199 | [1 1 1] | FCC | 2.139 | 3.705 | γ |
| 45.420 | - | HCP | - | - | $\alpha_2$ |
| 48.088 | [2 2 0] | FCC | 1.889 | 3.779 | γ |
| 63.540 | [2 1 1] | BCC | 1.462 | 3.582 | β |
| 70.196 | [2 2 0] | FCC | 1.340 | 3.787 | γ |
| Heat treated | | | | | |
| 35.626 | [1 1 1] | FCC | 2.517 | 4.359 | γ |

| | | | | | |
|---|---|---|---|---|---|
| 38.420 | - | HCP | - | - | $\alpha_2$ |
| 40.687 | [2 0 0] | FCC | 2.215 | 4.429 | $\gamma$ |
| 44.113 | - | HCP | - | - | $\alpha_2$ |
| 44.956 | [2 1 0] | HCP | 2.014 | 4.503 | $\alpha_2$ |
| 77,689 | [3 2 0] | HCP | 1.227 | 4.426 | $\alpha_2$ |
| 82,723 | [3 2 1] | BCC | 1.165 | 4.348 | $\beta$ |
| 82,986 | [3 2 1] | BCC | 1.162 | 4.359 | $\beta$ |

Figure 6 shows that post processing thermal crack lengths of heat treated samples were longer than the as produced samples. In the as produced state (Figure 6a), crack lengths have an average of *23.165 x10$^{-6}$ m*. The crack length in the heat treated state (Figure 6b) had an average crack length of *35.208 x10$^{-6}$ m*.

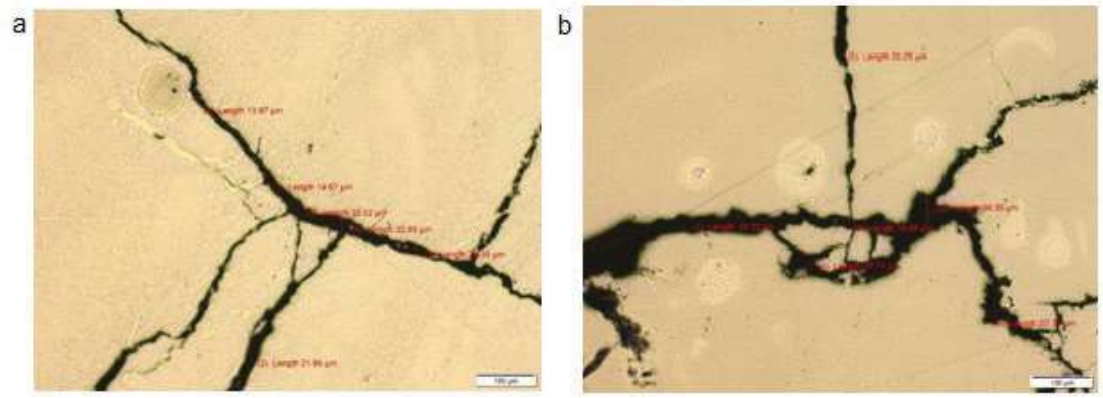


**Figure 6: (a) Average crack length of as a produced TiAl 2.3: 23.165 x10$^{-6}$ m (b) Average crack length of heat treated TiAl 2.3: 35.208 x10$^{-6}$ m**

The EBSD performed revealed the basket weave nature of TiAl-2.3 sample are primary and secondary basket weaves and were mostly comprised of the hexagonal close packed (HCP) α phase as displayed in colour coded image in Figure 7a. These HCP crystals have various orientations with respect to the z-axis as can be observed in the Inverse Polar Figure displayed in Figure 7b. The matrix phase is believed to be γ. But since the software used to identify the crystal orientations does not have FCC-γ in its databases, the solution does not appear on the images in colour codes.

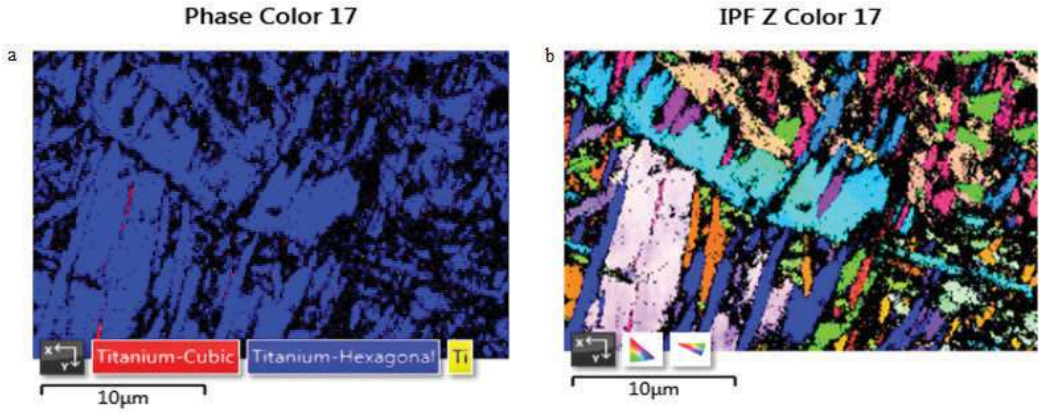


**Figure 7: (a) Colour coded EBSD image of as produced TiAl 2.3 (b) EBSD inverse pole figure (IPF) displaying crystal orientation map for as produced Ti-Al-2.3**

## 3. DISCUSSION

Inert gases such as Ar and He conserves thermal energy [25], [26]. This conservation of heat energy is influenced by Ar gas conductivity which enhances higher ratios of convective heat transfer of Ar gas to radiative heat transfer at melt free solidified surfaces during laser deposition [27]. This enables higher radiative heat transfer to melt free surface which enable solid state phase reactions [8] on melt free surface post laser deposition. This leads to the formation of nearly lamellar and fully lamella microstructures which form through solid state phase transformation reactions [7]. As Ar gas flow rates increase, it becomes easier to blow the gas on the solid melt free surface, which increases heat transfer ratios [27].

At low Al concentrations (45 – 49 at.% Al), solidification takes place through recrystallization of the ß dendrites from the melt, followed by the peritectic formation of α phase upon cooling [19], [28] cooling. The development of these microstructures as Ar gas flow rates are increased are evident in microstructures observed in as produced state as Ar gas flow rates were increased. These microstructures provide evidence that increasing Ar gas flow rates allow peritectic phase reaction: $\beta \rightarrow \beta + \alpha \rightarrow \alpha$ where α plates are formed and while Ti segregates to remaining ß ribs [20]. As Ar flow rates are increased further, γ lamellae precipitate within α plates forming α+γ nearly lamellar or basket weave structure through the following solid state phase transformation reactions: $\alpha \rightarrow \alpha + \gamma$ [19], [20].

At higher Al concentrations above 49 at.% Al, α columnar dendrites recrystalize from molten [19] during solidification which occurs post laser deposition. This microstructure later transforms into the γ phase due to annealing at 950°C [8], [21]. This is a result of solid state phase transformation reactions which occur due to heating ( $\alpha \rightarrow \alpha + \gamma \rightarrow \alpha_2 + \gamma$), and leads to fully lamellar equiaxed microstructure [19]. These microstructural developments are observed as Ar flow rates are increased. This confirms that increasing Ar gas volumetric flow rates allow for solid state transformation reactions which produce equiaxed granular structures [20] and enhances the production of γ phase.

Heat treating at 950°C causes low Al concentration builds to produce fully lamellar $\alpha_2$+γ microstructures [7], while higher Al concentrations (>49 at.% Al) produce uniform duplex γ fine grained microstructures [3]. According to Schuster and Palm [28], phases produced during heat treatment are generally thermodynamically favourable at 950°C [28].

At low Al feed rate as Ar carrier gas flow rates were increased during production, the equiaxed microstructure appeared coarser in the heat treated state. This indicates a reduction in cooling rates as Ar flow rates are increased since grain growth and coarsening is enhanced by slower cooling rates [29].

Heat treatment also lead to the increase in interplanar spacing and reduced microhardness values. This could be attributed to thermal stress relief due to heat treatment [30] which softens the material and reduces microhardness values during the annealing process [31]. The increase in interplanar spacings can be attributed to the ability of heat treatment to increase diffusion rates of both Ti and Al [32]. Faster diffusion rates lead to reduced lattice constant c/a [32], [33], since diffusion rates increases during heat treatment. Lattice constants such as c/a ratio are affected by thermal expansion which expands the lattice at higher temperatures during heat treatment [34] , which can account for the increase in interplanar spacings and lattice parameter a. Thermal expansion also accounts for increased crack lengths post heat treatment. However, the nature of post processing thermal cracks can also be accounted by the general fracture behaviour of the material [18], [24] such as strength and ductility.

The $\alpha_2+\gamma$ phase has higher microhardness than the uniform γ-phase [35]. The uniform γ-phase microstructures have significantly lower microhardness due to the absence of $\alpha_2$ phase [36]. However, uniform γ had a higher number of post processing thermal cracks than $\alpha_2+\gamma$ since thermal cracks were initiated at γ phase and propagated rapidly in a cleavage fashion through the microstructure. While in two phase $\alpha_2+\gamma$ microstructure, $\alpha_2$ which is harder and serves as crack initiation sites and prevent rapid crack propagation during thermal strain. These two phase microstructures allow cracks to propagate on $\alpha_2$ in a ligament fashion, hindering rapid crack propagation during thermal stress to which materials are subjected [9].

## 4. CONCLUSIONS

From the analysis of all experimental work performed, it was concluded that higher Ar carrier gas flowrates led to slower cooling rates. It was also established that Al is a γ phase stabiliser. Based on XRD findings, it can be concluded that heat treatment induced thermal expansion in the material leading therefore to an increase in the interplanar spacing and thermal crack lengths. Reduction in microhardness values are due to stress relief during heat treatment.

## REFERENCES


**[1]** **T. J. Kelly, M. J. Weimer, C. M. Austin, B. London, D. E. Larson Jr, and D. A. Wheeler**, 'Heat treatment of gamma titanium aluminide alloys', May 2001.

**[2]** **J. C. Chesnutt**, 'GE Aircraft Engines One Neumann Way', pp. 45212–6301, 1992.

**[3]** **Y.-W. Kim**, 'Ordered intermetallic alloys, part III: gamma titanium aluminides', *Jom*, vol. 46, no. 7, pp. 30–39, 1994.

**[4]** **H. Zhang, X. Tang, C. Zhou, H. Zhang, and S. Zhang**, 'Comparison of directional solidification of γ-TiAl alloys in conventional Al2O3 and novel Y2O3-coated Al2O3 crucibles', *Journal of the European ceramic society*, vol. 33, no. 5, pp. 925–934, 2013.

**[5]** **M. Kim, M. Oh, J. Lee, H. Inui, M. Yamaguchi, and D.-M. Wee**, 'Composition and growth rate effects in directionally solidified TiAl alloys', *Materials Science and Engineering: A*, vol. 239, pp. 570–576, 1997.

**[6]** **Y.-W. Kim, W. Smarsly, J. Lin, D. Dimiduk, and F. Appel**, *Gamma Titanium Aluminide Alloys 2014: A Collection of Research on Innovation and Commercialization of Gamma Alloy Technology*. John Wiley & Sons, 2014.

**[7]** **F. Appel**, 'TiAl Intermetallics', *Encyclopedia of Aerospace Engineering*, 2010.

**[8]** **F. Appel, J. D. H. Paul, and M. Oehring**, *Gamma titanium aluminide alloys*. Wiley Online Library, 2011.

**[9]** **S.-W. Kim, Y.-S. Na, J.-T. Yeom, S. E. Kim, and Y. S. Choi**, 'An in-situ transmission electron microscopy study on room temperature ductility of TiAl alloys with fully lamellar microstructure', *Materials Science and Engineering: A*, vol. 589, pp. 140–145, 2014.

**[10]** **M. Yamaguchi, D. Johnson, H. Lee, and H. Inui**, 'Directional solidification of TiAl-base alloys', *Intermetallics*, vol. 8, no. 5–6, pp. 511–517, 2000.

**[11]** **Z. Jiao, J. Luan, and C. Liu**, 'Strategies for improving ductility of ordered intermetallics', *Progress in Natural Science: Materials International*, vol. 26, no. 1, pp. 1–12, 2016.
**[12]** **J. Cahoon, W. Broughton, and A. Kutzak**, 'The determination of yield strength from hardness measurements', *Metallurgical transactions*, vol. 2, no. 7, pp. 1979–1983, 1971.
**[13]** **S. C. Krishna, N. K. Gangwar, A. K. Jha, and B. Pant**, 'On the prediction of strength from hardness for copper alloys', *J. Mater*, vol. 2013, pp. 1–6, 2013.
**[14]** **H. Clemens *et al.***, 'Grain refinement in γ-TiAl-based alloys by solid state phase transformations', *Intermetallics*, vol. 14, no. 12, pp. 1380–1385, 2006.
**[15]** **M. Griffith, D. Keicher, and C. L. Atwood**, 'Free form fabrication of metallic components using laser engineered net shaping (LENS {trademark})', Sandia National Labs., Albuquerque, NM (United States), 1996.
**[16]** **D. Gu**, *Laser additive manufacturing of high-performance materials*. Springer, 2015.
**[17]** **W. Liu and J. DuPont**, 'Fabrication of Titanium Aluminide Matrix Composites by Laser Engineered Net Shaping 124', presented at the 2002 International Solid Freeform Fabrication Symposium, 2002.
**[18]** **A. Sharman, J. Hughes, and K. Ridgway**, 'Characterisation of titanium aluminide components manufactured by laser metal deposition', *Intermetallics*, vol. 93, pp. 89–92, 2018.
**[19]** **C. McCullough, J. Valencia, C. Levi, and R. Mehrabian**, 'Phase equilibria and solidification in Ti-Al alloys', *Acta Metallurgica*, vol. 37, no. 5, pp. 1321–1336, 1989.
**[20]** **V. Küstner *et al.***, 'Gamma titanium aluminides 2003', 2003.
**[21]** **Y.-W. Kim and D. M. Dimiduk**, 'Progress in the understanding of gamma titanium aluminides', *Jom*, vol. 43, no. 8, pp. 40–47, 1991.
**[22]** **P. W. Stephens**, 'Phenomenological model of anisotropic peak broadening in powder diffraction', *Journal of Applied Crystallography*, vol. 32, no. 2, pp. 281–289, 1999.
**[23]** **S. O. Kasap**, *Principles of electronic materials and devices*. Tata McGraw-Hill, 2006.
[24] W. E. Voice, M. Henderson, E. F. Shelton, and X. Wu, 'Gamma titanium aluminide, TNB', *Intermetallics*, vol. 13, no. 9, pp. 959–964, 2005.
**[25]** **A. Traidia, F. Roger, A. Chidley, J. Schroeder, and T. Marlaud**, 'Effect of helium-argon mixtures on the heat transfer and fluid flow in gas tungsten arc welding', *Journal of Chemistry and Chemical Engineering*, vol. 5, no. 9, pp. 854–861, 2011.
**[26]** **Y. Ogino and Y. Hirata**, 'Numerical simulation of metal transfer in argon gas-shielded GMAW', *Welding in the World*, vol. 59, no. 4, pp. 465–473, 2015.
**[27]** **Z. Li, L. Liu, W. Ma, and K. Kakimoto**, 'Effects of argon flow on heat transfer in a directional solidification process for silicon solar cells', *Journal of Crystal Growth*, vol. 318, no. 1, pp. 298–303, 2011.
**[28]** **J. C. Schuster and M. Palm**, 'Reassessment of the binary aluminum-titanium phase diagram', *Journal of phase equilibria and diffusion*, vol. 27, no. 3, pp. 255–277, 2006.
**[29]** **F. Gil, M. Ginebra, J. Manero, and J. Planell**, 'Formation of α-Widmanstätten structure: effects of grain size and cooling rate on the Widmanstätten morphologies and on the mechanical properties in Ti6Al4V alloy', *Journal of Alloys and Compounds*, vol. 329, no. 1–2, pp. 142–152, 2001.
**[30]** **F. Bassani**, *Encyclopedia of condensed matter physics*. Elsevier acad. press, 2005.
**[31]** **S. Hashmi**, *Comprehensive materials finishing*. Elsevier, 2016.
**[32]** **I. Polmear, D. StJohn, J.-F. Nie, and M. Qian**, *Light alloys: metallurgy of the light metals*. Butterworth-Heinemann, 2017.
**[33]** **C. Suryanarayana and M. G. Norton**, 'Crystal structure determination. II: hexagonal structures', in *X-Ray Diffraction*, Springer, 1998, pp. 125–152.
**[34]** **J. Elmer, T. Palmer, S. Babu, and E. Specht**, 'In situ observations of lattice expansion and transformation rates of α and ß phases in Ti–6Al–4V', *Materials Science and Engineering: A*, vol. 391, no. 1–2, pp. 104–113, 2005.
**[35]** **S. Gebhard, F. Pyczak, and M. Göken**, 'Microstructural and micromechanical characterisation of TiAl alloys using atomic force microscopy and nanoindentation', *Materials Science and Engineering: A*, vol. 523, no. 1–2, pp. 235–241, 2009.

**[36]** **J. Kuang, R. Harding, and J. Campbell**, 'Microstructures and properties of investment castings of γ-titanium aluminide', *Materials Science and Engineering: A*, vol. 329, pp. 31–37, 2002.